On the dynamic thermal and thermoelastic contact interaction between a rotor and an auxiliary bearing

Yong, Woon Yik

Award date:
2006

Awarding institution:
University of Bath

ON THE DYNAMIC THERMAL AND THERMOELASTIC CONTACT INTERACTION BETWEEN A ROTOR AND AN AUXILIARY BEARING

Submitted by WOON YIK YONG
for the degree of
Doctor of Philosophy
of the University of Bath
2006

ProQuest LLC
789 East Eisenhower Parkway
P.O. Box 1346
Ann Arbor, MI 48106-1346

Summary

Magnetic bearing systems are protected by auxiliary bearings to prevent damage to the laminated core by the high speed rotor during system failure. In the event of the contact, a high speed rotor will induce localised frictional heating on the inner surface of the auxiliary bearing. This energy dissipation process takes place over a short period of time and the surface temperature rise may be sufficiently high so as to reduce the life-span of the auxiliary bearing.

Research has been undertaken to investigate the thermal and thermoelastic behaviour of the auxiliary bearing when subjected to various contact conditions. The governing equations are fully uncoupled, and thus the thermal and thermoelastic analyses are carried out separately. Thermal Green's function solutions for hole and annular problems are developed for instantaneous sources. Solutions in direct Fourier series form are poorly convergent for short timescale analysis due to the singular nature of the Green's functions. This is improved by implementing the half-space thermal solution to remove the singular behaviour. The final form of the Green's functions consist of analytical half-space solutions together with a well-converged Fourier series remainder solution.

A general annular thermoelastic solution is developed using Fourier expansions and a state-space approach. Two boundary conditions are considered, i.e. rigidly and resiliently mounted outer boundaries. The solution is improved using a remainder function for the thermoelastic annular problem.

The Green's functions are then applied to several contact problems, typical of those likely in realistic magnetic bearing systems. The results show that localised material melting is possible at higher operating speeds. The consideration of rolling element or rigidly mounted bush auxiliary bearings is quantifiable in terms of different temperature rises. For thermoelastic deformation, a simple model is used to investigated the thermoelastic growth of an imperfection when subjected to repeated contact and continuous forward rubbing.

Acknowledgement

I would like to express enormous gratitude to my supervisor for his unfaltering direction and support. The encouragement and guidance of Dr Patrick Keogh has been invaluable.

This PhD was undertaken with the support of Overseas Research Studentship Award and Departmental Studentship. Thanks must also go to my close family and friends, whose faith, support and encouragement has made the hardest goals achievable. Particular mention must go to Meng Ling, Tony, Danny, Jimmy and Siew Leh.

I would like to dedicate this thesis to my parents.

Contents

Nomenclature

The majority of the nomenclature used throughout this thesis is given in the following sections. Any deviations from the conventions described below are explained within the text of the appropriate chapter.

General

x, y	Cartesian coordinate system
x', y'	Half-plane Cartesian coordinate system
r, θ	Polar coordinate system
r', φ	Half-plane Polar coordinate system
t	Time (s)

Rotor Dynamic

a	Acceleration (m/s^2)
c_{db}	Resilient mounting viscous damping (Ns/m)
c_m	Rotor/magnetic bearing radial clearance (m)
c_r	Rotor/auxiliary bearing radial clearance (m)
e	Unbalance eccentricity (m)
$E_{1,2}$	Modulus of elasticity for materials 1 and 2 (N/m^2)

f_c	Contact force (N)
$f_{mx,y}$	Magnetic force (N)
g	Gravitational acceleration (m/s^2)
k_{sb}	Resilient mounting stiffness (N/m)
k_m, k_f	Magnetic force coefficients
K_I	Admittance (A/V)
l_b	Length of auxiliary bearing (m)
m_b, m_r	Masses of auxiliary bearing and rotor
r_{bi}, r_{bo}	Inner and outer radii of auxiliary bearing
s	Travel distance (m)
t_p	Contact period (s)
V	Initial velocity (m/s)
V_0, V_c	Reference and control voltages (V)
β	Incidence angle
μ	Coefficient of friction
υ_1, υ_2	Poisson ratio of materials 1 and 2
ω_f	Contact frequency (rad/s)
ϕ	Unbalance phase (rad)
Ω	Rotor speed (rad/s)

Green's Function Thermal Analysis

c_p	Heat capacity (J/kgK)
E	Modulus of elasticity (N/m^2)
k	Thermal conductivity (W/mK)
r_i, r_o	Inner and outer radii (m)
T	Temperature
T_{Gh}	Green's function half-plane temperature
T_{Ghn}	Fourier coefficient of Green's function half-plane temperature
$\hat{T}_{Gh}$	Green's function second term of half-space temperature
$\overline{T}_{Gh}$	Green's function half-space temperature in Laplace domain
$\overline{T}_{Ghn}$	Fourier coefficient of $\overline{T}_{Gh}$
$T_{G_{annulus}}$	Green's function annular temperature in time domain

$T_{Gn_{annulus}}$	Fourier coefficient of $T_{G_{annulus}}$
$\overline{T}_{G_{annulus}}$	Green's function annular temperature in Laplace domain
$\overline{T}_{Gn_{annulus}}$	Fourier coefficient of $\overline{T}_{G_{annulus}}$
$\overline{T}_{GRn_{annulus}}$	Fourier coefficient of annular remainder function in Laplace domain
$T_{G_{hole}}$	Green's function hole temperature in time domain
$T_{Gn_{hole}}$	Fourier coefficient of $T_{G_{hole}}$
$\overline{T}_{G_{hole}}$	Green's function hole temperature in Laplace domain
$\overline{T}_{Gn_{hole}}$	Fourier coefficient of $\overline{T}_{G_{hole}}$
$\overline{T}_{GRn_{hole}}$	Fourier coefficient of hole remainder function in Laplace domain
α_e	Thermal expansion coefficient (K^{-1})
ρ_d	Density (kg/m^3)
η	Radius ratio, r/r_i
κ	Heat diffusivity (m/s^2)
υ	Poisson ratio

Green's Function Thermoelastic Analysis

$\mathbf{c}_n^{\text{fix}}$, $\mathbf{c}_n^{\text{res}}$	Fixed and resiliently mounted boundary conditions
$\mathbf{E}_n$	Input-vector
G	Shear modulus (N/m^2)
P	Force per unit length (N/m)
u_r, v_θ	Radial and angular displacements (m)
u_{rn}, $v_{\theta n}$	Fourier coefficients of u_r, v_θ
u_{Gr}, $v_{G\theta}$	Green's function radial and angular displacements (m)
$\hat{u}_{Gr'}$, $\hat{v}_{G\varphi'}$	Full-plane Green's function radial and tangential displacements (m)
$u_{Ghx'}$, $u_{Ghy'}$	Half-plane Green's function normal and tangential displacements (m)
u_{Ghr}, $v_{Gh\theta}$	Half-space Green's function radial and tangential displacements (m)
U_{rn}, $V_{\theta n}$	u_{rn}, $v_{\theta n}$ in z-domain

$\mathbf{Y}_n$	Output-vector
z	z-domain ($r = e^z$)
z_i, z_o	Inner and outer radii in z-domain
$\mathbf{Z}_n$	State-vector
λ, β	Elastic constants
σ_y	Yield stress (N/m^2)
σ_1, σ_2	Principal stresses (N/m^2)
χ_r, χ_θ	Stiffnesses per unit length (N/m)
$\sigma_{Fr'}$, $\sigma_{F\varphi}$, $\tau_{Fr'\varphi}$	Flamant's radial, hoop and shear stresses (N/m^2)
$\hat{\sigma}_{Gr'}$, $\hat{\sigma}_{G\varphi}$	Full-plane Green's function radial and hoop stresses (N/m^2)
σ_r, σ_θ, $\tau_{r\theta}$	Radial, hoop and shear stresses (N/m^2)
Λ_r, Λ_θ, $\Lambda_{r\theta}$	σ_r, σ_θ, $\tau_{r\theta}$ in z-domain
ε_r, ε_θ, $\gamma_{r\theta}$	Radial, angular and shear strains
$\varepsilon_{Fr'}$, $\varepsilon_{F\varphi}$, $\gamma_{Fr'\varphi}$	Flamant's radial, angular and shear strains

Contact Model

a	Half-width contact zone (m)
$E_{r,b}$	Elastic modulii of rotor and bearing (N/m^2)
f_{cmax}	Maximum contact force
F	Total load per unit length (N/m)
I	Effective inertia of bearing inner race
$k_{b,r}$	Thermal conductivities of bearing and rotor (W/mK)
m_b, m_{rol}	Masses of inner race and rolling element
p	Pressure distribution (N/m^2)
$Pe_{r,b}$	Peclet numbers for rotor and bearing
q	Total heat flux (W/m^2)
q_0	Amplitude of heat flux (W/m^2)
q_b	Heat flux applied to the bearing (W/m^2)
r_r	Radius of rotor (m)
r_{rol}	Ball element radius (m)
r_{bi}, r_{bo}	Inner and outer radii of the bearing (m)
t_p	Contact period (s)

t_s	Synchronous period (s)
t_Ω	Heat dissipation period (s)
T_c	Contact temperature (K)
T_{ch}	Half-plane contact temperature (K)
$\hat{T}_{ch}$	Second term of the half-plane contact temperature (K)
T_{cn}	Contact temperature Fourier harmonic (K)
T_{cR}	Remainder function contact temperature (K)
$T_{cRn_{annulus}}$	Annular remainder function contact Fourier coefficient (K)
$\hat{u}_{cr}$	Radial contact displacements after n contacts (m)
u_{cr}, $v_{c\theta}$	Radial and tangential contact displacements (m)
u_{chr}, $v_{ch\theta}$	Radial and tangential half-space displacements (m)
u_{cRrn}, $v_{cR\theta n}$	Radial and tangential Fourier harmonics
u_{GRrn}, $v_{GR\theta n}$	Green's function radial and tangential displacements
	Fourier harmonics
α	Heat partition coefficient
β_d	Dundur's constant
κ_b	Thermal diffusivity of bearing (m/s^2)
$\upsilon_{r,b}$	Poisson ratios of rotor and bearing
θ_b	Moving angular position for rotating race problem (rad)
θ_m	Moving angular position for rubbing problem (rad)
θ_0	Half-width angular contact length (rad)
ω_b	Angular velocity of bearing inner race (rad/s)
ω_s	Slip angular velocity (rad/s)

Chapter 1

Introduction

Active magnetic bearings (AMBs) use electromagnetic force to provide non-contacting, friction-free levitation in rotating machinery. These features allow high-speed applications without friction and wear. Furthermore, no lubrication system is required hence AMBs can be incorporated into systems that are sensitive to contamination. Figure 1.1 shows an active magnetic bearing system test rig with the rotor coupled to a motor. There are two AMBs with two rolling element bearings (B,E) embedded in the housing. Components A, C, D and F are bronze bush bearings. An active magnetic bearing system comprises three distinct parts: the magnetic bearing (figure 1.1(c)); the controller/interface system (figure 1.1(d)); and the auxiliary bearing (figure 1.1(e)). The physical structure of the magnetic bearing part is similar to that of an electrical motor. The stator iron core is wound with coils, in which electric current is fed to generate an electromagnetic field to levitate the rotor. The electronic control system is used to position the rotor by altering the electric current in the coils. It incorporates the power and control electronics with signal conditioning prior to calculation of compensating forces, and issues commands to the power amplifier for each axis of control. The auxiliary bearing is used to support the rotor when the machine is non-operational, with the system shut down, or in the event of a system fail-

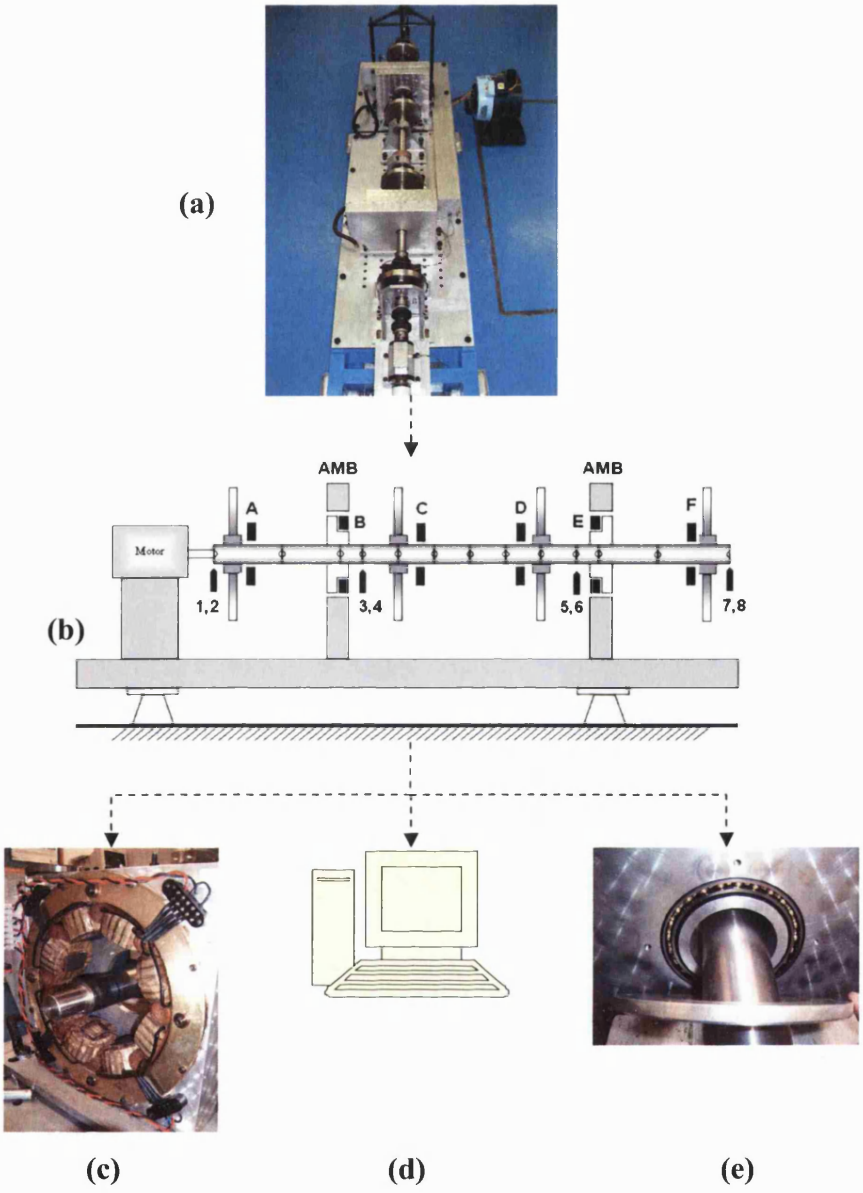

Figure 1.1: (a) Active magnetic bearing system test rig; (b) Schematic diagram of the test rig: bronze bush bearings (A,C,D,F), rolling element bearings (B,E) and sensors (1,2,3,4,5,6,7,8) ; (c) Eight-pole magnetic bearing; (d) Electronic controller/interface system; (e) Rolling element auxiliary bearing.

ure. It allows the rotor to be run down without damage to the rotor itself nor to stator components, such as the iron core, seals etc. Typically, the clearance of an auxiliary bearing is half of that of the magnetic bearing. The most common types of auxiliary bearings are rolling element bearings and bushings. Details of the theoretical knowledge for the design of AMBs are provided in [1].

1.1 Rotor Dynamics

The use of magnetic bearings in rotating machinery applications enables high speed operation since the rotor is levitated without the usual wear and heating problems associated with passive bearings. Thus the designs of compressors, vacuum pumps, centrifuges, generators, and gas turbines have benefited through gains in efficiency and power density. However, magnetic bearings have limited load capacity and may suffer from occasional fault conditions. To protect a magnetic bearing from rotor-stator lamination contacts, auxiliary bearings are incorporated into the system to limit the shaft motion.

An analytical study of the dynamics of interaction for a rigid and balanced rotor-bearing was carried out by Schweitzer *et al.* [2]. Their study considers the dynamic behaviour of the rotor/auxiliary bearing under sliding modelled with a Coulomb friction law. Generally, the sliding contact motion between a rigid rotor and a rigid bearing can be categorised into conical and cylindrical modes. For most of their work, they assumed the rotor to undergo cylindrical mode motion with a sliding condition. High dissipation power, which is associated with thermal and wear problems was noted. Further investigation of similar issues was undertaken by Schweitzer and Fumagalli [3, 4]. Different stator materials, such as carbon graphite and beryllium bronze were investigated experimentally under

various rotor dynamic conditions.

Ishii and Kirk [5] proposed a theoretical formulation to examine the transient response following dropping of a flexible rotor onto auxiliary bearings. The transient response of rotor rotating at full speed caused excessive dynamic loading and high amplitude rotor vibration. If the destructive motion of the rotor in backward whirl takes hold, the rotor displacements and contact forces increase to levels that damage the machinery. Rotor drop tests carried out by Kirk *et al.* [6] suggest that the velocities of the inner race of an auxiliary bearing and the bearing cage determine the auxiliary bearing performance, particularly with regard to ball/roller element skid, which induces excessive heating and premature failure. Ramesh and Kirk [7] developed a computational FEA model to analyse the steady state response of AMB machinery and compared their results with experimental data published in [6]. These modelling techniques were extended for the transient analysis of rotor drop [8]. Similar work on rotor drop transient analysis was conducted by Kirk [9] with parameters appropriate to a full scale compressor.

The studies on rotor drop have greatly enhanced the understanding of the dynamics of rotors supported by auxiliary bearings. However, most of the papers assume the input torque of the rotor is cut off if the magnetic bearings fail. On the other hand, Lawen and Flowers [10] conducted an investigation into the dynamic behaviour of a flexible rotor system supported by linear spring-like bearings and an auxiliary bearing with clearance. Their research focused on the influence of the coupled shaft/bearing/housing vibration modes on the rotor dynamic behaviour. Wang and Noah [11] conducted a steady state analysis of the dynamic interaction of a rotor in contact with an auxiliary bearing. The system was subjected to imbalance excitation, gravitational and side forces. Sets of nonlinear dynamic equations and auxiliary bearing design parameter guidelines

were presented. Lawen and Flowers [12] also performed a similar investigation to gain a better understanding of the rotor dynamic response and to devise suitable guidelines for the design of auxiliary bearings. With regards to magnetic bearing systems most studies do not consider the options for restoration of position control. The work reported in [13, 14, 15] focuses on the problem when control force is available.

1.2 Mechanical Contact

The dynamic behaviour of a rotor in an AMB system is governed by shaft flexibility, auxiliary bearing stiffness, damping, mass, unbalance, location of the auxiliary bearings and clearances. Recent research, undertaken by Cole *et al.* [16], considers the influence of contact on rotor dynamic behaviour, which includes the interaction mechanism and the bulk heat dissipation in the auxiliary bearing. Their research involved analysis of the energy transfer between the rotor and the bearings. The energy transfer between the two components may be influenced by the rotor dynamics, the contact mechanism and the material properties. Theoretically, the system equations can be solved and fully understood by coupling in all of these factors. However, this involves highly complex and non-linear analysis. Generally, the most common failure of an auxiliary bearing is due to heating effects induced by the combination of physical loading and friction forces.

Johnson [17] gives a comprehensive overview of the range of contact problems. A more relevant guide for the contact problem in a rolling element bearing system is presented in [18]. Most of the analyses are based on an elastic half-plane condition, i.e. for small contact area. On the other hand, they ignore the contribution of the physical geometry and boundary conditions of a body and

hence the theories are not fully complete. A general review and discussion on the forces of contact together with their relationship to the material, mechanical properties of the contacting bodies and geometry are given by Adam [19].

1.2.1 Hertzian Contact

Hertzian contact theory, which gives the solution for the frictionless contact of two elastic bodies of ellipsoidal profile, is a well known and widely used theory in contact mechanics. A brief review on Hertzian point/line contact theories was published by Tripp [20]. The article by Tanaka [21] improves the efficiency and accuracy of the contact pressure in Hertzian elliptical contact problem by using numerical integration instead of the elliptical integral methodology of [17]. A more practical consideration of the use of Hertzian line and point contact theory in bearing systems was studied by Houpert [22]. He simplified the relationship between the normal contact load and the normal deformation, which is always required for the study of bearing and gear contact problems. This was achieved by eliminating the reference depth parameter corresponding to zero local displacement. His following paper [23] considers the contact problem of a bearing and gear system, which involves evaluation of contact forces, moments, deformation and race/roller misalignment. Most of the numerous studies on contact mechanics have focused on the solution of particular contact problems to understand the phenomena and mechanism in practical contacting systems.

1.2.2 Frictional Contact

The contact between a rotor and bearing system is always associated with friction. This mechanism will take place whenever relative motion of two surfaces occurs. If the loading rate is sufficiently slow, it is possible to assume that the system is quasi-static, so that the inertia effect can be neglected. The simplest friction model uses the Coulomb representation. Comninou and Dundurs [24] presented some simple examples associated with Coulomb friction. Cattaneo's [25] technique is a well-known procedure solving a contact problem with partial slip using a Coulomb friction model. Here the surface is subjected to a constant normal force along with monotonically increasing tangential traction initiated from zero to a limiting level for a general three dimensional Hertzian contact between similar materials. If the tangential traction crosses the limiting friction threshold, sliding will take place. Cattaneo's procedure was further improved and generalised by Ciavarella [25] and Jäger [26], independently. Both of them showed that the shearing traction distribution, which satisfying both equality (within contact area) and inequality (outside contact area), is comprised of a superposition of limiting friction distribution and opposing distribution. The opposing distribution is known as a corrective shearing distribution in [25], which is equal to the product of coefficient of friction and the normal pressure distribution corresponding to the stick zone, i.e. smaller value of the normal load. This hypothesis was further used in several examples of Cattaneo's contact problem to give explicit solutions [27], which involves reduction the partial slip problem to a superposition of frictionless normal contact problems. Solutions for more general loading scenarios have been established by Jäger [28] using similar procedure.

1.2.3 Dynamic Instability

Recently, a phenomenon associated with quasi-static frictional problems, known as the dynamic instability, or friction-induced vibration, was reported by Ibrahim [29]. This mechanism is a major concern in a wide variety of mechanical systems, especially for braking systems, where friction is a potential cause of vibrations, noise, and excessive wear. Other works relating to dynamic instability, include Adam [30, 31] on sliding of two elastic half-spaces; McMillan [32] and Michaux *et al.* [33] using single degree freedom modelling; Cho and Barber [34] for three-dimensional two degree of freedom contact; and Becker and Oden [35] and Baillet *et al.* [36] for direct numerical solution.

1.2.4 Contact with Asperities

The studies on frictional contact using Amontons-Coulomb friction laws are based on single asperity contact between two surfaces. In fact, a real surface is not entirely smooth microscopically and the contact is generally take place near the asperities of the rough surface. Greenwood and Williamson [37] discovered that the contribution of the asperity of a surface can be neglected if the asperities have a statistical distribution of heights. Many other studies on rough surfaces contact have been undertaken, e.g. Bush *et al* [38], Chang *et al.* [39], Zhao *et al* [40], and Kogut and Etslon[41]. Further exploration on the effect of surface roughness to thermoelastic responses have also been conducted recently, e.g. Liu and Wang [42], Lin and Ovaert [43] on two-dimensional sliding rough surface contact; Ciavarella *et al.* [44] on two dimensional rough surface contacts with thermoelastic instability (TEI); and three-dimensional analysis by Liu and Wang [45].

1.2.5 Numerical Methods

The finite element method (FEM) is a powerful tool for solving contact problems due to its highly adaptive nature for complex geometrical shapes. The majority of studies utilise Lagrange multipliers [46, 47, 48, 49] or penalty function methods [50, 51] to impose the constraints at the contact surface. Recently, the boundary element method (BEM) [52, 53, 54] has emerged as a powerful computational engineering tool as it offers lower computational time and requires boundary discretization only. Another interesting approach by Guyot *et al.* [55] combines FEM-BEM to evaluate displacements by FEM and later method for stresses by BEM for a spherical contact problem.

1.2.6 Green's Functions - Elastic and Thermoelastic Analysis

Ju and Farris [56] were the first to introduce the Fast Fourier transform (FFT) technique into contact analyses to evaluate the linear convolutions for the dry contact problem, i.e.

$$y(t) = \int_{-\infty}^{\infty} X(\tau)G(t-\tau)d\tau \tag{1.1}$$

where $y(t)$ is the linear convolution of $X(t)$ and $G(t)$, and $G(t)$ is a unit impulse response, also known as the Green's function. The same technique was employed in their study on the thermoelastic problem on moving heat sources on a elastic half-space boundary [57].

The fundamental point force elastic solutions for full three-dimensional space have been derived by Kelvin [58]. Boussinesq and Cerruti [59] also presented the

point force solution for an elastic half-plane, where a normal force was applied on the surface boundary. Meanwhile, Mindlin's [60] solutions provide insight of elastic behaviour for point force acting inside an elastic half-space. For the two-dimensional problem, Flamant [17, 59] was the first to develop the stress function due to line loading on the surface boundary of an elastic half-plane. This was followed by Muskhelishvili [61] using the complex variable method to solve the same problem. The complex variable method is a useful tool for developing theories of elasticity without having to determine the stress function. Sokolnikoff [62], Stevenson [63] and Thompson [64] also provide details of the procedure for deriving complex potentials in two-dimensional elasticity.

The study of a concentrated force in an elastically embedded disk was investigated by Dundurs [65]. The disk was embedded in an unbounded elastic plane. The problem was solved by obtaining the proper Airy stress function. Additionally, the solution for the disk with a free boundary was also presented, suitable for any disk system subjected to concentrated forces and moments in equilibrium. Hanson and Wang [66] investigated the elastic responses of a three-dimensional body under ring loadings. Both half-space and full-space applications were considered in their study. The solutions were obtained by directly integrating the fundamental point force solution around the circumference of the ring.

The Green's functions for a static point force in an annular region were developed by Worden and Keer [67]. Two types of annular region were investigated, namely an annulus with the inner boundary as a free surface, and an annulus with inner boundary bounded to a rigid inclusion. They employed the complex variable method discussed in [61] to form the equations for stresses and displacements in terms of Kolosov potentials. These potentials consists of three terms. Firstly, the singular solution for a point load in an infinite plane. The other two are the reactive singular potentials for the sources corresponding to

the origin and the non singular potential, which describe the boundary condition associated with the annular problem. A similar approach was carried out by Chao and Tan [68] to solve the annular problem subjected to a point heat source. This was a steady state thermoelastic analysis solved by using the complex variable method. The expressions for stress and displacement components relating to Kolosov potentials are similar except that an extra potential function representing the temperature field is also included. The heat source was applied within an annular region, where outer and inner boundaries were assumed to be isothermal. The temperature function was expressed in terms of a temperature potential consisting of a singular potential and a power series describing the desired boundary condition. Their research was based on study of Chao and Shen [69], who formulated two distinct types of solution for the circular hole problem. The first type is for the point heat source applied on the infinite plane with circular hole and the second type is for the point heat source inside the inclusion.

The steady state thermoelastic problem for a half-space subjected to a steady state unit strength point temperature source was studied by Sternberg and McDowell [70] using Green's theorem. A classical work using transient thermoelastic Green's functions was published by Barber and Martin-Moran [71]. They utilised the Flamant point force solution together with the hoop stress, which is induced by a unit impulse line heat source on a plane, to obtain an equal and opposite surface pressure by means of the linear convolution theorem. The pressure was then superimposed with the original stress field to give a stress free surface condition. Difficulties were encountered in determining the stress field within the elastic half-space due to the constraint imposed by the Flamant point force solution while calculating the offset pressure. Therefore, only displacements for various distributions of transient surface heating were presented. The displacements and surface stresses induced by a moving heat source over a

two-dimensional half-plane surface were also investigated by Barber [72] using Green's functions developed in [71]. A similar work on developing Green's function displacement was again conducted by Barber [73] using a potential method. His later work with Azarkhin [74] overcame the difficulties in [71] by means of the complex variable method. Other literature on frictional heating thermoelastic analysis including two-dimensional sliding contact is given by Yevtushenko *et al.* [75, 76] and thermal analysis by Pauk [77]. The two-dimensional frictional heating rolling contact problem is considered in [78] and the three-dimensional point heat source thermoelastic transient analysis by Liu and Wang [79]. Most of these results are based on the knowledge of heat conduction that is systematically presented by Carslaw and Jaeger [80].

Surface temperature rise due to moving heat source applied to a surface of a finite or infinite body was studied extensively in tribology by Blok [81]. The temperature is given in terms of a linear convolution expression, where the controlling parameter is the Peclet number, $Pe = va/2\kappa$, where v, a and κ are the sliding velocity, half-length contact zone and thermal diffusivity respectively. Tian and Kennedy [82] analysed the temperature rise at the sliding contact interface for a coated semi-infinite body using integral transforms and the finite element method. Their following publication [83] studied the rise of surface temperature with different Peclet numbers and various heat source profiles. They also presented the heat partition coefficient between two contacting bodies experiencing uniform square heat source in terms of Peclet number. They noted that the temperature distribution for large Pe tends to the two-dimensional solution of the high sliding case. Gao *et al.* [84] presented a transient flash temperature model for three-dimensional rough surface contacts and employed FFT technique to solve the heat partitioning problem.

1.2.7 Thermoelastic Instability

Frictional contact between elastic surfaces takes place in various engineering application such as clutches, gears, brakes etc. The nominal uniform pressure distribution becomes unstable if the relative velocity is higher than a critical speed [85], when hot spots will develop on the deformed surface. This coupled thermal and mechanical phenomenon is known as thermoelastic instability and was investigated by Barber [86] experimentally for a braking system. Thermoelastic analysis has been conducted by various authors [87, 88, 89, 90] on stability analysis and practical consideration of engineering applications [91, 92, 93].

1.3 Scope of this Research

The purpose of this research is to bring attention to issues that are associated with the rotor/auxiliary bearing contact problem. The thermal heating and elastic distortion arising from contact dynamics has received little attention in the open literature. It is conceivable that the limited life of auxiliary bearings may be due to thermoelastic distortion of races and rolling elements. A first step toward assessing the level of this effect is the evaluation of contact temperature.

A brief investigation of the dynamic interaction between rotor and an auxiliary bearing is conducted in chapter 2. It provides a guide to the nature of the contact forces and periods, which are the governing factors in the thermal and thermoelastic contact analysis.

Chapter 3 describes the mathematical approach to obtain the fundamental solution due to unit impulse heat source subjected at the inner boundary of a

hole/annulus. The problem is solved using the Laplace transformation, Fourier series and the Bromwich contour integral (inverse Laplace transform). Moreover, the singular nature associated with the thermal Green's functions as time $t \rightarrow 0$ is examined analytically.

Chapter 4 introduces a technique to remove the singularities in the annular thermal Green's function. This is achieved by subtracting the annular solution with the half-space thermal Green's function and leaving a remainder function. The remainder function has a well converged Fourier series that also retains information on the thermal boundary condition. The explicit half-space solution is then reinstated to give a complete solution. In Chapter 5, a general annular thermoelastic solution, which is expressed in Fourier series representation, is developed using the State-Space technique. The annular thermal solution obtained in Chapter 4 is then implemented into the thermoelastic solution to give the thermoelastic Green's function due to an instantaneous unit heat source on the inner boundary. A similar approach as introduced in Chapter 4, is implemented in Chapter 6 to improve the poorly convergent Fourier series representation of thermoelastic Green's function. The half-plane thermoelastic Green's function is obtained from the work of Barber and Martin-Moran [71] and modified to cover both the plane stress and plane strain conditions.

Chapter 7 focuses on the practical application of the developed Green's functions. The dynamic heat distribution subjects to the inner boundary of a bush bearing is derived based on Hertzian contact/non-Hertzian contact theories and Coulomb friction laws. The thermal investigation is further extended to a moving heat source, which is useful for analysing the rotating inner race problem. The contact of a steel rotor and bronze bush bearing is also investigated in the thermal analysis.

The rise of temperature in the bearing determines the thermal expansion of the body. Chapter 8 conducts investigations on the thermoelastic responses of a bush bearing subjected the heat-flux developed from Hertzian contact theory. Two boundary problems are considered, i.e. rigidly and resiliently mounted bearings. A mechanistic model is built to investigate the thermoelastic growth of the bearing imperfection subjected to cyclic rub contact. Chapter 9 presents the conclusions of this thesis and describes some possible areas for future research and development.

Chapter 2

Dynamic Interaction of Bearing and Rotor

2.1 Overview

In this chapter, the dynamic interaction of a rigid rotor with a resiliently mounted auxiliary bearing is investigated. The dynamic analysis was carried out using Simulink, and was modelled using a single input and single output model (SISO) together with a proportional-integral-derivative controller (PID controller). Several interaction scenarios are presented to provide an idea of the magnitude of the contact force and period subjected to auxiliary bearing.

2.2 Force Components

Consider a simple rotor/AMB dynamic model. Figure 2.1 shows a rotor section in contact with a resiliently mounted auxiliary bush bearing. The bearing is considered to be mounted with a resilient component, such as an elastomeric ring, to provide spring (k_{sb}) and damper (c_{db}) effects. The normal contact force is defined by f_c and assuming that a simple Coulomb friction law applies, the

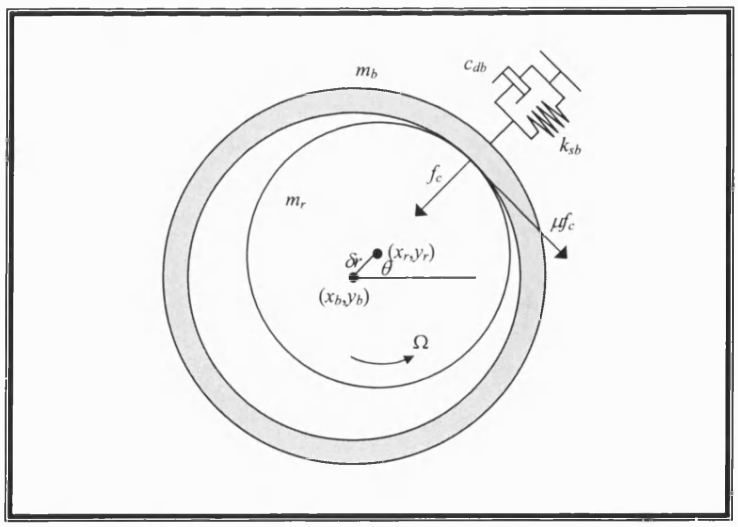

Figure 2.1: Rotor forces due to contact with auxiliary bearing.

frictional force is μf_c. The absolute displacement of the auxiliary bearing in a fixed reference frame is (x_b, y_b) while that of the rotor is (x_r, y_r). The rotor will be in contact with the auxiliary bearing if $\delta r = \sqrt{(x_r - x_b)^2 + (y_r - y_b)^2} \geq c_r$, where c_r is the radial clearance. The non-linear contact force/displacement relation is then given by [94],

$$\delta r - c_r = \frac{f_c}{\pi E^* l_b} \left(\frac{2}{3} + \ln \frac{\pi E^* c_r l_b}{f_c} \right) \tag{2.1}$$

where l_b is the length of the auxiliary bearing and E^* satisfies

$$\frac{1}{E^*} = \frac{1 - \upsilon_1^2}{E_1} + \frac{1 - \upsilon_2^2}{E_2} \tag{2.2}$$

where E_1 and E_2 are the modulii of elasticity of materials 1 and 2, respectively; υ_1 and υ_2 are the Poisson ratios of materials 1 and 2, respectively. Equation (2.1) was stored in a data array corresponding to variables $(\delta r - c_r, f_c)$. The intermediate values were estimated using curve fitting method, i.e. interpolation or extrapolation (built-in block "lookup table").

2.2.1 Magnetic Bearing Forces

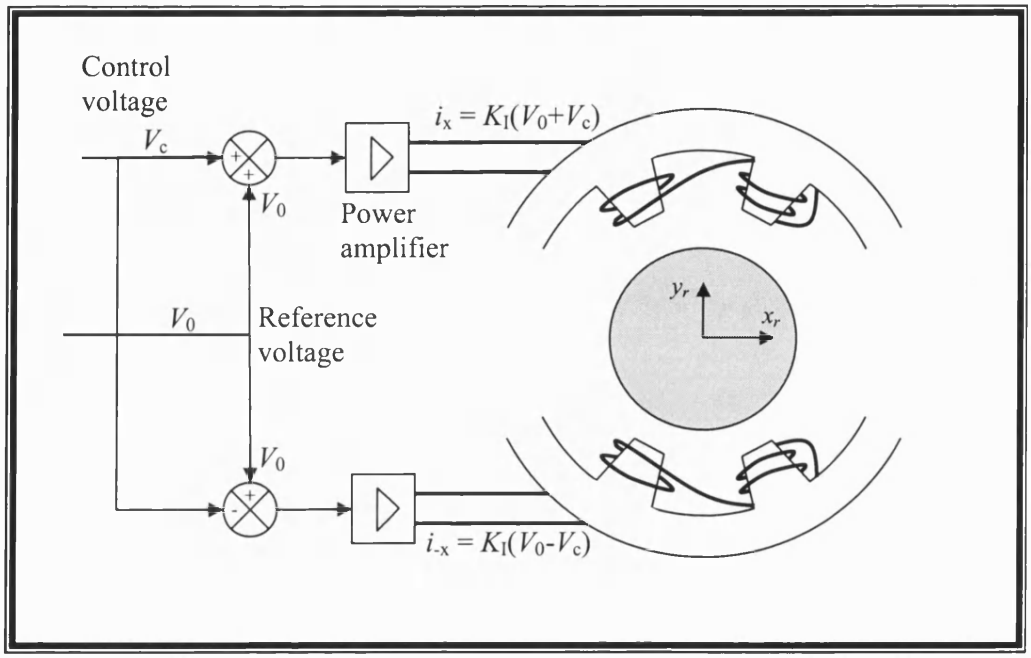

Figure 2.2: Magnetic bearing control axis using opposing pole pairs.

Figure 2.2 shows the control circuit connect to an AMB. A standard model for an eight-pole radial magnetic bearing in a differential driving mode is used in this study. The bearing forces, including a simplified saturation limit, are written as [1],

$$f_{mx,y} = -\frac{k_m}{k_f} \tanh \left\{ k_f \left(\frac{(V_0 + V_c)^2}{(c_m + z)^2} - \frac{(V_0 - V_c)^2}{(c_m - z)^2} \right) \right\} \tag{2.3}$$

where V_0 and V_c are the reference and control voltage respectively; k_m and k_f are the magnetic bearing force coefficients; $z = -x_r$ or $-y_r$, and it is taken that $c_r < c_m$, where c_m is the rotor/magnetic bearing clearance. Control of rotor in each axis is achieved using a PID (Proportional, Integral and Derivative) feedback law on the rotor displacements (x_r, y_r), which are assumed to correspond with the measurement signals.

2.3 Dynamic Equation of Motion

The equations of motion for the auxiliary bearing are

$$m_b\ddot{x}_b + c_{db}\dot{x}_b + k_{sb}x_b = f_c\cos\theta - \mu f_c\sin\theta \tag{2.4}$$

$$m_b\ddot{y}_b + c_{db}\dot{y}_b + k_{sb}y_b = f_c\sin\theta + \mu f_c\cos\theta \tag{2.5}$$

For rotor dynamic behaviour,

$$m_r\ddot{x}_r = f_{mx} - f_c\cos\theta + \mu f_c\sin\theta + m_r e\Omega^2\cos(\Omega t + \phi) \tag{2.6}$$

$$m_r\ddot{y}_r = f_{mx} - f_c\sin\theta - \mu f_c\cos\theta + m_r e\Omega^2\sin(\Omega t + \phi) \tag{2.7}$$

which include unbalance forces. Static forces on the rotor are considered to be compensated by the integral control action and are thus omitted. The initial conditions are,

$$\begin{aligned} x_b(0) &= y_b(0) = \dot{x}_b(0) = \dot{y}_b(0) = 0 \\ x_r(0) &= x_{r0} \quad , \quad y_r(0) = y_{r0} \\ \dot{x}_r(0) &= V\cos\beta \quad , \quad \dot{y}_r(0) = V\sin\beta \end{aligned} \tag{2.8}$$

where the velocity V is applied at an angle of incidence β relative to x-axis shown in figure 2.3. These conditions could be considered as arising from external base acceleration. The position of the rotor (x_r, y_r) and the movement of the auxiliary bearing (x_b, y_b) were evaluated using equations (2.4-2.7). These utilised a Simulink built-in Runge-Kutta-Fehlberg integration method to produce solutions within a relative tolerance of 1×10^{-6}.

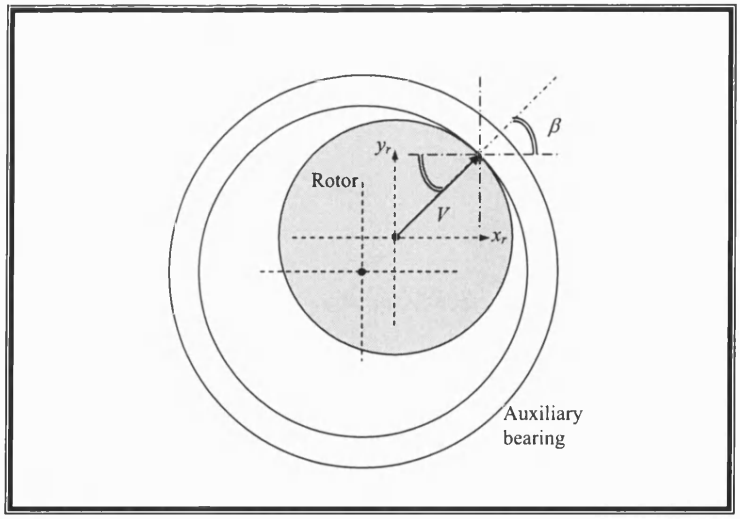

Figure 2.3: Initial velocity of the rotor is applied at an angle of β.

2.4 Case Study of Rotor/Auxiliary Bearing Interaction

The rigid rotor model was built based on a turbomolecular pump system and the rotor/auxiliary/magnetic bearing data are as shown in Table 2.1. The magnetic bearing PID parameters were chosen to give a linearized radial damping of around 1MN/m and linearised radial stiffness of around 1kNs/m. With these parameters, the expected steady synchronous response of the rotor without auxiliary bearing contact is a near circular forward whirl orbit of radius close to $e = 0.2$mm. To estimate a possible impact velocity, suppose that the rotor is unrestrained and experiences a constant acceleration across the full clearance circle:

$$V = \sqrt{4ac_r} \tag{2.9}$$

If $a = 10\text{m/s}^2$ and $c_r = 0.5$mm, then $V = 0.14$m/s. This value could be varied to suit expected conditions. To induce rotor/auxiliary bearing contact, the initial velocity was selected at $V = 0.2$m/s with initial rotor position $(x_r(0), y_r(0)) =$

$(-c_r, 0)$, just touching the auxiliary bearing.

Table 2.1: System data for case study.

Input Parameters	Value
Rotor mass, m_r	20 kg
Radius of rotor, r_r	19.5 mm
Unbalance eccentricity, e	0.2 mm
Young's modulus, E	$2 \times 10^9 \text{N/m}^2$
Unbalance phase, ϕ	0 rad
Bearing mass, m_b	0.1 kg
Inner radius of bearing, r_{bi}	20 mm
Outer radius of bearing, r_{bo}	22 mm
Auxiliary bearing length, l_b	6 mm
Resilient mounting viscous damping rate, c_{db}	1×10^4 Ns/m
Resilient mounting stiffness, k_{sb}	2×10^8 N/m
Rotor/auxiliary bearing radial clearance, c_r	0.5 mm
Rotor/magnetic bearing radial clearance, c_m	0.8 mm
Coefficient of friction, μ	0.1
Rotor angular speed, Ω	1000-3000 rad/s

This section presents several scenarios of the rotor/auxiliary bearing by changing the system parameters.

2.4.1 Angle of Incidence, $\beta = -135°, 135°$

Figure 2.4 shows the system response for an angle of incidence of $\beta = -135°$ with a rotor speed of 1000rad/s. The rotor maintains contact for three bounces

and then loses contact. In the fixed reference frame (figure 2.4), the rotor is seen into settle in the expected forward whirl orbit. The contact force levels remain below 6kN. The angle of incidence was then changed to $\beta = 135°$. Figure 2.6 indicates increased interaction between the rotor and auxiliary bearing. In the fixed frame (figure 2.6), the rotor settles into a steady forward circular rub mode. The contact force behaviour of figure 2.7 shows that multiple bounces occur with a peak levels exceeding 40kN before continuous rub occurs with an eventual steady state of around 15kN. The residual oscillation on the steady level is due to unbalance excitation.

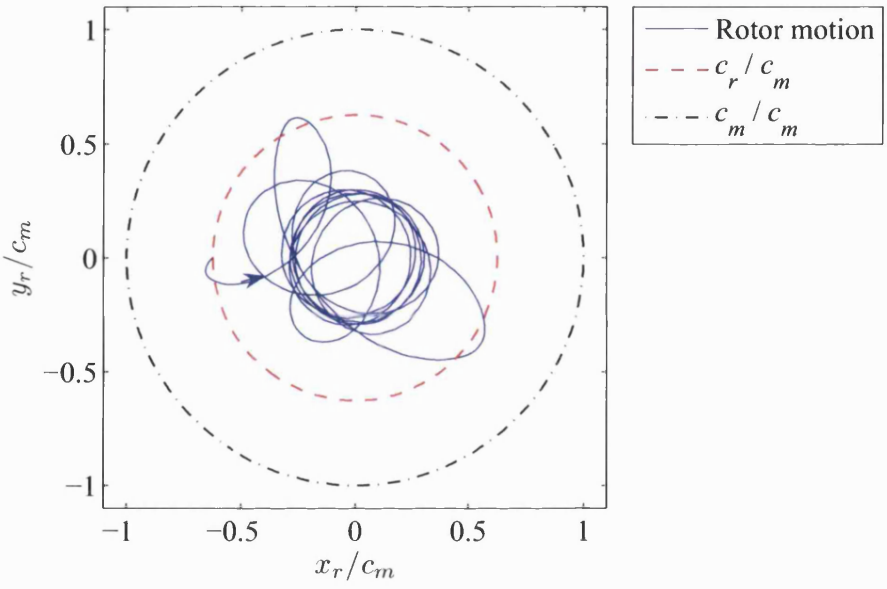

Figure 2.4: Rotor motion in fixed frame. Initially $(x_r(0), y_r(0)) = (-c_r, 0)$, $V = 0.2\text{m/s}$ and $\beta = -135°$.

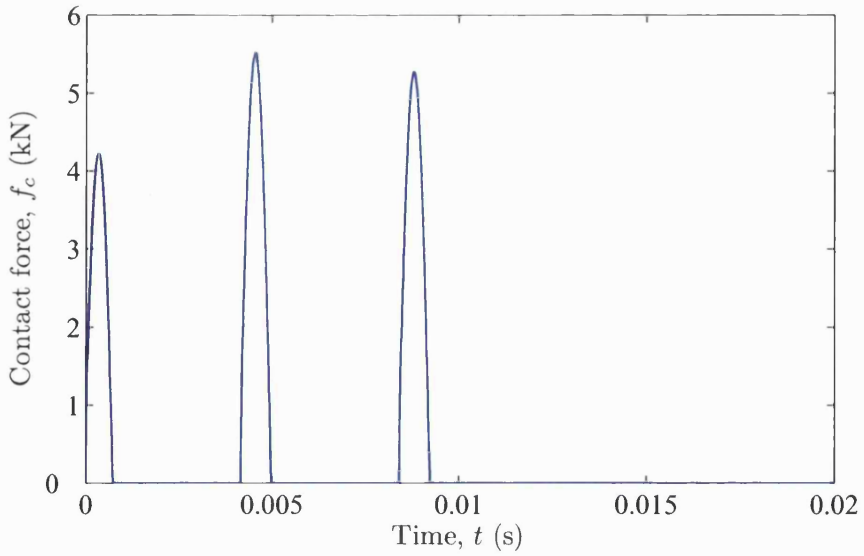

Figure 2.5: Contact force response on auxiliary bearing. Initially condition, $(x_r(0), y_r(0)) = (-c_r, 0)$, $V = 0.2\text{m/s}$ and $\beta = -135°$.

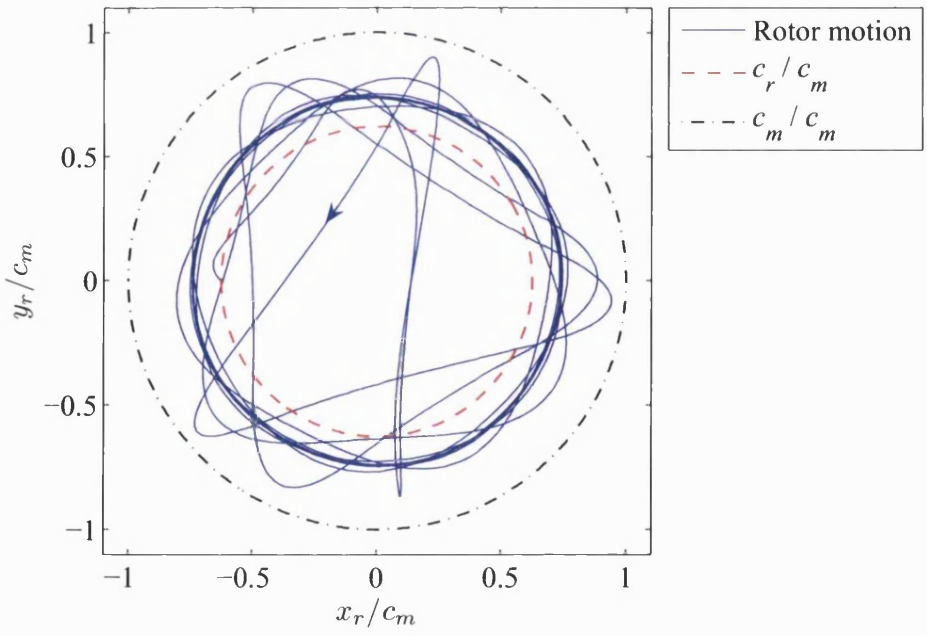

Figure 2.6: Rotor motion in fixed frame. The initial condition was set to $(x_r(0), y_r(0)) = (-c_r, 0)$, $V = 0.2\text{m/s}$ and $\beta = 135°$.

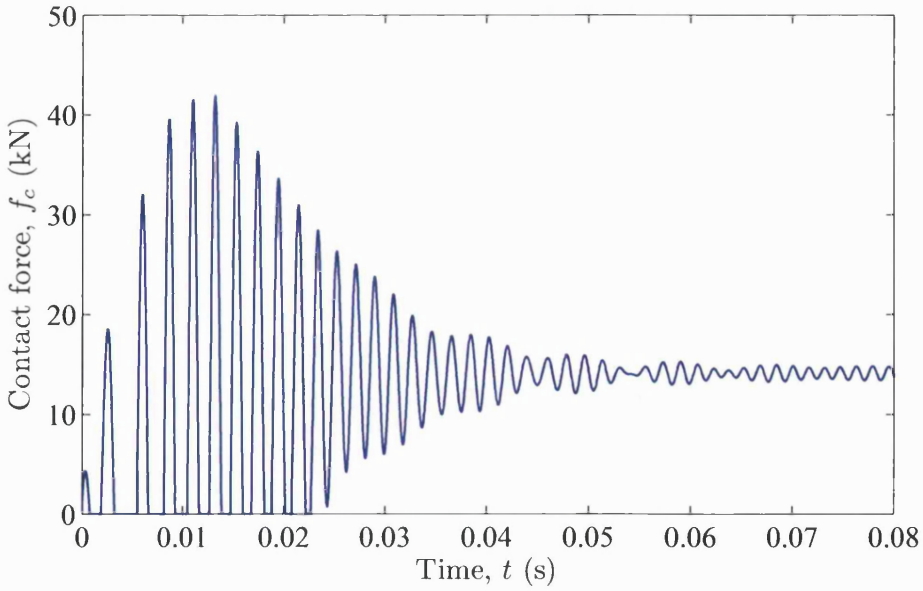

Figure 2.7: Contact force response with initial condition $(x_r(0), y_r(0)) = (-c_r, 0)$, $V = 0.2\text{m/s}$ and $\beta = 135°$.

2.4.2 Variation of Auxiliary Bearing Stiffness and Damping Coefficient

Figure 2.6 shows that the rotor deflections due to the bounce motion may be close to the rotor/magnetic bearing clearance circle. However, for large auxiliary bearing deflection, the mounting stiffness characteristic will be non-linear and increasing. The value of the mounting stiffness was therefore increased $k_{sb} = 4 \times 10^8\text{N/m}$ and the contact forces are shown in figure 2.8 ($\Omega = 1000\text{rad/s}$). Rotor bounce motion is more severe and persistent (figure 2.9) with peak levels almost reaching 55kN. With all other data as for figure 2.6, increasing the damping rate to $c_{db} = 2 \times 10^4\text{Ns/m}$ resulted in fewer contacts, settling into a rubbing mode at 15kN and peak forces around 35kN.

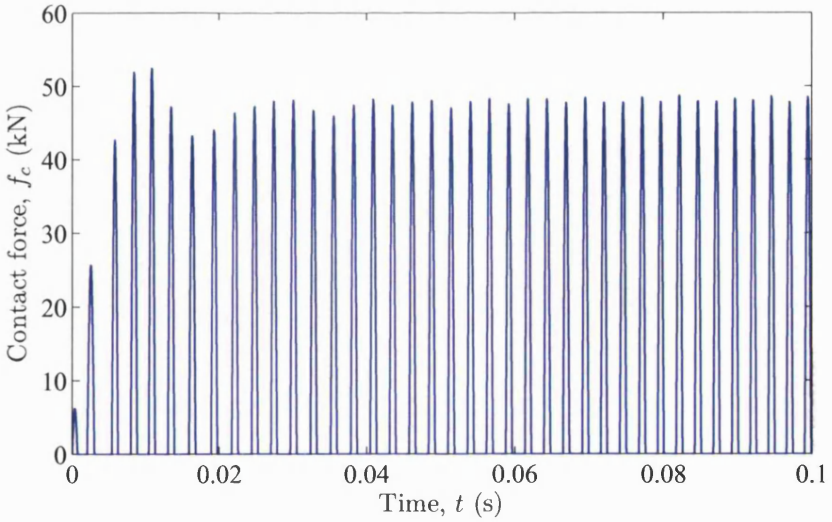

Figure 2.8: Rotor contact force responses (data changes from figure 2.7: $k_{sb} = 4 \times 10^8$N/m).

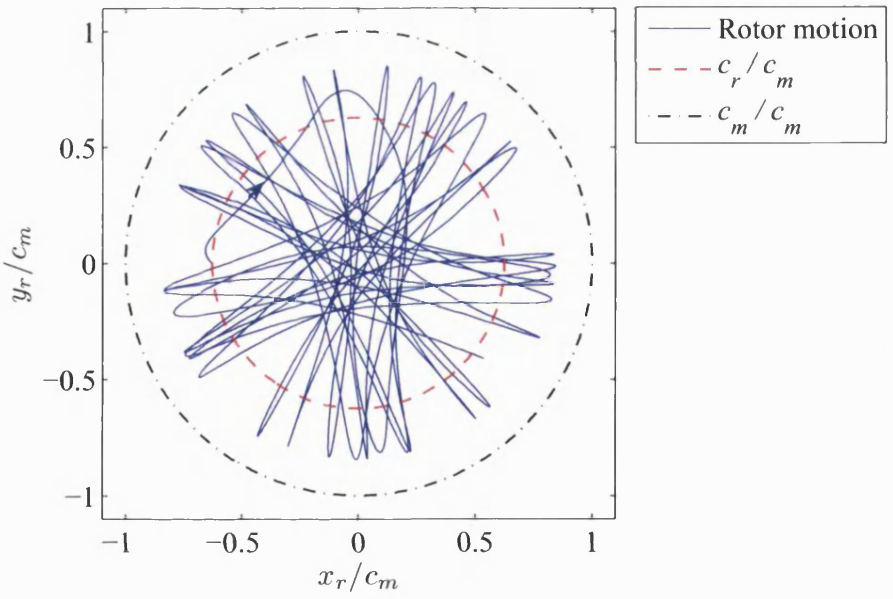

Figure 2.9: Rotor motion in fixed frame (data changes from figure 2.7: $k_{sb} = 4 \times 10^8$N/m).

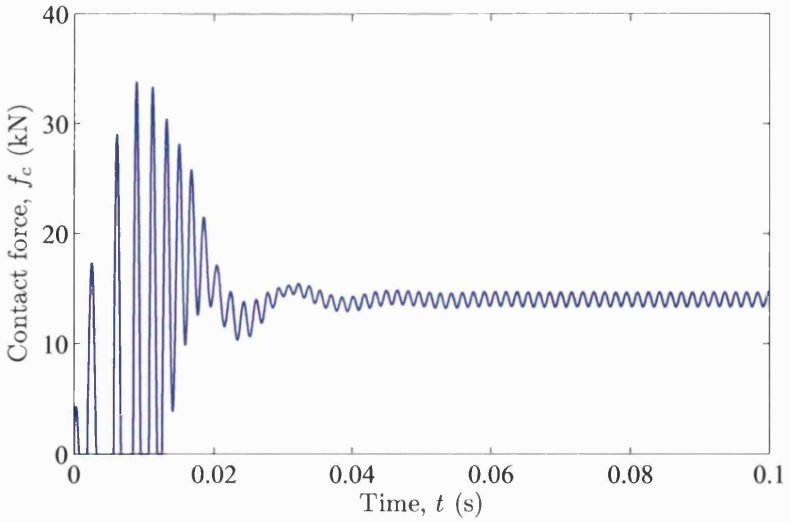

Figure 2.10: Rotor contact force responses (data changes from figure 2.7: $c_{db} = 2 \times 10^4$N/m).

2.4.3 Variation of Rotor Speed

The rotor speed in sections 2.4.1 and 2.4.2 was 1000rad/s. Figures 2.11 and 2.12 show the rotor trajectories at speeds 2000rad/s and 3000rad/s respectively, with all other data as for figure 2.4. Both figures show that the increase of rotor speed induces more severe rotor motion and higher contact forces associate with higher rotor deflection, which exceeds the rotor/magnetic bearing clearance. However, the rotor motion can be constrained to be within the rotor/magnetic bearing clearance by configuring the parameters properly. Figure 2.13 shows the rotor motion in a fixed frame operating at $\Omega = 3000$rad/s, the auxiliary bearing stiffness and damping coefficient being set to 1×10^7 and 5×10^4 respectively, $\beta = -90°$ with initial velocity V =0.14m/s. The rotor maintains contact for three bounces (figure 2.13) and then loses contact settling to forward whirl orbit. The peak contact force is around 43kN.

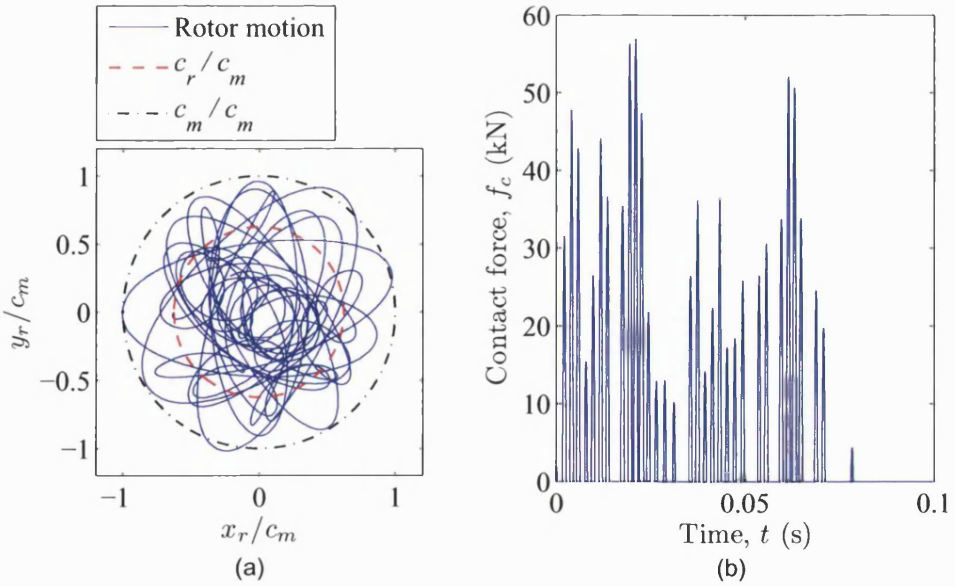

Figure 2.11: (a) Rotor motion in fixed frame; (b) Rotor contact force responses (data changes from figure 2.4: $\Omega = 2000$rad/s).

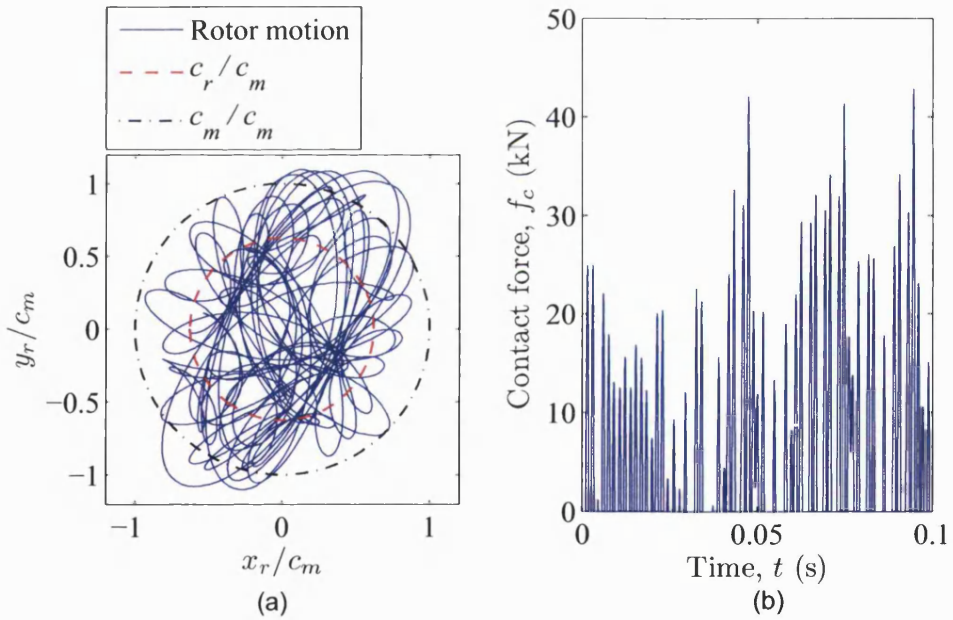

Figure 2.12: (a) Rotor motion in fixed frame; (b) Rotor contact force responses (data changes from figure 2.4: $\Omega = 3000$rad/s).

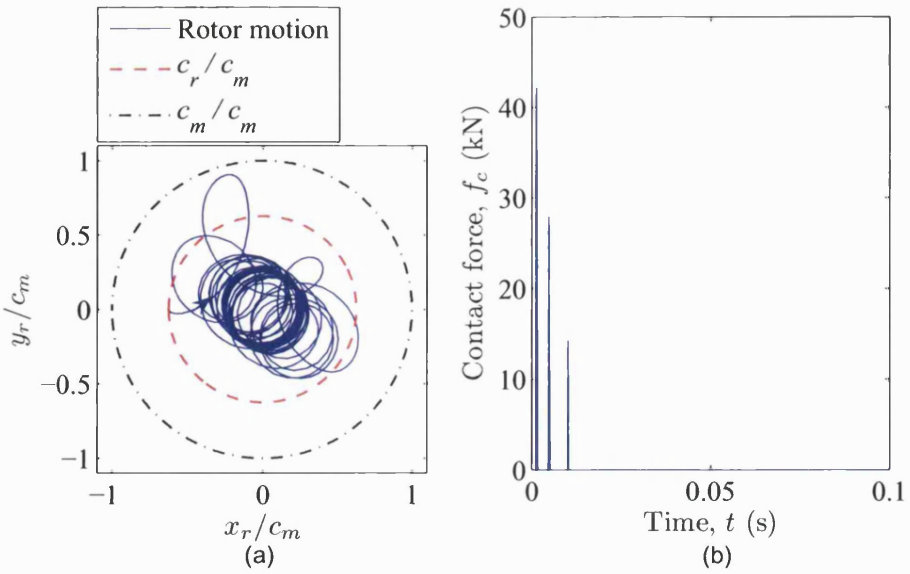

Figure 2.13: (a) Rotor motion in fixed frame; (b) Rotor contact force responses (data changes from figure 2.4: $\Omega = 3000$rad/s, $k_{sb} = 1 \times 10^7$N/m, $c_{db} = 5 \times 10^4$Ns/m, $V = 0.14$m/s and $\beta = -90°$).

2.4.4 Alternative Configurations

The dynamic simulation results indicate that a range of contact force levels is likely depending on the initial and operating conditions. Table 2.2 show the peak forces corresponding to various initial and operating conditions. The friction coefficient values $\mu = 0.1, 0.2$ are typical for a lubricated bush bearing. However, the friction coefficient would be higher for dry conditions. In this case, backward rotor whirl may be initiated. To avoid this problem, rolling element bearings are commonly used. As the inner race of such as bearing spins up to the rotor speed, the effective friction seen by the rotor is decreased. Hence the values of $\mu = 0.1, 0.2$ used in Table 2.2 are also equivalent levels for a typical rolling element bearing during dynamic contact periods. Table 2.2 shows that with increase of rotor speed and coefficient of friction, it is easy to induce rotor deflection greater than the rotor/magnetic bearing clearance. An expanded view

of the force response of figure 2.7 is shown in figure 2.14. It is seen that the response is similar to a positive half-cycle of $\sin \omega_\phi t$ where ω_ϕ is the contact frequency equal to π/t_p and t_p is the contact period.

2.5 Closure

A rotor/magnetic bearing/auxiliary bearing model has been established using SISO control with PID parameters. The dynamic interaction between the rotor and the bearing is a complex phenomena, and it is governed by the bearing stiffness, damping, unbalance, clearances and initial conditions. Operating parameters, such as contact forces and period, were predicted, which are essential information for any thermal and thermoelastic analysis. The dynamic response of the contact force for a single contact event was found to be similar to positive half-cycle of a sine curve profile.

Table 2.2: Maximum contact force corresponding to various configurations.

	Ω (rad/s)	k_{sb} (N/m) ($\times 10^8$)	c_{db} (Ns/m) ($\times 10^4$)	μ	β	V (m/s)	f_{cmax} (N)	t_p (s)	Comment
P1	1000	2.0	1.0	0.1	-135°	0.2	5500	0.0009	
P2	1000	0.2	1.0	0.1	-135°	0.2	2600	0.0015	
P3	1000	2.0	1.0	0.1	135°	0.2	42000	0.0010	
P4	1000	4.0	1.0	0.1	135°	0.2	53000	0.0008	
P5	1000	4.0	1.0	0.1	-135°	0.2	6200	0.0006	
P6	1000	2.0	1.0	0.2	-135°	0.2	11000	0.0010	
P7	1000	2.0	1.0	0.2	135°	0.2	180000		Exceed c_m
P8	1000	0.2	1.0	0.2	135°	0.2	7900	0.0020	Exceed c_m
P9	2000	1.0	1.0	0.1	-135°	0.1	24600	0.0011	
P10	2000	1.0	1.0	0.1	-135°	0.2	23000	0.0010	
P11	2000	1.0	1.0	0.2	-135°	0.2	24000	0.0012	
P12	2000	2.0	4.0	0.1	135°	0.1	36000	0.0009	
P13	3000	1.0	5.0	0.1	-90°	0.1	45000	0.0006	
P14	3000	0.1	4.0	0.1	-135°	0.2	36000	0.0009	
P15	3000	0.1	4.0	0.1	-90°	0.2	40000	0.0008	
P16	3000	0.2	1.0	0.1	-135°	0.2	13000	0.0012	Exceed c_m

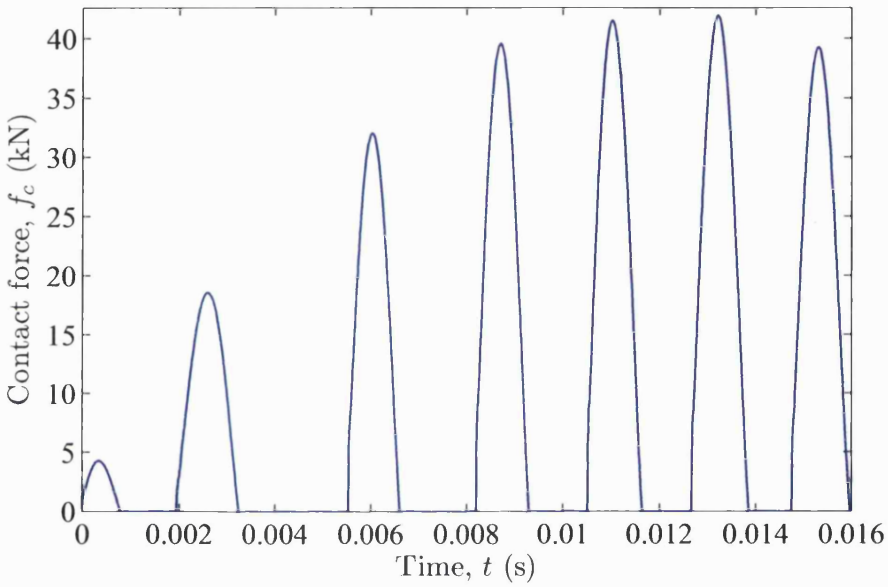

Figure 2.14: Closer observation of contact force in figure 2.7. Note that the dynamic contact profile is similar to a half-length sinusoid.

Chapter 3

Green's Function For Auxiliary Bearing Thermal Analysis

3.1 Overview

In this chapter, it will be shown how to develop the transient temperature integration kernels for a circular hole in an infinite plane and an annular region. The Green's functions for thermal transient analysis is the fundamental solution for a unit instantaneous heat source in a given body with a specified boundary condition of zero heat flux. It allows determination of the solution to other boundary and initial conditions in terms of definite integrals. For two-dimensional transient analysis, it represents the temperature at (r, θ) at time t due to an instantaneous unit line source generated at position (r', θ') at time τ'. Direct solutions are already available from the Carslaw and Jaeger [80]. However, it will be shown that these forms are limited in terms of accurate short time behaviour. The methodology to overcome these limitations is explained.

3.2 Laplace Transformation

The Laplace transform is a useful tool for solving linear ordinary differential equations, such as the heat conduction equation, which will be discussed in the following sections. The Laplace transform $\mathcal{L}$ is defined by,

$$\mathcal{L}[f(t)](s) = \int_0^\infty f(t)e^{-st}dt = \overline{f}(s) \tag{3.1}$$

Standard results include,

$$\mathcal{L}[f'(t)](s) = s\overline{f}(s) - f(0) \tag{3.2}$$

and the inverse Laplace transform from the Bromwich integral,

$$f(t) = \frac{1}{2\pi i}\int_{c-i\infty}^{c+i\infty} \overline{f}(s)e^{st}ds \tag{3.3}$$

where all singularities of $\overline{f}(s)$ lie to the left of $\mathrm{Re}(s) = c$.

3.3 Two-Dimensional Line Source for Circular Hole in Infinite Plane

This section presents the derivation of the thermal solution of circular hole problem subjected to a unit instantaneous line heat source (1W/ms). The reader is referred to a standard text such as Carslaw and Jaeger [80] for basic results.

3.3.1 Solution for Region Bounded Internally by Circular Hole

Let (r, θ) be the polar coordinates in a region bounded by a circular hole and infinite plane, $(r_i \leq r \leq \infty, 0 \leq \theta \leq 2\pi)$. At time $t = 0$, an instantaneous unit line source is applied at the point $(r, \theta) = (r_i, 0)$. For a fixed region, the thermal Green's function, which is denoted by $T_{G_{hole}}(r, \theta, t)$, satisfies the general heat conduction equation,

$$\nabla^2 T_{G_{hole}} = \frac{1}{\kappa} \frac{\partial T_{G_{hole}}}{\partial t} \tag{3.4}$$

In this case the heat liberated may be written as,

$$-kr_i \left. \frac{\partial T_{G_{hole}}}{\partial r} \right|_{r=r_i} = \delta(t)\, \delta(\theta) \tag{3.5}$$

where $\delta(\theta)$ and $\delta(t)$ are the Dirac-delta function impulse at $\theta = 0$ and $t = 0$ respectively. The condition (3.5) indicates that the boundary behaves adiabatically after application of the heat source. Taking the Laplace transformation of equation (3.4) with respect to time,

$$\frac{\partial^2 \overline{T}_{G_{hole}}}{\partial r^2} + \frac{1}{r} \frac{\partial \overline{T}_{G_{hole}}}{\partial r} + \frac{1}{r^2} \frac{\partial^2 \overline{T}_{G_{hole}}}{\partial \theta^2} - \frac{s}{\kappa} \overline{T}_{G_{hole}} - T_{G_{hole}}(r, \theta, 0) = 0 \tag{3.6}$$

If the initial temperature is zero $T_{G_{hole}}(r, \theta, 0) = 0$, equation (3.6) can be solved as a Fourier series in the circumferential coordinate:

$$\overline{T}_{G_{hole}}(r, \theta, s) = \sum_{n=-\infty}^{\infty} \overline{T}_{Gn_{hole}}(r, s)\, e^{in\theta} \tag{3.7}$$

where

$$r^2\frac{\partial^2\overline{T}_{Gn_{hole}}}{\partial r^2}+r\frac{\partial\overline{T}_{Gn_{hole}}}{\partial r}-\left(n^2+\frac{s}{\kappa}r^2\right)\overline{T}_{Gn_{hole}}=0 \tag{3.8}$$

The temperature must decay to zero as $r \rightarrow \infty$, therefore the general solution for equation (3.8) can be written in term of Bessel functions as,

$$\overline{T}_{Gn_{hole}}=B_n(s)K_n\left(\lambda r\right) \tag{3.9}$$

where $\lambda=\sqrt{s/\kappa}$. The boundary condition of equation (3.5) is satisfied by taking,

$$B_n(s)=-\frac{1}{2\pi k\lambda r_i K_n'\left(\lambda r_i\right)} \tag{3.10}$$

Hence,

$$\overline{T}_{Gn_{hole}}=-\frac{K_n\left(\lambda r\right)}{2\pi k\lambda r_i K_n'\left(\lambda r_i\right)} \tag{3.11}$$

Therefore, the temperature response of the circular hole problem in the Laplace transform domain can be written as,

$$\overline{T}_{Ghole}\left(r,\theta,s\right)=\sum_{n=-\infty}^{\infty}\left(-\frac{K_n\left(\lambda r\right)}{2\pi k\lambda r_i K_n'\left(\lambda r_i\right)}\right)e^{in\theta} \tag{3.12}$$

3.3.2 Inverse Laplace Transformation for Circular Hole Problem

The Fourier coefficients of the temperature response given in equation (3.11) can be transformed to the time domain by means of the Bromwich contour

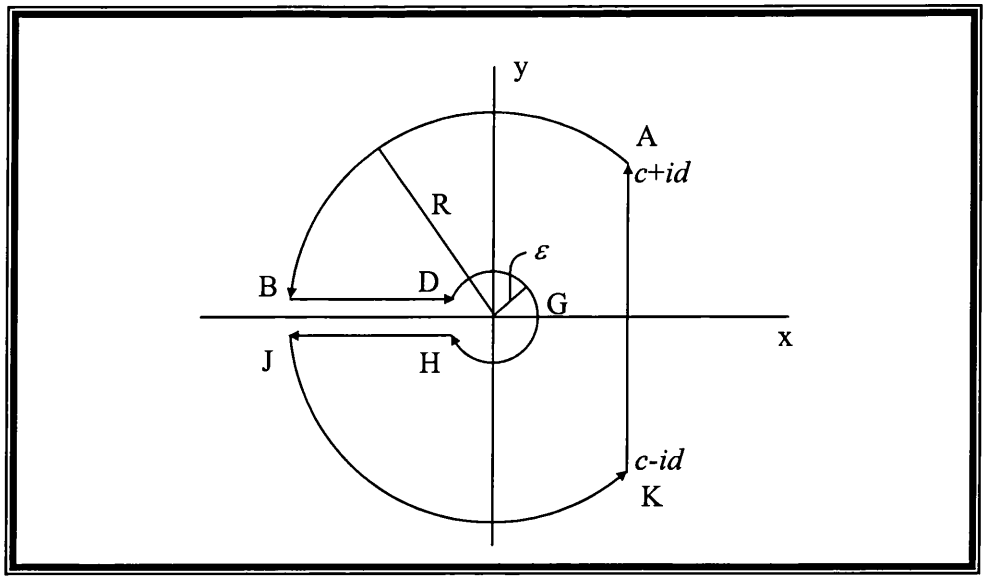

Figure 3.1: Bromwich contour for inverse Laplace transformation with a possible branch point at the origin. For the circular hole problem, the effect of the branch point is zero as $\varepsilon \to 0$. The contributions of AB and JK are also tend to zero as $R \to \infty$.

integral,

$$T_{Gn_{hole}}(r,t) = \frac{1}{2\pi k} \times \frac{1}{2\pi i} \int_{c-i\infty}^{c+i\infty} \left(-\frac{K_n(\lambda r)}{\lambda r_i K_n'(\lambda r_i)} \right) e^{st} ds \tag{3.13}$$

The contour (see figure 3.1) maybe completed in the left half of the complex plane. In general, the branch cut contribution yields the following form,

$$\begin{aligned} &\frac{1}{2\pi i} \int_{c-i\infty}^{c+i\infty} f_n(\lambda r)\, e^{st} ds \\ &= \underbrace{-\frac{\kappa}{\pi i} \int_0^{\infty} f_n\left(rve^{\frac{\pi i}{2}}\right) e^{-\kappa v^2 t} dv}_{\text{Integration along the positive phase of the branch cut (DB)}} \\ &+ \underbrace{\frac{\kappa}{\pi i} \int_0^{\infty} f_n\left(rve^{-\frac{\pi i}{2}}\right) e^{-\kappa v^2 t} dv}_{\text{Integration along the negative phase of the branch cut (HJ)}} \\ &= -\frac{2\kappa}{\pi i} \int_0^{\infty} \text{Imag}\left[f_n\left(rve^{\frac{\pi i}{2}}\right) \right] e^{-\kappa v^2 t} dv \end{aligned} \tag{3.14}$$

Derivation of the Bromwich contour integration results (3.14) is shown in Appendix A. Therefore, equation (3.13) can be reduced to,

$$T_{Gn_{hole}}(r,t) = -\frac{1}{2\pi k} \times \frac{2\kappa}{\pi i} \int_0^\infty \text{Imag}\left[-\frac{K_n\left(rve^{\frac{\pi i}{2}}\right)}{ve^{\frac{\pi i}{2}} r_i K_n'\left(r_i ve^{\frac{\pi i}{2}}\right)} \right] e^{-\kappa v^2 t} v dv \quad (3.15)$$

Simplification of individual terms in equation (3.15) gives

$$K_n\left(rve^{\frac{\pi i}{2}}\right) = -\frac{\pi i^{-n+1}}{2} H_n^{(2)}(vr) \quad (3.16)$$

$$K_n'\left(rve^{\frac{\pi i}{2}}\right) = -K_{n+1}\left(rve^{\frac{\pi i}{2}}\right) + \frac{n}{\left(rve^{\frac{\pi i}{2}}\right)} K_n\left(rve^{\frac{\pi i}{2}}\right) \quad (3.17)$$

$$K_{n+1}\left(rve^{\frac{\pi i}{2}}\right) = -\frac{\pi i^{-n}}{2} H_{n+1}^{(2)}(vr) \quad (3.18)$$

Therefore, the relevant form to evaluate temperature is

$$T_{Gn_{hole}}(r,t) = \frac{1}{2\pi k} \times \frac{2\kappa}{\pi i} \times \int_0^\infty \text{Imag}\left[\frac{H_n^{(2)}(vr)}{vr_i H_{n+1}^{(2)}(vr_i) - n H_n^{(2)}(vr_i)} \right] e^{-\kappa v^2 t} v dv \quad (3.19)$$

Since $H_n^{(2)}(x) = J_n(x) - iY_n(x)$, it can be further deduced that

$$\begin{aligned} T_{Gn_{hole}}(r,t) &= \frac{1}{2\pi k} \times \frac{2\kappa}{\pi i} \int_0^\infty \frac{\phi_n(vr_i) Y_n(vr) - \psi_n(vr_i) J_n(vr)}{\phi_n^2(vr_i) + \psi_n^2(vr_i)} e^{-\kappa v^2 t} v dv \\ &= \frac{1}{2\pi k r_i} \times \frac{2\kappa}{\pi i} \int_0^\infty \frac{\phi_n(x) Y_n(x\eta) - \psi_n(x) J_n(x\eta)}{\phi_n^2(x) + \psi_n^2(x)} e^{-\beta x^2} x dx \end{aligned} \quad (3.20)$$

where $\eta = r/r_i \geq 1$, dimensionless time function, $\beta = \kappa t / r_i^2$, and

$$\phi_n(x) = xJ_{n+1}(x) - nJ_n(x)$$

$$\psi_n(x) = xY_{n+1}(x) - nY_n(x)$$

Thus the temperature response of the exterior region bounded by the circular hole is

$$T_{G_{hole}}(r,\theta,t) = \sum_{n=-\infty}^{\infty} T_{Gn_{hole}}(r,t)\, e^{in\theta} \tag{3.21}$$

3.3.3 Thermoelastic Properties and Input Parameters

The parameters correspond to a standard stainless bearing steel, X105CrMo17 (EN 10088-1:1995), which is normally used in SKF roller bearings. The dimensions were taken from the auxiliary bearing that was used in a turbomolecular pump test rig. The bearing properties and the input parameters for the thermal and thermoelastic analysis are given in Tables 3.1 and 3.2.

Table 3.1: Elastic properties of stainless bearing steel for thermal and thermoelastic analysis.

Properties	**Values**
Density, ρ	7700 kg/m^3
Modulus of Elasticity, E	200×10^9 N/m^2
Poisson ratio, υ	0.283
Yield Stress	1280×10^6 N/m^2
Thermal Conductivity, k	15 W/mK
Heat Capacity, c_p	460 J/kgK
Typical Melting Point	1400 K
Thermal Expansion Coefficient, α_e	11×10^{-6} K^{-1}

Table 3.2: Parameters for inner race of auxiliary bearing.

Input Parameter	Magnitude
Inner radius - annulus/hole	20 mm
Annulus outer radius	22 mm
Outer radius for circular hole problem	∞
Width of inner race	6 mm

3.3.4 Graphical Presentation of the Solution for Circular Hole Problem

This section provides visual results for the circular hole Green's function solution evaluated using equation (3.21) with a truncated series consisting of 50 harmonics. A maximum of 50 harmonics was chosen due to limitations of the Matlab software relating to Bessel function evaluation. The integration in equation (3.20) was achieved using the Matlab built-in function "quadl", which requires a finite upper limit. Figure 3.2 shows the variation of the integrand in equation (3.20) corresponding to the integrating variable x at different time points. It can be seen that the integrand decays exponentially to zero for large values of x with known $\beta = \kappa t/r_i^2 \geq 0$. Therefore, the upper limit of the integration can be set to a finite value, i.e. 1000 for this particular problem. $T_{Gn_{hole}}$ was stored as a three-dimensional data array corresponding to (n, r, t) prior to the full model simulation. The size of the array is $(50 \times 25 \times 50)$ corresponded to 50 harmonics, 25 evenly distributed radius $(r_i \leq r \leq 0.04)$ and 50 exponentially decay distribution of time points $(0.001 \leq t \leq 2s)$. The estimated CPU time for the data storage process was up to 4 hours with a 2.4GHz processor. A built-in curve fitting function "interp2" was used to estimate the intermediate values and a full model analysis took up to 20 minutes CPU time.

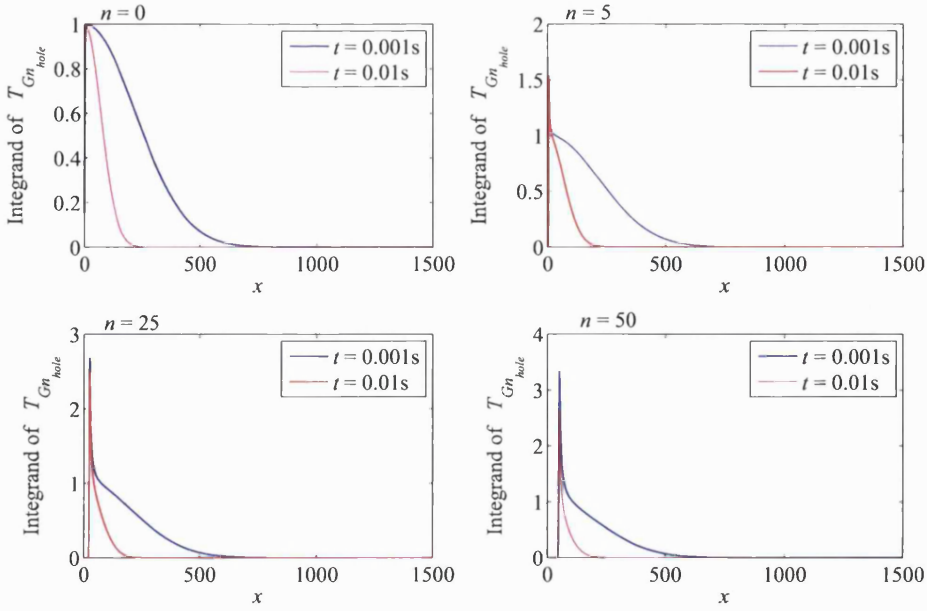

Figure 3.2: Variation of the integrand of equation (3.20) corresponding to integrating variable, x.

Figure 3.3 shows the temperature distribution in the region at $t = 0.5$s of a stainless bearing steel material with a hole of 0.02m in radius. The basic input parameters and thermal properties of the bearing stainless steel are given in Tables 3.1 and 3.2. The temperature contour plot clearly shows that the contour lines approach the circular boundary with normal intersection, which is consistent with the adiabatic boundary condition, i.e. $\partial T/\partial r = 0$. Figure 3.4, shows the circular boundary temperatures corresponding to different time points with identical input parameters. For short timescale analysis, oscillatory temperature behaviour is observed owing to the poor convergence of the Fourier series. In fact the series representation of (3.21) must diverge at $(\theta, t) = (0, 0)$ due to the singular nature of the Green's function, which will be discussed further in a later section.

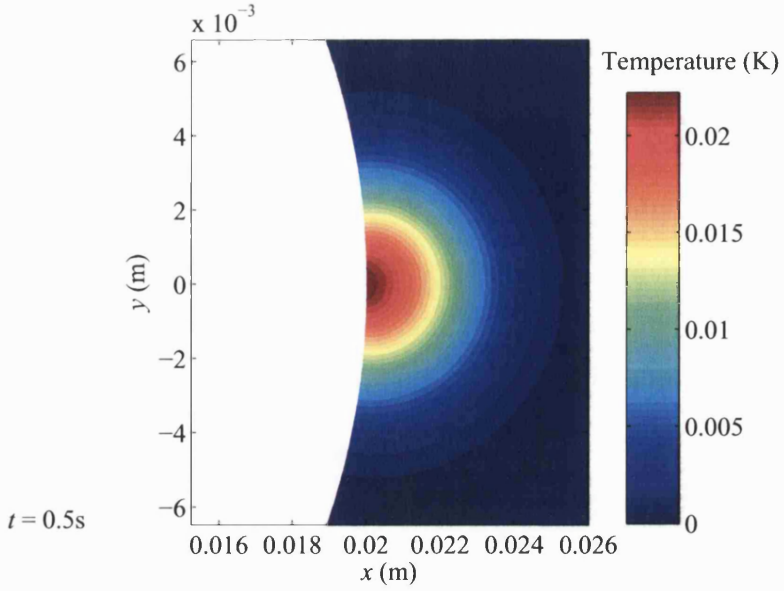

Figure 3.3: Contour plot of the circular hole solution at $t = 0.5$s. Contour lines approach the inner circular boundary with normal intersection, which is consistent with the zero heat flux condition.

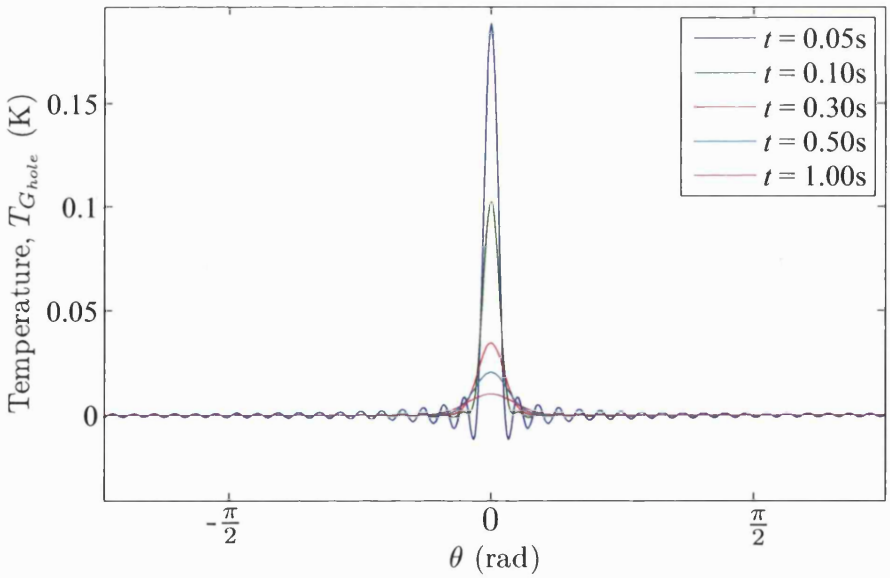

Figure 3.4: Inner boundary temperatures corresponding to different time points, $t = 0.05$s, 0.1s, 0.3s, 0.5s, 1s for the circular hole problem.

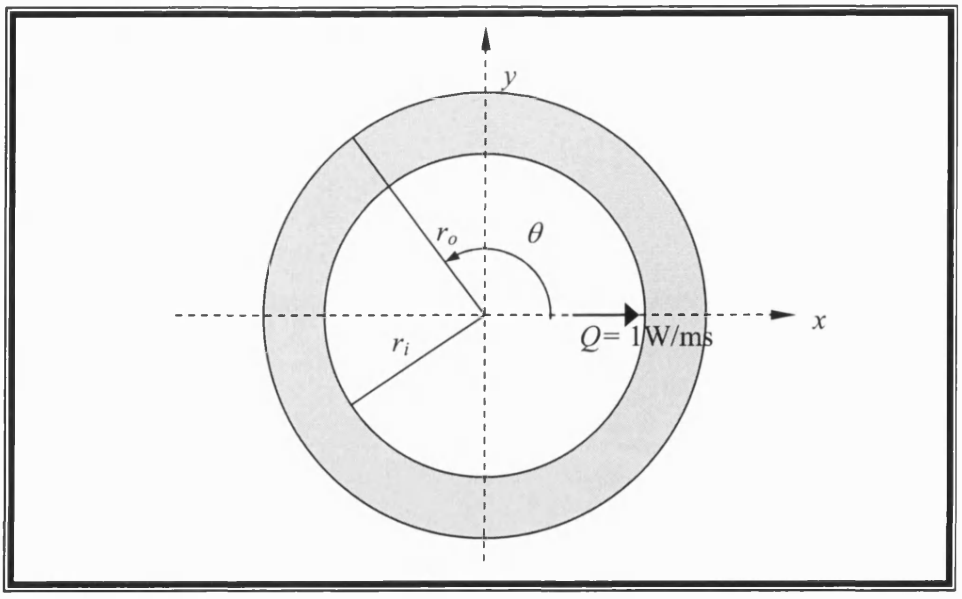

Figure 3.5: Region bounded by two concentric circular contours. Instantaneous unit heat source applied at $(r, \theta) = (r_i, 0)$, at $t = 0$. Both inner and outer boundaries comply with adiabatic conditions.

3.4 Two-Dimensional Line Source for Annular Region

The solution for an annular region can be obtained by following a similar procedure as for the circular hole problem.

3.4.1 Solution for Annular Region

Consider a region bounded by two concentric circular contours (Figure 3.5), where $(r_i \leq r \leq r_o, 0 \leq \theta \leq 2\pi)$. At $t = 0$, an instantaneous unit heat source is applied at $(r_i, 0)$. Both inner and outer boundaries must satisfy adiabatic

conditions, which can be expressed mathematically,

$$-kr_i \left.\frac{\partial T_{G_{annulus}}}{\partial r}\right|_{r=r_i} = \delta(t)\,\delta(\theta) \tag{3.22}$$

$$-kr_o \left.\frac{\partial T_{G_{annulus}}}{\partial r}\right|_{r=r_o} = 0 \tag{3.23}$$

Taking the Laplace transform and Fourier series expansion of equation (3.4), and solving the heat conduction equation (identical to equation (3.8)). The general solution is

$$\overline{T}_{Gn_{annulus}}(r,s) = B_n(s)K_n(\lambda r) + C_n(s)I_n(\lambda r) \tag{3.24}$$

where K_n and I_n are the modified Bessel functions. Laplace transformation of the inner boundary condition with respect to t yields,

$$-2\pi kr_i \left.\frac{\partial \overline{T}_{Gn_{annulus}}}{\partial r}\right|_{r=r_i} = 1 \tag{3.25}$$

Hence,

$$B_n(s)K_n'(\lambda r_i) + C_n(s)I_n'(\lambda r_i) = -\frac{1}{2\pi kr_i\lambda} \tag{3.26}$$

Similarly, for the outer boundary condition,

$$-2\pi r_o k \left.\frac{\partial \overline{T}_{Gn_{annulus}}}{\partial r}\right|_{r=r_o} = 0 \tag{3.27}$$

giving,

$$B_n(s)K_n'(\lambda r_o) + C_n(s)I_n'(\lambda r_o) = 0 \tag{3.28}$$

Therefore,

$$B_n(s) = -\frac{1}{2\pi k} \times \frac{I_n'(\lambda r_o)}{r_i\lambda\Delta_n(\lambda)} \tag{3.29}$$

$$C_n(s) = \frac{1}{2\pi k} \times \frac{K_n'(\lambda r_o)}{r_i\lambda\Delta_n(\lambda)} \tag{3.30}$$

where

$$\Delta_n(\lambda) = K_n'(\lambda r_i) I_n'(\lambda r_o) - I_n'(\lambda r_i) K_n'(\lambda r_o) \tag{3.31}$$

Subsequently, the transformed solution for the annular region subjected to instantaneous unit heat source is,

$$\overline{T}_{G_{annulus}}(r,\theta,t) = \frac{1}{\pi k} \sum_{n=-\infty}^{\infty} \left(\frac{-K_n(\lambda r) I_n'(\lambda r_o) + I_n(\lambda r) K_n'(\lambda r_o)}{2\lambda r_i \Delta_n(\lambda)} \right) e^{in\theta} \tag{3.32}$$

3.4.2 Inverse Laplace Transformation of Annular Problem

The technique for obtaining the inverse Laplace transform of the annular solution (3.32) using Bromwich contour integration still applies. However, in this particular case, the Bessel functions terms possess poles along the negative real axis, together with a branch point at the origin. Although, mathematically, this issue can be resolved by using the Residue theorem, each pole must be located numerically. However the combination of poles and a branch point singularity complicates matters.

To overcome this problem, an angular ratio is introduced into the inversion formula. This can be achieved by completing the inversion contour as shown in figure 3.6.

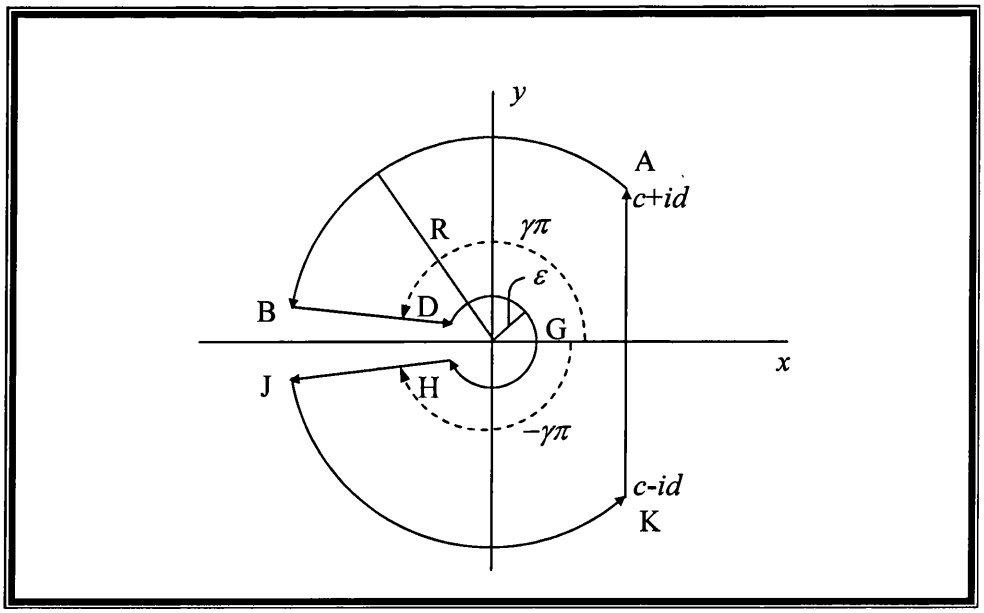

Figure 3.6: Bromwich contour for inverse Laplace transformation of annulus solution. The ratio γ, must be chosen to be less than unity to bypass the singularities along the negative x-axis.

The poles are avoided on the contours BD and JH on which it is appropriate to change the variable according to

$$s = \kappa v^2 e^{\pm\gamma\pi i} \tag{3.33}$$

where $0.5 < \gamma < 1$. When $\gamma = 1$, the outcome is identical to equation (3.14). Following the details given in Appendix B, the general inversion formula applies:

$$\begin{aligned}
&\frac{1}{2\pi i}\int_{c-i\infty}^{c+i\infty} f_n(\lambda r)e^{st}ds \\
&= \frac{2\kappa}{\pi r_i^2}\int_0^{\infty} \text{Imag}\left\{ f_n\left(\frac{r}{r_i}xe^{i\pi\gamma/2}\right) e^{\frac{\kappa x^2 t e^{i\pi\gamma}}{r_i^2}+i\pi\gamma}\right\} xdx \\
&\quad + \underbrace{\lim_{\varepsilon\to 0}\int_{-\gamma\pi}^{\gamma\pi} f_n\left(\sqrt{\frac{\varepsilon}{\kappa}}e^{i\theta/2}r\right) e^{\varepsilon e^{i\theta}t} i\varepsilon e^{i\theta}d\theta}_{\text{contribution from the contour around the branch point}}
\end{aligned} \tag{3.34}$$

where

$$f_n(\lambda r) = \frac{-K_n(\lambda r)I_n'(\lambda r_o) + I_n(\lambda r)K_n'(\lambda r_o)}{\lambda r_i \Delta_n(\lambda)} \tag{3.35}$$

The Fourier coefficients for the annular solution can be then expressed as,

$$T_{Gn_{annulus}}(r,t) = \frac{1}{2\pi k} \times \frac{2\kappa}{\pi r_i^2} \times \begin{cases} \int_0^\infty \text{Imag}\left\{ f_0\left(\eta e^{\frac{i\pi\gamma}{2}}\right) e^{\beta x^2 e^{i\pi\gamma} + i\pi\gamma} \right\} x dx & \\ + \left(\frac{\pi\gamma}{\eta_o^2 - 1}\right) & (n=0) \\ \int_0^\infty \text{Imag}\left\{ f_n\left(\eta x e^{\frac{i\pi\gamma}{2}}\right) e^{\beta x^2 e^{i\pi\gamma} + i\pi\gamma} \right\} x dx & (n \neq 0) \end{cases} \tag{3.36}$$

where $\beta = \kappa t / r_i^2$, and

$$f_n\left(\eta x e^{i\pi\gamma/2}\right) = \frac{-K_n\left(\eta x e^{i\pi\gamma/2}\right) I_n'\left(\eta_o x e^{i\pi\gamma/2}\right) + I_n\left(\eta x e^{i\pi\gamma/2}\right) K_n'\left(\eta_o x e^{i\pi\gamma/2}\right)}{x e^{i\pi\gamma/2} \Delta_n\left(x e^{i\pi\gamma/2}\right)} \tag{3.37}$$

where $\eta = r/r_i$, $\eta_o = r_o/r_i$ and,

$$\Delta_n\left(x e^{\frac{i\pi\gamma}{2}}\right) = K_n'\left(x e^{\frac{i\pi\gamma}{2}}\right) I_n'\left(\eta_o x e^{\frac{i\pi\gamma}{2}}\right) - I_n'\left(x e^{\frac{i\pi\gamma}{2}}\right) K_n'\left(\eta_o x e^{\frac{i\pi\gamma}{2}}\right) \tag{3.38}$$

Hence, the Green's function for the annular problem is,

$$T_{G_{annulus}}(r,\theta,t) = \sum_{n=-\infty}^{\infty} T_{Gn_{annulus}}(r,t) e^{in\theta} \tag{3.39}$$

Figure 3.7 shows the variation of the integrand of equation (3.36) with respect to the integrating argument x corresponding to $\gamma = 0.75$, $\gamma = 0.85$ and $\gamma = 0.95$ respectively. The input parameters are similar to the circular hole thermal analysis with the outer radius, $r_o = 0.022$m. Although the variation with γ is obvious, evaluation of the integrals in (3.36) must yield a results that is independent of γ. This is evident from figure 3.8. The dotted line shows the difference between the

solution evaluated using $\gamma = 0.75$ and $\gamma = 0.95$.

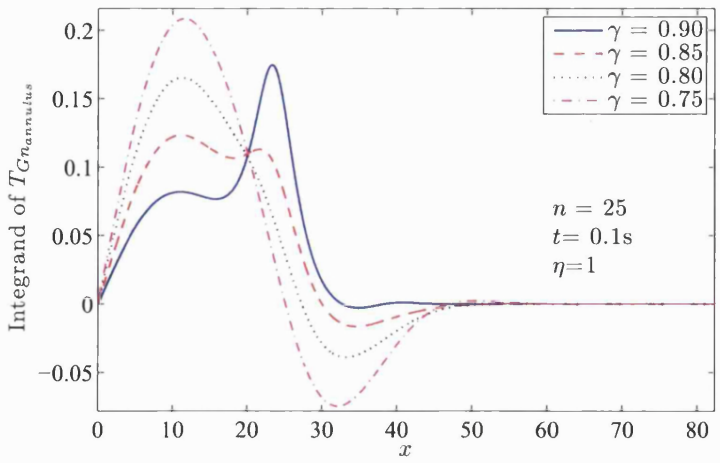

Figure 3.7: Variation of the integrand of equation (3.34) with respect to the integrating argument correspond to various angular ratio, i.e. $\gamma = 0.75$, $\gamma = 0.80$, $\gamma = 0.85$ and $\gamma = 0.95$. Although all three γ give different curves, the final outcome of equation (3.36) independent of γ.

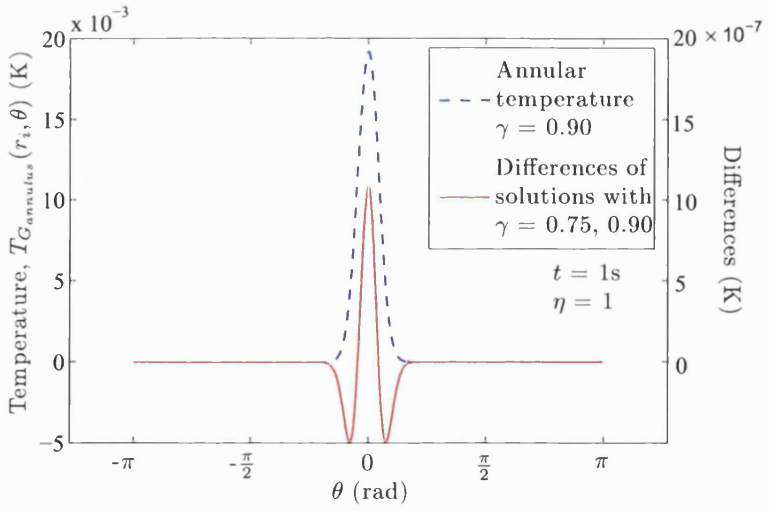

Figure 3.8: The dashed line represents the temperature (left axis) at $t = 1$s at the inner boundary when subjected to an instantaneous unit line source at $t = 0$. The solid line represents the difference (right axis) between the solutions evaluated using $\gamma = 0.75$ and $\gamma = 0.90$.

3.4.3 Graphical Presentation of the Solution for Annular Problem

Figure 3.9 shows the variation in the integrand in equation (3.36) corresponding to the integrating variable x. An exponential decay of the integrand was noted and the upper limit of equation (3.36) was set to 1000 in the Matlab modelling. The storage process of $T_{Gn_{annulus}}$ took up to 6 hours due to the higher accuracy required for the oscillatory behaviour of the integrand. The size of the array was identical to the circular hole problem, i.e. $(50 \times 25 \times 50)$ with $r_i \leq r \leq r_o$. It took 20-30 minutes to run a full model analysis.

Figure 3.10 shows the contour plot of the temperatures at time points, 0.1s and 0.5s. The contour lines clearly show that both boundaries are consistent with adiabatic conditions as they approach the both inner and outer boundary with normal intersection. Figure 3.11 shows the inner surface temperature at five different time points $(0.05 - 1)$s. For short timescale analysis, oscillatory responses can be observed owing to the singular nature of Green's function, which will be discussed in the next section. The comparison of the circular hole and annular region results show that similar temperature arise over short timescale, as shown in Figure 3.12. However, for long time periods, after heat has propagated, the annular temperature is higher than the circular hole temperature, as expected (Figure 3.13).

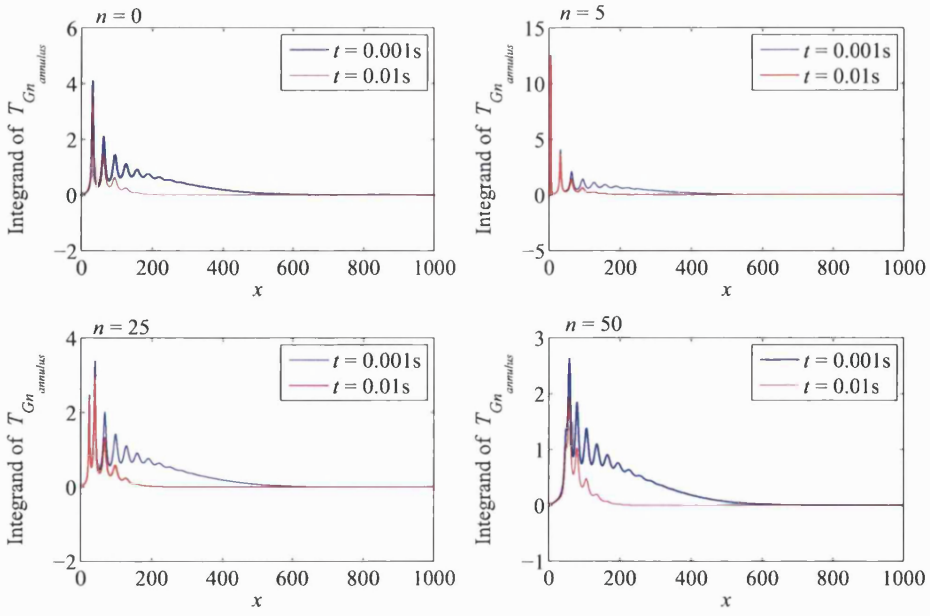

Figure 3.9: Variation of the integrand of equation (3.36) corresponding to integrating variable, x with various harmonics at $t = 0.001,\ 0.01$s.

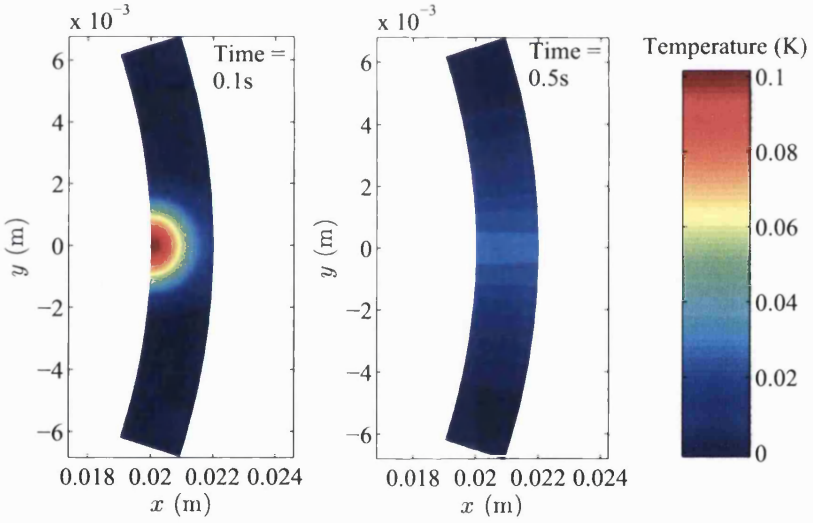

Figure 3.10: Contour plot of the annulus temperature at $t = 0.1$s and $t = 0.5$s. The temperature is localised initially. Since the system is adiabatic, the heat is retained in the body. Eventually the temperature would settle to a permanently increased body temperature.

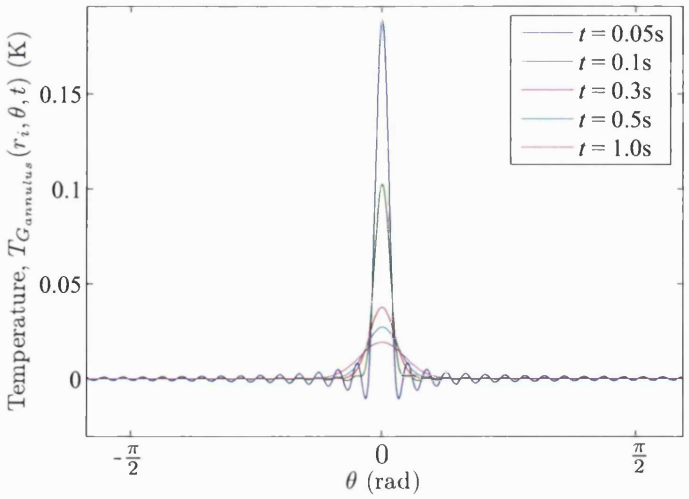

Figure 3.11: Temperature rise at the inner boundary of the annular region at various time points. The oscillations visible at 0.05s and 0.10s are due to the truncation of the Fourier series representation with 50 harmonics.

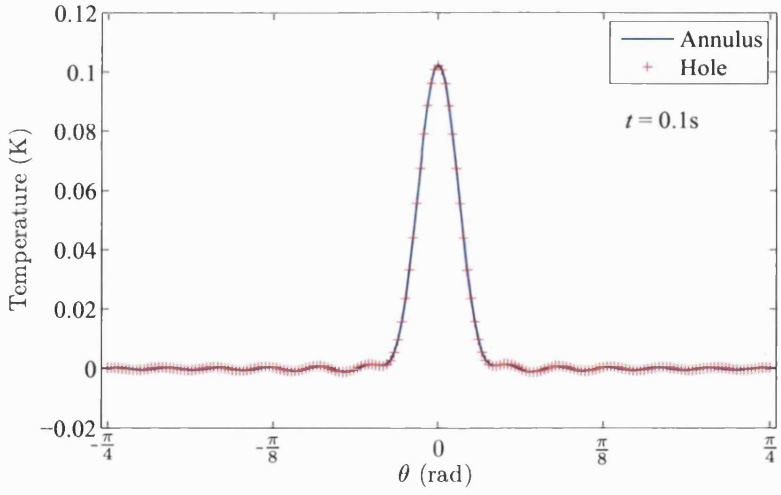

Figure 3.12: The inner boundary temperature rises for the circular hole and annular regions for short timescale analysis are very similar since the heat remains localised.

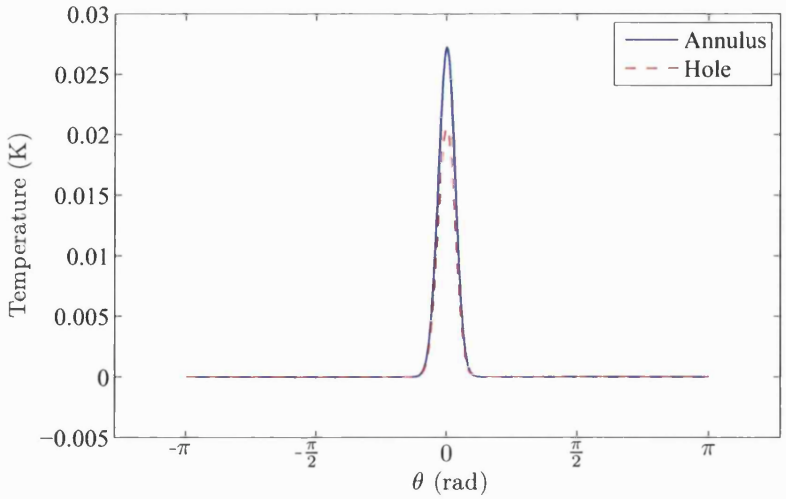

Figure 3.13: Inner boundary temperatures of annular and circular hole problems at $t = 0.5s$. The annular temperature is higher than the circular hole temperature due to heat being retained in an finite body and that boundary conditions are assumed adiabatic.

3.5 Nature of Thermal Green's Functions for Circular Hole and Annulus

The singular nature of Green's functions results in poor convergence of the series representations of the solutions, particular when t is small. This implies that a large number of harmonics is required for short timescale analysis. The following subsections illustrate the singular nature of the solutions.

3.5.1 Singular Nature of Green's Function for Circular Hole

The solution of line source acting on the inner boundary of a circular hole in in an infinite plane is governed by the term (see section 3.3.2),

$$\overline{T}_{Gn_{hole}}(r,s) = \frac{K_n(\lambda r)}{2\pi k \lambda r_i K_n'(\lambda r)} \tag{3.40}$$

Short timescale analysis is asymptotically related to large s behaviour. The asymptotic expansion of each individual Bessel function for large argument gives,

$$\begin{aligned} K_n(\lambda r) \sim & \sqrt{\frac{\pi}{2\lambda r}} e^{-\lambda r} \left\{ 1 + \frac{\mu - 1}{8\lambda r} + \frac{(\mu-1)(\mu-9)}{2(8\lambda r)^2} \right. \\ & \left. + \mathbf{O}\left(\frac{1}{\lambda^3}\right) \right\} \end{aligned} \tag{3.41}$$

$$\begin{aligned} K_n'(\lambda r) \sim & -\sqrt{\frac{\pi}{2\lambda r}} e^{-\lambda r} \left\{ 1 + \frac{\mu + 3}{8\lambda r} + \frac{(\mu-1)(\mu+15)}{2(8\lambda r)^2} \right. \\ & \left. + \mathbf{O}\left(\frac{1}{\lambda^3}\right) \right\} \end{aligned} \tag{3.42}$$

$$\begin{aligned} \frac{1}{K_n(\lambda r)} \sim & -\sqrt{\frac{2\lambda r}{\pi}} e^{\lambda r} \left\{ 1 - \frac{\mu + 3}{8\lambda r} \right. \\ & \left. + \frac{(\mu-1)(\mu+15) - 2(\mu+3)^2}{2(8\lambda r)^2} + \mathrm{O}\left(\frac{1}{\lambda^3}\right) \right\} \end{aligned} \tag{3.43}$$

where $\mu = 4n^2$. Hence the Fourier coefficients can be written as,

$$\begin{aligned} \overline{T}_{Gn_{hole}}(r,s) \sim & \frac{e^{-\lambda(r-r_i)}}{2\pi k \lambda \sqrt{r r_i}} \left\{ 1 + \left(\frac{\mu - 1}{r} - \frac{\mu + 3}{r_i} \right) \frac{1}{8\lambda} \right. \\ & + \left(\frac{(\mu-1)(\mu-9)}{r^2} - \frac{2(\mu-1)(\mu+3)}{r r_i} \right. \\ & \left. \left. - \frac{(\mu-1)(\mu+15) - 2(\mu+3)^2}{r_i^2} \right) \frac{1}{2(8\lambda)^2} + \mathrm{O}\left(\frac{1}{\lambda^3}\right) \right\} \end{aligned} \tag{3.44}$$

The leading term is indicative of [95, page 246] ,

$$T_{Gn_{hole}}(r,t) \sim \frac{\sqrt{\kappa}}{2\pi k r_i \sqrt{\pi t}} \tag{3.45}$$

as $t \rightarrow 0$. This behaviour is valid for all harmonics. Figure 3.14 shows the time variation of the harmonics evaluated using the inverse Laplace transform of equation (3.11).

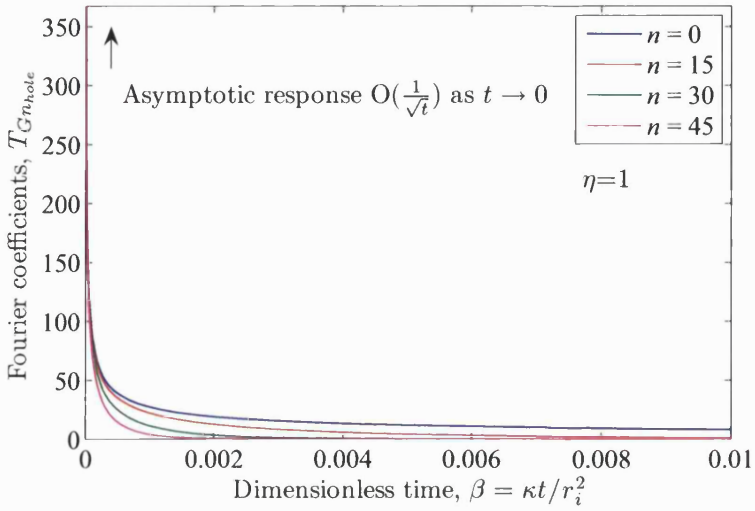

Figure 3.14: Variation of the Fourier coefficients ($\eta = 1$) of the circular hole solution as $t \rightarrow 0$ since they are governed by term the $1/\sqrt{t}$ for short timescale analysis.

3.5.2 Singular Nature of Green's Function for Annular Region

The Fourier coefficients for the temperature response of the annular region must possess similar asymptotic behaviour to the circular hole problem at $r = r_i$ for short timescale analysis. The governing term comprises of two types of modified Bessel functions, namely $K_n(x)$, which decays exponentially to zero as $x \rightarrow \infty$, and $I_n(x)$, which increases exponentially as $x \rightarrow \infty$. The governing term from equation (3.32) is

$$\overline{T}_{Gn_{annulus}}(r, s) = \frac{-K_n(\lambda r) I_n'(\lambda r_o) + I_n(\lambda r) K_n'(\lambda r_o)}{2\lambda r_i \Delta_n(\lambda)} \tag{3.46}$$

Expanding each Bessel function term asymptotically for large s gives [96, page 377],

$$I_n(\lambda r) \sim \frac{e^{\lambda r}}{\sqrt{2\pi\lambda r}}\left\{1-\frac{\mu-1}{8\lambda r}+\frac{(\mu-1)(\mu-9)}{2(8\lambda r)^2} +\mathrm{O}\left(\frac{1}{\lambda^3}\right)\right\} \tag{3.47}$$

$$I_n'(\lambda r) \sim \frac{e^{\lambda r}}{\sqrt{2\pi\lambda r}}\left\{1-\frac{\mu+3}{8\lambda r}+\frac{(\mu-1)(\mu+15)}{2(8\lambda r)^2} +\mathrm{O}\left(\frac{1}{\lambda^3}\right)\right\} \tag{3.48}$$

It follows from (3.16), (3.17), (3.47) and (3.48) with $r = r_i$, that

$$\begin{aligned}\overline{T}_{Gn_{annulus}}(r,s) &\sim \frac{1}{2\pi k\lambda r_i}\times\frac{e^{\lambda(r_o-r_i)}+e^{-\lambda(r_o-r_i)}}{e^{\lambda(r_o-r_i)}-e^{-\lambda(r_o-r_i)}}\\ &= \frac{1}{2\pi k\lambda r_i}\times\frac{1+e^{-2\lambda(r_o-r_i)}}{1-e^{-2\lambda(r_o-r_i)}}\end{aligned} \tag{3.49}$$

as $s \to \infty$. Hence [95, page 246],

$$T_{Gn_{annulus}} \sim \frac{\sqrt{\kappa}}{2\pi k r_i\sqrt{\pi t}} \tag{3.50}$$

as $t \to 0$. Therefore, the singular nature of each Fourier coefficient of the annular problem is the same as for the circular hole. Figure 3.15 shows the responses of the harmonics with time evaluated using the inverse Laplace transform of equation (3.35).

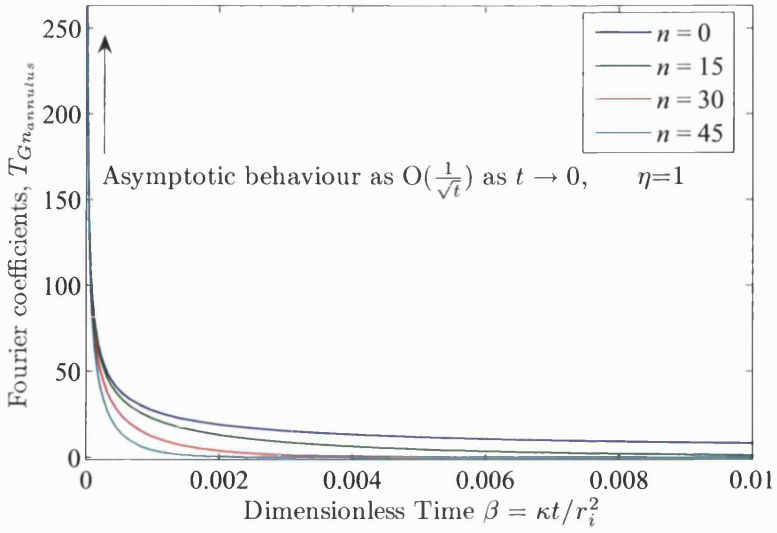

Figure 3.15: Fourier coefficients of annulus solution ($\eta = 1$) with respect to time correspond to various harmonics.

3.6 Closure

Transient thermal analyses for instantaneous line sources applied to circular hole and annular regions have been studied. Both cases were solved using the Laplace transform and Fourier harmonics together with adiabatic boundary conditions. The Fourier series are poorly convergent at short time scales. In fact the Fourier harmonics behave asymptotically as $O(1/\sqrt{t})$ as $t \to 0$ at the point source. If the line sources are to be applied in a meaningful and efficient manner to rotor/auxiliary bearing contact problems, the convergence problem associated with the current representations needs to be overcome.

Chapter 4

Use of Half-Plane and Remainder Solution for Improved Short Timescale Convergence

4.1 Overview

In Chapter 3, the poorly convergent representations of the line source solution are not efficient for analysing short time responses associated with localised rotor/auxiliary bearing contact problems. This chapter proposes an effective approach to overcome the stated problem by utilising the half-plane solution to capture the singular nature of the full-plane solutions.

4.2 Half-Plane Solution for Instantaneous Line Source

The temperature distribution is highly localised around the instantaneous line source for short durations, and decreases rapidly in intensity with distance from the heat source. Therefore, the temperature can be expected to approximate of the half-plane temperature solution over short times.

4.2.1 Statement of Full-Plane Problem

This subsection illustrates the derivation of a full plane solution subjected to an instantaneous unit line source at the origin $(x', y') = (0, 0)$ at $t = 0$. It is well known [80], but its derivation is shown here for later consideration. For the two-dimensional transient problem, the temperature distribution for full-plane is axis-symmetric. Hence, the heat conduction equation can be reduced to,

$$\frac{\partial^2 T}{\partial r'^2} + \frac{1}{r'}\frac{\partial T}{\partial r'} - \frac{1}{\kappa}\frac{\partial T}{\partial t} = 0 \tag{4.1}$$

Taking the Laplace transform with respect to time,

$$\frac{\partial^2 \overline{T}}{\partial r'^2} + \frac{1}{r'}\frac{\partial \overline{T}}{\partial r'} - \frac{s}{\kappa}\overline{T} = 0 \tag{4.2}$$

Since the temperature decays to zero as $r' \to 0$, the general solution is,

$$\overline{T}(r', s) = BK_0(\lambda r') \tag{4.3}$$

where $\lambda = \sqrt{s/\kappa}$ and K_0 is the modified Bessel function with zero order. The temperature gradient in radial direction is,

$$\frac{\delta \overline{T}(r', s)}{\delta r'} = -B\lambda K_1(\lambda r') \sim -\frac{B}{r'} \tag{4.4}$$

as $r' \to 0$. Suppose that the line source emits unit heat per unit length, instantaneously at $t = 0$. By integrating over a cylinder of radius r' that surrounds the line source,

$$\lim_{r' \to 0} \int_0^{2\pi} \left(-k\frac{\delta \overline{T}(r', s)}{\delta r'} \right) r' d\varphi = 2\pi k B = 1 \tag{4.5}$$

Hence,

$$B = \frac{1}{2\pi k} \tag{4.6}$$

and the transformed temperature is,

$$\overline{T}(r', s) = \frac{1}{2\pi k} K_0(\lambda r') \tag{4.7}$$

Taking the inverse Laplace transformation gives [95, page 283],

$$T(r', t) = \frac{1}{4\pi k t} e^{-\frac{r'^2}{4\kappa t}} \tag{4.8}$$

4.2.2 Half-Plane Case

Consider the shaded half-plane as shown in Figure 4.1. The plane boundary ($x' = 0$) must be adiabatic. Note that the full-plane solution (4.8) satisfies a condition of zero heat flux on any straight line boundary through the source point:

$$\left.\frac{\partial T_h(r', t)}{\partial x'}\right|_{x'=0} = \frac{1}{4\pi k t} e^{-\frac{r'^2}{4\kappa t}} \left(-\frac{2r'}{4\kappa t}\right) \frac{x'}{r'} = 0 \tag{4.9}$$

$$\left.\frac{\partial T_h(r', t)}{\partial y'}\right|_{y'=0} = \frac{1}{4\pi k t} e^{-\frac{r'^2}{4\kappa t}} \left(-\frac{2r'}{4\kappa t}\right) \frac{y'}{r'} = 0 \tag{4.10}$$

If a unit instantaneous line heat source is applied to the surface of a half-plane and the surface remains adiabatic, the full-plane solution is simply doubled. Therefore the Green's function temperature response, T_{Gh}, for the half-plane is

$$T_{Gh}(r', t) = \frac{1}{2\pi k t} e^{-\frac{r'^2}{4\kappa t}} \tag{4.11}$$

In the Laplace transform domain,

$$\overline{T}_{Gh}(r', s) = \frac{1}{\pi k} K_0(\lambda r') \tag{4.12}$$

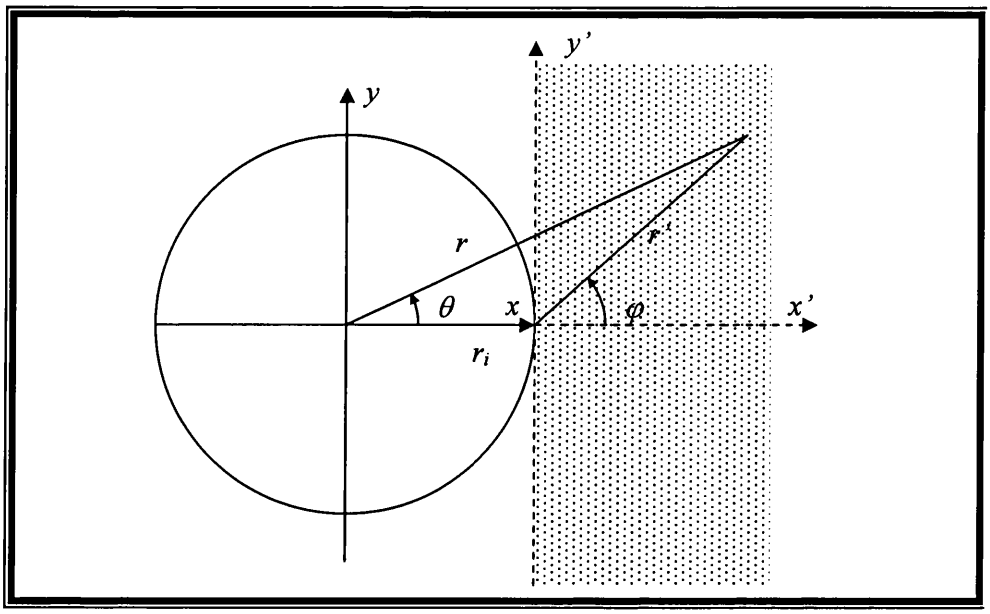

Figure 4.1: Global (r, θ) and local (r', φ) coordinate systems correspond to full-plane and half-plane regions respectively.

4.2.3 Coordinate Transformation of Half-Plane Solution

The half-plane solution (4.11) is stated in a local coordinate system, i.e. (r', φ), and needs to be transformed to a coordinate system used for the circular hole and annulus problems. Referring to Figure 4.1, $r'^2 = r_i^2 + r^2 - 2rr' \cos\theta$ and equation (4.11) gives,

$$T_{Gh}(r, \theta, t) = \frac{1}{2\pi kt} e^{-\frac{r_i^2\left(1+\eta^2-2\eta\cos\theta\right)}{4\kappa t}} \tag{4.13}$$

where $\eta = r/r_i$. Using the summation theorem for Bessel functions [97, page 979], it is possible to express

$$K_0(\lambda r') = \sum_{n=-\infty}^{\infty} I_n(\lambda r_i) K_n(\lambda r) e^{in\theta} \tag{4.14}$$

Therefore the half-plane solution also has the form,

$$\overline{T}_{Gh}(r,\theta,s) = \sum_{n=-\infty}^{\infty} \frac{1}{\pi k} I_n(\lambda r_i) K_n(\lambda r) e^{in\theta} = \sum_{n=-\infty}^{\infty} \overline{T}_{Ghn}(r,s) e^{in\theta} \tag{4.15}$$

where

$$\overline{T}_{Ghn}(r,s) = \frac{1}{\pi k} I_n(\lambda r_i) K_n(\lambda r) \tag{4.16}$$

4.3 Concept of Remainder Function

The half-plane solution takes no consideration of the physical geometry and the boundary conditions associated with circular region. However, it is useful in evaluating the localised thermal response of a body for short timescale analysis. The concept of a remainder function is to yield the correct adiabatic boundary conditions that are not satisfied by the half-plane solution. The general mathematical expression for the remainder function is contained in

$$f_G(r,\theta,t) = f_{Gh}(r,\theta,t) + \underbrace{\sum_{n=-\infty}^{\infty} \left[f_{Gn}(r,t) - f_{Ghn}(r,t) \right] e^{in\theta}}_{\text{remainder function}} \tag{4.17}$$

where

$$f_G(r,\theta,t) = \sum_{n=-\infty}^{\infty} f_{Gn}(r,t) e^{in\theta} \tag{4.18}$$

is either the circular hole or annular solution and

$$f_{Gh}(r,\theta,t) = \sum_{n=-\infty}^{\infty} f_{Ghn}(r,t) e^{in\theta} \tag{4.19}$$

is the half-plane solution. The convenient feature of the remainder function is that the half-plane term can be replaced with any kind of expression without

changing the final outcome, f_G. It offers great flexibility in choosing the most appropriate half-plane term for the system. However, the half-plane term must remove the singular nature of f_G effectively.

4.3.1 In-Depth Study of Remainder Function

This subsection provides the derivation and the in-depth understanding of the remainder function. In sections 3.5.1 and 3.5.2, it has been shown that the singular nature for short timescales of the circular hole and annular line source solutions can be inferred from the transformed solutions for large s. The Fourier coefficients for the circular hole problem in the Laplace transform domain are given by (see equation (3.40)),

$$\overline{T}_{Gn_{hole}}(r,s) = -\frac{K_n(\lambda r)}{2\pi k \lambda r_i K_n'(\lambda r_i)} \tag{4.20}$$

The asymptotic expansion of equation (4.20) for large s is given in equation (3.44). For the half-plane solution given in equation (4.15), it is noted that for large λ,

$$I_n(\lambda r) \sim \sqrt{\frac{1}{2\pi\lambda r}} e^{\lambda r} \left\{ 1 - \frac{\mu - 1}{8\lambda r} + \frac{(\mu-1)(\mu-9)}{2(8\lambda r)^2} + \mathrm{O}\left(\frac{1}{\lambda^3}\right) \right\} \tag{4.21}$$

$$K_n(\lambda r) \sim \sqrt{\frac{\pi}{2\lambda r}} e^{-\lambda r} e^{\lambda r} \left\{ 1 + \frac{\mu - 1}{8\lambda r} + \frac{(\mu-1)(\mu-9)}{2(8\lambda r)^2} + \mathrm{O}\left(\frac{1}{\lambda^3}\right) \right\} \tag{4.22}$$

where $\mu = 4n^2$. Thus, the Fourier harmonics of equation (4.15) for large s can be approximated asymptotically by,

$$\begin{aligned}\overline{T}_{Ghn}(r,s) &= \frac{1}{\pi k} I_n(\lambda r_i) K_n(\lambda r) \\ &= \frac{e^{-\lambda(r-r_i)}}{\pi k \lambda \sqrt{r r_i}} \left\{ 1 + \left(\frac{1}{r} - \frac{1}{r_i}\right) \frac{(\mu-1)}{8\lambda} + \left(\frac{(\mu-1)(\mu-9)}{r^2} \right. \right. \\ &\quad \left. \left. - \frac{2(\mu-1)^2}{r r_i} + \frac{(\mu-1)(\mu-9)}{r_i^2} \right) \frac{1}{2(8\lambda)^2} + \mathrm{O}\left(\frac{1}{\lambda^3}\right) \right\}\end{aligned} \tag{4.23}$$

The difference between the circular hole and half-plane Fourier harmonics is,

$$\begin{aligned}&\overline{T}_{Gn_{hole}}(r,s) - \overline{T}_{Ghn}(r,s) \\ &= \frac{1}{2\pi k} \left(-\frac{K_n(\lambda r)}{\lambda r_i K_n'(\lambda r_i)} - 2 I_n(\lambda r_i) K_n(\lambda r) \right) \\ &\sim \frac{e^{-\lambda(r-r_i)}}{2\pi k \lambda \sqrt{r r_i}} \left\{ -\frac{1}{2\lambda r_i} + \left[-\frac{8(\mu-1)}{r r_i} + \frac{8(\mu+3)}{r_i^2} \right] \frac{1}{2(8\lambda)^2} + \mathrm{O}\left(\frac{1}{\lambda^3}\right) \right\}\end{aligned} \tag{4.24}$$

Taking the leading term on the right hand side of equation (4.24), the remainder function Fourier coefficients for short time are governed by the term ,

$$\mathcal{L}^{-1}\left\{ -\frac{1}{4\pi k r_i^2 \sqrt{\eta}} \cdot \frac{e^{-\lambda(r-r_i)}}{\lambda^2} \right\} = -\frac{\kappa}{4\pi k r_i^2 \sqrt{\eta}} \mathrm{erfc}\left(\frac{r-r_i}{2\sqrt{\kappa t}}\right) \tag{4.25}$$

where $\eta = r/r_i$ and $\mathrm{erfc}(x)$ is the complementary error function. Since the leading term on the right hand side is now $\mathrm{O}(1/s)$ and independent of n, the deduction is that

$$T_{Gn_{hole}}(r_i,t) - T_{Ghn}(r_i,t) \sim -\frac{\kappa}{4\pi k r_i^2} \tag{4.26}$$

as $t \longrightarrow 0$ for every n.

Repeating the process of removing the leading term from the right hand side of equation (4.24),

$$\overline{T}_{Gn_{hole}}(r,s) - \overline{T}_{Ghn}(r,s) \left(1 - \frac{1}{2\lambda r_i}\right) \sim \frac{e^{-\lambda(r-r_i)}}{2\pi k \lambda \sqrt{r r_i}} \left\{ \frac{1}{(2\lambda r_i)^2} + \mathrm{O}\left(\frac{1}{\lambda^3}\right) \right\} \tag{4.27}$$

as $s \to \infty$, for $-\pi < \arg s \leq \pi$. Yet again,

$$\overline{T}_{Gn_{hole}}(r,s) - \overline{T}_{Ghn}(r,s)\left(1 - \frac{1}{2\lambda r_i} + \frac{1}{(2\lambda r_i)^2}\right) \sim \frac{e^{-\lambda(r-r_i)}}{2\pi k\lambda\sqrt{rr_i}} \cdot \mathrm{O}\left(\frac{1}{\lambda^3}\right) \quad (4.28)$$

as $s \to \infty$, for $-\pi < \arg s \leq \pi$.

The removal of higher order terms from the right hand side of equation (4.28) could be continued. On inverting the Laplace transform, the benefit of removing the higher order terms would be improved short timescale representation of the harmonics components. However, higher order singularities are introduced into the left hand side of equation (4.28) at $\lambda = 0$, which would result in larger long timescale behaviour in each harmonic component. To address this issue it is observed from (4.28) that

$$1 - \frac{1}{2\lambda r_i} + \frac{1}{(2\lambda r_i)^2} - \frac{1}{(2\lambda r_i)^3} + \ldots = 1 - \frac{1}{1 + 2\lambda r_i} \quad (4.29)$$

Hence, it eliminates the singular response at $\lambda = 0$. Therefore, equation (4.28) reduces to,

$$\overline{T}_{Gn_{hole}}(r,s) - \overline{T}_{Ghn}(r,s)\left(1 - \frac{1}{1 + 2\lambda r_i}\right) \sim \frac{e^{-\lambda(r-r_i)}}{2\pi k\lambda\sqrt{rr_i}} \cdot \mathrm{O}\left(\frac{1}{\lambda^3}\right) \quad (4.30)$$

as $s \to \infty$, for $-\pi < \arg s \leq \pi$.

4.3.2 Remainder Function for Circular Hole Problem

Based on equation (4.30), the Fourier series representation of the remainder function, $\overline{T}_{GR_{hole}}$ in the Laplace domain can be expressed as,

$$\overline{T}_{GR_{hole}}(r,\theta,s) = \sum_{n-\infty}^{\infty} \left\{ \overline{T}_{Gn_{hole}}(r,s) - \overline{T}_{Ghn}(r,s) \left(1 - \frac{1}{1+2\lambda r_i}\right) \right\} e^{in\theta} \quad (4.31)$$

The inverse Laplace transform of the first term of the Fourier coefficients in equation (4.31) is given by equation (3.20). The second term is,

$$\overline{T}_{Ghn}(r,s) \left(1 - \frac{1}{1+2\lambda r_i}\right) = \frac{1}{\pi k} I_n(\lambda r_i) K_n(\lambda r) \left(1 - \frac{1}{1+2\lambda r_i}\right) \quad (4.32)$$

Equation (4.32) may be inverted using equation (3.14) together with

$$I_n\left(vre^{\frac{\pi i}{2}}\right) = i^n J_n(vr) \quad (4.33)$$

$$K_n\left(vre^{\frac{\pi i}{2}}\right) = -\frac{\pi i}{2} i^{-n} H_n^{(2)}(vr) \quad (4.34)$$

Thus equation (4.32) can be written as,

$$\begin{aligned} &\frac{1}{2\pi i} \int_{c-i\infty}^{c+i\infty} \overline{T}_{Ghn}(r,s) \left(1 - \frac{1}{1+2\lambda r_i}\right) e^{st} ds \\ &= -\frac{2\kappa}{i\pi^2 k} \int_0^{\infty} \text{Imag} \left[I_n\left(vre^{\frac{\pi i}{2}}\right) K_n\left(vre^{\frac{\pi i}{2}}\right) \left(1 - \frac{1}{1+2ivr_i}\right) \right] e^{-\kappa v^2 t} v dv \quad (4.35) \\ &= -\frac{2\kappa}{\pi^2 k} \int_0^{\infty} \text{Imag} \left[-\frac{\pi i}{2} J_n(vr_i) H_n^{(2)}(vr) \left(1 - \frac{1-2ivr_i}{1+4v^2 r_i^2}\right) \right] e^{-\kappa v^2 t} v dv \end{aligned}$$

Since $H_n^{(2)}(x) = J_n(x) - iY_n(x)$, it follows that,

$$\begin{aligned} &-\frac{2\kappa}{\pi^2 k} \int_0^{\infty} \text{Imag} \left[-\frac{\pi i}{2} J_n(vr_i) H_n^{(2)}(vr) \left(1 - \frac{1-2ivr_i}{1+4v^2 r_i^2}\right) \right] e^{-\kappa v^2 t} v dv \\ &= \frac{2\kappa}{\pi^2 k} \int_0^{\infty} \left\{ \frac{\pi}{2} J_n(vr_i) J_n(vr) \left(1 - \frac{1}{1+4v^2 r_i^2}\right) + \frac{\pi v r_i J_n(vr_i) Y_n(vr)}{1+4v^2 r_i^2} \right\} e^{-\kappa v^2 t} v dv \end{aligned} \quad (4.36)$$

Putting $v = x/r_i$,

$$\begin{aligned}
&\frac{1}{2\pi i}\int_{c-i\infty}^{c+i\infty}\overline{T}_{Ghn}(r,s)\left(1-\frac{1}{1+2\lambda r_i}\right)e^{st}ds \\
&=\frac{2\kappa}{\pi^2 k r_i^2}\int_0^\infty\left\{\frac{\pi}{2}J_n(x)J_n(x\eta)\left(1-\frac{1}{1+4x^2}\right)\right. \\
&\left.+\frac{\pi x J_n(x)Y_n(x\eta)}{1+4x^2}\right\}e^{-\kappa x^2 t/r_i^2}xdx
\end{aligned} \tag{4.37}$$

Therefore, the remainder function for circular hole problem is

$$T_{GR_{hole}}(r,\theta,t)=\sum_{n=-\infty}^{\infty}T_{GRn_{hole}}(r,t)e^{in\theta} \tag{4.38}$$

where

$$T_{GRn_{hole}}(r,t)=\frac{1}{2\pi k}\times\frac{2\kappa}{\pi r_i^2}\int_0^\infty f_{Rn_{hole}}(r)e^{-\kappa x^2 t/r_i^2}xdx \tag{4.39}$$

and

$$\begin{aligned}
f_{Rn_{hole}}(r)=&\frac{\phi_n(x)\,Y_n(x\eta)-\psi_n(x)\,J_n(x\eta)}{\phi_n^2(x)+\psi_n^2(x)} \\
&-\pi J_n(x)J_n(x\eta)\left(1-\frac{1}{1+4x^2}\right)-\frac{2\pi x J_n(x)Y_n(x\eta)}{1+4x^2}
\end{aligned} \tag{4.40}$$

4.3.3 Remainder Function for Annular Problem

The procedure for deriving the remainder function for the annulus problem is similar to the circular hole problem with,

$$\begin{aligned}
\overline{T}_{GR_{annulus}}(r,\theta,s)=\sum_{n=-\infty}^{\infty}&\left\{\overline{T}_{Gn_{annulus}}(r,s)\right. \\
&\left.-\overline{T}_{Ghn}(r,s)\left(1-\frac{1}{1+2\lambda r_i}\right)\right\}e^{in\theta}
\end{aligned} \tag{4.41}$$

The only difference is the first term of the remainder function Fourier coefficient. However, the procedure for transforming the second term in the right hand side of equation (4.41) needs to be modified to adapt the different method of inverting the Laplace transform of the annular problem compared to the circular hole problem (Chapter 3). Nevertheless, it must emphasised that the change of the integration path in contour integration by varying γ for the inverse Laplace transform does not exert any influence on the final outcome.

The inverse Laplace transform of the first term of equation (4.41) is given in equation (3.34). For the second term,

$$\begin{aligned}&\mathcal{L}^{-1}\left\{\overline{T}_{Ghn}(r,s)\left(1-\frac{1}{1+2\lambda r_i}\right)\right\}\\&=\frac{1}{2\pi k}\times\frac{2\kappa}{\pi r_i^2}\int_0^\infty \text{Imag}\left\{f_{hn}\left(\frac{r}{r_i}xe^{\frac{i\pi\gamma}{2}}\right)e^{\frac{\kappa x^2 te^{i\pi\gamma/2}}{r_i^2}+i\pi\gamma}\right\}xdx\end{aligned} \tag{4.42}$$

where

$$f_{hn}\left(\frac{r}{r_i}xe^{\frac{i\pi\gamma}{2}}\right)=2I_n\left(xe^{\frac{i\pi\gamma}{2}}\right)K_n\left(\eta xe^{\frac{i\pi\gamma}{2}}\right)\left(1-\frac{1}{1+2xe^{\frac{i\pi\gamma}{2}}}\right) \tag{4.43}$$

Therefore the Fourier coefficients of the remainder function for annulus are

$$T_{GRn_{annulus}}(r,t)$$

$$= \frac{\kappa}{\pi^2 k r_i^2} \times \begin{cases} \int_0^\infty \text{Imag}\left\{\left[f_n\left(\frac{r}{r_i}xe^{\frac{i\pi\gamma}{2}}\right)\Big|_{n=0}\right. \right. \\ \left. - f_{hn}\left(\frac{r}{r_i}xe^{\frac{i\pi\gamma}{2}}\right)\Big|_{n=0}\right] \times e^{\frac{\kappa x^2 t e^{i\pi\gamma/2}}{r_i^2}+i\pi\gamma} \Bigg\} xdx\,, \quad n=0 \\ + \left(\frac{\pi\gamma}{\eta_o^2-1}\right) \\ \\ \int_0^\infty \text{Imag}\left\{\left[f_n\left(\frac{r}{r_i}xe^{\frac{i\pi\gamma}{2}}\right) - f_{hn}\left(\frac{r}{r_i}xe^{\frac{i\pi\gamma}{2}}\right)\right]\right. \\ \left. \times e^{\frac{\kappa x^2 t e^{i\pi\gamma/2}}{r_i^2}+i\pi\gamma}\right\} xdx \quad , \quad n \neq 0 \end{cases} \tag{4.44}$$

where $f_n(x)$ is given in equation (3.37). Subsequently, the Fourier series representation is,

$$T_{GR_{annulus}}(r,\theta,t) = \sum_{n=-\infty}^{\infty} T_{GRn_{annulus}}(r,t)e^{in\theta} \tag{4.45}$$

4.4 Time Dependent Forms

With reference to equations (4.31) and (4.41), the term,

$$\sum_{n=-\infty}^{\infty} \overline{T}_{Ghn}(r,s)\left(1-\frac{1}{1+2\lambda r_i}\right)e^{in\theta} \tag{4.46}$$

was removed from the annular solution to improve the convergence of the Fourier series presentation. The explicit inverse of (4.46) can be deduced using the direct inverse Laplace transformation of $\overline{T}_{Ghn}(r,s)$ and a convolution integral. The

inversion of the first term of equation (4.46) is obviously

$$\begin{aligned} T_{Gh}(r,\theta,t) &= \sum_{n=-\infty}^{\infty} \mathcal{L}^{-1}\left\{\overline{T}_{Ghn}(r,s)\right\} e^{in\theta} \\ &= \frac{1}{2\pi kt} e^{-\frac{r_i^2\left(1+\eta^2-2\eta\cos\theta\right)}{4\kappa t}} \end{aligned} \tag{4.47}$$

The second term can be expressed as,

$$\begin{aligned} \hat{T}_{Gh}(r,\theta,t) &= \mathcal{L}^{-1}\left\{\sum_{n=-\infty}^{\infty}\left(-\overline{T}_{Ghn}(r,s)\frac{1}{1+2\lambda r_i}\right)e^{in\theta}\right\} \\ &= \mathcal{L}^{-1}\left\{-\overline{T}_{Gh}(r,\theta,s)\frac{1}{1+2\lambda r_i}\right\} \end{aligned} \tag{4.48}$$

It is noted that [96, page 1023],

$$\mathcal{L}^{-1}\left\{\frac{1}{a+\sqrt{s}}\right\} = \frac{1}{\sqrt{\pi t}} - ae^{a^2t}\operatorname{erfc}\left(a\sqrt{t}\right) \tag{4.49}$$

This enables the second term of equation (4.46) to be expressed as the convolution integral,

$$\begin{aligned} \hat{T}_{Gh}(r,\theta,t) &= -\int_0^t g(\tau)T_{Gh}(r,\theta,t-\tau)d\tau \\ &= -\frac{1}{2\pi k}\int_0^t \frac{g(\tau)}{t-\tau} e^{-\frac{r_i^2\left(1+\eta^2-2\eta\cos\theta\right)}{4\kappa(t-\tau)}} d\tau \end{aligned} \tag{4.50}$$

where,

$$g(t) = \frac{\sqrt{\kappa}}{2r_i}\left(\frac{1}{\sqrt{\pi t}} - \frac{\sqrt{\kappa}}{2r_i}e^{\frac{\kappa t}{4r_i^2}}\operatorname{erfc}\left(\frac{\sqrt{\kappa t}}{2r_i}\right)\right) \tag{4.51}$$

Hence, the full expression for thermal Green's function for a region with a circular hole is,

$$T_{G_{hole}}(r,\theta,t) = T_{Gh}(r,\theta,t) + \hat{T}_{Gh}(r,\theta,t) + \sum_{n=-\infty}^{\infty} T_{GRn_{hole}}(r,t)e^{in\theta} \tag{4.52}$$

For the annular problem,

$$T_{G_{annulus}}(r,\theta,t) = T_{Gh}(r,\theta,t) + \hat{T}_{Gh}(r,\theta,t) + \sum_{n=-\infty}^{\infty} T_{GRn_{annulus}}(r,t)e^{in\theta} \quad (4.53)$$

4.5 Graphical Results for Thermal Green's Function

This section provides graphical presentations of the thermal Green's functions solutions for the circular hole and annulus problems using the improved expressions (4.52) and (4.53). Figure 4.2 shows the variation of the circular hole remainder function Fourier coefficients at the inner radius with respect to dimensionless time, β, where $\beta = \kappa t/r_i^2$. The subtraction of the half-plane solutions from the circular-hole solution completely removes the asymptotic behaviour of the system as $t \to 0$, hence the remainder function has greatly improved Fourier series convergence for short timescale analysis. This approach has a similar effect on the Fourier coefficients for the annulus solution (Figure 4.3). Figures 4.4 and 4.5 show the comparison of the inner boundary temperature responses for the circular hole and annular solutions with and without using the remainder function. The results show the benefits of introducing the remainder function through improved representation of short timescale prediction.

Figures 4.6 and 4.7 show the variation of the temperature with time at points $(r,\theta) = (r_i, 0)$ and $(r,\theta) = ((r_o - r_i)/2, 0)$ respectively. The first figure shows the temperature singularity as $t \to 0$. The second figure shows the temperature at the mean radius to increase from zero temperature and then decay as the heat defuses throughout the annulus. Figures 4.8 and 4.9 shows that the temperature contour

lines approach the inner and outer boundaries boundary with normal intersection, which indicates that the boundary conditions are satisfied. For short timescale analysis, the temperature distribution is highly localised, and the dimension of the thermal field is very small compared to the physical geometry of the annulus as shown in figure 4.10.

4.6 Closure

The remainder functions for hole and annular problems were developed in this chapter by subtracting the half-plane solution from the hole and annular solutions derived in Chapter 3. It was found that this approach greatly improves the convergence of Fourier series solutions for short timescale analysis while also complying with the boundary conditions. Equations (4.52) and (4.53) are central results for the application to problems involving rotor/auxiliary bearing contact.

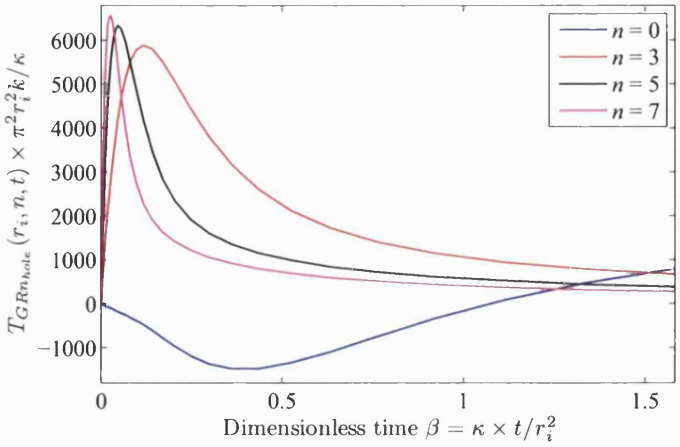

Figure 4.2: Fourier harmonic coefficients on inner surface of the circular hole remainder as functions of dimensionless time, β, where $\beta = \kappa t/r_i^2$. The deduction of the half-plane solution from the full-plane solution eliminates the singular behaviour (Figure 3.14) completely as $t \to 0$.

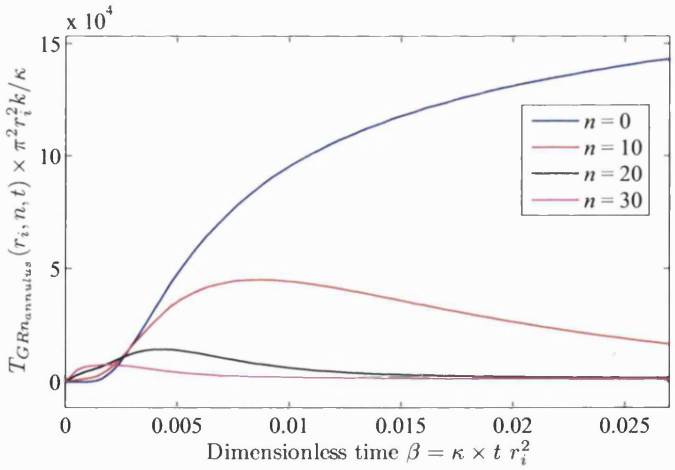

Figure 4.3: Fourier harmonic coefficients on inner surface of the annular remainder as functions of dimensionless time, β, where $\beta = \kappa t/r_i^2$. The deduction of the half-plane solution from the full-plane solution eliminates the singular behaviour (Figure 3.15) completely as $t \to 0$.

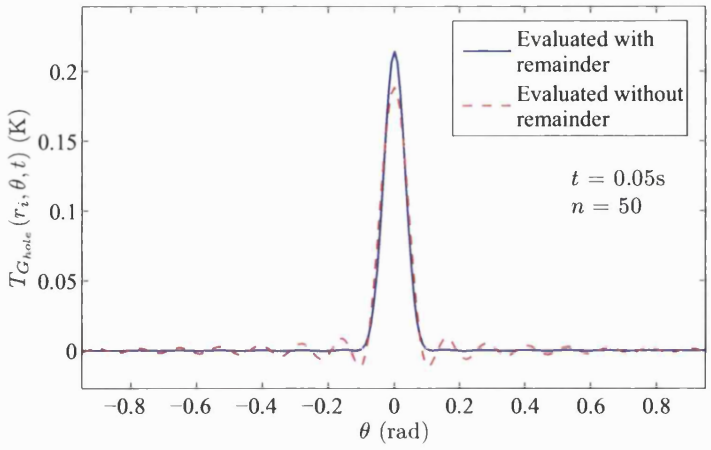

Figure 4.4: Comparison between the solutions evaluated with remainder function and full-plane solution for circular hole at $t = 0.05s$ ($\beta = 5.3 \times 10^{-4}$). The remainder function method improves the convergence of the solution significantly for short timescale analysis.

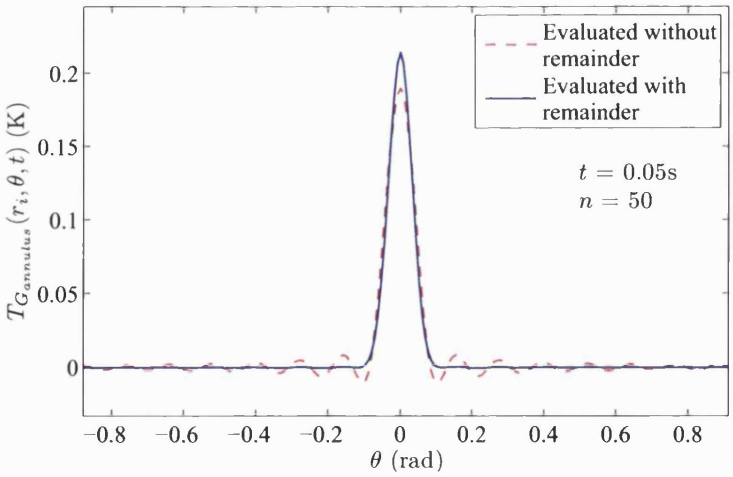

Figure 4.5: Influence of the remainder function on annulus solution at $t = 0.05s$. The implementation of the remainder function gives well converged solution for short timescale analysis.

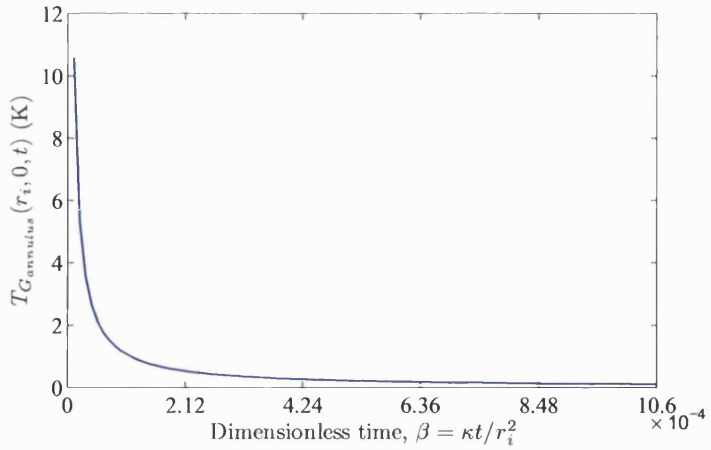

Figure 4.6: Temperature variation with time of annular solution at point $(r, \theta) = (r_i, 0)$. Instantaneous unit line source introduce asymptotic behaviour of temperature response as $t \to 0$.

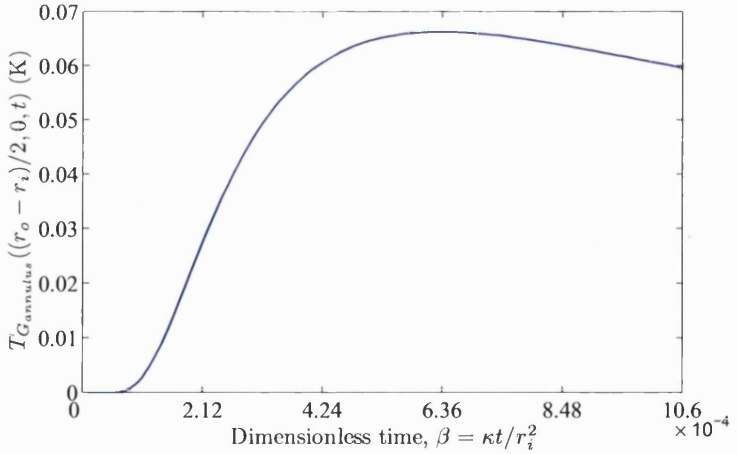

Figure 4.7: Time variation of temperature at the mean radius in the annular region. Temperature increases as heat dissipates across the annulus, followed by decay.

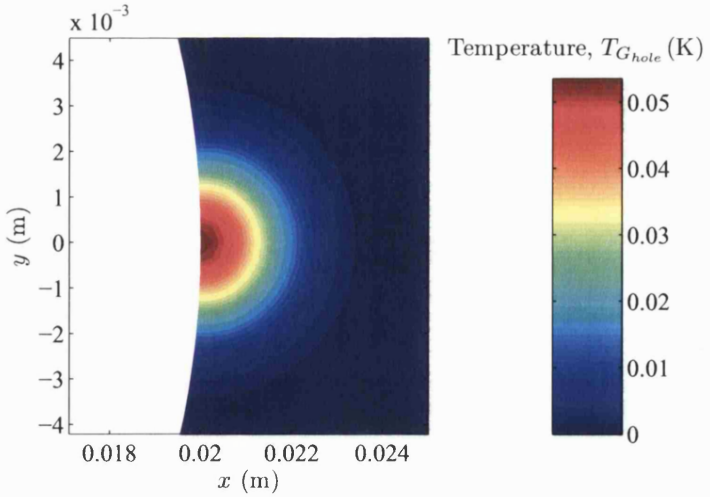

Figure 4.8: Green's function temperature distribution in a plane with a circular hole. This result is evaluated using the remainder function at $t = 0.2$s ($\beta = 2.1 \times 10^{-3}$).

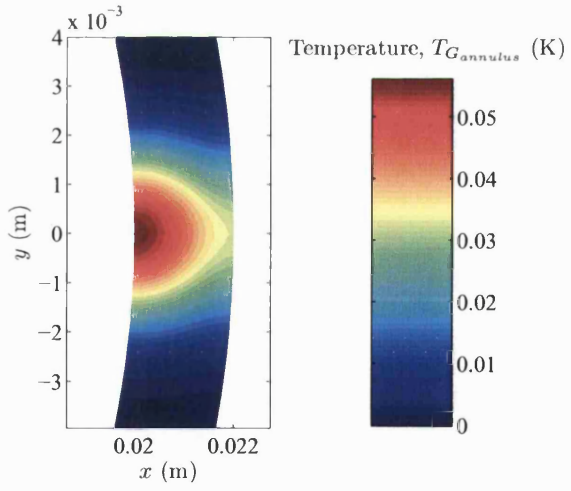

Figure 4.9: Temperature distribution of annulus due to unit instantaneous line heat source applied at a point at the inner boundary. The result is evaluated using the remainder function at $t = 0.2$s ($\beta = 2.1 \times 10^{-4}$) and it is evident that zero heat flux boundary conditions are satisfied.

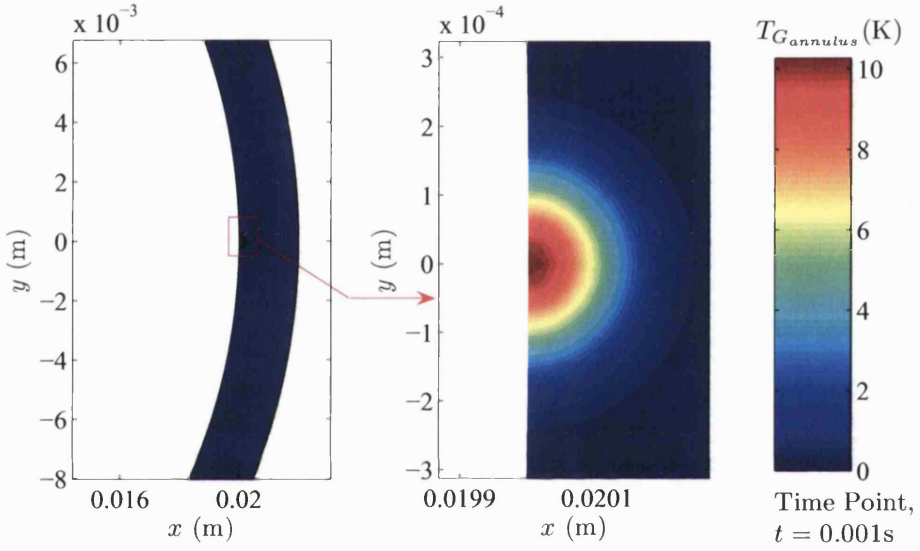

Figure 4.10: Green's function temperature distribution in annular region at time $t = 0.001$s ($\beta = 1.06 \times 10^{-5}$), which shows the highly localised nature of the solution at short timescales.

Chapter 5

Quasi-Static Thermoelastic Analysis for Annulus

5.1 Overview

This chapter investigates the influence of a non-uniform temperature distribution in a homogeneous elastic annulus. The general solutions for stresses and deformations of the annulus under thermal input are developed by using fundamental thermoelastic theory together with a state-space approach. Two distinct physical boundaries are considered in this analysis, namely, rigidly and resiliently mounted outer boundaries, both with a stress free inner boundary.

5.2 Fundamental Thermoelastic Behaviour

Suppose a homogeneous elastic body experiences change in temperature such that corresponding deformations may be considered to be quasi static, i.e. elastic waves are not excited. In addition, the temperature field may be determined independently of stresses and strains.

5.2.1 Stress-Strain Relations for Two-Dimensional Problem

To determine stresses and strains in an annulus, it is advantageous to use a polar coordinate system. By ignoring the body forces, the equilibrium equations are given as follows [58]:

$$\frac{\partial \sigma_r}{\partial r} + \frac{1}{r}\frac{\partial \tau_{r\theta}}{\partial \theta} + \frac{\sigma_r - \sigma_\theta}{r} = 0 \tag{5.1}$$

$$\frac{1}{r}\frac{\partial \sigma_\theta}{\partial \theta} + \frac{\partial \tau_{r\theta}}{\partial r} + \frac{2\tau_{r\theta}}{r} = 0 \tag{5.2}$$

The strain-displacement equations are

$$\varepsilon_r = \frac{\partial u_r}{\partial r} \tag{5.3}$$

$$\varepsilon_\theta = \frac{u_r}{r} + \frac{1}{r}\frac{\partial v_\theta}{\partial \theta} \tag{5.4}$$

$$\gamma_{r\theta} = \frac{1}{r}\frac{\partial u_r}{\partial \theta} + \frac{\partial v_\theta}{\partial r} - \frac{v_\theta}{r} \tag{5.5}$$

The two-dimensional stress-strain equations for thermoelasticity can be written as

$$\sigma_r = \lambda\left[\beta\varepsilon_r + \upsilon\varepsilon_\theta - (1+\upsilon)\alpha_e T\right] \tag{5.6}$$

$$\sigma_\theta = \lambda\left[\beta\varepsilon_\theta + \upsilon\varepsilon_r - (1+\upsilon)\alpha_e T\right] \tag{5.7}$$

$$\tau_{r\theta} = G\gamma_{r\theta} \tag{5.8}$$

where these equations are applicable either for plane-strain or plane-stress problems. G is the shear modulus and is defined as $G = E/2(1+\upsilon)$. For plane-strain analysis, where $\varepsilon_z = 0$; $\sigma_z = \upsilon(\sigma_r + \sigma_\theta) - E\alpha_e T$,

$$\lambda = \frac{2G}{(1-2\upsilon)} \tag{5.9}$$

$$\beta = (1-\upsilon) \tag{5.10}$$

For plane-stress, i.e. $\sigma_z = 0$; $\varepsilon_z = -\upsilon(\sigma_r + \sigma_\theta)/E + \alpha_e T$, are defined as,

$$\lambda = \frac{2G}{(1-\upsilon)} \tag{5.11}$$

$$\beta = 1 \tag{5.12}$$

It is possible to determine equations for components, u_r and v_θ. Using (5.3-5.8) to replace the stresses in (5.1) and (5.2), the displacement equations are

$$\frac{\partial^2 u_r}{\partial r^2} + \frac{1}{r}\frac{\partial u_r}{\partial r} - \frac{u_r}{r^2} + \frac{G}{\lambda\beta r^2}\frac{\partial^2 u_r}{\partial \theta^2} + \frac{(\upsilon\lambda + G)}{\lambda\beta r}\frac{\partial^2 v_\theta}{\partial r \partial\theta} - \frac{(\beta\lambda + G)}{\lambda\beta r^2}\frac{\partial v_\theta}{\partial\theta} = \frac{(1+\upsilon)}{\beta}\alpha_e\frac{\partial T}{\partial r} \tag{5.13}$$

$$\frac{\partial^2 v_\theta}{\partial r^2} + \frac{1}{r}\frac{\partial v_\theta}{\partial r} - \frac{v_\theta}{r^2} + \frac{\lambda\beta}{Gr^2}\frac{\partial^2 v_\theta}{\partial\theta^2} + \frac{(\upsilon\lambda + G)}{Gr}\frac{\partial^2 u_r}{\partial r\partial\theta} + \frac{(\beta\lambda + G)}{Gr^2}\frac{\partial u_r}{\partial\theta} = \frac{\lambda(1+\upsilon)}{Gr}\alpha_e\frac{\partial T}{\partial\theta} \tag{5.14}$$

Solution of equation (5.13) and (5.14) using a novel state-space approach will be presented in section 5.3.

5.2.2 Von Mises Criterion

The Von Mises stress, σ_v in three dimensions is

$$\sigma_v = \sqrt{\frac{(\sigma_1 - \sigma_2)^2 + (\sigma_2 - \sigma_3)^2 + (\sigma_3 - \sigma_1)^2}{2}}$$

where σ_1, σ_2 and σ_3 are denoted as the first, second and third principal stresses, respectively. The Von Mises criteria states that failure of an elastic body occurs when the maximum shear strain energy of components in the complex stress system is equal to the yield stress, i.e.

$$(\sigma_1 - \sigma_2)^2 + (\sigma_2 - \sigma_3)^2 + (\sigma_3 - \sigma_1)^2 = 2\sigma_y^2$$

For plane stress problem, where $\sigma_3 = 0$, the relationship reduces to

$$(\sigma_1 - \sigma_2)^2 + \sigma_2^2 + \sigma_1^2 = 2\sigma_y^2 \tag{5.15}$$

The principal stresses for two dimensional problem are given by

$$\sigma_1 = (\sigma_r + \sigma_\theta) + \frac{1}{2}\sqrt{(\sigma_r - \sigma_\theta)^2 + 4\tau_{r\theta}^2} \tag{5.16}$$

$$\sigma_2 = (\sigma_r + \sigma_\theta) - \frac{1}{2}\sqrt{(\sigma_r - \sigma_\theta)^2 + 4\tau_{r\theta}^2} \tag{5.17}$$

5.3 State-Space Modelling

This technique is widely use in dynamic system modelling, but has received little attention for elasticity problems. A state-space model consists of state-equation and output-equation. The state-equation is a system of first order ordinary differential equations that describe fully the physical behaviour. The output-equation represents user defined parameters of the system. The following analysis shows how the approach maybe used represent the behaviour of auxiliary bearing in a realistic manner.

5.3.1 State-Equation

Initially, equations (5.13) and (5.14) are combined by introducing the vector

$$\mathbf{w} = \begin{bmatrix} u_r \\ v_\theta \end{bmatrix} \tag{5.18}$$

Then equations (5.13) and (5.14) have the vector form,

$$\frac{\partial^2 \mathbf{w}}{\partial r^2} + \frac{1}{r}\frac{\partial \mathbf{w}}{\partial r} - \frac{\mathbf{w}}{r^2} + \begin{bmatrix} \frac{G}{\lambda\beta r^2} & 0 \\ 0 & \frac{\lambda\beta}{Gr^2} \end{bmatrix} \frac{\partial^2 \mathbf{w}}{\partial \theta^2} + \begin{bmatrix} 0 & \frac{(\upsilon\lambda+G)}{\lambda\beta r} \\ \frac{(\upsilon\lambda+G)}{Gr} & 0 \end{bmatrix} \frac{\partial^2 \mathbf{w}}{\partial r \partial \theta} + \begin{bmatrix} 0 & -\frac{(\beta\lambda+G)}{\lambda\beta r^2} \\ \frac{(\beta\lambda+G)}{Gr^2} & 0 \end{bmatrix} \frac{\partial \mathbf{w}}{\partial \theta} = (1+\upsilon)\alpha_e \begin{bmatrix} \frac{1}{\beta}\frac{\partial T}{\partial r} \\ \frac{\lambda}{GR}\frac{\partial T}{\partial \theta} \end{bmatrix} \tag{5.19}$$

Now define the angular variation through Fourier series representations of $\mathbf{w}$ and T:

$$\mathbf{w} = \sum_{n=-\infty}^{\infty} \mathbf{w}_n e^{in\theta} \; ; \; T = \sum_{n=-\infty}^{\infty} T_n e^{in\theta} \tag{5.20}$$

Equation (5.19) then yields,

$$r^2 \frac{\partial^2 \mathbf{w}_n}{\partial r^2} + r\mathbf{B}_n \frac{\partial \mathbf{w}_n}{\partial r} - \mathbf{C}_n \mathbf{w}_n = \mathbf{f}_n(r) \tag{5.21}$$

where the matrix coefficients are defined by,

$$\mathbf{B}_n = \begin{bmatrix} 1 & i\frac{(\upsilon\lambda+G)n}{\lambda\beta} \\ i\frac{(\upsilon\lambda+G)n}{G} & 1 \end{bmatrix} \tag{5.22}$$

$$\mathbf{C}_n = \begin{bmatrix} 1+\frac{Gn^2}{\lambda\beta} & i\frac{(\lambda\beta+G)n}{\lambda\beta} \\ -i\frac{(\lambda\beta+G)n}{G} & 1+\frac{\lambda\beta n^2}{G} \end{bmatrix} \tag{5.23}$$

and the right hand side input vector is

$$\mathbf{f}_n(r,t) = (1+\upsilon)\alpha_e r^2 \begin{bmatrix} \frac{1}{\beta}\frac{\partial T_n}{\partial r} \\ i\frac{\lambda n}{Gr}T_n \end{bmatrix} \tag{5.24}$$

Equation (5.21) is a second-order ordinary differential equation with variable coefficients. It can be transformed into an equation with constant coefficients by

setting $r = e^z$:

$$\mathbf{w}_n(r,t) = \mathbf{w}_n(e^z,t) = \mathbf{W}_n(z,t) \tag{5.25}$$

$$\frac{\partial \mathbf{w}_n(r,t)}{\partial r} = \frac{\partial \mathbf{W}_n(z,t)}{\partial z} \times \frac{1}{r} \tag{5.26}$$

$$\frac{\partial^2 \mathbf{w}_n(r,t)}{\partial r^2} = \frac{1}{r^2}\left(\frac{\partial^2 \mathbf{W}_n(z,t)}{\partial z^2} - \frac{\partial \mathbf{W}_n(z,t)}{\partial z}\right) \tag{5.27}$$

Equation (5.21) therefore becomes,

$$\frac{\partial^2 \mathbf{W}_n}{\partial z^2} + (\mathbf{B}_n - \mathbf{I})\frac{\partial \mathbf{W}_n}{\partial z} - \mathbf{C}_n \mathbf{W}_n = \mathbf{F}_n(z,t) \tag{5.28}$$

where

$$\mathbf{F}_n(z,t) = (1+\upsilon)\alpha_e e^z \begin{bmatrix} \frac{1}{\beta}\frac{\partial \hat{T}_n(z,t)}{\partial z} \\ i\frac{\lambda n}{G}\hat{T}_n(z,t) \end{bmatrix} \tag{5.29}$$

and

$$\hat{T}_n(z,t) = T_n(e^z,t) \tag{5.30}$$

Although pseudo-static, the time variable t is shown for completeness.

Equation (5.28) may be reduced to first order form through,

$$\begin{aligned} &\mathbf{X}_n = \frac{\partial \mathbf{W}_n}{\partial z} = \mathbf{W}_n' \\ &\mathbf{X}_n' + (\mathbf{B}_n - \mathbf{I})\,\mathbf{X}_n - \mathbf{C}_n \mathbf{W}_n = \mathbf{F}_n \end{aligned} \tag{5.31}$$

By defining,

$$\mathbf{Z}_n(z,t) = \begin{bmatrix} \mathbf{W}_n(z,t) \\ \mathbf{X}_n(z,t) \end{bmatrix} = \begin{bmatrix} U_{rn}(z,t) \\ V_{\theta n}(z,t) \\ U'_{rn}(z,t) \\ V'_{\theta n}(z,t) \end{bmatrix} \tag{5.32}$$

It follows that

$$\frac{\partial \mathbf{Z}_n}{\partial z} = \mathbf{Z}'_n = \begin{bmatrix} \mathbf{W}'_n \\ \mathbf{X}'_n \end{bmatrix} = \begin{bmatrix} \mathbf{0} & \mathbf{I} \\ \mathbf{C}_n & (\mathbf{I} - \mathbf{B}_n) \end{bmatrix} \begin{bmatrix} \mathbf{W}_n \\ \mathbf{X}_n \end{bmatrix} + \begin{bmatrix} \mathbf{0} \\ \mathbf{F}_n \end{bmatrix} \tag{5.33}$$

Consequently, the general form of the state-equation is

$$\mathbf{Z}'_n(z,t) = \mathbf{A}_n \mathbf{Z}_n(z,t) + \mathbf{D}_n \mathbf{E}_n(z,t) \tag{5.34}$$

where $\mathbf{Z}_n$ and $\mathbf{E}_n$ are the state-vector and input-vector, respectively. The constant coefficient state matrix is

$$\mathbf{A}_n = \begin{bmatrix} \mathbf{0} & \mathbf{I} \\ \mathbf{C}_n & (\mathbf{I} - \mathbf{B}_n) \end{bmatrix} \tag{5.35}$$

while the z-dependence of the input is specified by

$$\mathbf{E}_n(z,t) = \begin{bmatrix} \mathbf{0} \\ \mathbf{F}_n(z,t) \end{bmatrix} = (1+\upsilon)\alpha_e e^z \begin{bmatrix} 0 \\ 0 \\ \frac{1}{\beta}\frac{\partial \hat{T}_n(z,t)}{\partial z} \\ i\frac{\lambda n}{G}\hat{T}_n(z,t) \end{bmatrix} \tag{5.36}$$

$$\mathbf{D}_n = \mathbf{I} \tag{5.37}$$

5.3.1.1 General Solution of the State-Equation

The state-equation (5.34) may be solved using an integrating factor approach [98]. The general solution may be expressed in the form

$$\mathbf{Z}_n(z,t) = e^{\mathbf{A}_n(z-z_i)}\mathbf{Z}_n(z_i,t) + \int_{z_i}^{z} e^{\mathbf{A}_n(z-p)}\mathbf{D}_n\mathbf{E}_n(p,t)dp \tag{5.38}$$

The "initial" condition $\mathbf{Z}_n(z_i)$ has yet to be determined. It must be related to the boundary conditions, which are specified in term of zero stress. To make further progress, an output-equation must be defined.

5.3.2 Output-Equation

The output-equation defines the parameters that are of interest in terms of the state and input vectors. The mathematical expression for an output-equation is

$$\mathbf{Y}_n(z,t) = \mathbf{G}_n(z)\mathbf{Z}_n(z,t) + \mathbf{H}_n(z)\mathbf{E}_n(z,t) \tag{5.39}$$

where $\mathbf{Y}_n$ is the output-vector. In term of the polar coordinates, for the auxiliary bearing problem it is appropriate to define

$$\mathbf{y}(r,\theta,t) = \sum_{n=-\infty}^{\infty} \mathbf{y}_n(r,t)e^{in\theta} = \begin{bmatrix} u_r(r,\theta,t) \\ v_\theta(r,\theta,t) \\ \sigma_r(r,\theta,t) \\ \sigma_\theta(r,\theta,t) \\ \tau_{r\theta}(r,\theta,t) \end{bmatrix} = \sum_{n=-\infty}^{\infty} \begin{bmatrix} u_{rn}(r,t) \\ v_{\theta n}(r,t) \\ \sigma_{rn}(r,t) \\ \sigma_{\theta n}(r,t) \\ \tau_{r\theta n}(r,t) \end{bmatrix} e^{in\theta} \tag{5.40}$$

where $\mathbf{y}(r,t) = \mathbf{Y}_n(z,t)$, and σ_r, σ_θ, $\tau_{r\theta}$ are the usual radial, hoop and shear stresses. Setting $r = e^z$ implies that

$$\begin{bmatrix} u_{rn}(r,t) \\ v_{\theta n}(r,t) \\ \sigma_{rn}(r,t) \\ \sigma_{\theta n}(r,t) \\ \tau_{r\theta n}(r,t) \end{bmatrix} \Leftrightarrow \begin{bmatrix} U_{rn}(z,t) \\ V_{\theta n}(z,t) \\ \Lambda_{rn}(z,t) \\ \Lambda_{\theta n}(z,t) \\ \Lambda_{r\theta n}(z,t) \end{bmatrix} \tag{5.41}$$

Now it is clear that

$$U_{rn}(z,t) = u_{rn}(e^z,t) \tag{5.42}$$

$$V_{\theta n}(z,t) = v_{\theta n}(e^z,t) \tag{5.43}$$

For the stress components in the output-equation, from (5.3) to (5.8),

$$\sigma_r(r,\theta,t) = \lambda\left(\beta\frac{\partial u_r}{\partial r} + \frac{\upsilon}{r}u_r + \frac{\upsilon}{r}\frac{\partial v_\theta}{\partial \theta}\right) - \lambda(1+\upsilon)\alpha_e T \tag{5.44}$$

$$\sigma_\theta(r,\theta,t) = \lambda\left(\upsilon\frac{\partial u_r}{\partial r} + \frac{\beta}{r} + \frac{\beta}{r}\frac{\partial v_\theta}{\partial \theta}\right) - \lambda(1+\upsilon)\alpha_e T \tag{5.45}$$

$$\tau_{r\theta}(r,\theta,t) = G\left(\frac{\partial v_\theta}{\partial r} - \frac{1}{r}v_\theta + \frac{1}{r}\frac{\partial u_r}{\partial \theta}\right) \tag{5.46}$$

Under the transformation $r = e^z$, the stress components in (5.44) to (5.46) may be expressed in term of the derivatives with respect to z. By further decomposing as Fourier series in θ, the result is that

$$\Lambda_{rn} = \frac{\lambda}{e^z}\left(\beta U'_{rn} + \upsilon U_{rn} + in\upsilon V_{\theta n}\right) - \lambda(1+\upsilon)\alpha_e \hat{T}_n \tag{5.47}$$

$$\Lambda_{\theta n} = \frac{\lambda}{e^z}\left(\upsilon U'_{rn} + \beta U_{rn} + in\beta V_{\theta n}\right) - \lambda(1+\upsilon)\alpha_e \hat{T}_n \tag{5.48}$$

$$\Lambda_{r\theta n} = \frac{G}{e^z}\left(V'_{\theta n} + inU_{rn} - V_{\theta n}\right) \tag{5.49}$$

It is now possible to deduce that the output-equation matrices in (5.39) must have the forms

$$\mathbf{G}_n = \begin{bmatrix} 1 & 0 & 0 & 0 \\ 0 & 1 & 0 & 0 \\ \frac{\lambda\upsilon}{e^z} & i\frac{n\lambda\upsilon}{e^z} & \frac{\lambda\beta}{e^z} & 0 \\ \frac{\lambda\beta}{e^z} & i\frac{n\lambda\beta}{e^z} & \frac{\lambda\upsilon}{e^z} & 0 \\ \frac{inG}{e^z} & -\frac{G}{e^z} & 0 & \frac{G}{e^z} \end{bmatrix} \tag{5.50}$$

$$\mathbf{H}_n = \begin{bmatrix} 0 & 0 & 0 & 0 \\ 0 & 0 & 0 & 0 \\ 0 & 0 & 0 & i\frac{G}{ne^z} \\ 0 & 0 & 0 & i\frac{G}{ne^z} \\ 0 & 0 & 0 & 0 \end{bmatrix} \tag{5.51}$$

5.4 State-Space Model with Physical Boundary Conditions

The complete state space representation is given by

1. State-Equation, $\mathbf{Z}'_n = \mathbf{A}_n\mathbf{Z}_n + \mathbf{D}_n\mathbf{E}_n$, with solution given by equation (5.38)

2. Output-Equation, $\mathbf{Y}_n = \mathbf{G}_n\mathbf{Z}_n + \mathbf{H}_n\mathbf{E}_n$

These equations allow us to solve the thermoelastic problem for an annulus with appropriate boundary conditions. Two distinct types of boundary conditions are considered, namely,

B1. Fixed outer boundary with stress free inner boundary.

B2. Resiliently mounted outer boundary with stress free inner boundary.

The following subsections demonstrate the procedure for determining the unknown state-vector, $\mathbf{Z}_n(z_i)$, which is defined on the inner boundary.

5.4.1 Rigidly Mounted Outer Boundary with Stress Free Inner Boundary (B1)

Consider a two-dimensional annulus, where the inner and outer radii are r_i and r_o respectively. After transformation $z_i = \ln r_i$, $z_o = \ln r_o$. The annulus is considered to be mounted in a rigid housing, where the radial and tangential displacements at the outer boundary are considered to be zero. On the other hand, the inner boundary is stress free. Hence,

$$\begin{aligned} \sigma_r(r_i, t) &= \tau_{r\theta}(r_i, t) = 0 \\ u_r(r_o, t) &= v_\theta(r_o, t) = 0 \end{aligned} \tag{5.52}$$

First the state-vector at the inner boundary must be determined for B1. Let $\mathbf{Z}_n(z_i) = \mathbf{c}_n^{\text{fix}}$, then the state-vector at the outer boundary is

$$\mathbf{Z}_n(z_o, t) = e^{\mathbf{A}_n(z_o - z_i)}\mathbf{c}_n^{\text{fix}}(t) + \int_{z_i}^{z_o} e^{\mathbf{A}_n(z_o - p)}\mathbf{D}_n\mathbf{E}_n(p, t)dp \tag{5.53}$$

The inner and outer boundary conditions imply that the output vector may be expressed at $z = z_i, z_o$ according to

$$\mathbf{Y}_n(z_i,t) = \begin{bmatrix} U_{rn}(z_i,t) \\ V_{\theta n}(z_i,t) \\ 0 \\ \Lambda_{\theta n}(z_i,t) \\ 0 \end{bmatrix} = \mathbf{G}_n(z_i)\mathbf{c}_n^{\text{fix}}(t) + \mathbf{H}_n(z_i)\mathbf{E}_n(z_i,t) \tag{5.54}$$

$$\begin{aligned} \mathbf{Y}_n(z_o,t) &= \begin{bmatrix} 0 \\ 0 \\ \Lambda_{rn}(z_o,t) \\ \Lambda_{\theta n}(z_o,t) \\ \Lambda_{r\theta n}(z_o,t) \end{bmatrix} \\ &= \mathbf{G}_n(z_o)\left\{ e^{\mathbf{A}_n(z_o-z_i)}\mathbf{c}_n^{\text{fix}}(t) + \int_{z_i}^{z_o} e^{\mathbf{A}_n(z_o-p)}\mathbf{D}_n\mathbf{E}_n(p,t)dp \right\} \\ &\quad + \mathbf{H}_n(z_o)\mathbf{E}_n(z_o,t) \end{aligned} \tag{5.55}$$

The hoop stress components in (5.54) and (5.55) are not required to satisfy any boundary conditions. Deleting the fourth row equation in (5.54), the following 2×2 sub-block form may be derived:

$$\begin{aligned} \begin{bmatrix} \mathbf{U}_n(z_i,t) \\ \mathbf{0} \end{bmatrix} &= \begin{bmatrix} \mathbf{I} & \mathbf{0} \\ \mathbf{G}_{n21}(z_i) & \mathbf{G}_{n22}(z_i) \end{bmatrix} \begin{bmatrix} \mathbf{c}_{n1}^{\text{fix}}(t) \\ \mathbf{c}_{n2}^{\text{fix}}(t) \end{bmatrix} \\ &\quad + \begin{bmatrix} \mathbf{0} & \mathbf{0} \\ \mathbf{0} & \mathbf{H}_{n22}(z_i) \end{bmatrix} \begin{bmatrix} \mathbf{0} \\ \mathbf{F}_n(z_i,t) \end{bmatrix} \end{aligned} \tag{5.56}$$

Similarly, equation (5.55) yields the sub-block form:

$$\begin{bmatrix} \mathbf{0} \\ \mathbf{\Lambda}_n(z_o,t) \end{bmatrix} = \begin{bmatrix} \mathbf{I} & \mathbf{0} \\ \mathbf{G}_{n21}(z_o) & \mathbf{G}_{n22}(z_o) \end{bmatrix} \begin{bmatrix} \mathbf{\Delta}_{n11} & \mathbf{\Delta}_{n12} \\ \mathbf{\Delta}_{n21} & \mathbf{\Delta}_{n22} \end{bmatrix} \begin{bmatrix} \mathbf{c}_{n1}^{\text{fix}}(t) \\ \mathbf{c}_{n2}^{\text{fix}}(t) \end{bmatrix} + \begin{bmatrix} \mathbf{I} & \mathbf{0} \\ \mathbf{G}_{n21}(z_o) & \mathbf{G}_{n22}(z_o) \end{bmatrix} \begin{bmatrix} \mathbf{\Phi}_{n1} \\ \mathbf{\Phi}_{n2} \end{bmatrix} + \begin{bmatrix} \mathbf{0} & \mathbf{0} \\ \mathbf{0} & \mathbf{H}_{n22}(z_o) \end{bmatrix} \begin{bmatrix} \mathbf{0} \\ \mathbf{F}_n(z_o) \end{bmatrix} \tag{5.57}$$

Here

$$\mathbf{U}_n(z,t) = \begin{bmatrix} U_{rn}(z,t) \\ V_{\theta n}(z,t) \end{bmatrix} \quad , \quad \mathbf{\Lambda}_n(z,t) = \begin{bmatrix} \Lambda_{rn}(z,t) \\ \Lambda_{r\theta n}(z,t) \end{bmatrix}$$

$$\mathbf{G}_{n21}(z) = e^{-z} \begin{bmatrix} \lambda\upsilon & in\lambda\upsilon \\ inG & -G \end{bmatrix}$$

$$\mathbf{G}_{n22}(z) = e^{-z} \begin{bmatrix} \lambda\beta & 0 \\ 0 & G \end{bmatrix}$$

$$\mathbf{H}_{n22}(z) = e^{-z} \begin{bmatrix} 0 & inG \\ 0 & 0 \end{bmatrix}$$

$$\begin{bmatrix} \mathbf{\Delta}_{n11} & \mathbf{\Delta}_{n12} \\ \mathbf{\Delta}_{n21} & \mathbf{\Delta}_{n22} \end{bmatrix} = e^{\mathbf{A}_n(z_o - z_i)}$$

$$\begin{bmatrix} \mathbf{\Phi}_{n1}(t) \\ \mathbf{\Phi}_{n2}(t) \end{bmatrix} = \int_{z_i}^{z_o} e^{\mathbf{A}_n(z_o-p)} \mathbf{D}_n \mathbf{E}_n(p,t)\,dp$$

Taking,

$$\mathbf{J}_n = \begin{bmatrix} \mathbf{J}_{n11} & \mathbf{J}_{n12} \\ \mathbf{J}_{n21} & \mathbf{J}_{n22} \end{bmatrix} = \begin{bmatrix} \mathbf{I} & \mathbf{0} \\ \mathbf{G}_{n21}(z_o) & \mathbf{G}_{n22}(z_o) \end{bmatrix} \begin{bmatrix} \mathbf{\Delta}_{n11} & \mathbf{\Delta}_{n12} \\ \mathbf{\Delta}_{n21} & \mathbf{\Delta}_{n22} \end{bmatrix} \tag{5.58}$$

The second block row of equation (5.56) and the first block row of equation (5.57) yield,

$$\mathbf{G}_{n21}(z_i)\mathbf{c}_{n1}^{\text{fix}}(t) + \mathbf{G}_{n22}(z_i)\mathbf{c}_{n2}^{\text{fix}}(t) + \mathbf{H}_{n22}(z_i)\mathbf{F}_{n2}(z_i,t) = \mathbf{0} \tag{5.59}$$

$$\mathbf{J}_{n11}\mathbf{c}_{n1}^{\text{fix}}(t) + \mathbf{J}_{n12}\mathbf{c}_{n2}^{\text{fix}}(t) + \mathbf{\Phi}_{n1}(t) = \mathbf{0} \tag{5.60}$$

The solution of (5.59) and (5.60) is

$$\begin{aligned}\mathbf{c}_n^{\text{fix}}(t) &= \begin{bmatrix} \mathbf{c}_{n1}^{\text{fix}}(t) \\ \mathbf{c}_{n2}^{\text{fix}}(t) \end{bmatrix} \\ &= -\begin{bmatrix} \mathbf{G}_{n21}(z_i) & \mathbf{G}_{n22}(z_i) \\ \mathbf{J}_{n11} & \mathbf{J}_{n12} \end{bmatrix}^{-1} \begin{bmatrix} \mathbf{H}_{n22}(z_i)\mathbf{F}_{n2}(z_i,t) \\ \mathbf{\Phi}_{n1}(t) \end{bmatrix}\end{aligned} \tag{5.61}$$

With $\mathbf{c}_n^{\text{fix}}$ now known, the stresses and the deformations of the annular body under general thermal loading can be evaluated using the output-equation

$$\begin{aligned}\mathbf{Y}_n(z,t) =& \mathbf{G}_n(z)\left\{e^{\mathbf{A}_n(z-z_i)}\mathbf{c}_n^{\text{fix}}(t) + \int_{z_i}^{z} e^{\mathbf{A}_n(z_o-p)}\mathbf{D}_n\mathbf{E}_n(p,t)dp\right\} \\ &+ \mathbf{H}_n(z)\mathbf{E}_n(z,t)\end{aligned} \tag{5.62}$$

Of course, this equation must be transformed back to polar coordinates by using $z = \ln r$.

5.4.2 Resiliently Mounted Outer Boundary with Stress Free Inner Boundary (B2)

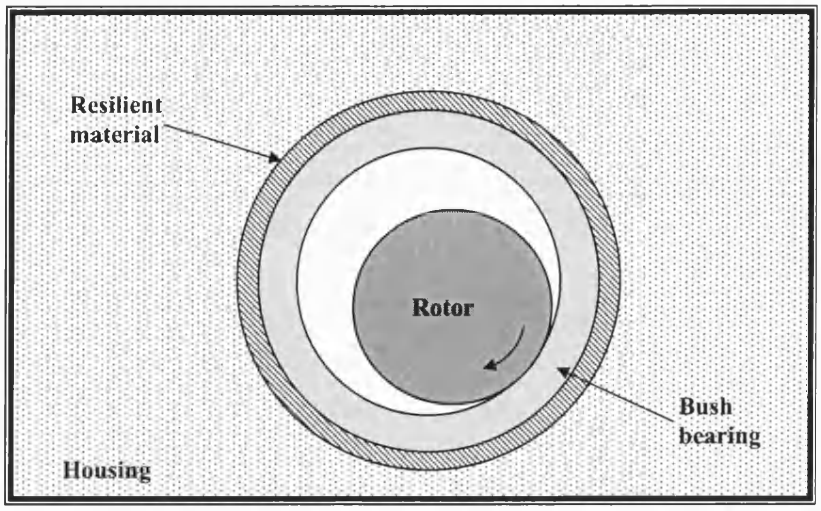

Figure 5.1: An annulus resiliently mounted in a housing.

Consider now a resiliently mounted annulus as shown in Figure 5.1, where outer boundary movement is permissible. The annulus is subjected to a thermal loading. Thermal deformations at the outer boundary are opposed by the resilient mounting ring. It is to be assumed that there is no slip between the surfaces of the annulus and the resilient ring. If the ring is considered to be a linear mechanical element, the outer boundary condition may be expressed as

$$\sigma_r(r_o) + \chi_r u_r(r_o) = 0 \tag{5.63}$$

$$\sigma_\theta(r_o) + \chi_\theta v_\theta(r_o) = 0 \tag{5.64}$$

where χ_r and χ_θ are stiffnesses per unit length opposing radial and angular displacements, respectively. Using the same notation as in section 5.4.1, the outer

boundary conditions yield

$$U_{rn}(z_o) = -\frac{1}{\chi_r}\Lambda_{rn}(z_o) \tag{5.65}$$

$$V_{\theta n}(z_o) = -\frac{1}{\chi_\theta}\Lambda_{\theta n}(z_o) \tag{5.66}$$

Note that, as $\chi_r \to \infty$ and $\chi_\theta \to \infty$, both $U_{rn}(z_o) \to 0$ and $V_{\theta n}(z_o) \to 0$, which reduces to the fixed boundary condition (B1). The inner boundary remains stress free. Thus the output-equation for the inner boundary must have a similar form as given in equation (5.54). However, it must be noted that new state-vector at the inner boundary, $\mathrm{Z}_n(z_i,t) = \mathbf{c}_n^{\mathrm{res}}(t)$ must be established for the resilient boundary problem. The output-equation of the outer boundary can be written as,

$$\begin{aligned}\mathbf{Y}_n(z_o,t) &= \begin{bmatrix} -\frac{1}{\chi_r}\Lambda_{rn}(z_o,t) \\ -\frac{1}{\chi_\theta}\Lambda_{\theta n}(z_o,t) \\ \Lambda_{rn}(z_o,t) \\ \Lambda_{\theta n}(z_o,t) \\ \Lambda_{r\theta n}(z_o,t) \end{bmatrix} \\ &= \mathbf{G}_n(z_o)\left\{e^{\mathbf{A}_n(z_o-z_i)}\mathbf{c}_n^{\mathrm{res}}(t) + \int_{z_i}^{z_o} e^{\mathbf{A}_n(z_o-p)}\mathbf{D}_n\mathbf{E}_n(p,t)dp\right\} \\ &\quad + \mathbf{H}_n(z_o)\mathbf{E}_n(z_o,t)\end{aligned} \tag{5.67}$$

Removing the last row of the output matrix equation, it yields,

$$\begin{bmatrix} -\boldsymbol{\chi}^{-1}\bar{\boldsymbol{\Lambda}}_n(z_o,t) \\ \bar{\boldsymbol{\Lambda}}_n(z_o,t) \end{bmatrix} = \begin{bmatrix} \bar{\mathbf{J}}_{n11} & \bar{\mathbf{J}}_{n12} \\ \bar{\mathbf{J}}_{n21} & \bar{\mathbf{J}}_{n22} \end{bmatrix} \begin{bmatrix} \mathbf{c}_{n1}^{\mathrm{res}}(t) \\ \mathbf{c}_{n2}^{\mathrm{res}}(t) \end{bmatrix} + \begin{bmatrix} \mathbf{K}_{n1}(t) \\ \mathbf{K}_{n2}(t) \end{bmatrix} \tag{5.68}$$

where

$$\boldsymbol{\chi} = \begin{bmatrix} \chi_r & 0 \\ 0 & \chi_\theta \end{bmatrix} \tag{5.69}$$

Manipulation of the sub-block rows of (5.68) gives

$$\mathbf{0} = \left(\boldsymbol{\chi}\bar{\mathbf{J}}_{n11} + \bar{\mathbf{J}}_{n21}\right)\mathbf{c}_{n1}^{\text{res}} + \left(\boldsymbol{\chi}\bar{\mathbf{J}}_{n12} + \bar{\mathbf{J}}_{n22}\right)\mathbf{c}_{n2}^{\text{res}} + \left(\boldsymbol{\chi}\mathbf{K}_{n1} + \mathbf{K}_{n2}\right) \tag{5.70}$$

where,

$$\begin{aligned}
\bar{\boldsymbol{\Lambda}}_n(z,t) &= \begin{bmatrix} \Lambda_{rn}(z,t) \\ \Lambda_{\theta n}(z,t) \end{bmatrix} \\
\begin{bmatrix} \bar{\mathbf{J}}_{n11} & \bar{\mathbf{J}}_{n12} \\ \bar{\mathbf{J}}_{n21} & \bar{\mathbf{J}}_{n22} \end{bmatrix} &= \begin{bmatrix} \mathbf{I} & \mathbf{0} \\ \bar{\mathbf{G}}_{n21}(z_o) & \bar{\mathbf{G}}_{n22}(z_o) \end{bmatrix} \begin{bmatrix} \boldsymbol{\Delta}_{n11} & \boldsymbol{\Delta}_{n12} \\ \boldsymbol{\Delta}_{n21} & \boldsymbol{\Delta}_{n22} \end{bmatrix} \\
\bar{\mathbf{G}}_{n21}(z) &= e^{-z} \begin{bmatrix} \lambda\upsilon & in\lambda\upsilon \\ \lambda\beta & in\lambda\beta \end{bmatrix} \\
\bar{\mathbf{G}}_{n22}(z) &= e^{-z} \begin{bmatrix} \lambda\beta & 0 \\ \lambda\upsilon & 0 \end{bmatrix} \\
\mathbf{K}_n(t) &= \begin{bmatrix} \mathbf{I} & \mathbf{0} \\ \bar{\mathbf{G}}_{n21}(z_o) & \bar{\mathbf{G}}_{n22}(z_o) \end{bmatrix} \begin{bmatrix} \boldsymbol{\Phi}_{n1}(t) \\ \boldsymbol{\Phi}_{n2}(t) \end{bmatrix} + \bar{\mathbf{H}}_{n22}(z_o)\mathbf{F}_n(z_o,t) \\
\bar{\mathbf{H}}_{n22}(z) &= \frac{iG}{n} e^{-z} \begin{bmatrix} 0 & 1 \\ 0 & 1 \end{bmatrix}
\end{aligned}$$

To determine $\mathbf{c}_n^{\text{res}}$, second relation is required for the output-equation at the inner boundary. Referring to equation (5.56), a similar form applies:

$$\begin{aligned}
\begin{bmatrix} \mathbf{U}_n(z_i,t) \\ \mathbf{0} \end{bmatrix} = &\begin{bmatrix} \mathbf{I} & \mathbf{0} \\ \bar{\mathbf{G}}_{n21}(z_i) & \bar{\mathbf{G}}_{n22}(z_i) \end{bmatrix} \begin{bmatrix} \mathbf{c}_{n1}^{\text{res}}(t) \\ \mathbf{c}_{n2}^{\text{res}}(t) \end{bmatrix} \\
&+ \begin{bmatrix} \mathbf{0} & \mathbf{0} \\ \mathbf{0} & \bar{\mathbf{H}}_{n22}(z_i) \end{bmatrix} \begin{bmatrix} \mathbf{0} \\ \mathbf{F}_n(z_i,t) \end{bmatrix}
\end{aligned} \tag{5.71}$$

Taking the second block row of matrix-equation (5.71) gives,

$$\mathbf{0} = \bar{\mathbf{G}}_{n21}(z_i)\mathbf{c}_{n1}^{\text{res}}(t) + \bar{\mathbf{G}}_{n22}(z_i)\mathbf{c}_{n2}^{\text{res}}(t) + \bar{\mathbf{H}}_{n22}(z_i)F_n(z_i,t) \tag{5.72}$$

Equations (5.70) and (5.72) now yield

$$\begin{aligned}\mathbf{c}_n^{\text{res}}(t) = \begin{bmatrix} \mathbf{c}_{n1}^{\text{res}}(t) \\ \mathbf{c}_{n2}^{\text{res}}(t) \end{bmatrix} = -&\begin{bmatrix} \bar{\mathbf{G}}_{n21}(z_i) & \bar{\mathbf{G}}_{n22}(z_i) \\ (\chi\bar{\mathbf{J}}_{n11} + \bar{\mathbf{J}}_{n21}) & (\chi\bar{\mathbf{J}}_{n21} + \bar{\mathbf{J}}_{n22}) \end{bmatrix}^{-1} \\ &\times \begin{bmatrix} \bar{\mathbf{H}}_{n22}(z_i)\mathbf{F}_n(z_i,t) \\ (\chi\mathbf{K}_{n21} + \mathbf{K}_{n22}) \end{bmatrix}\end{aligned} \tag{5.73}$$

Therefore, the thermoelastic solution for flexible boundary condition is

$$\begin{aligned}\mathbf{Y}_n(z,t) =& \mathbf{G}_n(z)\left\{e^{\mathbf{A}_n(z-z_i)}\mathbf{c}_n^{\text{res}}(t) + \int_{z_i}^{z} e^{\mathbf{A}_n(z_o-p)}\mathbf{D}_n\mathbf{E}_n(p,t)dp\right\} \\ &+ \mathbf{H}_n(z)\mathbf{E}_n(z,t)\end{aligned} \tag{5.74}$$

The fact is that equations (5.62) (B1 case) and (5.74) (B2 case) are elegant solutions for the auxiliary bearing problems. Differences in the boundary conditions on the outer surface are accounted for by the "initial" states $\mathbf{c}_n^{\text{fix}}$ or $\mathbf{c}_n^{\text{res}}$.

5.5 Thermoelastic Responses

The general output-equations for thermoelastic analysis developed in the previous sections can be implemented with any temperature profile that has a Fourier series representation. This section provides some simple case to validate the results of the analyses. Since the width of the inner race of the bush bearing is short (Table 3.2), all problems are analysed under a plane-stress condition.

5.5.1 Constant Temperature

Consider an increment of temperature, ΔT distributed evenly throughout the body. It required to set the first harmonic $n = 0$ of the temperature Fourier series to ΔT and the remaining terms to zero:

$$\hat{T}_0(z) = \Delta T \tag{5.75}$$

$$\hat{T}_{n\neq 0}(z) = 0 \tag{5.76}$$

If the movement of the annulus at the outer boundary is restrained, the deformations and stresses in the body can be analysed using equation (5.62) with (5.61). Figure 5.2 shows the distortion of the annulus under a constant temperature 100K. Since the outer boundary is fixed, there is no distortion at the outer radius. However, the heated body would expand radially inwards to achieve equilibrium state.

Further investigation was carried out using finite element analysis (FEA) to verify the results. An FEA commercial package, ANSYS, was used and element "Solid183" was chosen for two-dimensional steady-state thermoelastic analysis. The model was automatically meshed by the ANSYS program and no mesh refinement was required. The inner and outer boundary conditions were adiabatical and stress free. Therefore, a "zero displacement loading" was applied to the outer boundary. The solver was chosen automatically by ANSYS (Sparse Direct Solver) with a default tolerance of 0.001. Figure 5.3 shows the Von Mises stress distribution evaluated using equation (5.62), while figure 5.4 shows the Von Mises stress predicted using the finite element method (ANSYS). The results are comparable. The finite element method (FEM) is an excellent tool for solving complex shape model problem with loadings on a finite patch. However, it is not suitable for

a solving line source problem. The contact between the rotor and the bearing initiates from a line to a finite contact area over short period of time (see Chapter 7), and hence the use of the FEM in this situation is not viable.

The solution with flexible boundary condition would produce identical results provided χ_r and χ_θ are large enough to generate negligible displacement at the outer boundary, (see equations (5.65) and (5.66)). On the other hand, if both χ_r and χ_θ value are small, the annulus body would have no restraint in any direction, implying that it is free to move in free space. As a result, the later problem cannot be evaluated without including rigid body displacement errors.

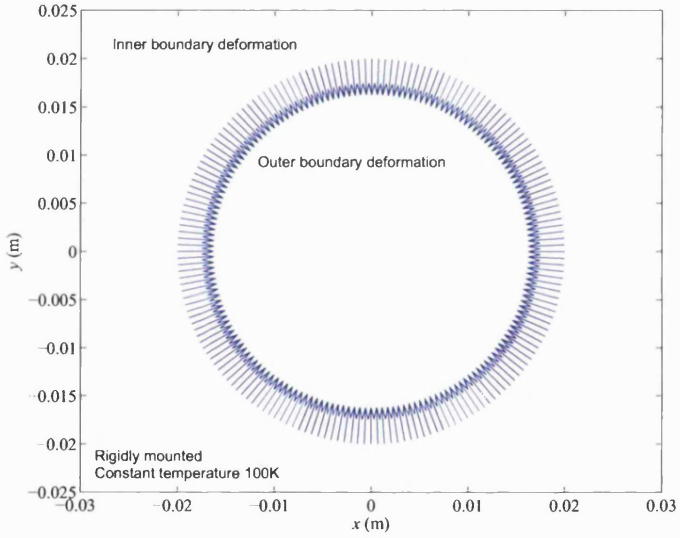

Figure 5.2: Inner and outer boundary displacements for constant temperature 100K distribution. The results were derived from equations (5.61) and (5.62)

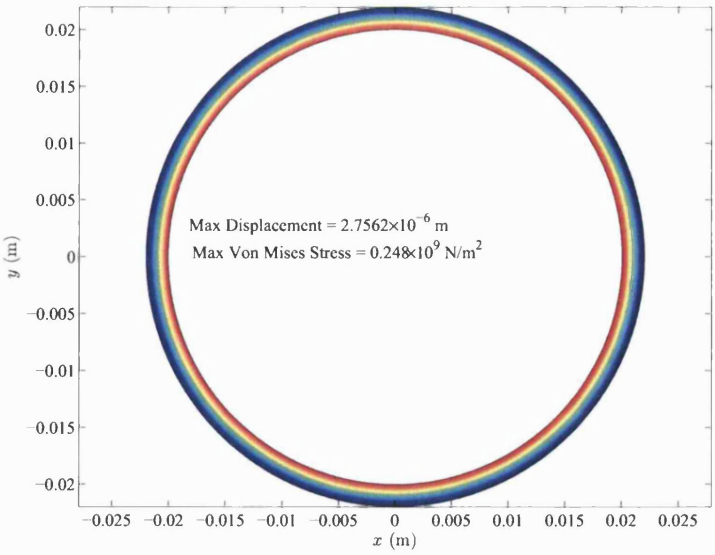

Figure 5.3: Von Mises stress due constant temperature distribution in an annular region evaluated using equation (5.62).

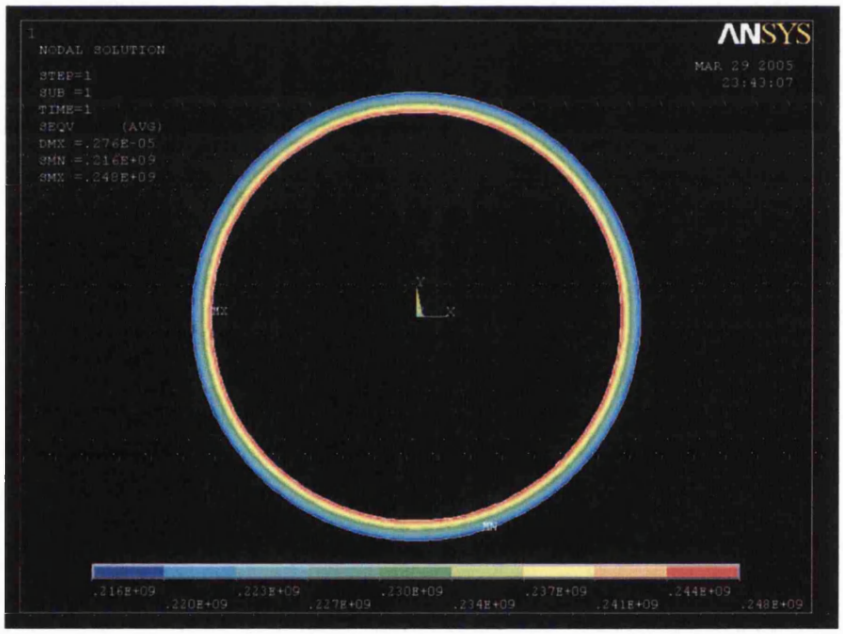

Figure 5.4: Von Mises stress evaluated using commercial FEA package ANSYS. DMX, SMN and SMX denoted as the maximum resultant displacement, minimum and maximum Von Mises stresses, respectively.

5.5.2 Green's Function Annulus Temperature

The Green's function thermoelastic displacement is defined as the deformation of the body induced by an unit instantaneous line heat source. Since the temperature Fourier coefficient is one of the core input parameters of the state-space model, equation (3.36) can be implemented in the state-space model directly. Rigidly and resiliently mounted outer boundaries are considered in this section.

5.5.2.1 Rigidly Mounted Outer boundary (B1)

Figure 5.5 shows the distorted annulus due to an instantaneous unit line heat source applied to the inner boundary. The material expands radially inwards because the outer boundary of the annulus is rigidly mounted. Further indication of the inward thermal expansion is shown in figure 5.6 with negative values of radial displacement at the inner boundary. Figure 5.7 shows the tangential displacements of the annulus. The radial and shear stress distributions are shown in figures 5.8 and 5.9, respectively. Both figures show that the inner boundary complies with a stress free boundary condition. The Von Mises stress distribution shown in figure 5.10 suggests that the annulus likely to experience a high stress field at the region below the heat source and that it is governed mainly by the hoop stress as shown in figure 5.11. Since it is known that $T_{Gn_{annulus}}$ is singular as $t \rightarrow 0$, the output-equation will inherit similar behaviour as the Green's function temperature function is used to form the input vector. Therefore, the influence of the poorly convergent Fourier series is noted for short timescale analysis as shown in figure 5.12. A similar approach of introducing a remainder function can be used to reduce the singularities of the Fourier coefficient in the displace-

ment. However, substituting the annular temperature remainder function into the state-space model directly is not a wise approach to remove the singularity behaviour, because explicit expressions are not generally possible. Therefore, an alternative approach to overcome this difficulty is to use thermoelastic half-space solution. Further explanation and derivation will be given in the next chapter.

5.5.2.2 Resiliently Mounted Annulus (B2)

For the resiliently mounted problem, the elements in the matrix $\boldsymbol{\chi}$ are evaluated using

$$\chi_r = \frac{E^{\text{res}}}{l^{\text{res}}} \tag{5.77}$$

$$\chi_\theta = \frac{E^{\text{res}}}{2\pi r_i^{\text{res}}} \tag{5.78}$$

where E^{res}, l^{res} and r_i^{res} are the elastic modulus, thickness and inner radius of the resilient ring. Consider an aluminium insert ring with $E^{\text{res}} = 69 \times 10^9$Pa, $l^{\text{res}} = 0.002$m and $r_i^{\text{res}} = 0.022$m, hence $\chi_r = 3.45 \times 10^{13}\text{N/m}^3$ and $\chi_\theta = 5 \times 10^{11}\text{N/m}^3$. When the annulus is heated, it expands radially inwards and outwards as shown in figure 5.13. Figures 5.14 and 5.15 show the radial and shear stresses of the annulus, which show that that stress free conditions prevail on the inner surface. Comparing the Von Mises stress distributions in figures 5.10 and 5.16, it is noted that the different boundary conditions cause the results to be non-comparable. It is an important issue in deriving the remainder function, which will be investigated in the next chapter.

5.6 Closure

General solutions for the annular thermoelastic problem have been developed using state-space theory. Studies are carried out with different boundary conditions and the general solutions for rigidly and resiliently mounted outer boundary conditions were developed. These solutions were then implemented with constant and Green's function temperature distributions for validation purposes. Poor Fourier series convergence was found for short timescale Green's function thermoelastic analysis. Nevertheless, this can be improved using a remainder function, which will be developed in Chapter 6.

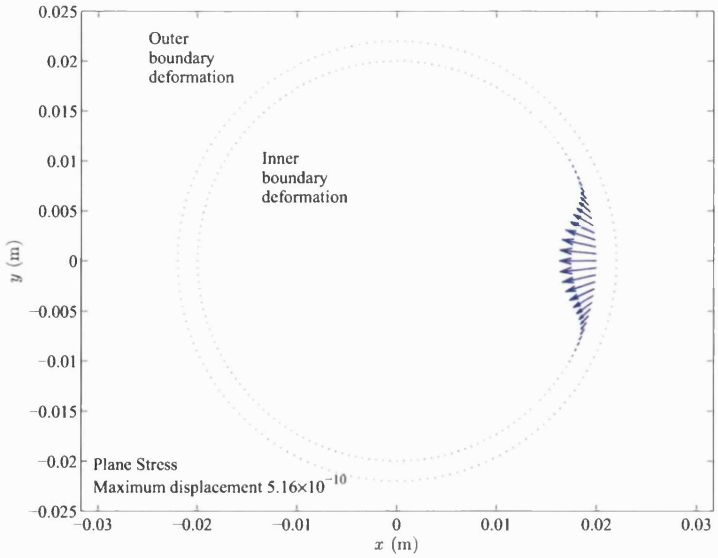

Figure 5.5: Distortion of annulus due to an unit instantaneous line heat source at the inner boundary at time point $t = 1$s ($\beta = 0.011$). The outer boundary is fixed.

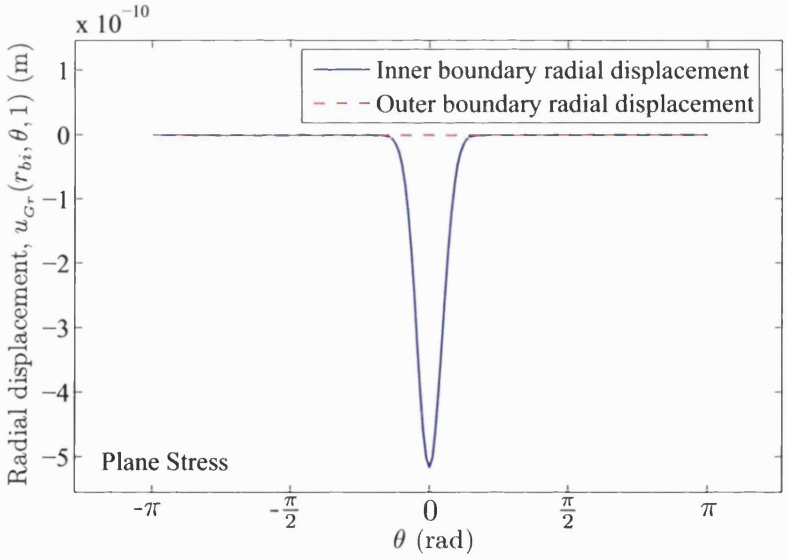

Figure 5.6: Inner and outer boundary radial displacements under the influences of Green's function temperature profile at $t = 1$s ($\beta = 0.011$). The outer boundary is fixed.

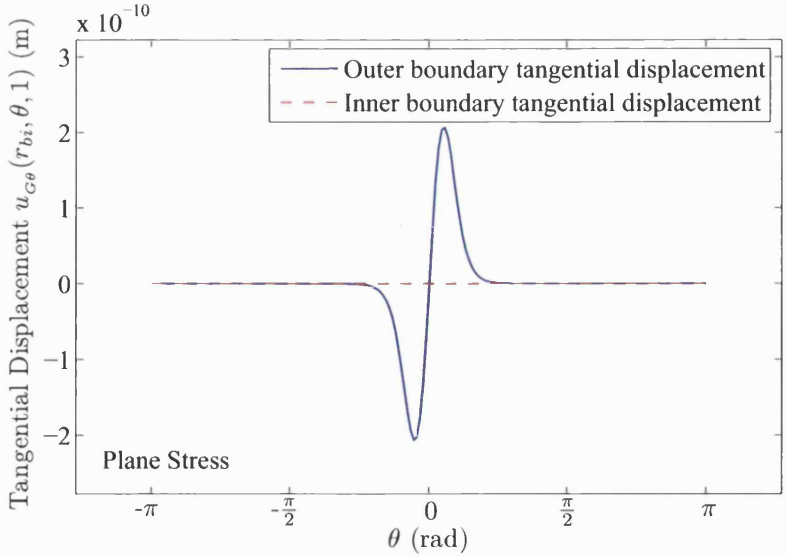

Figure 5.7: Inner and outer boundary tangential displacements at $t = 1$s ($\beta = 0.011$) of the inner boundary subjected to an unit instantaneous line heat source. The outer boundary is fixed.

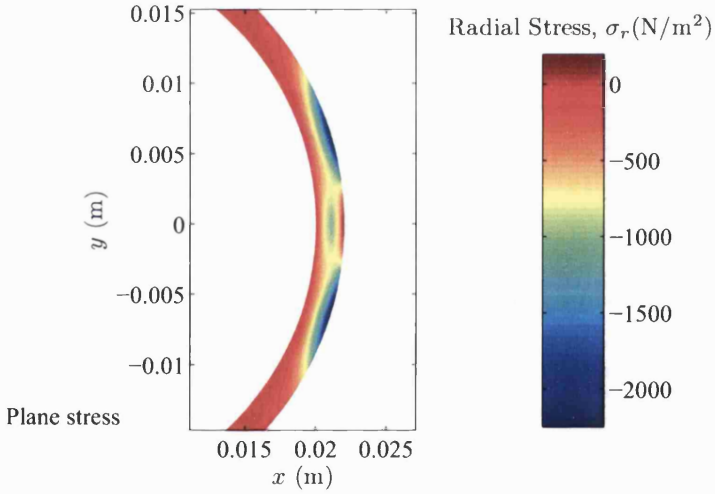

Figure 5.8: Radial stress distribution at $t = 1s$ ($\beta = 0.011$) due to a unit instantaneous line heat source applied to the point $(r_i, 0)$. The outer boundary is fixed.

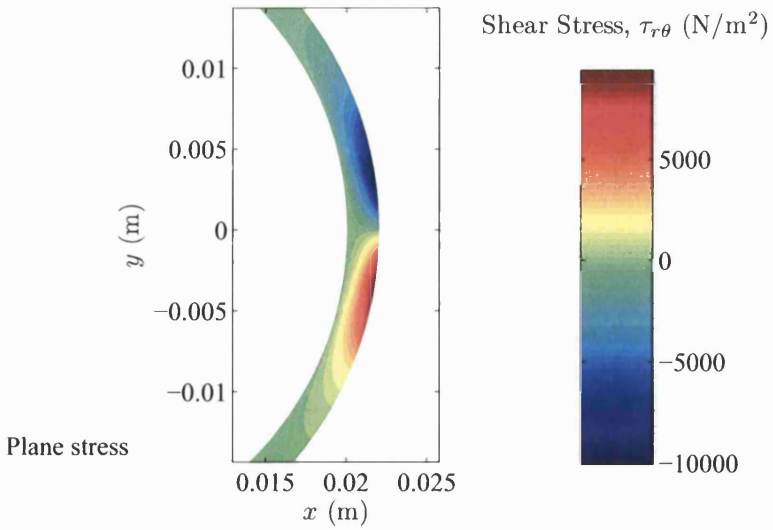

Figure 5.9: Shear stress distribution at $t = 1s$ ($\beta = 0.011$) due to a unit instantaneous line heat source applied to the point $(r_i, 0)$. The outer boundary is fixed.

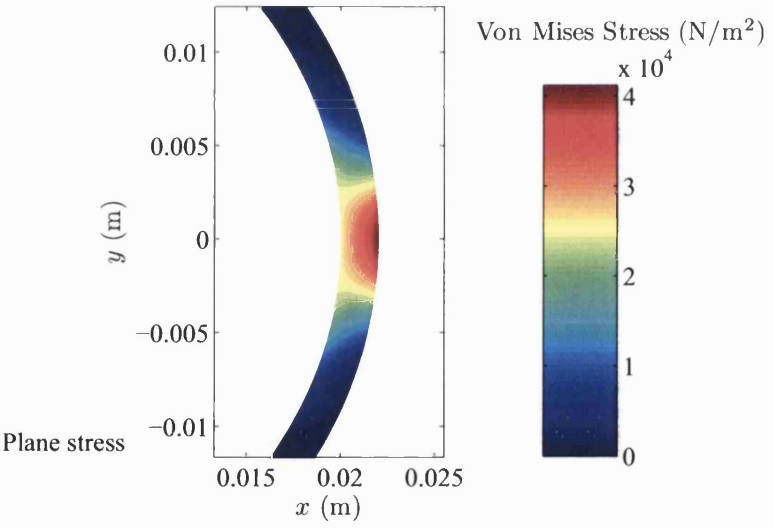

Figure 5.10: Von Mises stress in an annulus due to instantaneous line heat source at $t = 1s$ ($\beta = 0.011$).

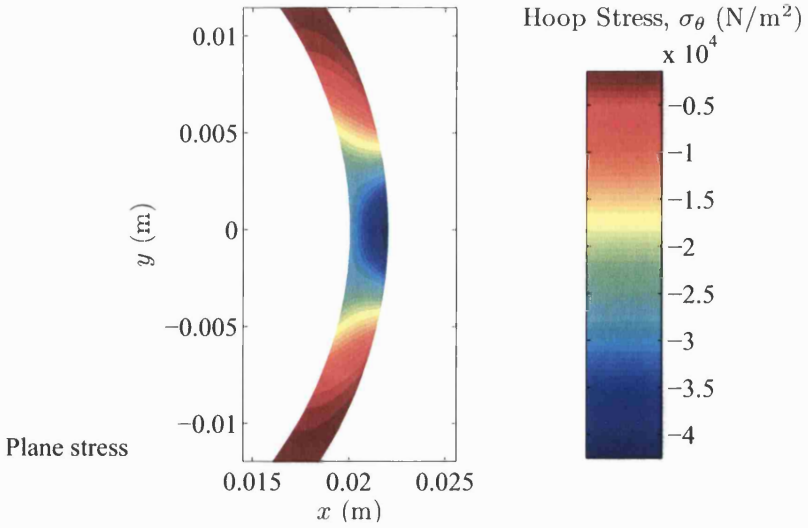

Figure 5.11: Greens function thermal induced hoop stress in annulus body at time point $t = 1$s ($\beta = 0.011$).

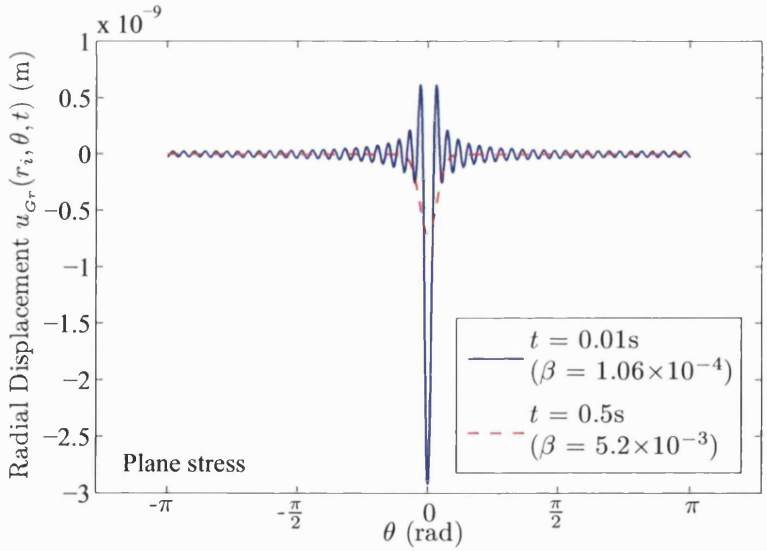

Figure 5.12: Inner boundary radial displacements at $t = 0.01$s ($\beta = 1.06 \times 10^{-4}$) and 0.5s ($\beta = 5.2 \times 10^{-3}$). The Fourier series is truncated at 50 harmonics. Poor Fourier series convergence is noted for short timescale analysis.

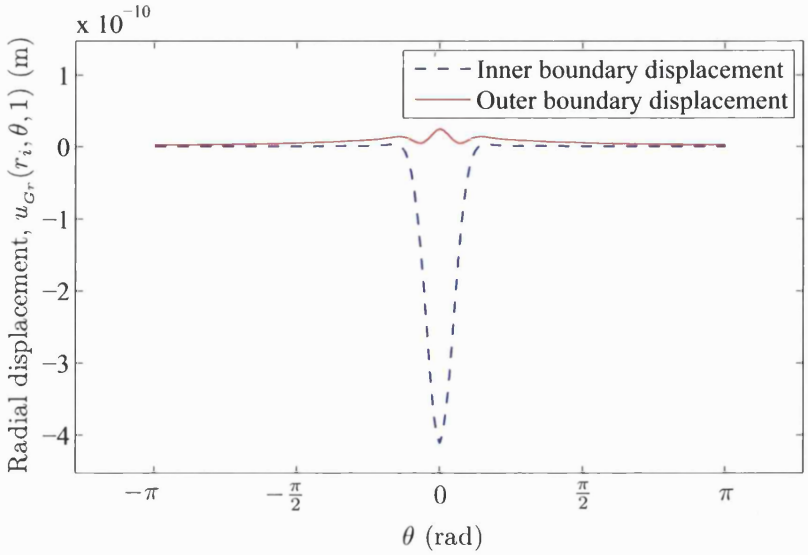

Figure 5.13: Inner and outer boundaries radial displacements at $t = 1$s ($\beta = 0.011$) with resiliently mounted boundary analysis. The heated material expands both radial inward and outward direction.

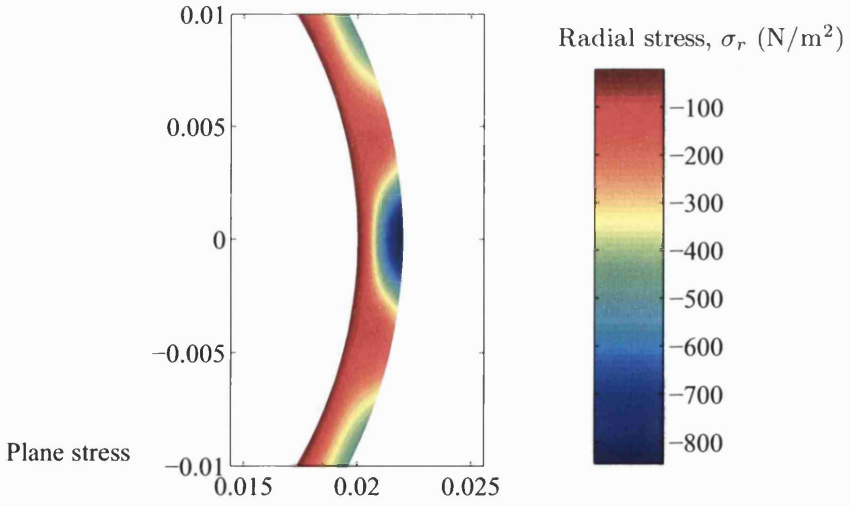

Figure 5.14: Radial stress distribution of resiliently mounted boundary analysis at $t = 1$s ($\beta = 0.011$). The inner boundary satisfied stress free boundary condition.

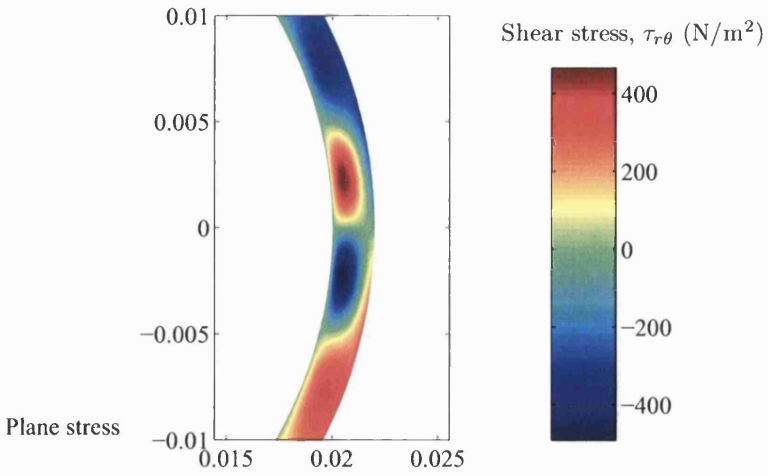

Figure 5.15: Shear stress distribution of resiliently mounted boundary analysis at $t = 1$s ($\beta = 0.011$). The inner boundary satisfied stress free boundary condition.

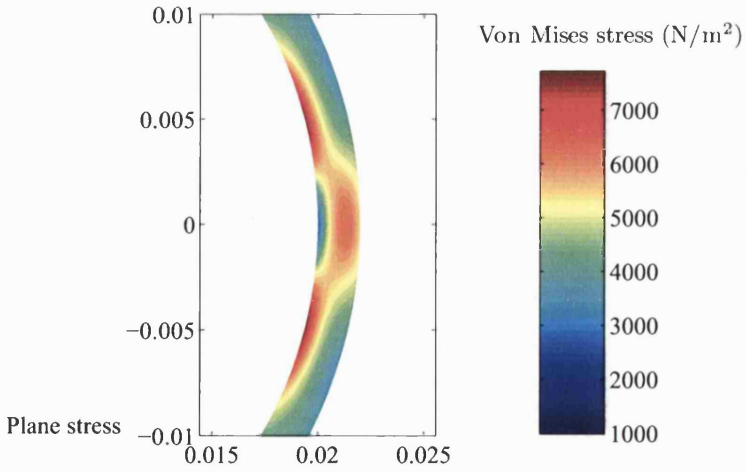

Figure 5.16: Von Mises stress distribution with resiliently mounted boundary analysis at $t = 1$s ($\beta = 0.011$).

Chapter 6

Remainder Function for Thermoelastic Analysis

6.1 Overview

A direct Fourier series representation of a Green's function is not an efficient method for solving short timescale problems due to increasingly poor convergence as $t \rightarrow 0$. The method proposed in Chapter 3 led to the derivation of a temperature remainder function that has a convergent Fourier series as $t \rightarrow 0$. The thermoelastic Green's function solution of Chapter 5, expressed in terms of Fourier components, also has singular behaviour as $t \rightarrow 0$. This chapter investigates further the application of a remainder function for the thermoelastic analysis by using Green's functions for the transient thermoelastic half-plane contact problem developed by Barber and Martin-Moran [71].

6.2 Green's Functions for Transient Thermoelastic Half-Plane Contact Problems.

The technique developed by Barber and Martin-Moran [71] uses the thermoelastic equilibrium equations and stress-strain relations, together with superposition of the Flamant line force solution. For completeness, the following section summarises the half-plane Green's function solution of Barber and Martin-Moran.

6.2.1 Instantaneous Line Source

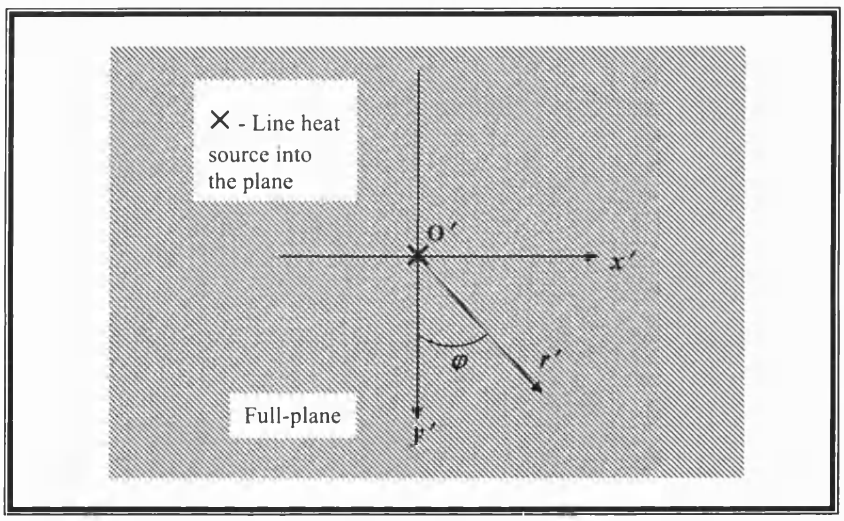

Figure 6.1: Line heat source applied in the full-plane at the origin.

Consider an unit instantaneous line heat source applied into the full-plane at the origin O′. The polar coordinate relative to the source point are (r', φ). If there is no heat flow across the boundary x-axis, the temperature distribution is given by equation (4.11). The following relationship can be established by substituting the stress-strain relations into the equilibrium equation (5.1) and

using axi-symmetry:

$$\lambda\frac{\partial}{\partial r'}\left(\beta\epsilon_{r'}+\upsilon\epsilon_{\varphi}\right)+\frac{\lambda\left(\beta-\upsilon\right)}{r'}\left(\epsilon_{r'}-\epsilon_{\varphi}\right)=\lambda\left(1+\upsilon\right)\alpha_e\frac{\partial T}{\partial r'} \tag{6.1}$$

where equations (5.3) and (5.4) reduce to,

$$\epsilon_{r'} = \frac{d\hat{u}_{r'}}{dr'} \tag{6.2}$$

$$\epsilon_{\varphi} = \frac{\hat{u}_{r'}}{r'} \tag{6.3}$$

Substituting these two equation into equation (6.1) and integrating gives

$$\hat{u}_{Gr'}(r,\varphi,t)=\frac{1+\upsilon}{\beta}\alpha_e\frac{1}{r'}\int r'T(r',\varphi,t)dr'+C_1r'+\frac{C_2}{r'} \tag{6.4}$$

and since the problem is axi-symmetric, the angular displacement

$$\hat{v}_{G\varphi}(r,\varphi,t)=0 \tag{6.5}$$

The radial and hoop stresses can be obtained by substituting the radial displacement in the stress-strain relations given by equations (5.6) and (5.7):

$$\begin{aligned}\hat{\sigma}_{Gr'}(r',\varphi,t) = &-\lambda\left(1-\frac{\upsilon}{\beta}\right)(1+\upsilon)\frac{\alpha_e}{r'^2}\int r'T(r',\varphi,t)dr' \\ &+\lambda\left(\upsilon+\frac{1}{\beta}\right)C_1+\lambda\left(\upsilon-\frac{1}{\beta}\right)\frac{C_2}{r'^2}\end{aligned} \tag{6.6}$$

$$\begin{aligned}\hat{\sigma}_{G\varphi}(r',\varphi,t) = &\lambda\left(1-\frac{\upsilon}{\beta}\right)(1+\upsilon)\,\alpha_e\left(\frac{1}{r'^2}\int r'T(r',\varphi,t)dr'\right. \\ &\left.-T(r',\varphi,t)\right)+\lambda\left(\upsilon+\frac{1}{\beta}\right)C_1+\lambda\left(\upsilon-\frac{1}{\beta}\right)\frac{C_2}{r'^2}\end{aligned} \tag{6.7}$$

The displacement field must remain finite as $r'\rightarrow\infty$, which implies that $C_1=0$. On the other hand, the displacement at the origin ($r'=0$) must also remain finite

for $t > 0$ and thus $C_2 = 0$. The result is that

$$\hat{\sigma}_{Gr'}(r', \varphi, t) = -\frac{\alpha_e}{4\pi kt}\left(1 - \frac{\upsilon}{\beta}\right)(1+\upsilon)\lambda\left(\frac{1 - e^{-R'^2}}{R'^2}\right) \tag{6.8}$$

$$\hat{\sigma}_{G\varphi}(r', \varphi, t) = \frac{\alpha_e}{4\pi kt}\left(1 - \frac{\upsilon}{\beta}\right)(1+\upsilon)\lambda\left(\frac{1 - e^{-R'^2}}{R'^2} - 2e^{-R'^2}\right) \tag{6.9}$$

$$\hat{u}_{Gr'}(r', \varphi, t) = \frac{\alpha_e}{2\pi\rho_d c_p\sqrt{\kappa t}}\frac{(1+\upsilon)}{\beta}\left(\frac{1 - e^{-R'^2}}{R'^2}\right) \tag{6.10}$$

where ρ_d and c_p are the density and specific heat capacity of the material, respectively, and R' is defined as,

$$R'^2 = \frac{r'^2}{4\kappa t} = \frac{r^2(1 + \eta^2 - 2\eta\cos\theta)}{4\kappa t} \tag{6.11}$$

This solution corresponds to the case in which the surface of the half-plane is restrained by the hoop stress, $\hat{\sigma}_{G\varphi}$. For a stress free surface boundary, the solution must be superimposed with another solution having equal and opposite stress to $\hat{\sigma}_{G\varphi}$. This can be achieved by using the Flamant point force result.

6.2.2 Flamant Solution

The Flamant's solution is induced by a line force on the half-plane and can be expressed in the following form:

$$\sigma_{Fr'} = -\frac{2P}{\pi r'}\cos\theta \tag{6.12}$$

$$\sigma_{F\varphi} = \tau_{Fr'\varphi} = 0 \tag{6.13}$$

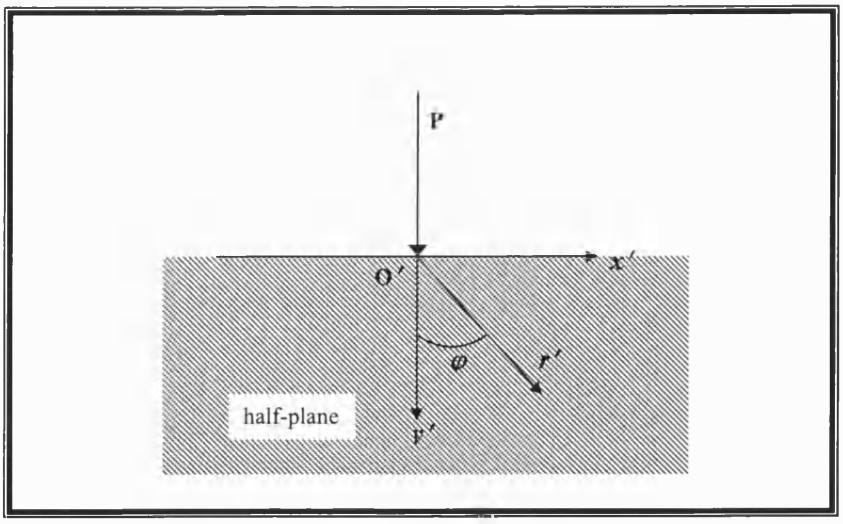

Figure 6.2: Half-plane subjected to a load per unit length, P at the origin O'.

where P is the load per unit length. The general stress-strain relations are,

$$\epsilon_{Fr'} = \frac{1}{\lambda\left(\upsilon^2-\beta^2\right)}\left[\upsilon\sigma_{Fr'}-\beta\sigma_{F\varphi}\right] \tag{6.14}$$

$$\epsilon_{F\varphi} = \frac{1}{\lambda\left(\upsilon^2-\beta^2\right)}\left[\upsilon\sigma_{F\varphi}-\beta\sigma_{Fr'}\right] \tag{6.15}$$

$$\gamma_{Fr'\varphi} = G\tau_{Fr'\varphi} \tag{6.16}$$

Substituting the Flamant stresses (6.12) and (6.13) into (6.14-6.16) yields

$$\epsilon_{Fr'} = \frac{\partial u_{Fr'}}{\partial r'} = \frac{\beta}{\lambda\left(\upsilon^2-\beta^2\right)}\frac{2P}{\pi r'}\cos\theta \tag{6.17}$$

$$\epsilon_{F\varphi} = \frac{u_{Fr'}}{r'}+\frac{\partial v_{F\varphi}}{r'\partial\varphi} = -\frac{\upsilon}{\lambda\left(\upsilon^2-\beta^2\right)}\frac{2P}{\pi r'}\cos\theta \tag{6.18}$$

$$\gamma_{Fr'\varphi} = \frac{\partial u_{Fr'}}{r'\partial\varphi}+\frac{\partial v_{F\varphi}}{\partial r'}-\frac{v_{F\varphi}}{r'} = 0 \tag{6.19}$$

The solutions of (6.17) and (6.18) are,

$$u_{Fr'} = \Psi\beta\cos\varphi\ln r'+f_1\left(\varphi\right) \tag{6.20}$$

$$v_{F\varphi} = -\Psi\upsilon\sin\varphi-\Psi\beta\sin\varphi\ln r'-\int f_1\left(\varphi\right)d\varphi+f_2\left(r'\right) \tag{6.21}$$

where $\Psi = -2P/\lambda\pi\,(\beta^2 - \upsilon^2)$. Functions f_1 and f_2 can be determined using equation (6.19). Substituting equations (6.20) and (6.21) into (6.19) yields

$$f_1'(\varphi) - \Psi\beta\sin\varphi + \int f_1(\varphi)\,d\varphi + \Psi\upsilon\sin\varphi + f_2'(r') - \frac{f_2(r')}{r'} = 0 \qquad (6.22)$$

Therefore

$$\frac{d^2 f_1}{d\varphi^2} + f_1 - \Psi(\beta - \upsilon)\cos\varphi = 0 \qquad (6.23)$$

$$\frac{df_2}{dr'} - \frac{f_2}{r'} = 0 \qquad (6.24)$$

which give

$$f_1 = \frac{\Psi(\beta - \upsilon)}{2}\varphi\sin\varphi + A\cos\varphi + B\sin\varphi \qquad (6.25)$$

$$f_2 = Cr' \qquad (6.26)$$

Therefore the radial and angular displacements are,

$$u_{Fr'} = \Psi\beta\cos\varphi\ln r' + \frac{\Psi(\beta - \upsilon)}{2}\varphi\sin\varphi + A\cos\varphi + B\sin\varphi \qquad (6.27)$$

$$\begin{aligned} v_{F\varphi} = &-\Psi\upsilon\sin\varphi - \Psi\beta\sin\varphi\ln r' + \frac{\Psi(\beta - \upsilon)}{2}\varphi\cos\varphi \\ &- \frac{\Psi(\beta - \upsilon)}{2}\sin\varphi - A\sin\varphi + B\cos\varphi + Cr' \end{aligned} \qquad (6.28)$$

Since there is no lateral displacement at $\varphi = 0$, B and C must be zero. On the surface boundary, where $\varphi = \pi/2, -\pi/2$, the normal displacement can be evaluated using

$$\begin{aligned} u_{Fy'} &= -\left[v_{F\varphi}\right]_{\varphi=-\frac{\pi}{2}} = \left[v_{F\varphi}\right]_{\varphi=\frac{\pi}{2}} \\ &= -\Psi\beta\ln r' - \frac{\Psi}{2}(\beta + \upsilon) - A \end{aligned} \qquad (6.29)$$

The constant A can be determined by specifying where there is no displacement. On the other hand, applying the same angular condition to equation (6.27) would give the tangential displacement of the half-plane surface boundary as

$$u_{Fx'} = -\frac{\Psi\pi(\beta - \upsilon)}{4} \tag{6.30}$$

Equations (6.29) and (6.30) are the Green's function displacements of the half-plane problem subjected to a statical line force.

6.2.2.1 Distributed Pressure on Half-Plane Surface

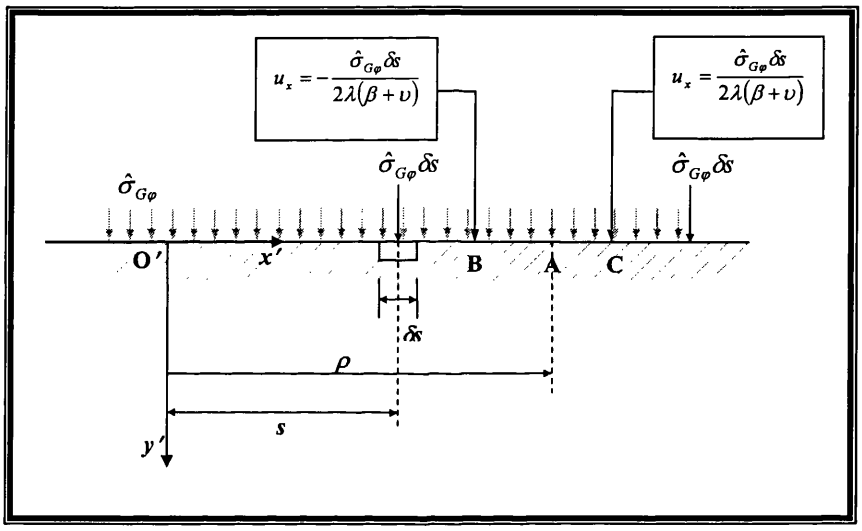

Figure 6.3: Half-plane subjected distributed pressure of magnitude $\hat{\sigma}_{G\varphi}$.

Consider the half-plane surface is subjected to a pressure distribution of magnitude $\hat{\sigma}_{G\varphi}$. Based on thermoelastic analysis stated in section 6.2.1, the half-plane surface has normal stress equal to the hoop stress given in equation (6.9). A zero surface stress condition can be deduced by combining the hoop stress with the Flamant point load solution. The normal displacement induced by the hoop stress, $\hat{\sigma}_{G\varphi}$, on the half-plane surface can be obtained by superimposing Flamant

point load solutions in the form of the convolution:

$$\bar{u}_{Gy'} = -\frac{2\beta}{\lambda\pi\left(\beta^2 - \upsilon^2\right)} \int_{-\infty}^{\infty} \sigma_{\varphi}(s) \ln|r' - s| \, ds \tag{6.31}$$

However, it is more complicated to evaluate the tangential displacement, $\bar{u}_{x'}$, due to the sign convention in (6.30). The negative sign in equation (6.30) indicates that the material would flow toward the direction where the point of the line force is applied to. However, it will be different once the system is transformed to Cartesian coordinate system, (x', y'). Figure 6.3 shows a half-plane subjected to distributed pressure on the surface boundary. The origin of the coordinate system is denoted by O′ and the point of investigation is A. Taking point A as the second datum, surface elements are taken on both side and assigned with points B and C points, respectively. Each element is subjected to a normal force with magnitude $\sigma_{\varphi}\delta s$. The force applied at B would pull point A toward point B and hence negative displacement. Meanwhile, force at point C induces a positive displacement of point A. Therefore, the surface tangential displacement can be expressed as,

$$\bar{u}_{Gx'}(x') = -\frac{1}{2\lambda(\beta + \upsilon)} \int_{-\infty}^{x'} \sigma_{\varphi}(s) ds + \frac{1}{2\lambda(\beta + \upsilon)} \int_{x'}^{\infty} \sigma_{\varphi}(s) ds \tag{6.32}$$

6.2.3 Half-Plane Green's Function Solution

Substituting the hoop stress (6.9) into the equations (6.31) and (6.32), and superimposing them with the full-plane displacements given by equations (6.5)

and (6.10) gives

$$\begin{aligned} u_{Ghy'}(r',\varphi,t) &= \hat{v}_{G\varphi} - \frac{2\beta}{\lambda\pi\left(\beta^2-\upsilon^2\right)}\int_{-\infty}^{\infty}\hat{\sigma}_{G\varphi}(r',\varphi,t)\ln|r'-s|\,ds \\ &= -\frac{2\beta}{\lambda\pi\left(\beta^2-\upsilon^2\right)}\int_{-\infty}^{\infty}\hat{\sigma}_{G\varphi}(r',\varphi,t)\ln|r'-s|\,ds \end{aligned} \tag{6.33}$$

Let $s = S/2\sqrt{\kappa t}$, then equation (6.33) can be transformed to

$$\begin{aligned} u_{Ghy'}(r',\varphi,t) = -\frac{4\beta\sqrt{\kappa t}}{\lambda\pi\left(\beta^2-\upsilon^2\right)}\Bigg\{&\int_{-\infty}^{\infty}\hat{\sigma}_{G\varphi}(S)\log|R'-S|\,dS \\ &+2\sqrt{\kappa t}\int_{-\infty}^{\infty}\hat{\sigma}_{G\varphi}(S)dS\Bigg\} \end{aligned} \tag{6.34}$$

where

$$R' = \frac{r'}{2\sqrt{\kappa t}} \tag{6.35}$$

Ignoring the second term, as it represents rigid body displacement, substituting the hoop stress given in equation (6.9) into (6.34) yields

$$\begin{aligned} u_{Ghy'}(r',\varphi,t) &= -\frac{\alpha_e}{\pi^2\rho_d c_p\sqrt{\kappa t}}\times\frac{(1+\upsilon)}{(\beta+\upsilon)}\int_{-\infty}^{\infty}\left(\frac{1-e^{-S^2}}{S^2}-2e^{-S^2}\right)\ln|R'-S|\,dS \\ &= -\frac{\alpha_e}{\pi\rho_d c_p\sqrt{\kappa t}}\times\frac{(1+\upsilon)}{(\beta+\upsilon)}\times F_1(R') \end{aligned} \tag{6.36}$$

where

$$F_1(R') = \frac{2}{\sqrt{\pi}}\cdot\frac{e^{-R'^2}}{R'}\int_0^{R'}e^{S^2}dS \tag{6.37}$$

Further details on the derivation of $F_1(R')$ are given in Appendix C. The tangential displacement is

$$\begin{aligned} u_{Ghx'}(X') &= \hat{u}_{Gr'} + \bar{u}_{Gx'}(X') \\ &= \frac{\alpha_e}{2\pi\rho_d c_p\sqrt{\kappa t}}\left[\frac{(\beta-\upsilon)(1+\upsilon)}{\beta(\beta+\upsilon)} + \frac{(1+\upsilon)}{\beta}\right]\left[\frac{1-e^{X'^2}}{X'}\right] \\ &= \frac{\alpha_e}{\pi\rho_d c_p\sqrt{\kappa t}}\frac{(1+\upsilon)}{(\beta+\upsilon)}\left(\frac{1-e^{X'^2}}{X'}\right) \end{aligned} \tag{6.38}$$

where $X' = x'/2\sqrt{\kappa t}$ and $\bar{u}_{Gx'}(X')$ can be obtained by substituting equation (6.9) into (6.32). For the plane-strain problem, substituting equation (5.10) into both equations (6.36) and (6.38) gives results identical to the Barber and Martin-Moran [71] solutions. Figure 6.4 show the normal displacement on the surface boundary of the half-plane due to instantaneous line heat source at $t = 1s$ ($\beta = 0.0106$) evaluated under plane-strain conditions. Figure 6.5 shows the surface boundary tangential displacement of the Barber and Martin-Moran solution. It must be emphasized that both solutions are only valid on the surface boundary. Hence, they are not suitable for determining the stress components.

6.3 Fourier Series Representation of Half-Plane Displacements

The general solutions for thermoelastic analysis designated for the annulus problem are expressed in term of Fourier series representations. The inclusion of half-plane remainder forms is an effective method to remove the asymptotically singular behaviour for short timescale analysis. Since the Green's function temperature is the core input to the thermoelastic analysis, the displacement/stress output equation must also inherit similar singular asymptotic behaviour. Hence, the same approach is taken to eliminate the singular behaviour

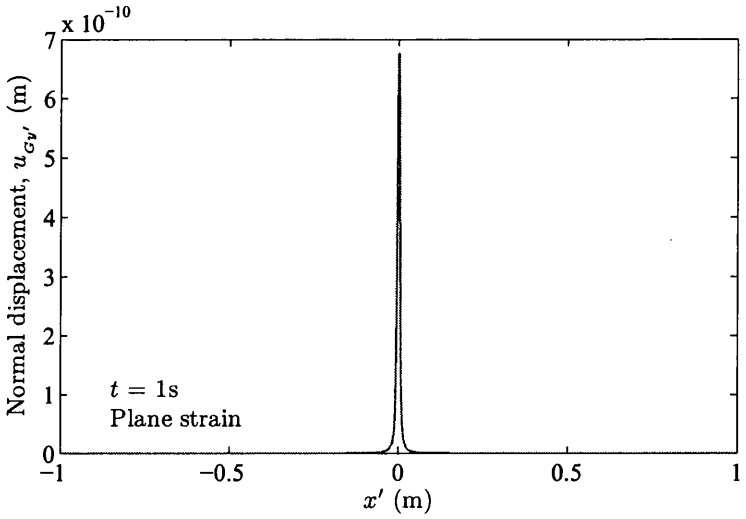

Figure 6.4: Green's functions half-plane thermoelastic normal displacement at $t = 1s$ ($\beta = 0.0106$).

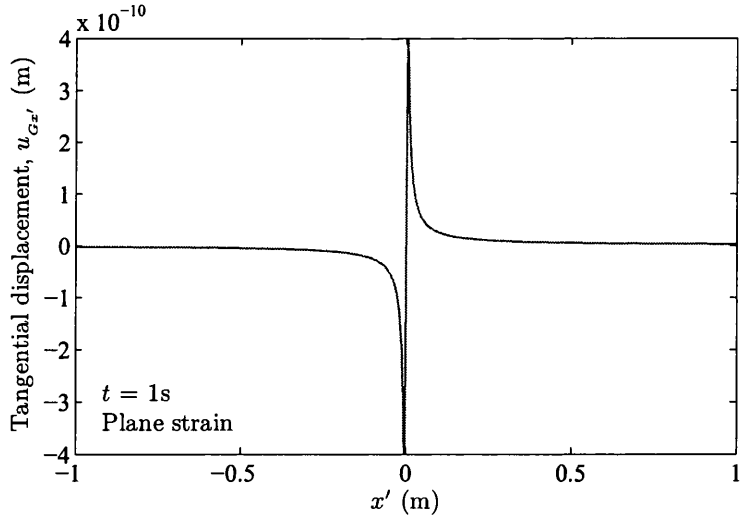

Figure 6.5: Green's function half-plane thermoelastic tangential displacement at $t = 1s$ ($\beta = 0.0106$).

in displacement/stress solution. To achieve a useful results the Barber and Martin Moran solutions must be considered in Fourier series form.

6.3.1 Specific Results

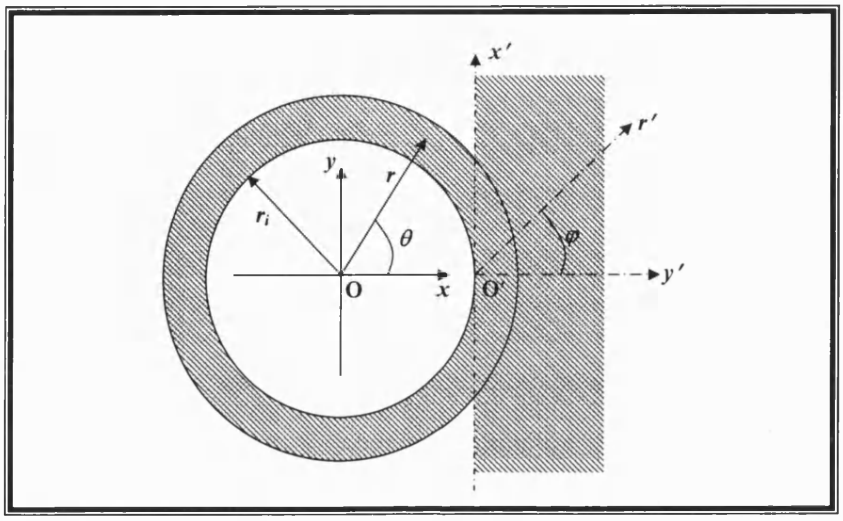

Figure 6.6: Half-plane and annulus region with different coordinate systems.

Figure 6.6 shows both annulus and half-plane regions. Equations (6.36) and (6.38) bounded to coordinate systems (r', φ) are "extended" onto the annulus region with coordinate system (r, θ).

This section introduces some fundamental Fourier series forms that will be appropriate for thermoelastic half-plane solutions. Firstly,

$$g(r,\theta,t) = \frac{1}{2t} e^{-\frac{r'^2}{4\kappa t}} = \sum_{n=-\infty}^{\infty} a_n(r,t)\epsilon^{in\theta} \tag{6.39}$$

Referring to section 4.2.3, the Laplace transform of $g(r,\theta,t)$ is,

$$\bar{g}(r,\theta,s) = K_0(\lambda r') = \sum_{n=-\infty}^{\infty} I_n(\lambda r_i) K_n(\lambda r) e^{in\theta} \tag{6.40}$$

where $r'^2 = r^2 + r_i^2 - 2rr_i\cos\theta$. Following through the inversion of the Laplace transform as shown in section 4.3.2,

$$a_n(r,t) = \frac{\kappa}{r_i^2}\int_0^{\infty} J_n(x)J_n(x\eta)xe^{-\kappa x^2 t/r'^2}dx \tag{6.41}$$

where $\eta = r/r_i$. Hence,

$$e^{-\frac{r'^2}{4\kappa t}} = \sum_{n=-\infty}^{\infty} c_n(r,t)e^{in\theta} \tag{6.42}$$

where

$$c_n(r,t) = 2ta_n(r,t) \tag{6.43}$$

6.3.2 Normal Displacement Component

Consider the term $F_1(R')$, which appears in (6.36). Writing $S = R'u$,

$$\begin{aligned} F_1(R') &= \frac{2}{\sqrt{\pi}}\cdot\frac{1}{R'}\int_0^{R'} e^{-\left(R'^2-S^2\right)}dS = \frac{2}{\sqrt{\pi}}\int_0^1 e^{-R'^2\left(1-u^2\right)}du \\ &= \frac{2}{\sqrt{\pi}}\int_0^1 e^{-\frac{r'^2\left(1-u^2\right)}{4\kappa t}}du \end{aligned} \tag{6.44}$$

Noting that,

$$e^{-\frac{r'^2\left(1-u^2\right)}{4\kappa t}} = \frac{2}{\sqrt{\pi}}\sum_{n=-\infty}^{\infty} c_n\left(r,\frac{t}{(1-u^2)}\right)e^{in\theta} \tag{6.45}$$

It follows that

$$F_1(R') = \frac{2}{\sqrt{\pi}} \sum_{n=-\infty}^{\infty} \int_0^1 c_n \left(r, \frac{t}{(1-u^2)} \right) du e^{in\theta} \tag{6.46}$$

Now define

$$\begin{aligned} d_n e^{in\theta} &= \frac{2}{\sqrt{\pi}} \int_0^1 c_n \left(r, \frac{t}{(1-u^2)} \right) du \\ &= \frac{2}{\sqrt{\pi}} \int_0^\infty J_n(x) J_n(x\eta) x \left(\int_0^1 \frac{2\kappa t}{r_i^2 (1-u^2)} e^{-\frac{\kappa x^2 t}{r_i^2 (1-u^2)}} du \right) dx \end{aligned} \tag{6.47}$$

Setting $v = 1/(1-u^2)$, then

$$\frac{du}{dv} = \frac{1}{2v^{3/2}\sqrt{v-1}} \tag{6.48}$$

and

$$\begin{aligned} \int_0^1 \frac{2\kappa t}{r_i^2 (1-u^2)} e^{-\frac{\kappa x^2 t}{r_i^2 (1-u^2)}} du &= \frac{2\kappa t}{r_i^2} \times \frac{1}{2} \int_1^\infty \frac{v}{v^{3/2}\sqrt{v-1}} e^{-\frac{\kappa x^2 t}{r_i^2} v} dv \\ &= \frac{\kappa t}{r_i^2} \left[\frac{1}{\sqrt{\pi}} \Gamma\left(\frac{1}{2}\right) e^{-\frac{\kappa x^2 t}{2r_i^2}} K_0 \left(\frac{\kappa x^2 t}{2r_i^2} \right) \right] \\ &= \frac{\kappa t}{r_i^2} e^{-\frac{\kappa x^2 t}{2r_i^2}} K_0 \left(\frac{\kappa x^2 t}{2r_i^2} \right) \end{aligned} \tag{6.49}$$

Thus,

$$d_n(r,t) = \frac{2\kappa t}{\sqrt{\pi} r_i^2} \int_0^\infty J_n(x) J_n(x\eta) x e^{-\frac{\kappa x^2 t}{2r_i^2}} K_0 \left(\frac{\kappa x^2 t}{2r_i^2} \right) dx \tag{6.50}$$

The "extended" normal displacement of the half-plane solution is then expressible

$$u_{Ghx}(r,\theta,t) = -\frac{\alpha_e}{\pi^2 \rho_d c_p \sqrt{\kappa t}} \times \frac{(1+\upsilon)}{(\beta+\upsilon)} \sum_{n=-\infty}^{\infty} d_n(r,t) e^{in\theta} \tag{6.51}$$

6.3.3 Tangential Displacement Component

For the tangential displacement of (6.38), note that

$$\begin{aligned}\int_0^1 e^{-R'^2 u} du &= \frac{1-e^{-R'^2}}{R'^2} \\ &= \sum_{n=-\infty}^{\infty} \int_0^1 c_n(r, t/u) du e^{in\theta}\end{aligned} \tag{6.52}$$

Define,

$$\begin{aligned}b_n(r,t) &= \int_0^1 c_n(r, t/u) du \\ &= \int_0^\infty J_n(x) J_n(x\eta) x \left(\int_0^1 \frac{2\kappa t}{r_i^2 u} e^{-\frac{\kappa x^2 t}{r_i^2 u}} du \right) dx\end{aligned} \tag{6.53}$$

Let $u = 1/v$, so that the integrand can be reduced to

$$\begin{aligned}J_n(x) J_n(x\eta) x \int_0^1 \frac{2\kappa t}{r_i^2 u} e^{-\frac{\kappa x^2 t}{r_i^2 u}} du &= J_n(x) J_n(x\eta) x \frac{2\kappa t}{r_i^2} \int_1^\infty \frac{1}{v} e^{-\frac{\kappa x^2 t}{r_i^2} v} dv \\ &= \frac{2\kappa t}{r_i^2} J_n(x) J_n(x\eta) x E_1 \left(\frac{\kappa x^2 t}{r_i^2} \right)\end{aligned} \tag{6.54}$$

where $E_1(x)$ is the first order exponential integral. Since,

$$\sum_{n=-\infty}^{\infty} b_n e^{in\theta} = \frac{1-e^{-R'^2}}{R'^2} \tag{6.55}$$

the horizontal displacement can be expressed as,

$$u_{Ghy}(r,\theta,t) = \frac{\alpha_e}{\pi \rho_d c_p \sqrt{\kappa t}} \cdot \frac{(1+\upsilon)}{(\beta+\upsilon)} \sum_{n=-\infty}^{\infty} b_n e^{in\theta} \times R' \tag{6.56}$$

Since the factor R' must remain in (6.56), this will be discussed further in section 6.4.1.

6.4 Remainder for Annulus Thermoelastic Solution

The fundamental concept of the remainder function for the thermoelastic analysis is similar to the thermal problem. The general expression for the thermoelastic Green's function displacement is written as

$$\mathbf{u}_G = \mathbf{u}_{Gh} + \sum_{n=-\infty}^{\infty} (\mathbf{u}_{Gn} - \mathbf{u}_{Ghn})\, e^{in\theta} \tag{6.57}$$

where

$$\mathbf{u}_G = \begin{bmatrix} u_{Gr} \\ v_{G\theta} \end{bmatrix} \tag{6.58}$$

$$\mathbf{u}_{Gh} = \begin{bmatrix} u_{Ghr} \\ v_{Gh\theta} \end{bmatrix} \tag{6.59}$$

$$\mathbf{u}_{Ghn} = \begin{bmatrix} u_{Ghrn} \\ v_{Gh\theta n} \end{bmatrix} \tag{6.60}$$

$$\mathbf{u}_{Gn} = \begin{bmatrix} u_{Grn} \\ v_{G\theta n} \end{bmatrix} \tag{6.61}$$

Here $\mathbf{u}_G$, $\mathbf{u}_{Gh}$ and $\mathbf{u}_{Ghn}$ are the Green's function displacement, half-plane analytical and Fourier coefficient displacements respectively, which will be defined in section 6.4.1; u_{Grn} and $v_{G\theta n}$ are the displacement components in (5.62) for the rigidly mounted problem or in (5.73) for the resiliently mounted problem corresponding to the annular Green's function temperature described in section 5.5.2. The second term on the right hand side of equation (6.57), which is expressed in Fourier series form, is known as the remainder function for the thermoelastic displacement. Thus singular behaviour of the Green's function is embedded in

the half-plane form of u_G, while the remainder series has a well convergent form, particularly over short timescales. The half-plane term can be replaced by any expression provided the singular displacement profiles for u_G and u_{Gh} are similar.

6.4.1 Coordinate System Transformation

To utilise the half-plane displacements, half-plane solutions are transformed from a Cartesian coordinate system to a polar coordinate system, i.e.,

$$\tilde{u}_{Ghr} = u_{Ghx}\cos\theta + u_{Ghy}\sin\theta \tag{6.62}$$

$$\tilde{v}_{\theta Gh} = -u_{Ghx}\sin\theta + u_{Ghy}\cos\theta \tag{6.63}$$

Since the singular behaviour is at $\theta = 0$ and $\sin\theta \to 0$ as $\theta \to 0$, the radial displacement is taken as

$$\begin{aligned} u_{Ghr}(r,\theta,t) &= -\frac{\alpha_e}{\pi\rho_d c_p\sqrt{\kappa t}}\cdot\frac{(1+\upsilon)}{(\beta+\upsilon)}\cdot\left(\frac{2e^{-R'^2}}{\sqrt{\pi}R'}\int_0^{R'} e^{S^2}dS\right)\cos\theta \\ &= -\frac{\alpha_e}{\pi\rho_d c_p\sqrt{\kappa t}}\cdot\frac{(1+\upsilon)}{(\beta+\upsilon)}\cdot\sum_{n=-\infty}^{\infty} d_n(r,t)e^{in\theta}\times\cos\theta \end{aligned} \tag{6.64}$$

Noting that,

$$\cos\theta = \frac{e^{i\theta}+e^{-i\theta}}{2} \tag{6.65}$$

The result is that

$$u_{Ghr}(r,\theta,t) = \sum_{n=-\infty}^{\infty} u_{Ghrn}(r,t)e^{in\theta} \tag{6.66}$$

where

$$u_{Ghrn}(r,t) = -\frac{\alpha_e}{\pi\rho_d c_p\sqrt{\kappa t}}\cdot\frac{(1+\upsilon)}{(\beta+\upsilon)}\cdot\frac{d_{n-1}(r,t)+d_{n+1}(r,t)}{2} \tag{6.67}$$

For the tangential displacement component

$$v_{Gh\theta}(r,\theta,t) = \frac{\alpha_e}{\pi\rho_d c_p\sqrt{\kappa t}} \cdot \frac{(1+\upsilon)}{(\beta+\upsilon)} \sum_{n=-\infty}^{\infty} b_n(r,t)e^{in\theta} \times R' \times \cos\theta \tag{6.68}$$

It is to be noted that the "extension" of the half-plane surface to the annular surface was achieved in (6.38) by setting $X' = R'$. Now $R' = \sqrt{r_i^2 + r^2 - 2rr_i\cos\theta} \geq 0$, while X' may be negative. Also R' in (6.68) may be replaced by $r_i \tan\theta/2\sqrt{\kappa t}$, without changing the nature of the singularity in $v_{Gh\theta}$. The reasoning behind this argument is that

$$\frac{r_i\sqrt{2}\sqrt{1-\cos\theta}}{2\sqrt{\kappa t}} = \frac{r_i\sqrt{2}}{2\sqrt{\kappa t}}\left[\frac{1}{2}\sqrt{2}\theta + \mathrm{O}(\theta^3)\right] \sim \frac{r_i\theta}{2\sqrt{\kappa t}} \tag{6.69}$$

and

$$\frac{r_i\tan\theta}{2\sqrt{\kappa t}} = \frac{r_i}{2\sqrt{\kappa t}}\left[\theta + \mathrm{O}(\theta^3)\right] \sim \frac{r_i\theta}{2\sqrt{\kappa t}} \tag{6.70}$$

as $\theta \to 0$. Additionally, the use of $r_i\tan\theta/2\sqrt{\kappa t}$ removes the $\cos\theta$ term in equation (6.68), which simplifies the Fourier series transformation. Thus

$$\begin{aligned}
v_{Gh\theta}(r,\theta,t) &= \frac{\alpha_e}{\pi\rho_d c_p\sqrt{\kappa t}} \cdot \frac{(1+\upsilon)}{(\beta+\upsilon)} \left(\frac{1-e^{R'^2}}{R'^2}\right) \times \frac{r_i\tan\theta}{2\sqrt{\kappa t}} \times \cos\theta \\
&= \frac{\alpha_e}{\pi\rho_d c_p\sqrt{\kappa t}} \cdot \frac{(1+\upsilon)}{(\beta+\upsilon)} \sum_{n=-\infty}^{\infty} b_n(r,t)e^{in\theta} \times \frac{r_i\sin\theta}{2\sqrt{\kappa t}} \\
&= \frac{\alpha_e}{\pi\rho_d c_p\sqrt{\kappa t}} \cdot \frac{(1+\upsilon)}{(\beta+\upsilon)} \sum_{n=-\infty}^{\infty} b_n(r,t)e^{in\theta} \times \frac{r_i}{2\sqrt{\kappa t}} \times \left(\frac{e^{i\theta}-e^{-i\theta}}{2i}\right) \\
&= \sum_{n=-\infty}^{\infty} v_{Gh\theta}(r,t)e^{in\theta}
\end{aligned} \tag{6.71}$$

where

$$v_{Gh\theta}(r,t) = -\frac{i\alpha_e r_i}{4\pi\rho_d c_p \kappa t} \cdot \frac{(1+\upsilon)}{(\beta+\upsilon)} \cdot (b_{n-1}(r,t) - b_{n+1}(r,t)) \tag{6.72}$$

Figure 6.7 shows the comparison between analytical and Fourier series representations with truncated (50) harmonics for radial and tangential displacements given by equations (6.64) and (6.71).

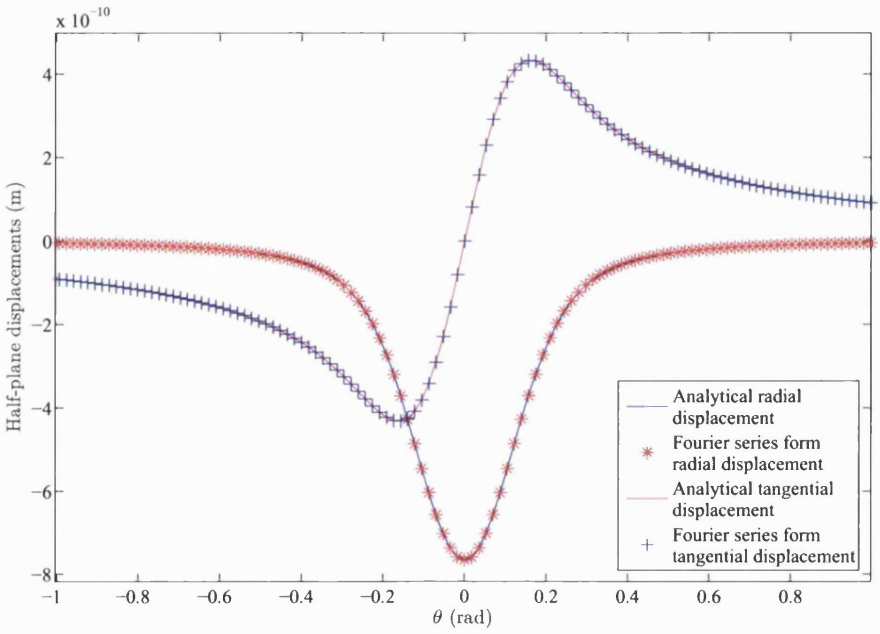

Figure 6.7: Comparison between analytical and Fourier series representations of radial and tangential displacements at $t = 0.5$s ($\beta = 5.3 \times 10^{-3}$).

6.4.2 Green's Functions for Thermoelastic Annular Displacements

The section provides a clear presentation of the overall displacement expressions with remainder functions. The Green's function radial displacement for the annular problem is

$$u_{Gr}(r,\theta,t) = u_{Ghr}(r,\theta,t) + \sum_{n=-\infty}^{\infty} \left\{ u_{Grn}\left(r, T_{Gn_{annulus}}(r,t)\right) - u_{Ghrn}(r,t) \right\} e^{in\theta} \tag{6.73}$$

where u_{Grn} is the radial displacement element in output-equation (5.39) with Green's function temperature (3.36) and $u_{Ghr}(r,\theta,t)$ is the explicit term given by (6.64). Furthermore, the second term in the series summation is the half-plane expression given by (6.67). For the tangential displacement,

$$v_{G\theta}(r,\theta,t) = v_{Gh\theta}(r,\theta,t) + \sum_{n=-\infty}^{\infty} \left\{ v_{G\theta n}\left(r, T_{Gn_{annulus}}(r,t)\right) - v_{Gh\theta n}(r,t) \right\} e^{in\theta} \tag{6.74}$$

Similarly, the first term on the right hand side of (6.74) is given explicitly by (6.71) and the second term in the series representation is the remainder function. The term $v_{G\theta n}$ is the tangential displacement component of the output-equation (5.39) with the Green's function temperature (3.36). Figure 6.8 shows the different between the inner boundary radial displacements evaluated with and without remainder function at $t = 0.01s$ ($\beta = 1.06 \times 10^{-3}$) with rigidly mounted outer boundary condition and plane-stress conditions. Similarly, figure 6.9 shows the comparison between the tangential displacements with and without remainder function at the same time point. The use of the remainder function is seen to reduce the oscillatory behaviour that is evident in the truncated direct Fourier series representation.

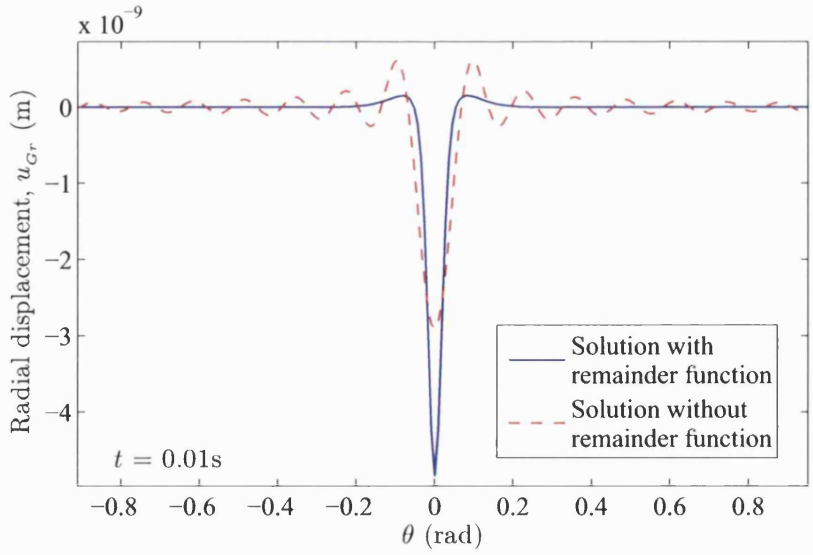

Figure 6.8: Comparison between the inner surface radial displacements of annulus solution with and without remainder function at $t = 0.01s$ ($\beta = 1.06\times10^{-4}$) under rigidly mounted outer boundary and plane-stress conditions.

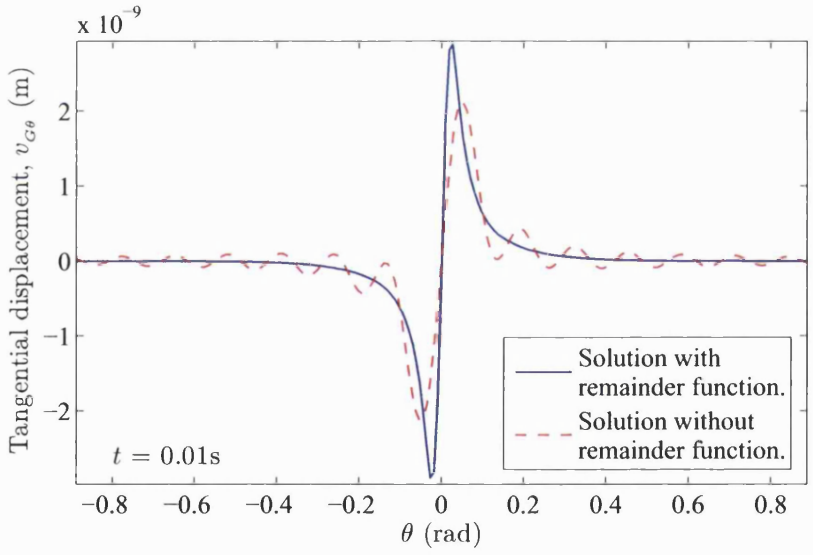

Figure 6.9: Comparison between the inner surface tangential displacements of annulus solution with and without remainder function at $t = 0.01s$ ($\beta = 1.06 \times 10^{-4}$) under rigidly mounted outer boundary and plane-stress conditions.

6.4.3 Thermoelastic Stress Analysis

The stresses of the annulus problem given in the output-equations (5.62) and (5.74) correspond to a unit instantaneous heat input. It is difficult to improve series convergence with a half-plane remainder function since the stress field depends on the outer boundary condition. Furthermore, the inner surface boundary stresses are always zero, i.e. the singular behaviour is not an issue for inner surface stresses. However, several methods are proposed and examined with the possibility of utilising them in a remainder function.

6.4.3.1 Barber and Martin-Moran: Superimposing Equal and Opposite Stress

Based on the work by Barber and Martin-Moran, the surface boundary must comply with a stress-free condition by superimposing a equal and opposite stress function according to equation (6.9). However, the resulting integral for an interior point is intractable [74] and also solutions obtained using Flamant's theorem are only valid on the half-plane surface boundary. Hence, direct derivatives of half-plane displacements do not give rise to stress free conditions, which invalidates their use as remainder functions. However, further work of Barber and Azarkhin [74] shows that the Green's function for sub-surface thermal stresses due to surface heating can be solved using a potential function and their solutions are expressed in terms of hypergeometric functions. Unfortunately, it is difficult to transform these solutions into Fourier series representations and thus the possibility of utilising these expressions was ruled out.

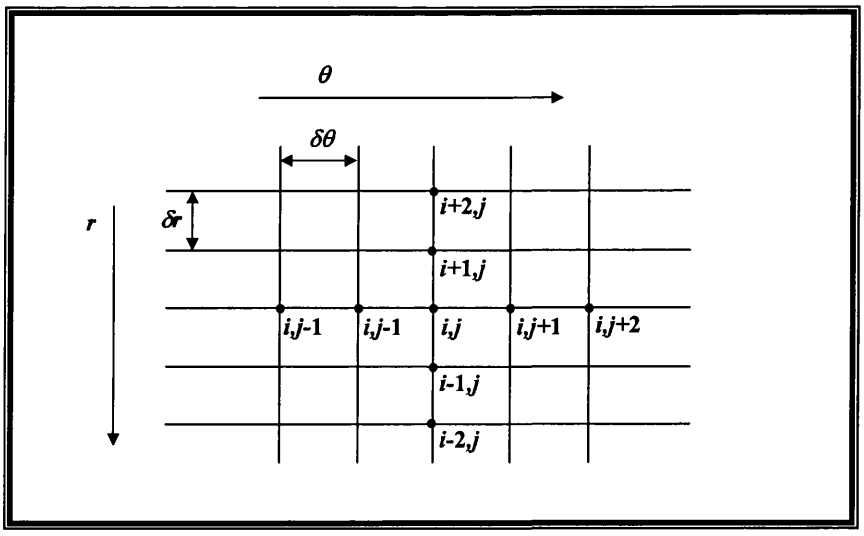

Figure 6.10: Indices position (i, j) for numerical method.

6.4.3.2 Numerical Method

This method was applied directly to the equations (6.73) and (6.74). The numerical value of a derivative of a radial displacement at a given node is

$$\frac{\partial u_r(i,j)}{\partial r} = \frac{u_r(i-2,j) - 8u_r(i-1,j) + 8u_r(i+1,j) - u_r(i+2,j)}{12\delta r} + \mathrm{O}(\delta r^4) \quad \text{(central-difference)} \tag{6.75}$$

where i and j are denoted as radial and angular node respectively and δr is the difference between two nodes (figure 6.10). This numerical derivative has fourth order error. Additionally, there are forward-difference and backward-difference methods, which are useful for evaluating nodes at the inner and outer boundaries respectively:

$$\frac{\partial u_r(i,j)}{\partial r} = \frac{-25u_r(i,j) + 48u_r(i+1,j) - 36u_r(i+2,j) + 16u_r(i+3,j) - 3u_r(i+4,j)}{12\delta r} + \mathrm{O}(\delta r^4) \quad \text{(forward-difference)} \tag{6.76}$$

$$\frac{\partial u_r(i,j)}{\partial r} = \frac{25u_r(i,j) - 48u_r(i-1,j) + 36u_r(i-2,j) - 16u_r(i-3,j) + 3u_r(i-4,j)}{12\delta r} + \mathrm{O}(\delta r^4) \quad \text{(backward-difference)} \tag{6.77}$$

The differential values for nodes situated along the second layer away from the inner and outer boundaries can be determined using the following expressions:

$$\frac{\partial u_r(i,j)}{\partial r} = \frac{-3u_r(i-1,j) - 10u_r(i,j) + 18u_r(i+1,j) - 6u_r(i+2,j) + u_r(i+3,j)}{12\delta r} + \mathrm{O}(\delta r^4) \tag{6.78}$$

$$\frac{\partial u_r(i,j)}{\partial r} = \frac{3u_r(i+1,j) + 10u_r(i,j) - 18u_r(i-1,j) + 6u_r(i-2,j) - u_r(i-3,j)}{12\delta r} + \mathrm{O}(\delta r^4) \tag{6.79}$$

Similarly for the derivative with respect to θ:

$$\frac{\partial u_r(i,j)}{\partial \theta} = \frac{u_r(i,j-2) - 8u_r(i,j-1) + 8u_r(i,j+1) - u_r(i,j+2)}{12\delta\theta} + \mathrm{O}(\delta\theta^4) \quad \text{(central-difference)} \tag{6.80}$$

The radial, angular and shearing strains are given by (5.3), (5.4) and (5.5) respectively. The stresses can be evaluated using the stress-strain equations given by (5.6), (5.7) and (5.8).

Figure 6.11 shows the contour plot of the numerically evaluated radial stress at time point $t = 0.7$s ($\beta = 7.42 \times 10^{-3}$). It was found that the inner surface was not entirely stress free condition because the half-plane displacements do not give

rise to stress free conditions, which is explained in section 6.4.3.1. The stressed inner surface would become more noticeable and greater in magnitude as $t \to 0$.

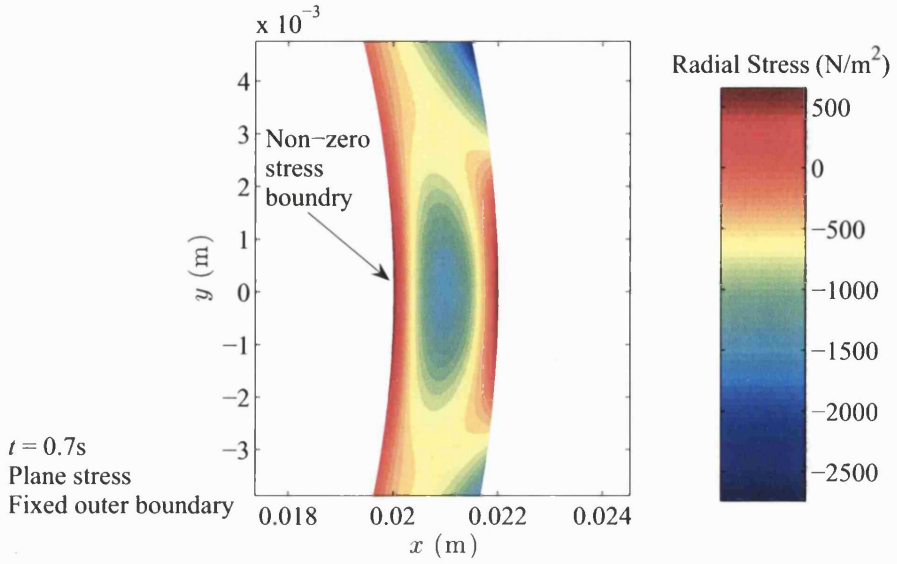

Figure 6.11: Radial stress contour evaluated numerically using equations (6.73) and (6.74). Non-zero stress is noted at the inner boundary.

6.5 Closure

Half-plane displacements developed by Barber and Martin-Moran were introduced. Modification of Barber and Martin-Moran solutions were made to accommodate both plane-stress and plane-strain problems. Additionally, Fourier series representation of half-plane displacements were also derived in order to utilise them in developing a remainder function. The remainder functions improve the representation in term of truncated Fourier series solutions of displacement for short timescale analysis. The use of half-plane displacements in developing remainder functions for stress analysis was found to be difficult since the Barber and Martin-Moran solutions do not give rise to stress free conditions. However, an alternative approach is proposed in Chapter 8 to investigate the annular stresses.

Chapter 7

Thermal Response with Single Dynamic Contact of Rotor and Auxiliary Bearing

7.1 Overview

In the event of power failure of an AMB or sudden excitation on the rotor, contact of a rotating journal with the inner surface of an auxiliary bearing will initiate a high dynamic heat source. Each contact will take place over a very short period of time. The rotor may also bounce at different locations within clearance plane offered by the auxiliary bearing. For a rolling element bearing, sliding contact will lead to rolling contact once the inner race picks up to the rotor speed. In this chapter, the temperature rise due to contact between the surfaces of a rotor and an auxiliary bearing are investigated. The heat flux is derived from non-Hertzian contact theory. However, it reduces to Hertzian contact theory if both contact bodies are made of same material. A single contact event is considered to reduce the problem complexity. Multiple contacts may be considered by a superposition argument.

7.2 Contact Theory

Consider a two dimensional rotor brought into contact with an auxiliary bearing, initially with a line contact. A small area of contact is then developed by increasing the contact load causing the load to be distributed over the contact surface (figure 7.1). In this section, two types of contact pressure distributions are considered:

(a) Hertzian pressure distribution.

(b) Non-Hertzian pressure distribution of sliding contact.

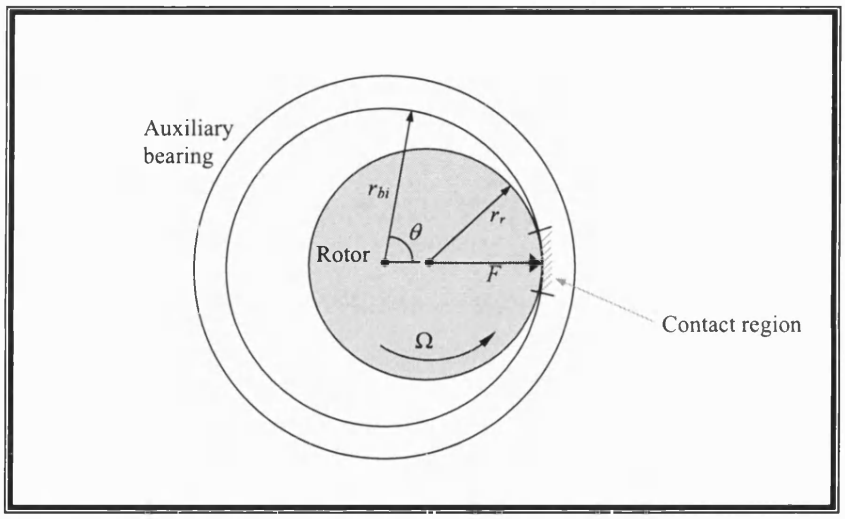

Figure 7.1: Contact of a rotating rotor and auxiliary bearing with a dynamic loading F.

7.2.1 Hertzian Contact

The Hertzian pressure distribution for a two-dimensional contact problem is given in [17],

$$p(x) = \frac{2F}{\pi a^2}\sqrt{a^2 - x^2} \tag{7.1}$$

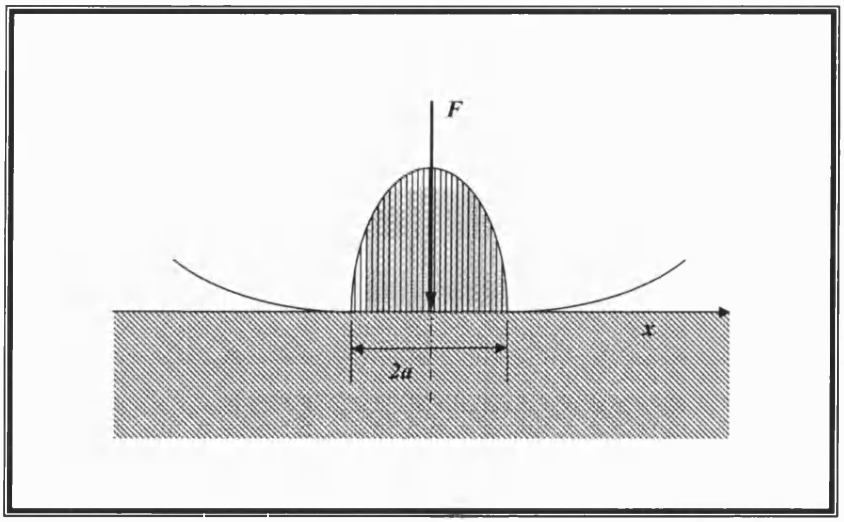

Figure 7.2: Hertzian pressure distribution with contact zone $2a$.

where, $-a \leq x \leq a$ and a is the half-width of the contact zone. The total load is defined as,

$$F = \frac{\pi a^2 E^*}{4R^*} \tag{7.2}$$

and E^* and R^* are defined as,

$$\frac{1}{R^*} = \frac{1}{r_{bi} - c_r} - \frac{1}{r_{bi}} \tag{7.3}$$

$$\frac{1}{E^*} = \frac{1 - \upsilon_b^2}{E_b} + \frac{1 - \upsilon_r^2}{E_r} \tag{7.4}$$

where c is the clearance between the journal and the inner radius of the bearing, $\nu_{b,r}$ and $E_{b,r}$ are the Poisson ratios and Elastic Modulii of the bearing and rotor, respectively.

7.2.2 Sliding Contact of Non-Conforming Surfaces

Hertzian contact theory is based on the assumption of frictionless contact. Practically, sliding contact takes place between the surfaces due to the high speed

rotating journal in contact with bearings. The tangential tractions do alter the pressure distribution on the contact surfaces [17] to become

$$p(x) = \frac{E^*}{2R^*\sqrt{1+\beta_d^2\mu^2}}\left(\frac{a+x}{a-x}\right)^{\gamma}\sqrt{a^2-x^2} \tag{7.5}$$

where β gives the measure of elastic mismatch and is known as the Dundurs' constant:

$$\beta_d = \frac{1}{2}\left[\frac{(1-2\upsilon_b)/G_b - (1-2\upsilon_r)/G_r}{(1-2\upsilon_b)/G_b + (1-2\upsilon_r)/G_r}\right] \tag{7.6}$$

The index γ is given by

$$\gamma = -\frac{1}{\pi}\tan^{-1}(\beta_d\mu) \approx -\beta_d\mu/\pi \tag{7.7}$$

The semi-width of the contact strip a is given by

$$a^2 = \frac{1}{1-4\gamma^2}\cdot\frac{4FR^*}{\pi E^*} \tag{7.8}$$

Note that the normal pressure distribution of sliding contact is due to the Hertzian contact pressure when the two solids have the same elastic constants, i.e. $\beta = 0$ and $\gamma = 0$.

7.3 Frictional Surface Heating - Rotor and Bearing of Same Material

Conditions of dry contact will be assumed, which is the case for system designated for operation in clean environments. The annular ring representing the auxiliary bearing will be fixed, as in the case of simple bush, or free to rotate, as is representative of the inner race of a rolling element bearing.

7.3.1 Fixed Bush

In section 2.4, the dynamic response of the contact forces on an auxiliary bearing are presented. The contact force per unit length is written as

$$F(t) = (f_{cmax}/l_b)\phi(t)^2 \tag{7.9}$$

where f_{cmax} is the maximum contact force (see Table 2.2), l_b is the length of the bearing and $\phi(t)$ is the contact time function so that the half-width contact patch (see equation (7.2)) can be written as

$$a(t)^2 = a_0^2\phi(t)^2 \tag{7.10}$$

where

$$a_0 = 2\sqrt{\frac{R^*(f_{cmax}/l_b)}{\pi E^*}} \tag{7.11}$$

Substituting equation (7.10) into equation (7.1) gives the dynamic pressure,

$$p(x,t) = \frac{E^*}{2R^*}\sqrt{a_0^2\phi(t)^2 - x^2} \tag{7.12}$$

Assuming that a Coulomb friction law applies, the total power dissipation per unit area is,

$$\begin{aligned} q(x,t) &= \mu p_F(x,t) r_r \omega_s \\ &= \frac{\mu E^* r_r \omega_s}{2R^*}\sqrt{a_0^2\phi(t)^2 - x^2} \end{aligned} \tag{7.13}$$

where ω_s is the slip velocity and r_r is the radius of the rotor. For a fixed bush problem, $\omega_s = \Omega$. Taking $x = r_{bi}\theta$, equation (7.13) can be rearranged to give,

$$q(\theta,t) = q_0\sqrt{\theta_0^2\phi(t)^2 - \theta^2} \tag{7.14}$$

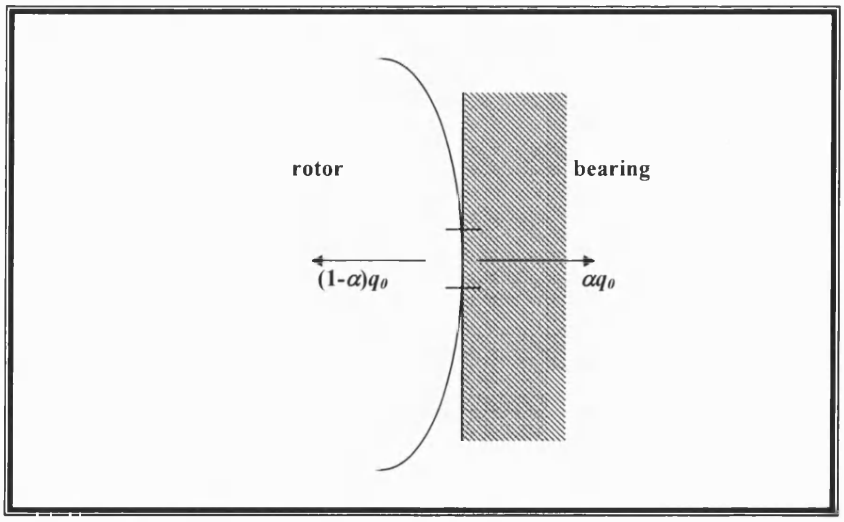

Figure 7.3: Heat partitioning between rotor and bearing.

where r_{bi} is the inner radius of the auxiliary bearing and

$$q_0 = \frac{\mu E^* r_r \Omega r_{bi}}{2R^*} \tag{7.15}$$

$$\theta_0 = \frac{a_0}{r_{bi}} \tag{7.16}$$

Of the dissipated power, the question of partitioning to the rotor and bearing now arises (figure 7.3). Based on the article published by Tian and Kennedy [83], the total frictional heat flux of equation (7.14) can be partitioned into $q_b = \alpha q$ and $q_r = (1-\alpha)q$, which are the heat fluxes transmitted into the bearing and rotor, respectively. The heat partition coefficient α is dependent on the slip speed and is taken as,

$$\alpha = \frac{1}{\left(1 + \frac{k_b}{k_r}\sqrt{\frac{1+Pe_b}{1+Pe_r}}\right)} \tag{7.17}$$

where k_b and k_r are the conductivity for bearing and rotor, respectively and

$$Pe_b = \frac{r_r \omega_s a}{2\kappa_b}, \quad Pe_r = \frac{r_r \omega_s a}{2\kappa_r} \tag{7.18}$$

are the Peclet numbers for bearing and rotor, respectively. If the rotor and bearing of the same material, $Pe_b = Pe_r$ so that $\alpha = 0.5$. Hence the heat flux transmitted to the inner ring of the auxiliary bearing is

$$q_b(\theta, t) = \alpha q_0 \sqrt{\theta_0^2 \phi(t)^2 - \theta^2} \tag{7.19}$$

In equation (7.19), $\theta_0\phi(t)$ is the dynamic half-width contact angle.

7.3.1.1 Convolved Temperature

The contact temperature T_c at point (r, θ) at time t of a contact period of t_p arising from the contact source can be determined using the convolution theorem:

$$\begin{aligned} &T_c(r, \theta, t) \\ &= l_b \int_{\tau=0}^{t} \int_{\beta=-\theta_0\phi(t)}^{\theta_0\phi(t)} q_b(\beta, \tau) \cdot T_{G_{annulus}}(r, \theta - \beta, t - \tau) d\beta d\tau \end{aligned} \tag{7.20}$$

where $q_b(\beta, \tau)$ conducted into bearing given by (7.19) and the Green's function annular temperature, $T_{G_{annulus}}$, is given by (4.53). From the form of (4.53),

$$T_c(r, \theta, t) = T_{ch}(r, \theta, t) + \hat{T}_{ch}(r, \theta, t) + \sum_{n=-\infty}^{\infty} T_{cRn_{annulus}}(r, t) \tag{7.21}$$

where

$$T_{ch}(r,\theta,t) = l_b \int_{\tau=0}^{t} \int_{\beta=-\theta_0\phi(t)}^{\theta_0\phi(t)} q_b(\beta,\tau) T_{Gh}(r,\theta-\beta,t-\tau) d\beta d\tau \quad (7.22)$$

$$\hat{T}_{ch}(r,\theta,t) = l_b \int_{\tau=0}^{t} \int_{\beta=-\theta_0\phi(t)}^{\theta_0\phi(t)} q_b(\beta,\tau) \hat{T}_{Gh}(r,\theta-\beta,t-\tau) d\beta d\tau \quad (7.23)$$

$$T_{cRn_{annulus}}(r,t) = l_b \int_{\tau=0}^{t} \int_{\beta=-\theta_0\phi(t)}^{\theta_0\phi(t)} q_b(\beta,\tau) T_{GRn_{annulus}}(r,t-\tau) \times e^{in(\theta-\beta)} d\beta d\tau \quad (7.24)$$

7.3.1.2 Programming Approach

The analytical expressions (7.21) and (7.22) are evaluated directly using standard array storage functions in Matlab. However, the Fourier series expansion of the remainder function needs to be stored in a three-dimensional array corresponding to (r,n,t) with curve fitting to recall the intermediate values.

7.3.1.3 Half-Plane Temperatures

Substituting equations (4.11) and (7.19) into equation (7.20) yields,

$$T_{ch}(r,\theta,t) = l_b \int_{\tau=0}^{t} \int_{\beta=-\theta_0\phi(t)}^{\theta_0\phi(t)} \frac{\alpha q_0}{2\pi k_b(t-\tau)} e^{-\frac{r_{bi}^2\left(1+\eta^2-2\eta\cos(\theta-\beta)\right)}{4\kappa_b(t-\tau)}} \times \sqrt{\theta_0^2\phi(\tau)^2-\beta^2}\, d\beta d\tau \quad (7.25)$$

Changing the variable $\beta = \theta_0\phi(\tau)u$ gives

$$\begin{aligned} & T_{ch}(r,\theta,t) \\ & = \frac{\alpha l_b q_0 \theta_0^2}{2\pi k_b} \int_{\tau=0}^{t} \int_{u=-1}^{1} \frac{\phi(\tau)^2}{(t-\tau)} e^{-\frac{r_{bi}^2\left(1+\eta^2-2\eta\cos(\theta-\theta_0\phi(\tau)u)\right)}{4\kappa_b(t-\tau)}} \\ & \qquad \times \sqrt{1-u^2}\,du\,d\tau \end{aligned} \tag{7.26}$$

In a similar manner

$$\begin{aligned} & \hat{T}_{ch}(r,\theta,t) \\ & = -\frac{\alpha l_b q_0}{2\pi k_b} \int_{\tau=0}^{t} \int_{\beta=-\theta_0\phi(t)}^{\theta_0\phi(t)} \int_{v=0}^{t-\tau} \frac{g(v)}{(t-\tau-v)} e^{-\frac{r_{bi}^2\left(1+\eta^2-2\eta\cos(\theta-\beta)\right)}{4\kappa_b(t-\tau-v)}} \\ & \qquad \times \sqrt{\theta_0^2\phi(\tau)^2-\beta}\,dv\,d\beta\,d\tau \\ & = -\frac{\alpha l_b q_0 \theta_0^2}{2\pi k_b} \int_{\tau=0}^{t} \int_{u=-1}^{1} \int_{v=0}^{t-\tau} \frac{\phi(\tau)^2 g(v)}{(t-\tau-v)} e^{-\frac{r_{bi}^2\left(1+\eta^2-2\eta\cos(\theta-\theta_0\phi(\tau)u)\right)}{4\kappa_b(t-\tau-v)}} \\ & \qquad \times \sqrt{1-u^2}\,dv\,du\,d\tau \end{aligned} \tag{7.27}$$

7.3.1.4 The Remainder Function

The remainder function harmonics are given by

$$\begin{aligned} T_{cRn}(r,\theta,t) = l_b \alpha q_0 \int_{\tau=0}^{t} \int_{\beta=-\theta_0\phi(t)}^{\theta_0\phi(t)} & T_{Gn_{annulus}}(r,t-\tau) e^{in(\theta-\beta)} \\ & \times \sqrt{\theta_0^2\phi(\tau)^2-\beta^2}\,d\beta\,d\tau \end{aligned} \tag{7.28}$$

The integrand involves the following integration,

$$\begin{aligned} & \int_{\beta=-\theta_0\phi(t)}^{\theta_0\phi(t)} e^{in(\theta-\beta)} \sqrt{\theta_0^2\phi(\tau)^2-\beta^2}\,d\beta \\ & = \theta_0^2\phi(\tau)^2 e^{in\theta} \int_{-1}^{1} \sqrt{1-u^2} e^{-in\theta_0\phi(\tau)u}\,du \end{aligned} \tag{7.29}$$

From [97, page 321] , the integration reduces to,

$$\begin{aligned}
&\theta_0^2\phi(\tau)^2 e^{in\theta}\int_{-1}^{1}\sqrt{1-u^2}e^{-in\theta_0\phi(\tau)u}du \\
&= -\frac{2\sqrt{\pi}\theta_0\phi(\tau)e^{in\theta}}{n}\cdot\Gamma\left(\frac{3}{2}\right)J_1(-n\theta_0\phi(\tau)) \qquad (7.30)\\
&= \frac{\pi\theta_0\phi(\tau)}{n}J_1(n\theta_0\phi(\tau))e^{in\theta} \qquad (n\neq 0)
\end{aligned}$$

If $n = 0$, the integral reduces to,

$$\theta_0^2\phi(\tau)^2\int_{-1}^{1}\sqrt{1-u^2}du = \frac{1}{2}\pi\theta_0^2\phi(\tau)^2 \qquad (7.31)$$

Note that,

$$\lim_{n\to 0}\frac{\pi\theta_0\phi(\tau)}{n}J_1(n\theta_0\phi(\tau))e^{in\theta} = \frac{1}{2}\pi\theta_0^2\phi(\tau)^2 \qquad (7.32)$$

It now follows that,

$$\begin{aligned}
&T_{cRn}(r,\theta,t)\\
&= \begin{cases} l_b\alpha q_0\int_{\tau=0}^{t}\frac{1}{2}\pi\theta_0^2\phi(\tau)^2 T_{GRn}(r,t-\tau)d\tau & (n=0) \\ l_b\alpha q_0\int_{\tau=0}^{t}\frac{\pi\theta_0\phi(\tau)}{n}J_1(n\theta_0\phi(\tau))T_{GRn}(r,t-\tau)d\tau e^{in\theta} & (n\neq 0)\end{cases} \qquad (7.33)
\end{aligned}$$

7.3.1.5 Case Study for a Fixed Bush

Based on the information given in section 2.4, the parameters (Table 2.1) and are used for case study. The following assumptions are made:

(a) Both rotor/bearing are made of same material (steel).

(b) The system is adiabatic.

The contact force is dynamic and defined by $F(t) = (f_{cmax}/l_b)\phi(t)^2$, where $\phi(t)^2$ varies between 0 and 1. With reference to the contact force profile presented in figure 2.14, an approximation for the time behaviour is

$$\phi(t) = \sqrt{\sin(\omega_\phi t)} \tag{7.34}$$

where $\omega_\phi = \pi/t_p$. This section will investigate the temperature variation corresponding to the governing parameters: Contact force, f_{cmax}; Rotor speed, Ω; Coefficient of friction, μ; and contact period, t_p. Later, the solutions are used to analyse the thermal responses of the bearing subjected to the operating conditions given by Table 2.2.

(a) Contact Force (f_{cmax} = 10-50kN)

Table 7.1 shows the operating conditions used for the case study in this section. Figure 7.4 shows the time variation of half-length contact zone, $\theta_0 \sin(\omega_\phi t)$ with different contact forces, f_{cmax}. The contact period is taken as t_p = 1ms and the zone angle varies between 0 and θ_0 as the rotor bounces on and off the inner surface of the bearing.

Table 7.1: Operating conditions for thermal contact analysis.

Input Parameters	**Value**
Slip Speed, $\omega_s = \Omega$	1000 rad/s
Contact Period, t_p	0.001 s
Heat partition, α	0.5
Coefficient of friction, μ	0.1

Figure 7.5 shows the time variation of the maximum surface temperature, evaluated from (7.21), at $(r_{bi}, 0)$ when subjected to various contact forces. The temperature increases as the contact area grows, then it drops with the reduction of the contact zone and keeps decreasing as the heat diffuses throughout the bearing. after the heat source has been being removed. It is seen that the temperature increases within the contact period to 650K with a contact force $f_{cmax} = 50$kN. The surface temperature distribution rises with time is shown in figure 7.6 for $f_{cmax} = 10$kN. Figure 7.7 shows the time variation of temperature below the contact surface where $(r, \theta) = (r_{bi} \leq r \leq r_{bo}, 0)$. Those points away from the source heat up gradually as the heat propagated throughout the body. Since the whole system is adiabatic, the heat is retained in the body and hence a permanent increase in steady state temperature follows. In practice, the heat would diffuse by other means, such as convection and radiation, even conduction between the rolling elements and the outer surface. Figure 7.8 shows the temperature distribution within the annulus at time $t = 10$ms while figure 7.9 corresponds with $t = 0.2$s. It is seen that both inner and outer boundary comply with adiabatic conditions.

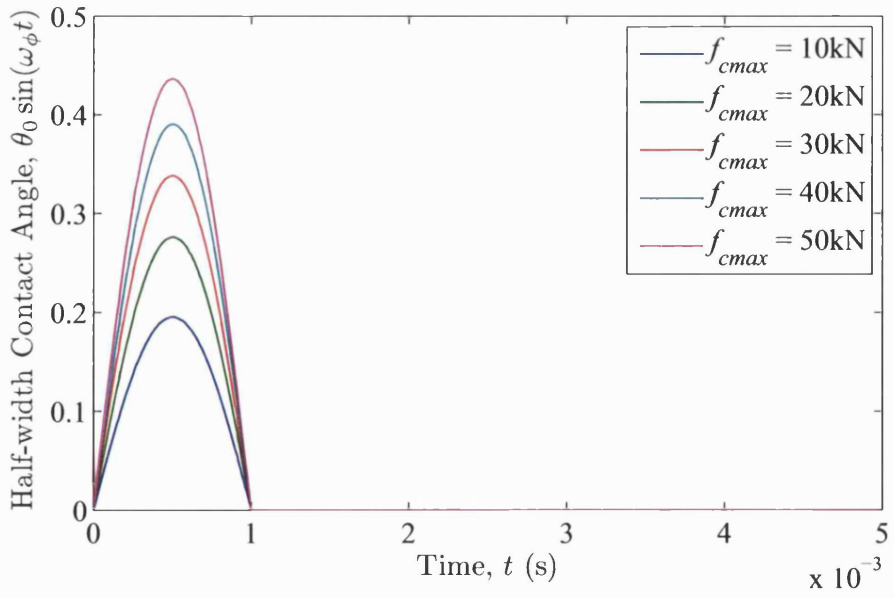

Figure 7.4: Variation of half-angle contact zone, $\theta_0\phi(t)$ with time for different contact forces, f_{cmax}.

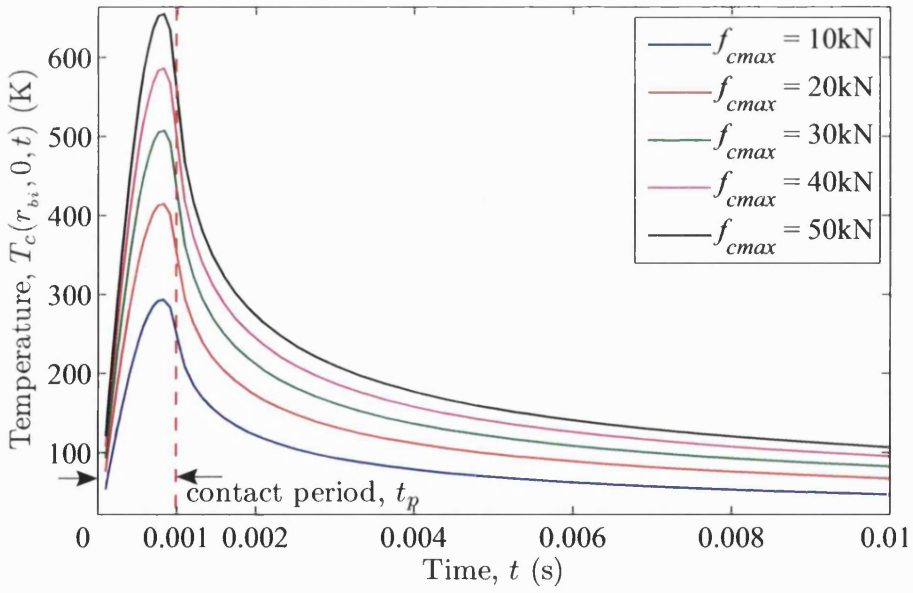

Figure 7.5: Time variation of the surface temperature at $(r, \theta) = (r_{bi}, 0)$ subjected to different contact force, f_{cmax} (t_p = 1ms).

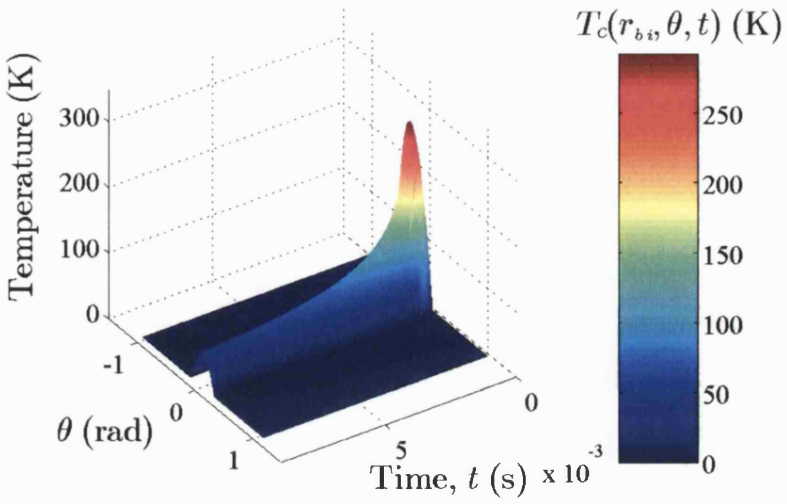

Figure 7.6: Time variation of surface temperature at inner surface (r_i, θ).

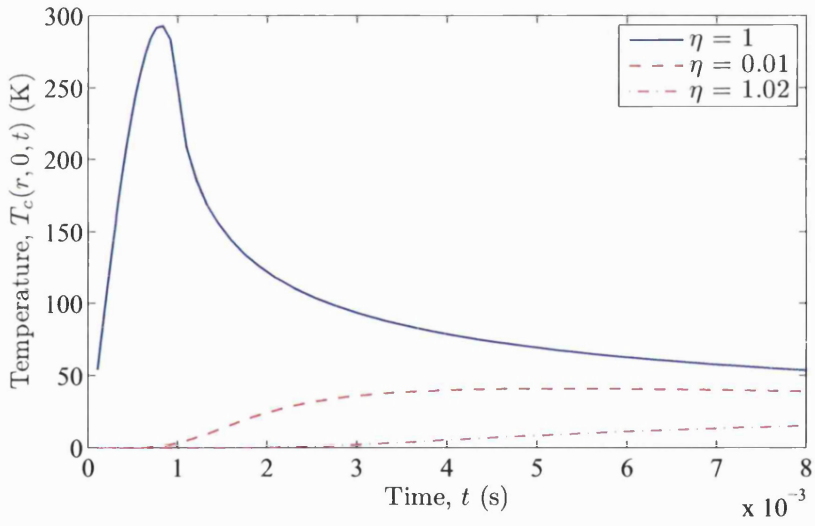

Figure 7.7: Time variation of temperature at different location within annulus subjected to frictional heating on the surface boundary with a normal dynamic contact force of amplitude, $f_{cmax} = 10$kN.

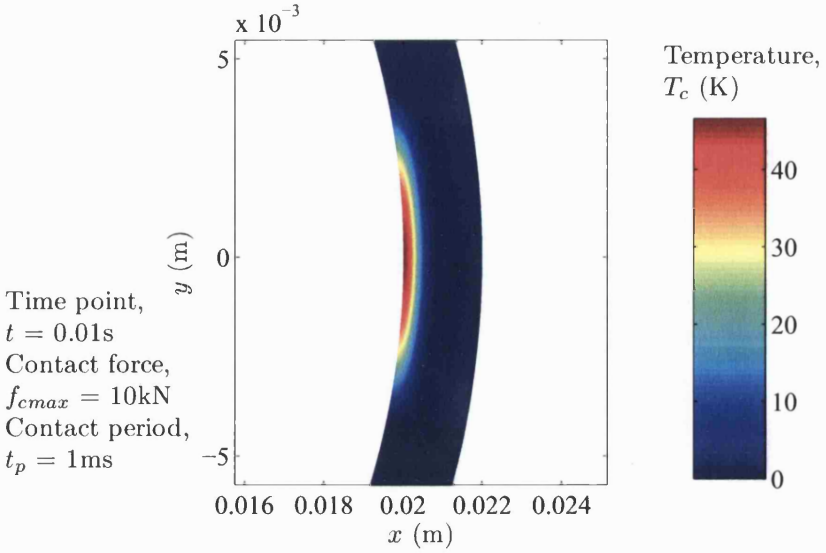

Figure 7.8: Temperature distribution, T_c at $t = 0.01$s of an annulus subjected to frictional surface heating induced by contact between rotating rotor and fixed bush with normal contact force, 10kN ($t_p = 1ms$).

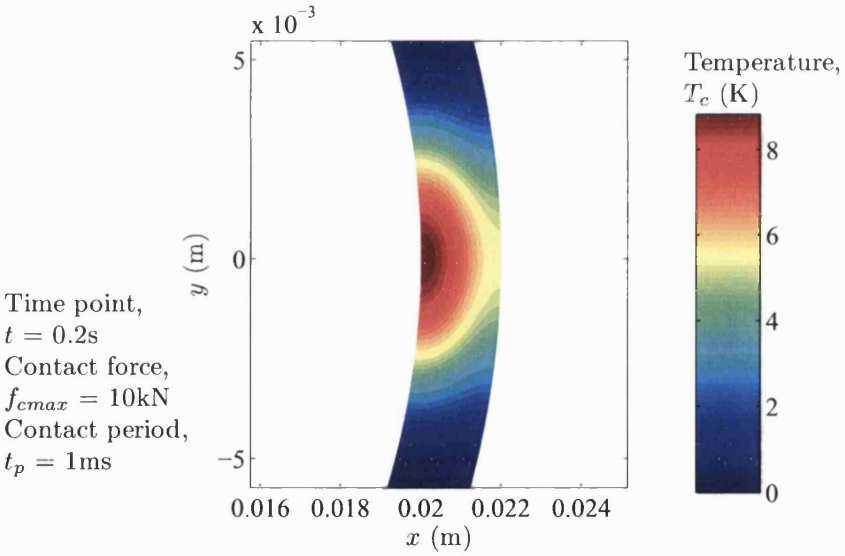

Figure 7.9: Temperature distribution, T_c at $t = 0.01$s of an annulus subjected to frictional surface heating induced by contact between rotating rotor and fixed bush with normal contact force, 10kN ($t_p = 1ms$).

(b) Rotor Speed (Ω = 1000-3000rad/s)

Figure 7.10 shows the time variation of maximum surface temperature corresponding to different rotor speeds. The bearing was subjected to contact force, f_{cmax} = 10kN, with coefficient of friction, $\mu = 0.1$ and the periodic taken is t_p = 1ms. It is seen that the temperature rise linearly corresponding to the rotor speed, the maximum temperature for rotor running at 3000rad/s is almost triple to the rotor running at 1000rad/s. Figures 7.11 and 7.12 show the time variation of the maximum surface temperature subjected to different contact forces, with rotor speed running at Ω = 2000rad/s and 3000rad/s respectively. It is seen that the surface of the bearing would melt if the contact force was greater than 20kN at the rotor speed Ω = 3000rad/s (figure 7.12).

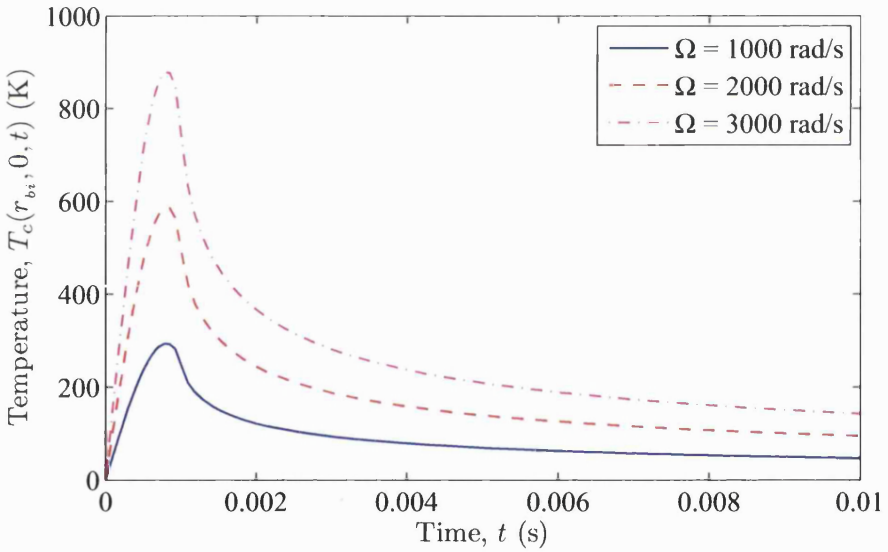

Figure 7.10: Time variation of maximum surface temperature subjected at contact force, f_{cmax} = 10kN (t_p = 1ms) corresponding to various rotor speed.

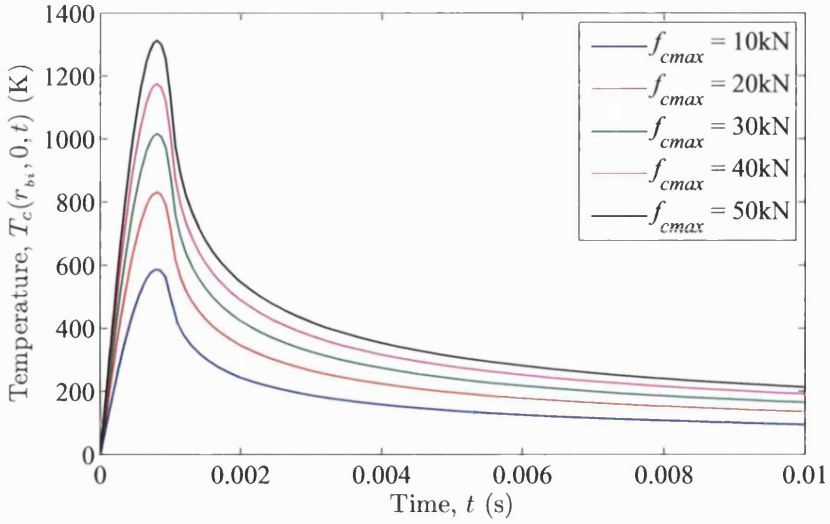

Figure 7.11: Time variation of maximum surface temperature subjected to various contact force with rotor speed $\Omega = 2000\text{rad/s}$ ($t_p = 1\text{ms}$).

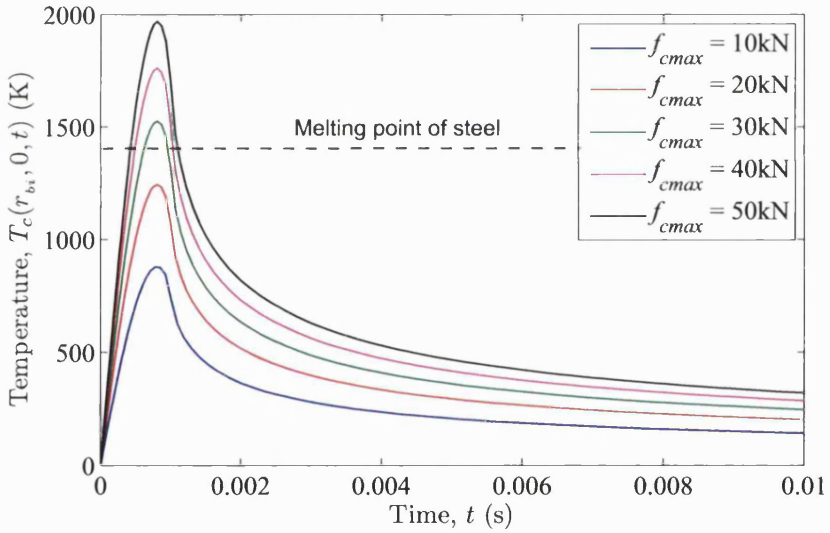

Figure 7.12: Time variation of maximum surface temperature subjected to various contact force with rotor speed $\Omega = 3000\text{rad/s}$ ($t_p = 1\text{ms}$).

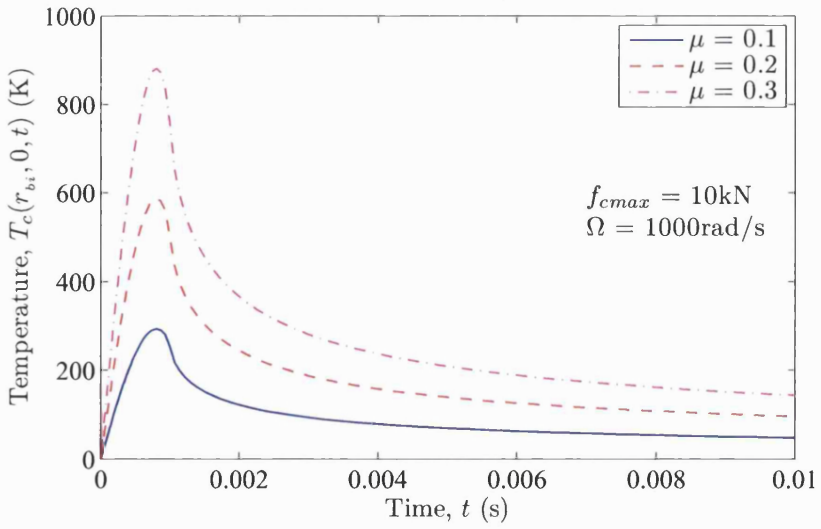

Figure 7.13: Time variation of maximum surface temperature at $(r_{bi}, 0)$ subjected to $f_{cmax} = 10$kN with rotor speed $\Omega = 1000$rad/s corresponding to different coefficients of friction ($t_p = 1$ms).

(c) Coefficient of Friction ($\mu = 0.1, 0.2, 0.3$)

Figure 7.13 shows the time variation of the maximum surface temperature corresponding to different coefficients of friction. Note that the temperature rise is direct proportional to the coefficient of friction, which governs the total heat flux (equation (7.15)).

(d) Contact Period ($t_p = 1$ms, 2ms)

The contact force and contact duration were taken from the typical results predicted by the dynamic simulations presented in section 2.4, which are highly dependent on the initial conditions. Any increase in either the contact period or contact force is associated with a rise of surface temperature. Figure 7.14 compares the inner surface temperature subjected to $f_{cmax} = 10$kN with different contact period, i.e. $t_p = 1, 2$ms.

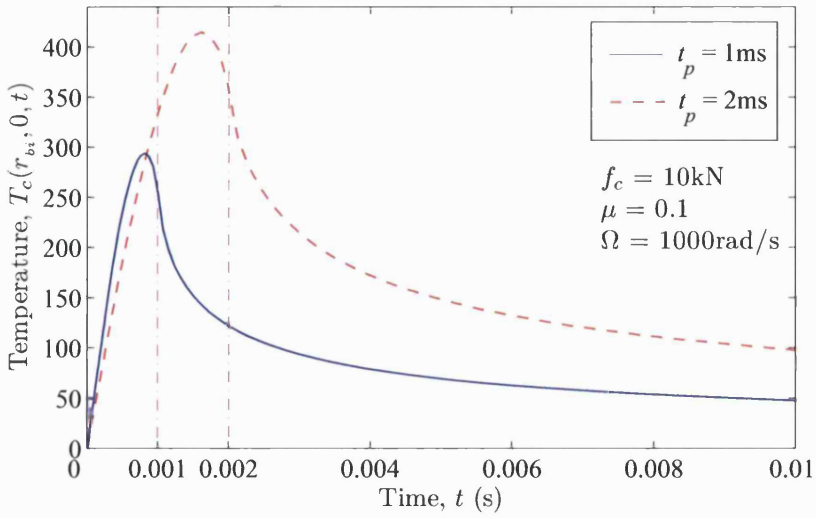

Figure 7.14: Time variation of maximum surface temperature at $(r_{bi}, 0)$ subjected to 10kN with different contact periods.

(e) Simulated Operating Conditions

With reference to Table 2.2, seven operating conditions and their corresponding maximum contact forces and periods chosen as summarised in Table 7.2.

Table 7.2: Summary of the chosen operating conditions and their corresponding contact forces and periods.

	Ω (rad/s)	μ	f_{cmax} (kN)	t_p (ms)
P3	1000	0.1	42	1.0
P6	1000	0.2	11	0.8
P9	2000	0.1	23	1.0
P11	2000	0.2	24	1.2
P12	2000	0.1	36	0.9
P13	3000	0.1	45	0.6
P15	3000	0.1	40	0.8

Figure 7.15 shows the time variation of maximum inner surface temperature corresponding to various operating conditions given in Table 7.2. It is seen that P11, P13 and P15 exceed the melting point of the bearing stainless steel. Although the deflection of the rotor of P13 and P15 does not exceed the rotor/magnetic bearing clearance, the heat induced by the maximum contact force is likely to initiate localised melting of the inner surface of the bearing. The temperature rise of P11 is higher than P9 due to higher coefficient of friction, longer contact period and higher contact force.

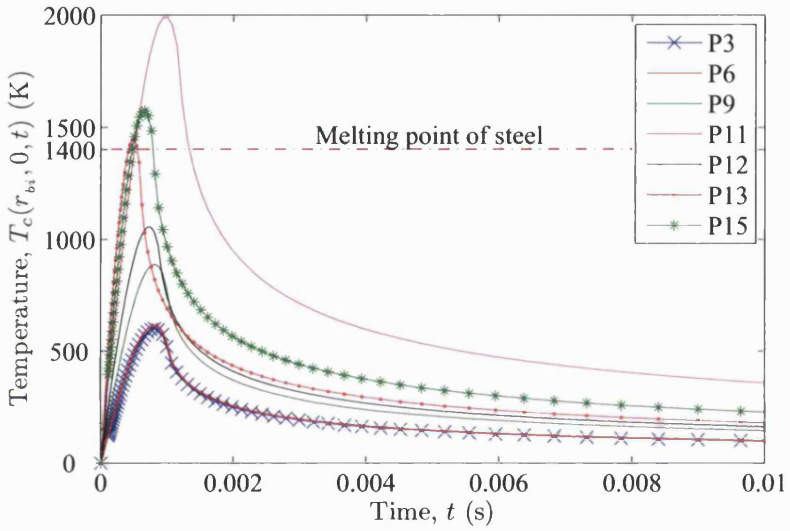

Figure 7.15: Time variation of maximum surface contact temperature for different operating conditions.

These results are based on the assumption that both body temperature and housing temperature are zero initially. The coefficient of friction, rotor speed and contact period are shown to have significant influence on the thermal responses. Later, an investigation of the thermal behaviour of the sliding contact between steel rotor and bronze bush bearing is undertaken.

7.3.1.6 Flash Temperature Comparison

The local flash temperature concept of Blok [81] will now be used to estimate the surface temperature induced by a moving heat source applied to a half-plane surface under steady state analysis (see figure 7.16).

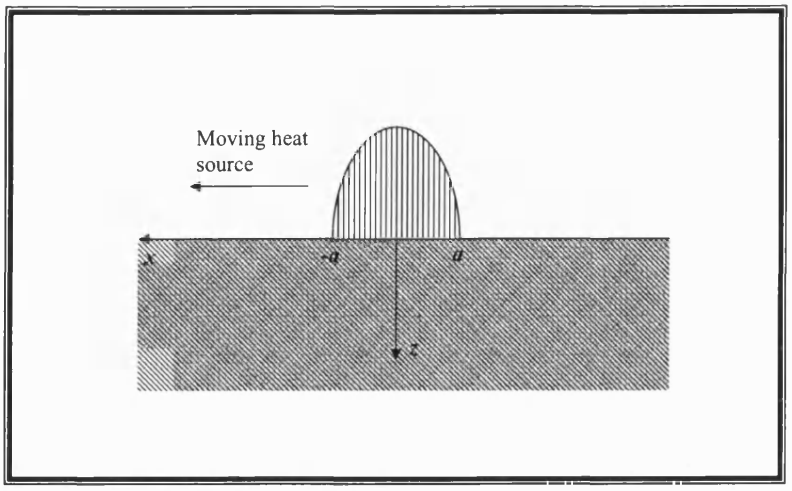

Figure 7.16: Moving heat source applied to a half-plane surface.

For a steady Hertzian Coulomb friction contact profile, the contact pressure is given by equation (7.1) and the total heat flux developed in the contact zone is

$$q = \frac{\mu E^* r_r \omega_s}{2R^*} \sqrt{a^2 - x^2} \tag{7.35}$$

The steady state flash temperature rise ($z = 0$) due to the moving heat source αq moving with speed U is

$$T_{cf}(x, z) = \alpha \frac{\mu E^* r_r \omega_s}{4\pi k R^*} \int_{-a}^{a} e^{\frac{U(x-x')}{2\kappa}} K_0 \left\{ \frac{U\sqrt{(x-x')^2 + z^2}}{2\kappa} \right\} \sqrt{a^2 - x'^2} dx' \tag{7.36}$$

where $U = r_r\Omega$. Setting,

$$\begin{aligned} u &= \frac{U(x-x')}{2\kappa} = \frac{Ux}{2\kappa} - \frac{Ux'}{2\kappa} = X - X' \\ du &= -dX' \end{aligned} \tag{7.37}$$

The surface flash temperature is

$$T_{cf}(x,0) = \alpha \frac{\mu\kappa^2 E^*}{\pi k_b r_r \omega_s R^*} \int_{X-Pe_b}^{X+Pe_b} e^u K_0(|u|)\sqrt{Pe_b^2 - X^2 + 2uX - u^2}du \tag{7.38}$$

Figure 7.17 shows the flash surface temperature around the contact zone $-1 \leq x/a \leq 1$ for bearing stainless bearing steel with various contact forces f_{cmax}. Comparing the peak temperatures corresponding to each contact forces of figures 7.17 and 7.5, it is seen that flash temperature overpredicts the surface temperature. This is due to the fact that the flash temperature is evaluated under steady state conditions, with no time variation heat input and dissipation period.

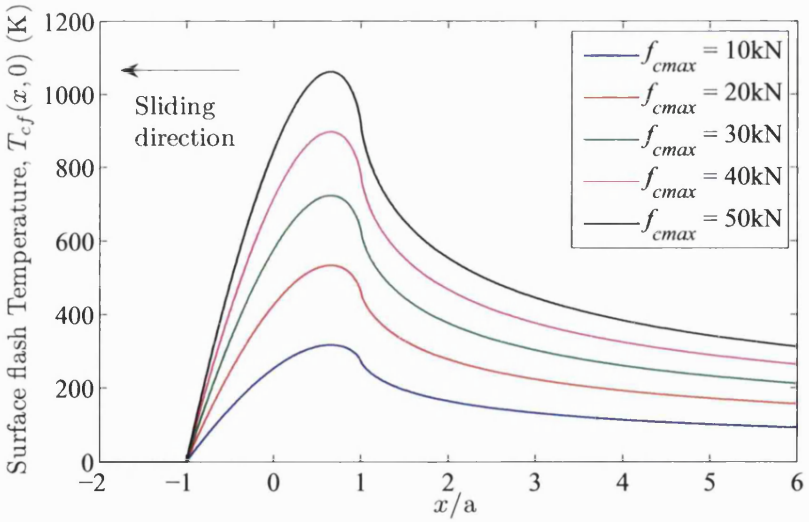

Figure 7.17: Surface temperature rise around contact zone $-1 \leq x/a \leq 1$, with $\mu = 0.1$ and various f_c shown. ($\mu = 0.1$, $\omega_s = \Omega = 1000$rad/s, $\alpha = 0.5$).

7.3.2 A Rotating Inner Race

In a rolling element bearing, any friction for between the rotor and the inner race of the bearing will cause the inner race to undergo angular acceleration. The dynamics will also involve the angular acceleration of the rolling elements and this may involve various regimes of rolling and skidding [16]. In an idealised case, the equation for angular motion of the inner race under a contact force of the form of equation (7.9) is,

$$I\dot{\omega}_b = \mu f_{cmax} r_{bi} \phi(t)^2 \tag{7.39}$$

where ω_b is the angular velocity of the inner race and I is the effective inertia representing the combined race and rollers (see Appendix D). It follows that for constant I,

$$\omega_b = \frac{\mu f_{cmax} r_{bi}}{I} \int_0^t \phi(\tau)^2 d\tau \tag{7.40}$$

Since both rotor and inner race are rotating, the angular slip velocity is the given by $\omega_s = \Omega - \omega_b$. If the inner race is regarded as stationary, the contact area between the rotor and inner race moves with angular velocity $-\omega_b$ with moving angular position of $\theta = -\theta_b$, where,

$$\theta_b(t) = \int_0^t \omega_b(\tau) d\tau \tag{7.41}$$

The heat flux is now modified to take account of the new slip velocity and the movement of the contact area relative to the inner race through,

$$q(\theta, t) = q_0 \frac{\Omega - \omega_b(t)}{\Omega} \sqrt{\theta_0^2 \phi(t)^2 - (\theta + \theta_b(t))^2} \tag{7.42}$$

whenever $-\theta_b(t) - \theta_0\phi(t) \leq \theta \leq -\theta_b(t) + \theta_0\phi(t)$.

7.3.2.1 Half-Plane Component for Rotating Race

Using a similar approach to that presented in 7.3.1.1, the half-plane contact temperature associated with the rotating race is written as,

$$\begin{aligned} & T_{ch}(r,\theta,t) \\ =&\frac{\alpha l_b q_0}{2\pi k_b}\int_0^t \int_{\beta=-\theta_b-\theta_0\phi(\tau)}^{-\theta_b+\theta_0\phi(\tau)} \frac{\Omega-\omega_b(\tau)}{\Omega}\sqrt{\theta_0^2\phi(\tau)^2-(\beta+\theta_b(\tau))^2} \\ & \times \frac{1}{(t-\tau)} e^{-\frac{r_{bi}^2(1+\eta^2-2\eta\cos(\theta-\beta)}{4\kappa_b(t-\tau)}} d\beta d\tau \end{aligned} \tag{7.43}$$

Let $\beta+\theta_b(\tau)=\theta_0\phi(\tau)u$, $d\beta=\theta_0\phi(\tau)du$, so that

$$\begin{aligned} T_{ch}(r,\theta,t) =&\frac{\alpha l_b q_0\theta_0^2}{2\pi k_b}\int_0^t\int_{u=-1}^1 \phi(\tau)^2\frac{\Omega-\omega_b(\tau)}{\Omega}\sqrt{1-u^2} \\ & \times \frac{1}{(t-\tau)} e^{-\frac{r_{bi}^2(1+\eta^2-2\eta\cos(\theta-\theta_0\phi(\tau)u+\theta_b)}{4\kappa_b(t-\tau)}} du d\tau \end{aligned} \tag{7.44}$$

The second term in (7.21) is

$$\begin{aligned} & \hat{T}_{ch}(r,\theta,t) \\ &= -\frac{\alpha l_b q_0}{2\pi k_b}\int_{\tau=0}^t \int_{\beta=-\theta_r-\theta_0\phi(\tau)}^{-\theta_r+\theta_0\phi(\tau)} \frac{\Omega-\omega_b(\tau)}{\Omega}\times\sqrt{\theta_0^2\phi(\tau)^2-(\beta+\theta_r(\tau))^2} \\ & \qquad \times\int_{v=0}^{t-\tau}\frac{g(v)}{(t-\tau-v)}\times e^{-\frac{r_{bi}^2\left(1+\eta^2-2\eta\cos(\theta-\beta)\right)}{4\kappa_b(t-\tau-v)}} dv d\beta d\tau \\ &= -\frac{\alpha l_b q_0\theta_0^2}{2\pi k_b}\int_{\tau=0}^t\int_{u=-1}^1 \phi(\tau)^2\frac{\Omega-\omega_b(\tau)}{\Omega}\sqrt{1-u^2} \\ & \qquad \times\int_{v=0}^{t-\tau}\frac{g(v)}{(t-\tau-v)} e^{-\frac{r_{bi}^2\left(1+\eta^2-2\eta\cos(\theta-\theta_0\phi(\tau)u)+\theta_b\right)}{4\kappa_b(t-\tau-v)}} dv du d\tau \end{aligned} \tag{7.45}$$

7.3.2.2 Statement of Remainder Function for Rotating Race

For the remainder function,

$$
\begin{aligned}
&T_{cR}(r,\theta,t)\\
=&\alpha l_b q_0 \sum_{n=-\infty}^{\infty} \int_0^t \int_{\beta=-\theta_r-\theta_0\phi(\tau)}^{-\theta_r+\theta_0\phi(\tau)} \frac{\Omega-\omega_b(\tau)}{\Omega}\sqrt{\theta_0^2\phi(\tau)^2-(\beta+\theta_r(\tau))^2}\\
&\qquad\qquad \times T_{GRn}(r,t-\tau)e^{in(\theta-\beta)}d\beta d\tau\\
=&\alpha l_b q_0\theta_0^2 \sum_{n=-\infty}^{\infty} \int_0^t \int_{u=-1}^{1} \phi(\tau)^2\frac{\Omega-\omega_b(\tau)}{\Omega}\sqrt{1-u^2}T_{GRn}(r,t-\tau)\\
&\qquad\qquad \times e^{in(\theta-\theta_0\phi(\tau)u+\theta_r(\tau))}dud\tau\\
=&\alpha l_b q_0\theta_0^2 \sum_{n=-\infty}^{\infty} \int_0^t \phi(\tau)^2\frac{\Omega-\omega_b(\tau)}{\Omega}T_{GRrn}(r,t-\tau)e^{in\theta_r(\tau)}\\
&\qquad\qquad \times\left\{\int_{u=-1}^{1}\sqrt{1-u^2}e^{-in\theta_0\phi(\tau)u}du\right\}d\tau e^{in\theta}
\end{aligned}
\tag{7.46}
$$

Hence,

$$
\begin{aligned}
&T_{cRn}(r,\theta,t)\\
=&\begin{cases}
\alpha l_b q_0\theta_0^2\displaystyle\int_0^t \frac{1}{2}\pi\phi(\tau)^2\frac{\Omega-\omega_b(\tau)}{\Omega}T_{GRn}(r,t-\tau)d\tau & (n=0)\\
\alpha l_b q_0\theta_0\displaystyle\int_0^t \frac{\pi\phi(\tau)}{n}J_1(n\theta_0\phi(\tau))\frac{\Omega-\omega_b(\tau)}{\Omega}T_{GRn}(r,t-\tau)e^{in\theta_r(\tau)}d\tau e^{in\theta} & (n\neq 0)
\end{cases}
\end{aligned}
\tag{7.47}
$$

7.3.2.3 Case Study for a Rotating Race

Table 7.3: Bearing Parameters.

Ball element radius, r_{rol}	1.873mm
Inner race mass, m_b	0.0129kg
Rolling element mass, m_{rol}	0.000215kg
Number of balls, n	40

Table 7.3 provides information on auxiliary bearing parameters to calculate the effective inertia I (Appendix D). This case study uses the same parameters and operating conditions given in sections 2.4 and Table 7.1. The same dynamic response of the normal contact force given by equation (7.34) is used. The integrals (7.40) and (7.41) yield,

$$\omega_b(t) = \frac{\mu f_{cmax} r_{bi}}{I\omega_\phi} \begin{cases} 1 - \cos\omega_\phi t, & 0 \leq t \leq t_p \\ 1, & t > t_p \end{cases} \tag{7.48}$$

The inner race angular velocity, ω_b is also bounded ($0 \leq \omega_b \leq \Omega$). The duration taken for the inner race speed synchronise with the rotor speed Ω is

$$t_\Omega = \frac{1}{\omega_\phi} \cos^{-1}\left\{1 - \frac{I\omega_\phi\Omega}{\mu f_{cmax} r_{bi}}\right\} \tag{7.49}$$

and

$$\theta_b(t) = \frac{\mu f_{cmax} r_{bi}}{I\omega_\phi} \begin{cases} t - \frac{1}{\omega_\phi}\sin\omega_\phi t, & 0 \leq t \leq t_p \text{ and } t_\Omega \leq t_p \\ t, & t > t_p \end{cases} \tag{7.50}$$

In reality, when contact ceases, the inner race angular displacement will not increase indefinitely since internal friction will be present. The following sections

compare the time variation of the temperature corresponds to various governing parameters.

(a) Contact Force (f_{cmax} = 10-50kN)

Figure 7.18 shows the rotating speeds of the inner race corresponding to different contact forces. Frictional heating take place at the contact surfaces when $\omega_b < \Omega = 1000\text{rad/s}$. No heat generation occurs within the rolling regime when $\omega_b = \Omega$. Figure 7.19 shows the time variation of the maximum temperature at the inner surface of the bearing corresponding to different contact forces. The rotor speed $\Omega = 1000\text{rad/s}$, coefficient of friction $\mu = 0.1$ and the contact period is $t_p = 1\text{ms}$. It is seen that little differences between the peak temperatures due to shorter heat dissipation period t_Ω as the inner race spins up faster with higher contact force (see figure 7.18). Meanwhile, it also decreases the total heat dissipation governed by the term $q_0 (\Omega - \omega_b) / \Omega$ in (7.42), where ω_b is given by equation (7.48).

(b) Rotor Speed (Ω = 1000-3000rad/s)

Figure 7.20 show the time variation of bearing inner race speed corresponding to various rotor speeds. It is seen that higher rotor speed offers a longer period of higher frictional heating, leading to higher surface temperature as shown in figure 7.21.

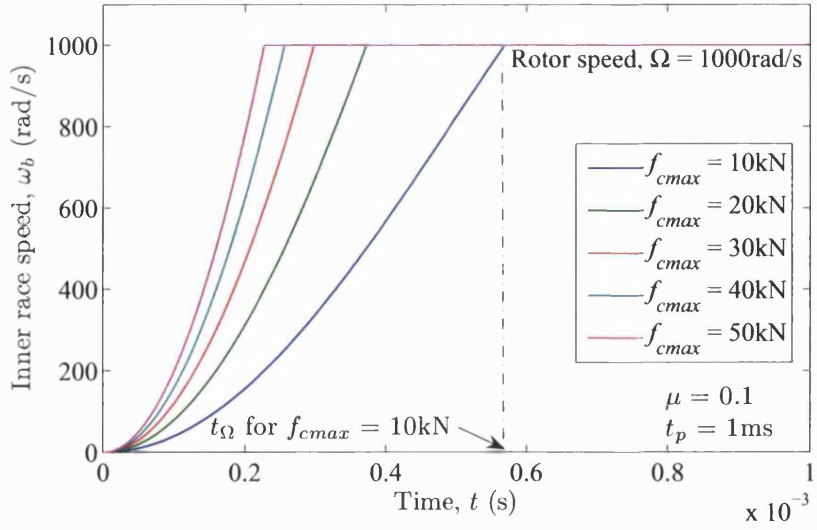

Figure 7.18: Time variation of inner race rotating speed corresponding to different contact forces.

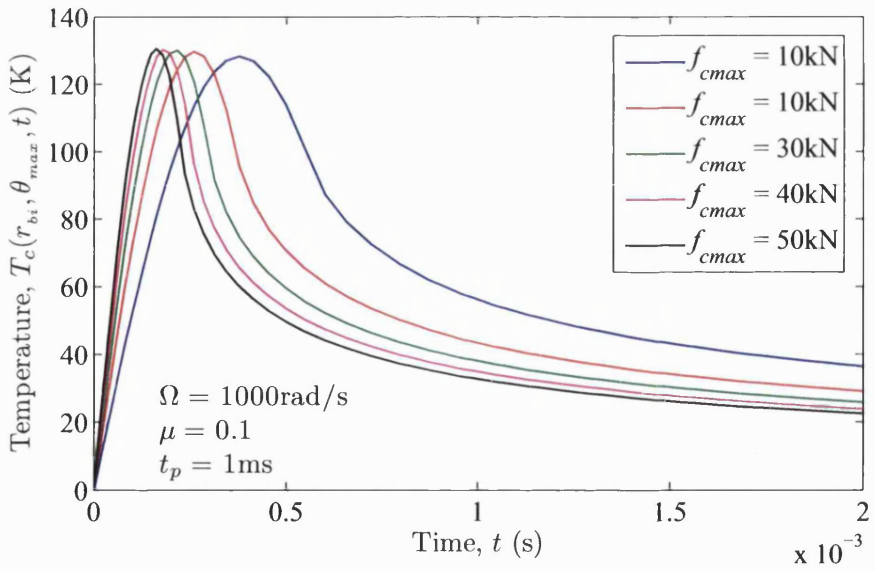

Figure 7.19: Time variation of temperature corresponding to different contact forces, f_{cmax}. θ_{max} is the angular position where maximum temperature was noted.

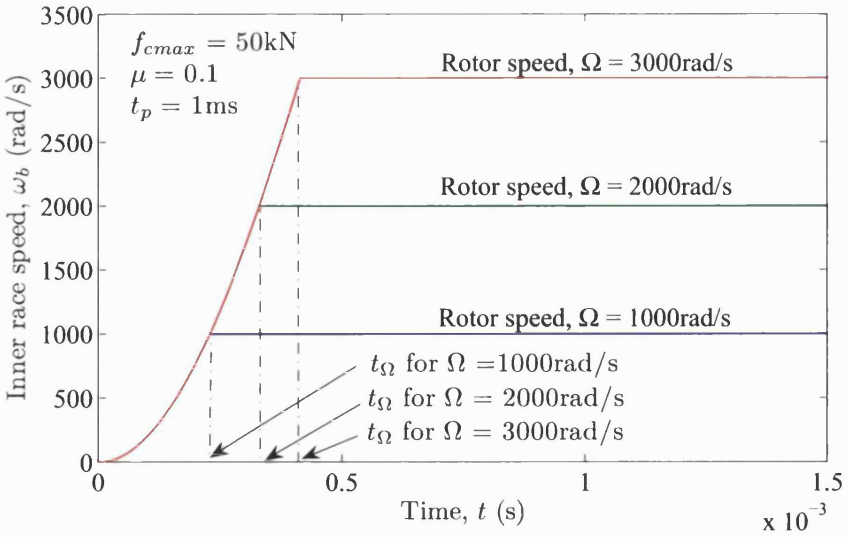

Figure 7.20: Time variation of inner race rotating speed corresponding to different rotor speeds.

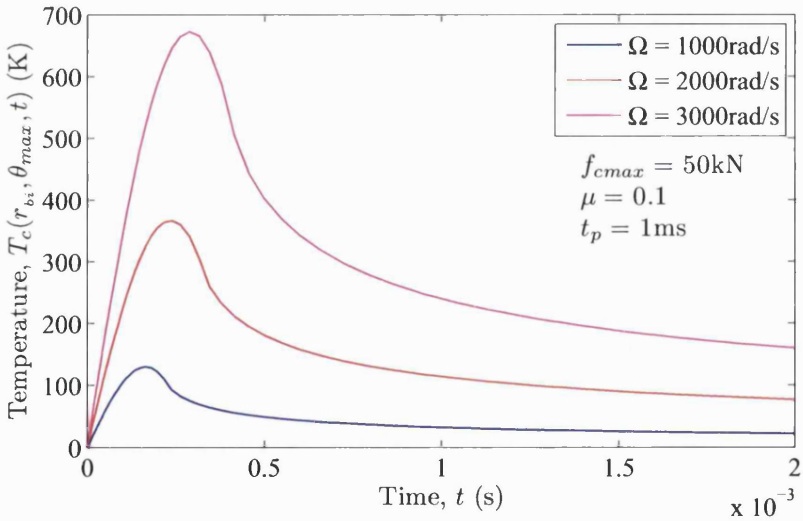

Figure 7.21: Time variation of temperature corresponding to different rotor speed, Ω.

(c) Coefficient of Friction

Figure 7.22 shows that the increase in the coefficient of friction reduces the heat dissipation period, t_Ω. On the other hand, it also increases the maximum inner surface temperature as shown in figure 7.23 due to the higher heat source applied to the inner surface.

(d) Simulated Operating Conditions

Identical operating conditions to those of section 7.3.1.5(e) are considered. Figure 7.24 shows the time variation of maximum inner surface temperature corresponding to operating conditions P3, P6, P9, P11, P12, P13 and P15, respectively. The temperature rises are lower than the fixed bush problem (figure 7.15). Practically, the coefficient of friction for the contact of a rotor on a rolling element bearing is higher [5, 9], e.g. $\mu = 0.3 - 0.5$. Two operating conditions that are likely to initiate localised melting are chosen (P11 and P15) for further investigation. Figures 7.25 and 7.26 show a significant rise in inner surface temperature by varying the coefficient of friction. The problem case of P15 with the rotor speed running at 3000rad/s, coefficient of friction $\mu = 0.5$ when subjected to contact force $f_{cmax} = 40$kN is noted. The surface temperature rise exceeds the melting point of bearing stainless steel. Figures 7.27 and 7.28 shows the temperature distribution of a rotating race subjected to $f_{cmax} = 10$kN for a periodic $t_p = 1$ms at $t = t_\Omega$ and 0.2s respectively ($\Omega = 1000$rad/s, $\mu = 0.1$). Note that both inner and outer boundaries are adiabatic.

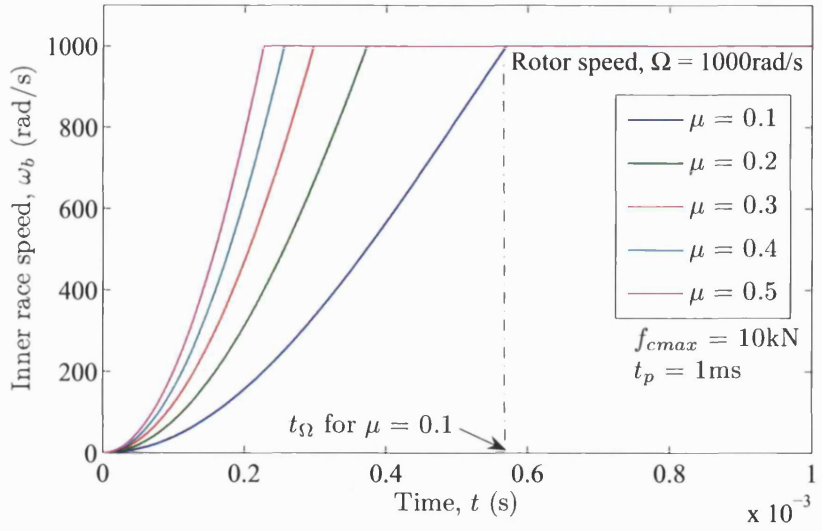

Figure 7.22: Time variation of inner race rotating speed corresponding to different coefficients of friction.

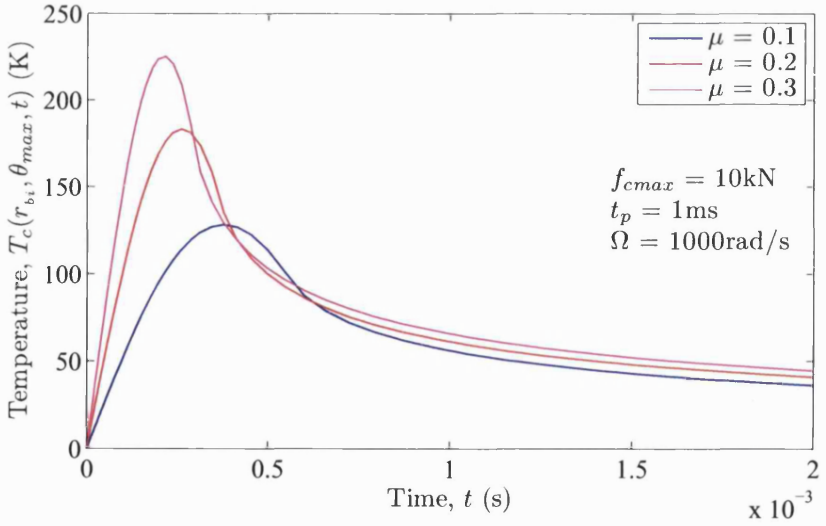

Figure 7.23: Time variation of temperature corresponding to different coefficients of friction.

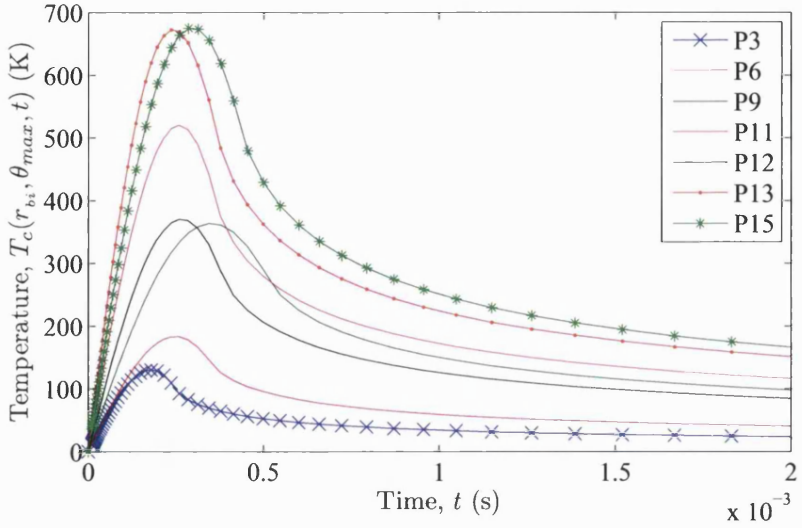

Figure 7.24: Time variation of inner surface temperature corresponding to operating conditions P3, P6, P9, P11, P12, P13 and P15.

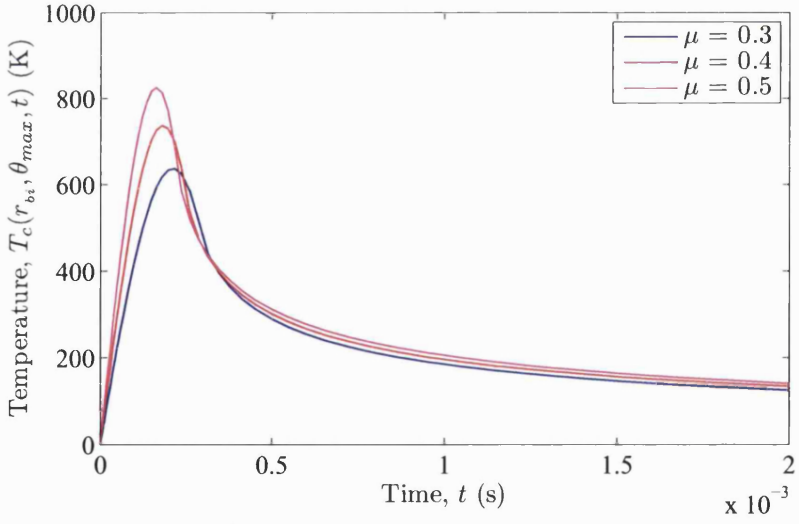

Figure 7.25: Time variation of inner surface temperature corresponding to different coefficients of friction (operating condition P11).

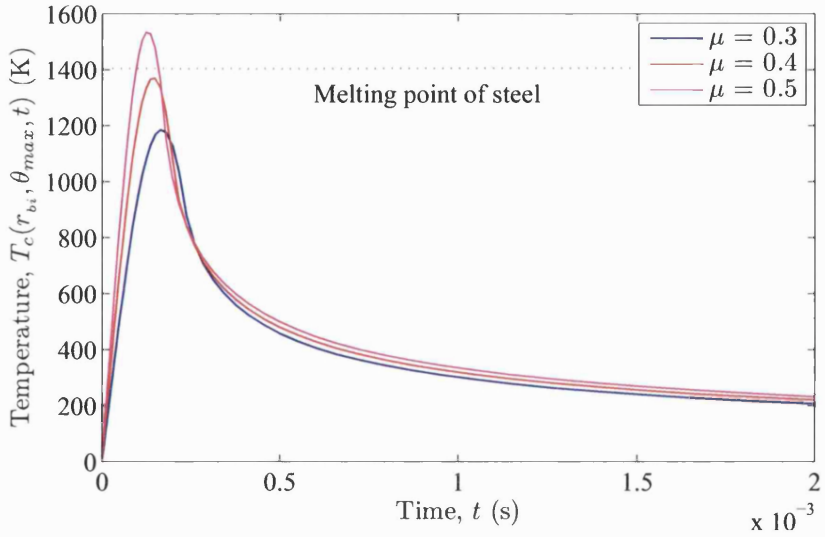

Figure 7.26: Time variation of inner surface temperature corresponding to different coefficient of friction (operating condition P15).

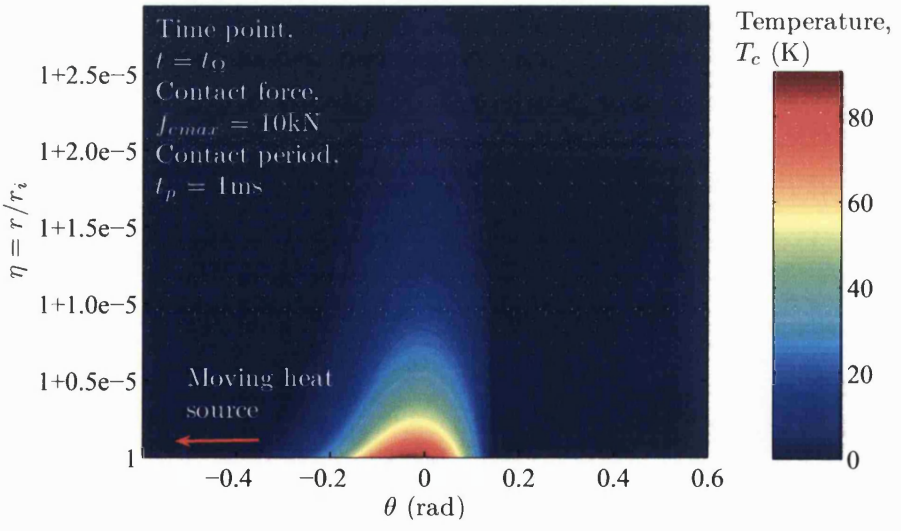

Figure 7.27: Temperature distribution in rotating inner race problem at time point, $t = t_\Omega$ subjected normal loading of 10kN ($\Omega = 1000$rad/s, $\mu = 0.1$).

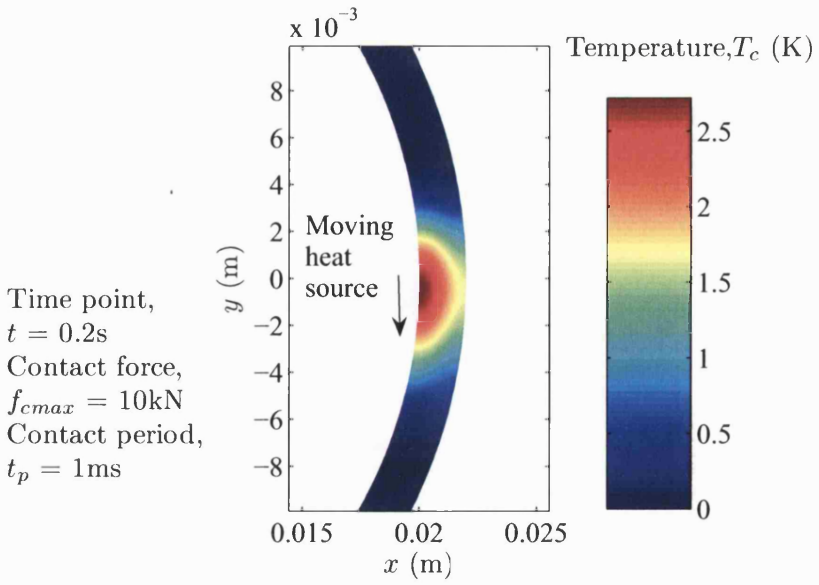

Figure 7.28: Temperature distribution for rotating inner race problem at time point, $t = 0.2$s subjected normal loading of 10kN ($\Omega = 1000$rad/s, $\mu = 0.1$).

7.4 Frictional Surface Heating - Steel Rotor and Bronze Bush Bearing

In this section, the temperature rise due to frictional heating induced by sliding contact of a steel rotor on a fixed bronze bush bearing is investigated. Table 7.4 shows the material properties of phosphor bronze (UNS C54400), which are used for the analysis.

Table 7.4: Material properties of phosphor bronze.

Properties	Values
Density, ρ_d	8890 kg/m^3
Modulus of elasticity, E	103 $\times$ 10^9 N/m^2
Poisson ratio, υ	0.321
Thermal conductivity, k	87 W/mK
Heat capacity, c_p	380 J/kgK
Typical melting point	1000 K
Thermal Expansion Coefficient, α_e	17.3 $\times$ 10^{-6} K^{-1}

7.4.1 Induced Heat Flux

Based on the analysis in section 7.2.2, the pressure distribution is given by equation (7.5). Using the contact force per unit length given by equation (7.9), the half-width contact patch can be written as (see equation (7.8)),

$$a^2 = \frac{1}{1-4\gamma^2} \times \frac{4R^*(f_{cmax}/l_b)}{\pi E^*}\phi(t)^2 = a_0^2\phi(t)^2 \tag{7.51}$$

where γ is given by equation (7.7). Substituting equation (7.51) into equation (7.5) yields,

$$p(x,t) = \frac{E^*}{2R^*\sqrt{1+\beta^2\mu^2}}\left(\frac{a_0\phi(t)+x}{a_0\phi(t)-x}\right)^{\gamma}\sqrt{a_0^2\phi(t)^2-x^2} \tag{7.52}$$

The total heat flux induced due to Coulomb friction is,

$$q(x,t) = \frac{\mu E^* r_r\omega_s}{2R^*\sqrt{1+\beta^2\mu^2}}\left(\frac{a_0\phi(t)+x}{a_0\phi(t)-x}\right)^{\gamma}\sqrt{a_0^2\phi(t)^2-x^2} \tag{7.53}$$

where $\omega_s = \Omega$ for a fixed bushing bearing. Taking $x = r_{bi}\theta$,

$$q(\theta,t) = \frac{\mu E^* r_r \omega_s r_{bi}}{2R^*\sqrt{1+\beta^2\mu^2}} \left(\frac{\theta_0\phi(t)+\theta}{\theta_0\phi(t)-\theta}\right)^{\gamma} \sqrt{\theta_0^2\phi(t)^2-\theta^2} \tag{7.54}$$

equation (7.13) can be rearranged to give,

$$q(\theta,t) = q_0 \left(\frac{\theta_0\phi(t)+\theta}{\theta_0\phi(t)-\theta}\right)^{\gamma} \sqrt{\theta_0^2\phi(t)^2-\theta^2} \tag{7.55}$$

where, r_r is the radius of the rotor andr_{bi} is the inner radius of the bushing. Also

$$q_0 = \frac{\mu E^* r_r \omega_s r_{bi}}{2R^*\sqrt{1+\beta^2\mu^2}} \tag{7.56}$$

$$\theta_0 = \sqrt{\frac{4R^*(f_{cmax}/l_b)}{(1-4\gamma^2)E^* r_{bi}^2}} \tag{7.57}$$

Since the bodies have different material properties, the heat partition coefficient α is modified according to equation (7.17). The heat flux into the bearing is

$$q_b(\theta,t) = \alpha q_0 \left(\frac{\theta_0\phi(t)+\theta}{\theta_0\phi(t)-\theta}\right)^{\gamma} \sqrt{\theta_0^2\phi(t)^2-\theta^2} \tag{7.58}$$

Based on the data given on phosphor bronze, $\gamma = -0.0039$. Figure 7.29 shows a symmetrical pressure distribution for a bronze bush bearing in contact with a steel rotor.

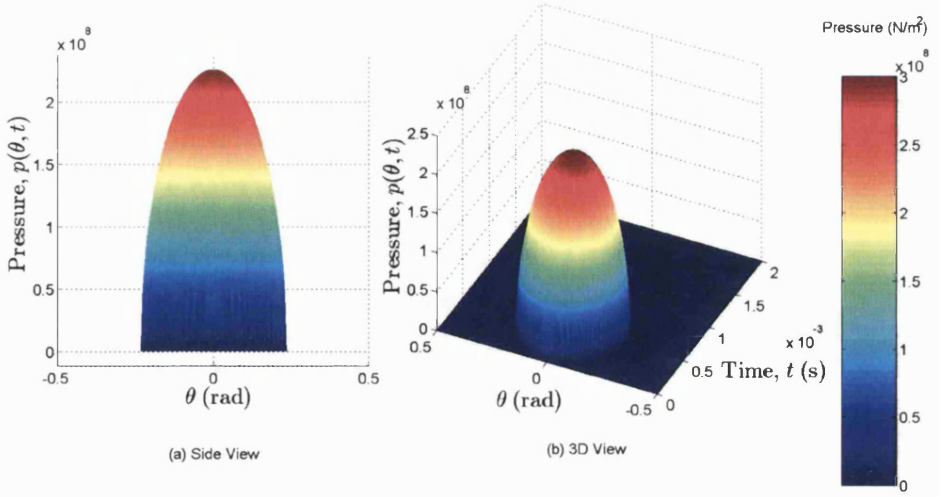

Figure 7.29: Time variation of pressure distribution for a bronze bush bearing in contact with a steel rotor $\gamma = -0.0039$.

7.4.2 Statement of Contact Temperature

The expression for half-plane terms is similar to that given in subsection 7.3.1.3. Using the convolution theorem, the first half-plane first term contact temperature is

$$\begin{aligned} & T_{ch}(r,\theta,t) \\ & = l_b \int_{\tau=0}^{t} \int_{\beta=-\theta_0\phi(t)}^{\theta_0\phi(t)} \frac{\alpha q_0}{2\pi k_b(t-\tau)} \cdot e^{-\frac{r_{bi}^2\left(1+\eta^2-2\eta\cos(\theta-\beta)\right)}{4\kappa_b(t-\tau)}} \\ & \qquad \times \left(\frac{\theta_0\phi(t)+\beta}{\theta_0\phi(t)-\beta}\right)^{\gamma} \sqrt{\theta_0^2\phi(\tau)^2-\beta^2}\, d\beta d\tau \end{aligned} \tag{7.59}$$

Taking $\beta = \theta_0\phi(\tau)u$,

$$\begin{aligned} & T_{ch}(r,\theta,t) \\ &= \frac{\alpha l_b q_0 \theta_0^2}{2\pi k_b} \int_{\tau=0}^{t} \int_{u=-1}^{1} \frac{\phi(\tau)^2}{(t-\tau)} \cdot e^{-\frac{r_{bi}^2\left(1+\eta^2-2\eta\cos(\theta-\theta_0\phi(\tau)u)\right)}{4\kappa_b(t-\tau)}} \\ &\qquad \times \left(\frac{1+u}{1-u}\right)^{\gamma} \sqrt{1-u^2}\, du d\tau \end{aligned} \tag{7.60}$$

The second half-plane term is

$$\begin{aligned} & \hat{T}_{ch}(r,\theta,t) \\ &= -\frac{\alpha l_b q_0}{2\pi k_b} \int_{\tau=0}^{t} \int_{\beta=-\theta_0\phi(t)}^{\theta_0\phi(t)} \int_{v=0}^{t-\tau} \frac{g(v)}{(t-\tau-v)} e^{-\frac{r_{bi}^2\left(1+\eta^2-2\eta\cos(\theta-\beta)\right)}{4\kappa_b(t-\tau-v)}} \\ &\qquad \times \left(\frac{\theta_0\phi(t)+\beta}{\theta_0\phi(t)-\beta}\right)^{\gamma} \sqrt{\theta_0^2\phi(\tau)^2-\beta}\, dv d\beta d\tau \\ &= -\frac{\alpha l_b q_0 \theta_0^2}{2\pi k_b} \int_{\tau=0}^{t} \int_{u=-1}^{1} \int_{v=0}^{t-\tau} \frac{\phi(\tau)^2 g(v)}{(t-\tau-v)} e^{-\frac{r_{bi}^2\left(1+\eta^2-2\eta\cos(\theta-\theta_0\phi(\tau)u)\right)}{4\kappa_b(t-\tau-v)}} \\ &\qquad \times \left(\frac{1+u}{1-u}\right)^{\gamma} \sqrt{1-u^2}\, dv du d\tau \end{aligned} \tag{7.61}$$

The remainder function is

$$\begin{aligned} & T_{cR}(r,\theta,t) \\ &= l_b \alpha q_0 \int_{\tau=0}^{t} \int_{\beta=-\theta_0\phi(t)}^{\theta_0\phi(t)} \sum_{n=-\infty}^{\infty} T_{Gn_{annulus}}(r,t-\tau) e^{in(\theta-\beta)} \\ &\qquad \times \left(\frac{\theta_0\phi(t)+\beta}{\theta_0\phi(t)-\beta}\right)^{\gamma} \sqrt{\theta_0^2\phi(\tau)^2-\beta^2}\, d\beta d\tau \\ &= l_b \alpha q_0 \theta_0^2 \int_{\tau=0}^{t} \int_{u=-1}^{1} \phi(\tau)^2 \sum_{n=-\infty}^{\infty} T_{Gn_{annulus}}(r,t-\tau) \\ &\qquad \times e^{-in\theta_0\phi(\tau)u} \left(\frac{1+u}{1-u}\right)^{\gamma} \sqrt{1-u^2}\, du d\tau e^{in\theta} \end{aligned} \tag{7.62}$$

7.4.3 Case Study for Contact of Steel Rotor on a Bronze Bush Bearing

Figure 7.30 shows the comparison of the maximum temperature of the bronze bush bearing and stainless steel bearing subjected to contact force $f_{cmax} = 50$kN. Higher heat diffusivity, κ, and lower heat partition coefficient, α, of bronze bush bearing induces lower surface temperature. The maximum surface temperature rise corresponding to operating conditions P3, P6, P9, P11, P12, P13 and P15 are shown in figure 7.31. In general, it is seen that the temperatures of each operating conditions are lower than the results evaluated based on the contact of rotor and bearing of same material (see figure 7.15). On the other hand, the results also show that the operating condition P11 is likely to initiate localised melting at the contact surface. From the comparison of figures 7.31 and 7.15, it can be seen that the bronze bush bearing is more suitable as an auxiliary bearing, giving lower temperature rise and reduces possibility of localised melting when subjected to high contact forces and rotor speed.

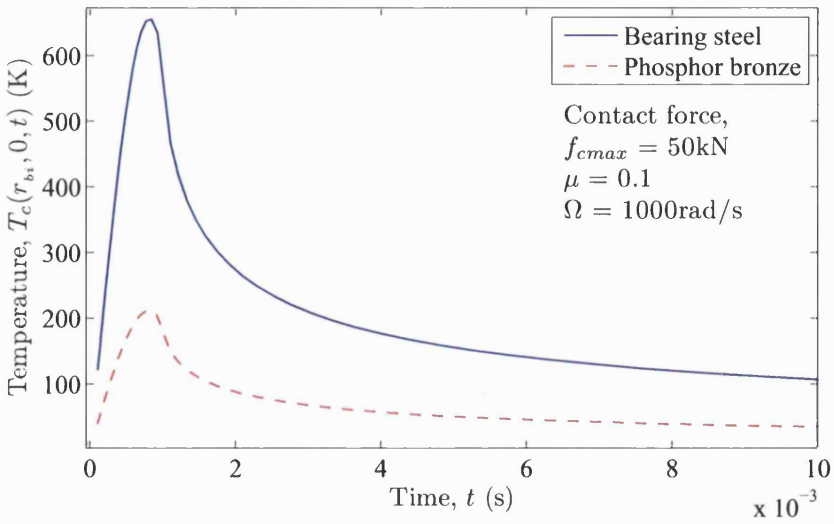

Figure 7.30: Comparison of maximum surface temperatures of phosphor bronze bush bearing and bearing steel bush. Both subjected to a normal contact force f_{cmax} = 50K.

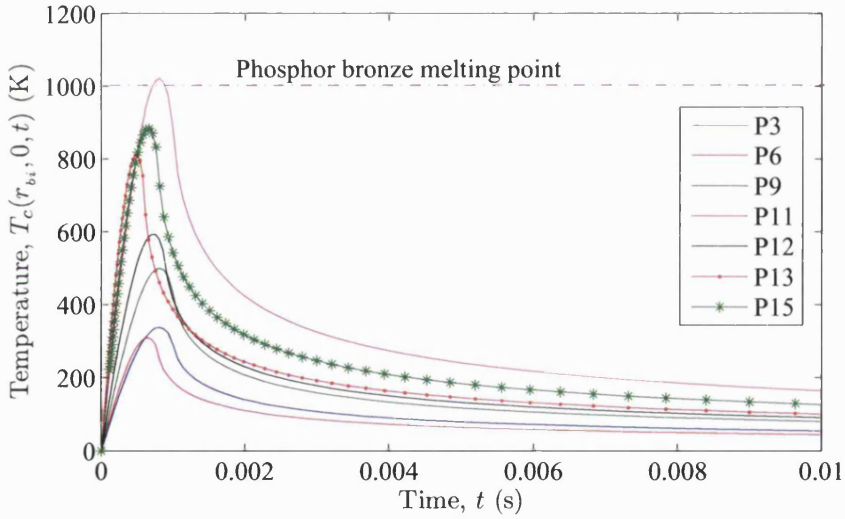

Figure 7.31: Time variation of inner surface temperature of a bronze bush bearing corresponding to operating conditions P3, P6, P9, P11, P12, P13 and P15.

7.5 Closure

The thermal solutions for a fixed bush and a rotating inner race contact problems have been developed. The contact for a rotor on a bearing of same and different materials were also considered. It was seen that any increase in contact force, coefficient of friction, contact period and rotor speed is associated with a rise of surface temperature for fixed bush problem. On the other hand, variations of the peak temperature were less for the rotating inner race problem, when the inner surface was subjected to higher contact forces, due to the shorter heat dissipation period. The thermal responses of the bearing corresponding to operating conditions derived from the dynamic analysis in Chapter 2 were also investigated. It was found that the system running at high rotor speed, high coefficient of friction together with with high contact force is likely to induce localised melting on the inner surface of an auxiliary bearing. The case study for a bronze bush bearing showed that it is more suitable as an auxiliary bearing resulting in lower temperature rises.

Chapter 8

Thermoelastic Analysis of a Single Dynamic Contact

8.1 Overview

This chapter focuses on the quasi-static thermal distortion of an auxiliary bearing when subjected to dynamic inner boundary heating arising from rotor contact. The rotor and bearing are considered to be made of same material, which means the sliding contact has a Hertzian pressure distribution. Two case studies are conducted, the first one is the thermal distortion of a rigidly mounted bearing and the second one is for a resiliently mounted bearing. The results are then applied in a practical manner to cases involving repeated contacts and synchronous rubbing. The manner in which thermoelastic growth could arise from repeated rubbing is indicated through a rubbing mechanistic model.

8.2 Thermal Contact Displacement - Hertzian Contact Pressure

Consider the inner surface of a stainless steel bush type bearing to be subjected to a heat source, q_b, given by equation (7.19). Using the convolution theorem, the thermal deformation of the auxiliary bearing is

$$\mathbf{u}_c(r,\theta,t) = l_b \int_{\tau=0}^{t} \int_{\beta=-\theta_0\phi(\tau)}^{\theta_0\phi(\tau)} q_b(\beta,\tau)\mathbf{u}_G(r,\theta-\beta,t-\tau)d\beta d\tau \tag{8.1}$$

where

$$\mathbf{u}_c(r,\theta,t) = \begin{bmatrix} u_{cr}(r,\theta,t) \\ v_{c\theta}(r,\theta,t) \end{bmatrix} \tag{8.2}$$

$$\mathbf{u}_G(r,\theta,t) = \begin{bmatrix} u_{Gr}(r,\theta,t) \\ v_{G\theta}(r,\theta,t) \end{bmatrix} \tag{8.3}$$

with u_{Gr} and $v_{G\theta}$ given by (6.73) and (6.74), respectively.

8.2.1 Radial Displacement

With reference to the thermoelastic Green's function for radial displacement given by equation (6.73), the general expression of the annular contact radial displacement can be written as

$$u_{cr}(r,\theta,t) = u_{chr}(r,\theta,t) + \sum_{n=-\infty}^{\infty} u_{cRrn}(r,\theta,t) \tag{8.4}$$

where u_{chr} and u_{cRn} are the half-plane and remainder function harmonics of the contact radial displacement, respectively. They are defined by

$$u_{chr}(r,\theta,t) = l_b \int_{\tau=0}^{t} \int_{\beta=-\theta_0\phi(\tau)}^{\theta_0\phi(\tau)} q_b(\beta,\tau) u_{Ghr}(r,\theta-\beta,t-\tau) d\beta d\tau \quad (8.5)$$

$$u_{cRrn}(r,\theta,t) = l_b \int_{\tau=0}^{t} \int_{\beta=-\theta_0\phi(\tau)}^{\theta_0\phi(\tau)} q_b(\beta,\tau) u_{GRrn}(r,\theta-\beta,t-\tau) \times e^{in(\theta-\beta)} d\beta d\tau \quad (8.6)$$

8.2.1.1 Half-Plane Radial Displacement

Referring to equations (6.64) and (7.19), the half-plane contact radial displacement can be expressed as

$$u_{chr}(r,\theta,t) = -\frac{2\alpha\alpha_e q_0 l_b}{\pi\rho_d c_p\sqrt{\kappa\pi}} \cdot \frac{(1+\upsilon)}{(\beta+\upsilon)} \cdot \int_{\tau=0}^{t} \int_{\beta=-\theta_0\phi(\tau)}^{\theta_0\phi(\tau)} \left\{ \frac{e^{-R'^2_{(t-\tau)}}}{\sqrt{t-\tau}R'_{(t-\tau)}} \times \int_0^{R'_{(t-\tau)}} e^{S^2} dS \right\} \times \cos(\theta-\beta)\sqrt{\theta_0^2\phi(\tau)^2-\beta^2} d\beta d\tau \quad (8.7)$$

The integration involves the term:

$$\begin{aligned} & I_r(r,\theta,t) \\ &= \int_{\tau=0}^{t} \int_{\beta=-\theta_0\phi(\tau)}^{\theta_0\phi(\tau)} \frac{1}{\sqrt{t-\tau}} \left(\frac{e^{-R'^2_{(t-\tau)}}}{R'_{(t-\tau)}} \int_0^{R'_{(t-\tau)}} e^{S^2} dS \right) \\ &\qquad \times \cos(\theta-\beta)\sqrt{\theta_0^2\phi(\tau)^2-\beta^2} d\beta d\tau \quad (8.8) \\ &= \int_{\tau=0}^{t} \int_{\beta=-\theta_0\phi(\tau)}^{\theta_0\phi(\tau)} \frac{1}{\sqrt{t-\tau}} \left(\int_0^{1} e^{(y^2-1)R'^2_{(t-\tau)}} dS \right) \\ &\qquad \times \cos(\theta-\beta)\sqrt{\theta_0^2\phi(\tau)^2-\beta^2} d\beta d\tau \end{aligned}$$

where

$$R'_{(t-\tau)} = \frac{r_{bi}}{2}\sqrt{\frac{1+\eta^2-2\eta\cos(\theta-\beta)}{\kappa(t-\tau)}} \quad (8.9)$$

Changing the variable, $\beta = \theta_0\phi(t)u$, gives

$$
\begin{aligned}
&I_r(r,\theta,t) \\
&= \theta_0^2 \int_{\tau=0}^{t}\int_{u=-1}^{1}\int_{y=0}^{1} \phi(\tau)^2 \frac{e^{\frac{(y^2-1)r_{bi}^2}{4\kappa(t-\tau)}(1+\eta^2-2\eta\cos(\theta-\theta_0\phi(\tau)u))}}{\sqrt{t-\tau}} \\
&\qquad\qquad \times \cos(\theta-\theta_0\phi(\tau)u)\sqrt{1-u^2}\,dy\,du\,d\tau
\end{aligned}
\tag{8.10}
$$

Thus the half-plane contact radial displacement reduces to

$$
u_{chr}(r,\theta,t) = -\frac{2\alpha_e q_b l_b}{\pi\rho_d c_p\sqrt{\kappa\pi}} \cdot \frac{(1+\upsilon)}{(\beta+\upsilon)} I_r(r,\theta,t) \tag{8.11}
$$

8.2.1.2 Remainder Function for Radial Displacement

In a similar manner as for the thermal contact problem given in section 7.3.1.4, the remainder function harmonics of the radial displacement are

$$
\begin{aligned}
&u_{cRrn}(r,\theta,t) \\
&= \alpha q_0 l_b \int_{\tau=0}^{t}\int_{\beta=-\theta_0\phi(\tau)}^{\theta_0\phi(\tau)} \sqrt{\theta_0^2\phi(\tau)^2-\beta^2}\; u_{GRrn}(r,\theta-\beta,t-\tau)e^{in(\theta-\beta)}d\beta d\tau \\
&= \begin{cases} \alpha q_0 l_b \displaystyle\int_{\tau=0}^{t} \frac{1}{2}\pi\theta_0^2\phi(\tau)^2\; u_{GRrn}(r,t-\tau)d\tau & (n=0) \\ \alpha q_0 l_b \displaystyle\int_{\tau=0}^{t} \frac{\pi\theta_0\phi(\tau)}{n} J_1(n\theta_0\phi(\tau))u_{GRrn}(r,t-\tau)d\tau e^{in\theta} & (n\neq 0) \end{cases}
\end{aligned}
\tag{8.12}
$$

where

$$
u_{GRrn}(r,t) = u_{Grn}(r, T_{Gn_{annulus}}(r,t)) - u_{Ghrn}(r,t) \tag{8.13}
$$

with u_{Grn} and u_{Ghrn} given by (5.39) and (6.67), respectively.

8.2.2 Tangential Displacement

The general expression for contact tangential displacement is

$$v_{c\theta}(r,\theta,t) = v_{ch\theta}(r,\theta,t) + \sum_{n=-\infty}^{\infty} v_{cR\theta n}(r,\theta,t) \tag{8.14}$$

where $v_{ch\theta}$ and $v_{cR\theta n}$ are the half-plane and remainder function harmonics of contact angular displacements, respectively. Here

$$v_{ch\theta}(r,\theta,t) = l_b \int_{\tau=0}^{t} \int_{\beta=-\theta_0\phi(\tau)}^{\theta_0\phi(\tau)} q_b(\beta,\tau) v_{Gh\theta}(r,\theta-\beta,t-\tau) d\beta d\tau \tag{8.15}$$

$$v_{cR\theta n}(r,\theta,t) = l_b \int_{\tau=0}^{t} \int_{\beta=-\theta_0\phi(\tau)}^{\theta_0\phi(\tau)} q_b(\beta,\tau) v_{GR\theta n}(r,\theta-\beta,t-\tau) \times e^{in(\theta-\beta)} d\beta d\tau \tag{8.16}$$

8.2.2.1 Half-Plane Tangential Displacement

Referring to equation (6.71), the half-plane tangential displacement for the contact problem is

$$v_{ch\theta}(r,\theta,t) = \frac{\alpha\alpha_e q_0 l_b}{\pi\rho_d c_p\sqrt{\kappa}} \cdot \frac{(1+\upsilon)}{(\beta+\upsilon)} \cdot \frac{r_{bi}}{2\sqrt{\kappa}} \int_{\tau=0}^{t} \int_{\beta=-\theta_0\phi(\tau)}^{\theta_0\phi(\tau)} \left\{ \frac{1-e^{-R'^2_{(t-\tau)}}}{(t-\tau)R'^2_{(t-\tau)}} \times \sin(\theta-\beta)\sqrt{\theta_0^2\phi(\tau)^2-\beta^2} \right\} d\beta d\tau \tag{8.17}$$

The integration involves the term:

$$
\begin{aligned}
& I_\theta(r,\theta,t) \\
&= \int_{\tau=0}^{t}\int_{\beta=-\theta_0\phi(\tau)}^{\theta_0\phi(\tau)} \frac{1}{t-\tau}\left(\frac{1-e^{-R'^2_{(t-\tau)}}}{R'^2_{(t-\tau)}}\right) \\
&\qquad\qquad \times \sin(\theta-\beta)\sqrt{\theta_0^2\phi(\tau)-\beta^2}\,d\beta d\tau \\
&= \int_{\tau=0}^{t}\int_{\beta=-\theta_0\phi(\tau)}^{\theta_0\phi(\tau)} \frac{1}{t-\tau}\left(\int_0^1 e^{-\frac{yr_i^2}{4\kappa(t-\tau)}(1+\eta^2-2\eta\cos(\theta-\beta)}dy\right) \\
&\qquad\qquad \times \sin(\theta-\beta)\sqrt{\theta_0^2\phi(\tau)-\beta^2}\,d\beta d\tau \\
&= \theta_0^2\int_{\tau=0}^{t}\int_{u=-1}^{1}\int_{y=0}^{1}\phi(\tau)^2\frac{e^{-\frac{yR_i^2}{4\kappa(t-\tau)}(1+\eta^2-2\eta\cos(\theta-\theta_0\phi(\tau)u))}}{t-\tau} \\
&\qquad\qquad \times \sin(\theta-\theta_0\phi(\tau)u)\sqrt{1-u^2}\,dy du d\tau
\end{aligned}
\tag{8.18}
$$

Thus it yields

$$
v_{ch\theta}(r,\theta,t) = \frac{r_{bi}\alpha_e q_b l_b}{2\pi\rho_d c_p \kappa}\cdot\frac{(1+\upsilon)}{(\beta+\upsilon)} I_\theta(r,\theta,t) \tag{8.19}
$$

8.2.2.2 Remainder Function for Tangential Displacement

The expression for the tangential displacement remainder function is derived using a similar approach as for the radial displacement remainder function. It is given by,

$$
\begin{aligned}
& v_{cR\theta}(r,\theta,t) \\
&= \begin{cases}
\alpha q_0 l_b \displaystyle\int_{\tau=0}^{t} \frac{1}{2}\pi\theta_0^2\phi(\tau)^2 v_{GR\theta n}(r,t-\tau)d\tau & (n=0) \\
\alpha q_0 l_b \displaystyle\int_{\tau=0}^{t} \frac{\pi\theta_0\phi(\tau)}{n} J_1(n\theta_0\phi(\tau)) v_{GR\theta n}(r,t-\tau)d\tau e^{in\theta} & (n\neq 0)
\end{cases}
\end{aligned}
\tag{8.20}
$$

where

$$
v_{GR\theta n}(r,t) = v_{G\theta n}(r, T_{Gn_{annulus}}(r,t)) - v_{Gh\theta n}(r,t) \tag{8.21}
$$

with $v_{G\theta n}$ and $v_{Gh\theta n}$ given by (5.39) and (6.68), respectively.

8.3 Case Study for Thermoelastic Contact Problem

The elastic properties of the bearing, input parameters and operating conditions used for the thermoelastic analysis are given in Tables 2.1, 3.1 and 7.1.

8.3.1 Thermal Deformation of Rigidly Mounted Bearing

For a rigidly mounted bearing problem, the "initial" conditions (see section 5.3.1.1) of u_{Grn} and $v_{G\theta n}$ in equations (8.13) and (8.21) need to be used with the fixed bush boundary condition $\mathbf{c}_n^{\text{fix}}$ given by equation (5.61).

Figure 8.1 shows the time variation of the maximum radial displacements at the inner surface of the bearing subjected when frictional heating is induced at various level of maximum normal contact force at $(r_{bi},0)$. The displacements are seen to have profiles that follow the transient temperatures (see figure 7.5). For the operating conditions shown, the peak displacement is close to 2.5μm ($\approx$ 0.5% of rotor and auxiliary bearing clearance, c_r) when the maximum contact force is 50kN. The time variation of the maximum surface deformations of the bearing corresponding to different operating conditions are shown in figure 8.2. Note that the operating conditions P11, P13 and P15 would have caused localised melting during the contact (see figure 7.15). Figure 8.3 shows the inner surface thermal distortion at 10ms after bearing is subjected to f_{cmax} =10kN for t_p = 1ms at a

rotor speed $\Omega = 1000$rad/s. The radial displacement at $t = 10$ms and $t = 1$s are shown in figure 8.4. Positive displacement is noted in figure 8.4 at short time period due to compressive radial stress in the bearing (see figure 8.8).

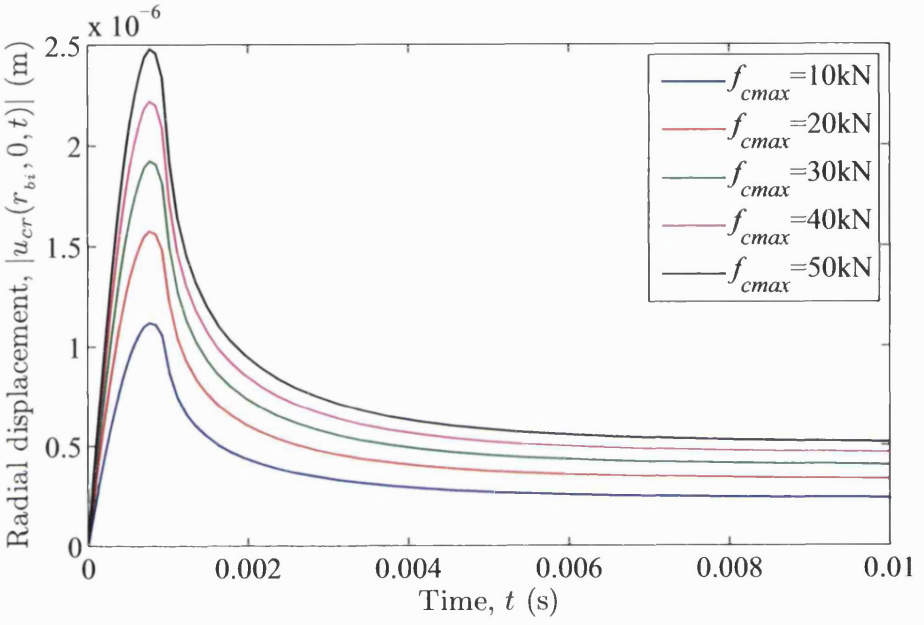

Figure 8.1: Time variation of maximum surface thermal deformations corresponding to different contact forces, f_{cmax} ($\mu = 0.1$, $\Omega = 1000$rad/s and $t_p = 1$ms).

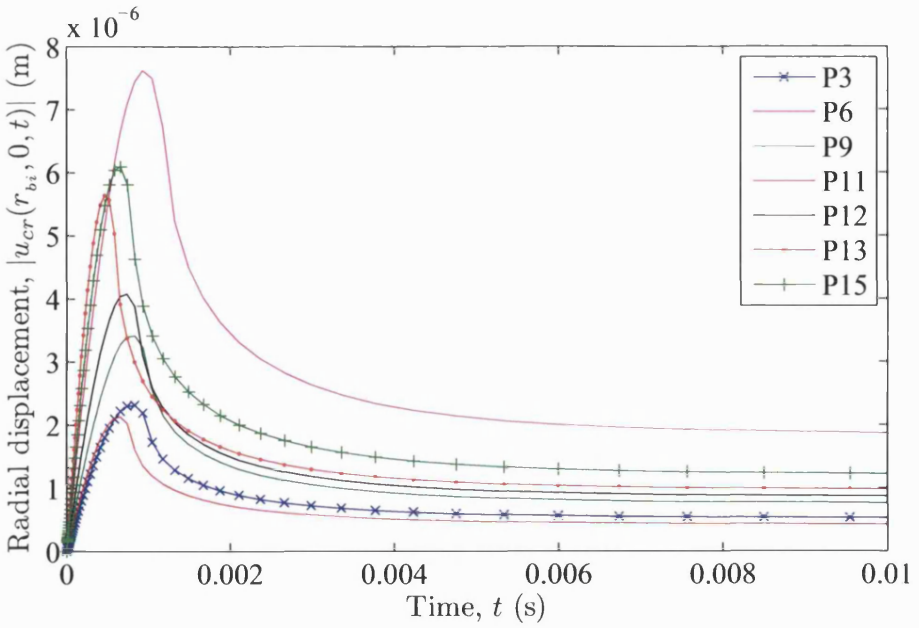

Figure 8.2: Time variation of maximum surface thermal deformations corresponding to different operating conditions, P3, P6, P9, P11, P12, P13 and P15, respectively.

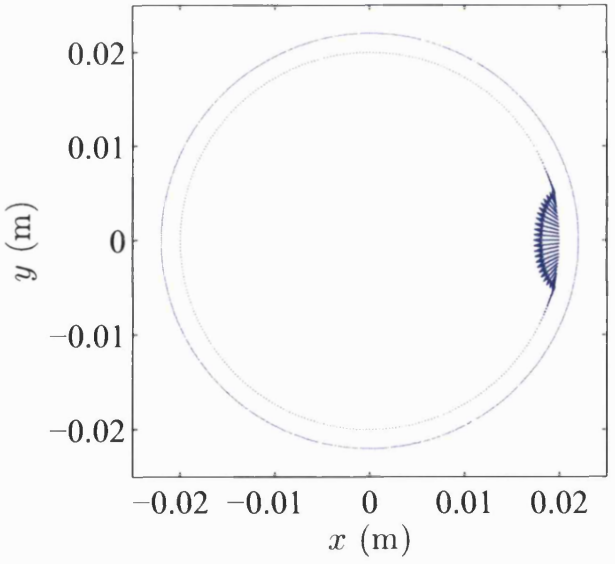

Figure 8.3: Inner surface distortion subjected to maximum contact force f_{cmax} = 10kN (t=1ms, Ω=1000rad/s and $\mu = 0.1$ at t = 10ms).

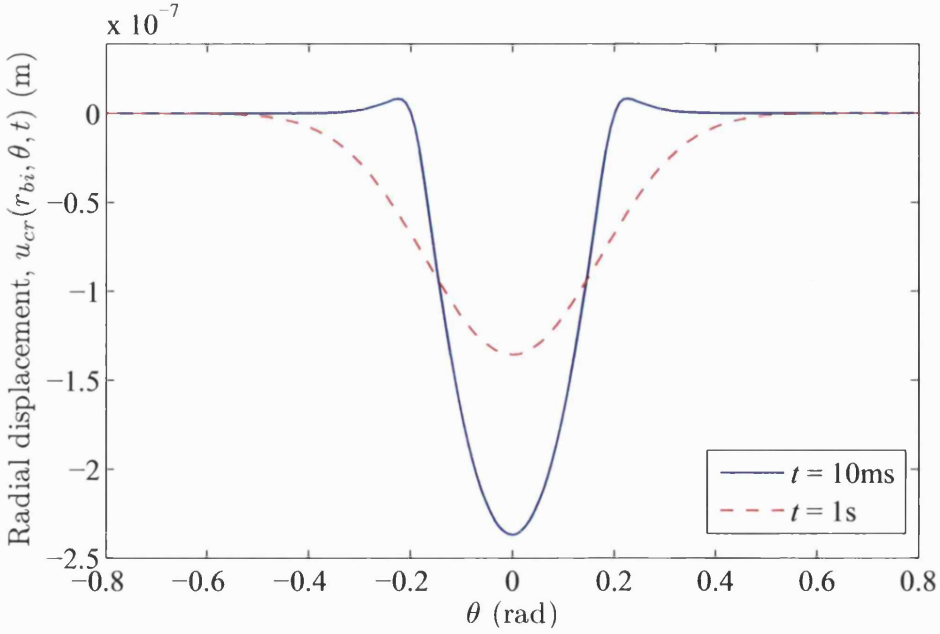

Figure 8.4: Inner surface radial displacement subjected to maximum contact force f_{cmax} =10kN at t = 10ms, 1s (t_p =1ms, Ω =1000rad/s and μ =0.1).

8.3.2 Resiliently Mounted Bearing

A resiliently mounted bearing is considered to be subjected to a similar heat flux distribution, q_b. In determining the u_{Grn} and $v_{G\theta n}$ of the remainder function of equations (8.13) and (8.21), the resiliently mounted "initial" condition, $\mathbf{c}_n^{\text{res}}$, given by equation (5.73) needs to be used. The two governing parameters, χ_r and χ_θ are assuming to be similar as given in section 5.5.2.2, where χ_r = $3.45 \times 10^{13}\text{N/m}^3$ and $\chi_\theta = 5 \times 10^{11}\text{N/m}^3$.

Figure 8.5 shows the time variation of maximum inner and outer boundaries deformation corresponding to various maximum contact forces. It is seen that the outer boundary expands radially inwards initially (figure 8.6). For longer time, the bearing would eventually heat up and starts to expand both radially

inwards and outwards, which can be seen in figure 8.6. The comparison of the rigidly and resiliently mounted problems shows that the latter problem has larger surface distortion.

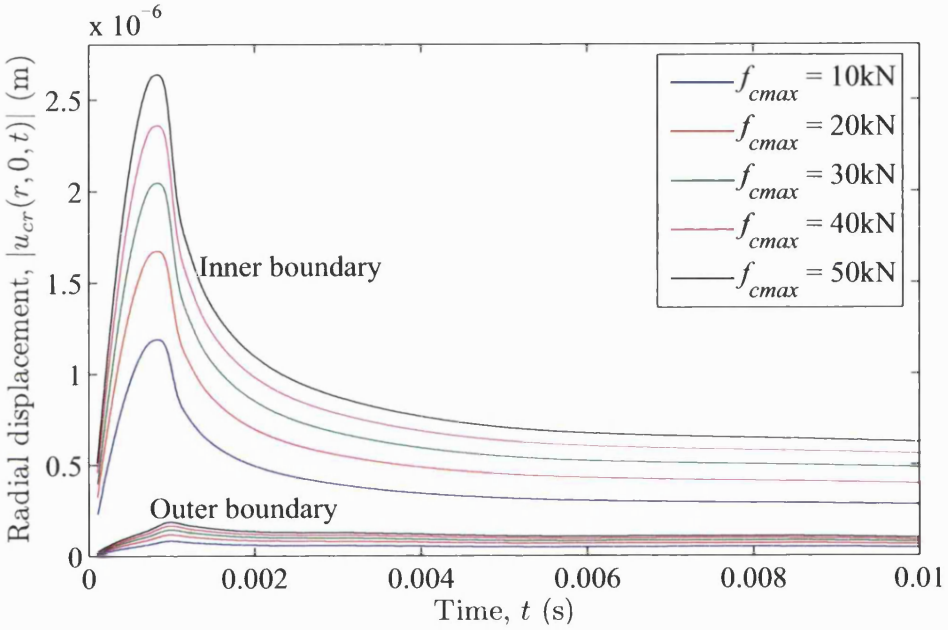

Figure 8.5: Time variation of maximum inner and outer boundaries deformations corresponding to different maximum contact force, f_{cmax} ($\mu = 0.1$, $\Omega = 1000$rad/s and $t_p = 1$ms).

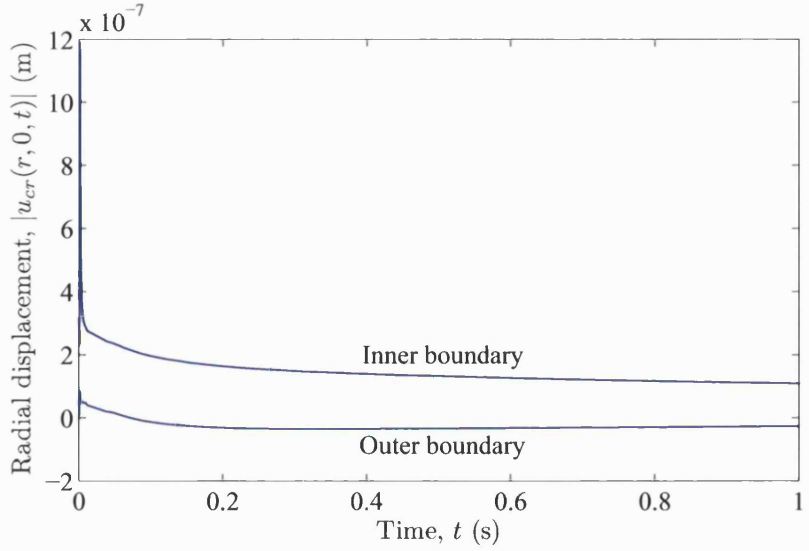

Figure 8.6: Time variation of maximum thermal deformations at inner and outer boundary corresponding to maximum contact force, $f_{cmax} = 10\text{kN}$ ($\mu = 0.1$, $\Omega = 1000\text{rad/s}$ and $t_p = 1\text{ms}$).

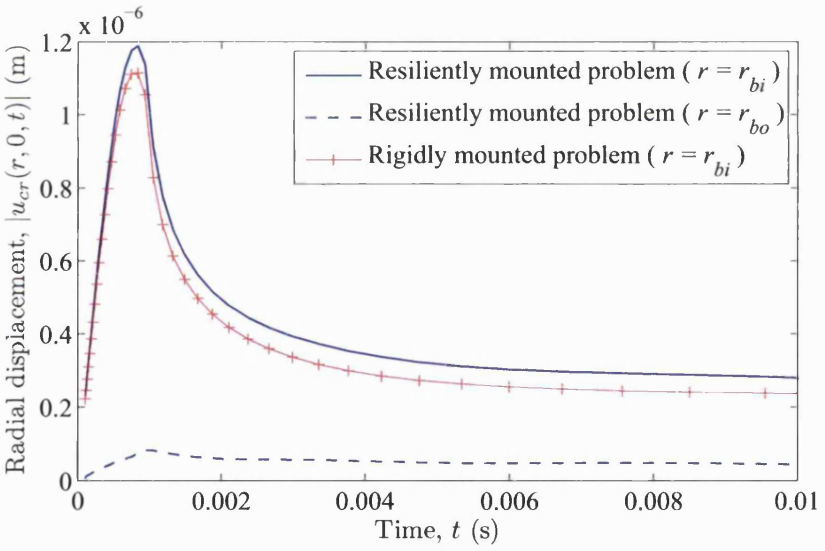

Figure 8.7: Comparison of surface displacement corresponding to different boundary conditions. ($f_{cmax} = 10\text{kN}$, $\mu = 0.1$, $\Omega = 1000\text{rad/s}$ and $t_p = 1\text{ms}$).

8.4 Thermal Stresses

The method proposed in this section uses the converged results from the thermal contact analysis to determine the temperature and temperature gradient, which are required for the thermoelastic state-space solution (5.62). Firstly, the temperature is converted into a Fourier series expansion using

$$T_{cn}(r,t) = \frac{1}{2\pi}\int_{-\pi}^{\pi} T_c(r,\theta,t)e^{-in\theta}d\theta$$

Then, the temperature gradient $\partial T_{cn}(r)/\partial r$ is evaluated using the finite difference method (see section 6.4.3.2). Substituting T_{cn} and $\partial T_{cn}(r)/\partial r$ into the thermoelastic state-space solution as an input element in the input vector (equation (5.36)) enables results to be obtained.

The accuracy of the stress results are highly dependent on the meshing of the thermal model, particularly for short timescale analysis. A finer mesh is required near the subsurface region where the heat flux is applied. However, finer meshing is always associated with an increase in computational time. On the other hand, coarse meshing introduces numerical errors when evaluating the temperature gradients. The advantage of this approach is that it allows convenient analysis of problems corresponding to different stress boundary conditions, but subjected to the same temperature distribution. This has the advantages over the curve fitting technique that is required to store the remainder function as an array for a specific stress boundary condition.

8.4.1 Rigidly Mounted Bearing

Figure 8.8 shows the radial stress distribution in the stainless steel bearing bush at 10ms after being subjected a maximum contact force of 10kN with duration 1ms. The stress free inner boundary is evident while the outer boundary is under tensile loading. Figure 8.9 shows the shear stress field in the body subjected to the same input conditions at $t = 10$ms. High Von Mises stresses are noted at the subsurface region and close to the location where the heat source is applied (see figure 8.10). These are governed mainly by the hoop stress in the body as shown in figure 8.11. When the heat diffuses through the body, it changes the stress distribution. Figure 8.12 shows the radial stress distribution of the bearing at $t = 1$s when subjected to similar operating conditions. It is seen that the radial stress distribution at the outer boundary changing from being tensile to compressive. On the other hand, high Von Mises stresses are now found to be closer to the outer boundary (figure 8.13).

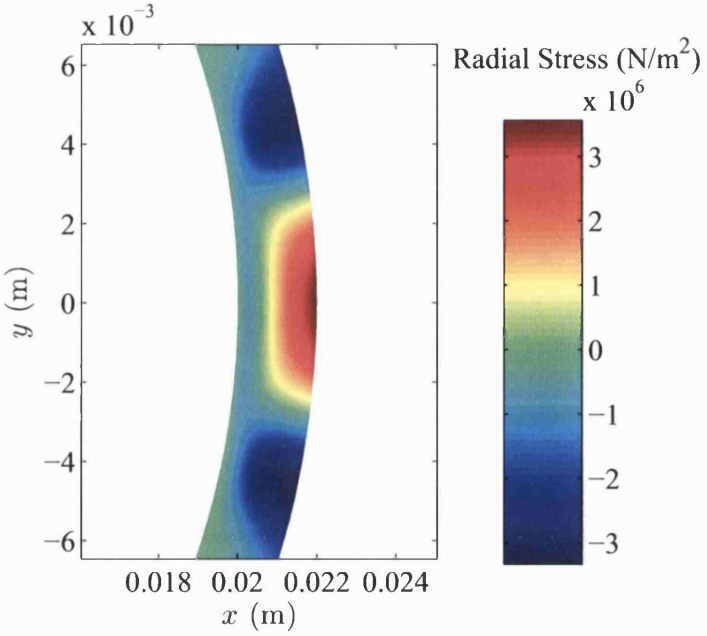

Figure 8.8: Radial stress field in a rigidly mounted steel bearing at $t = 10$ms ($\Omega = 1000$rad/s, $f_{cmax} = 10$kN, $\mu = 0.1$ and $t_p = 1$ms).

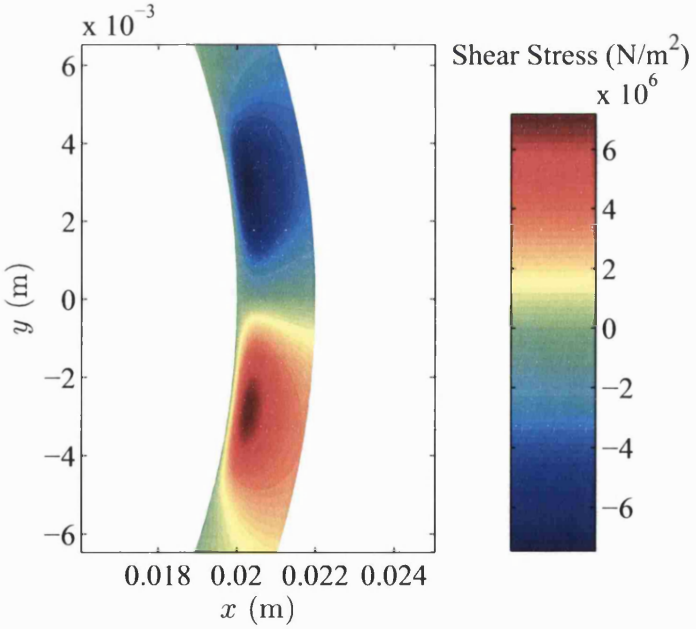

Figure 8.9: Shear stress field in a rigidly mounted steel bearing at $t = 10$ms ($\Omega = 1000$rad/s, $f_{cmax} = 10$kN, $\mu = 0.1$ and $t_p = 1$ms).

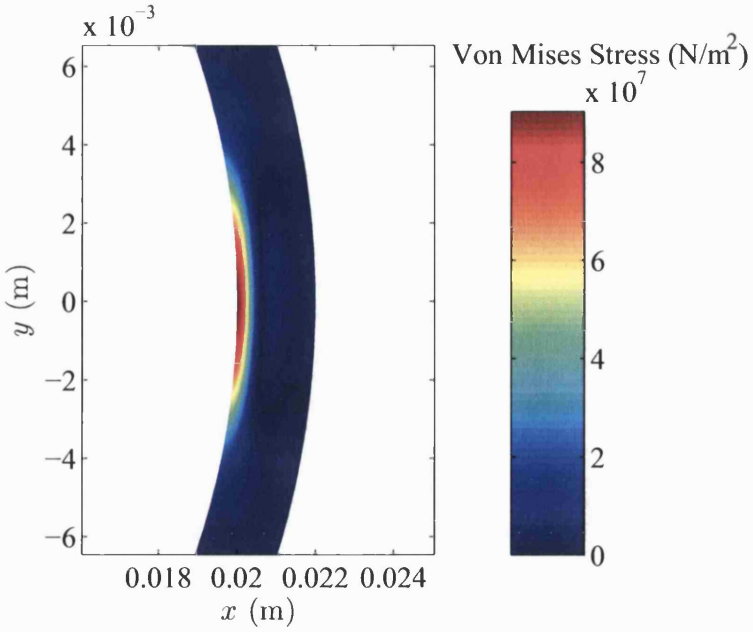

Figure 8.10: Von Mises stress field in a rigidly mounted steel bearing at $t = 10$ms ($\Omega = 1000$rad/s, $f_{cmax} = 10$kN, $\mu = 0.1$ and $t_p = 1$ms).

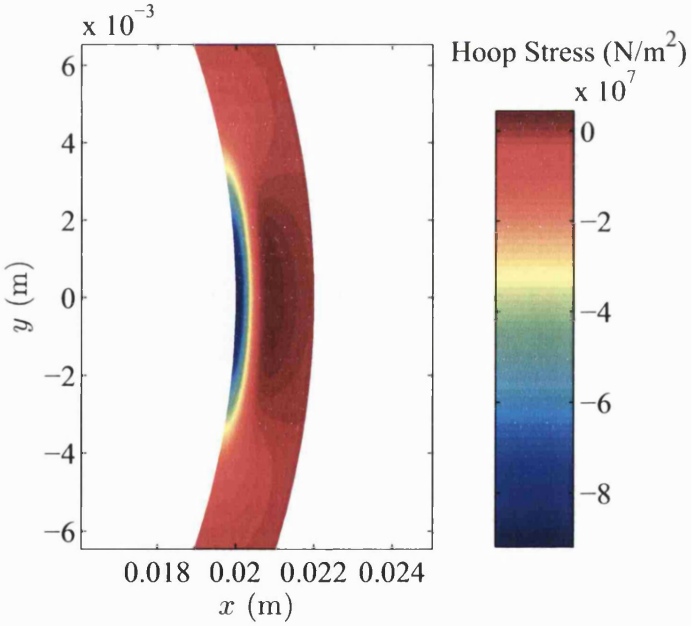

Figure 8.11: Hoop stress field in a rigidly mounted steel bearing at $t = 10$ms ($\Omega = 1000$rad/s, $f_{cmax} = 10$kN, $\mu = 0.1$ and $t_p = 1$ms).

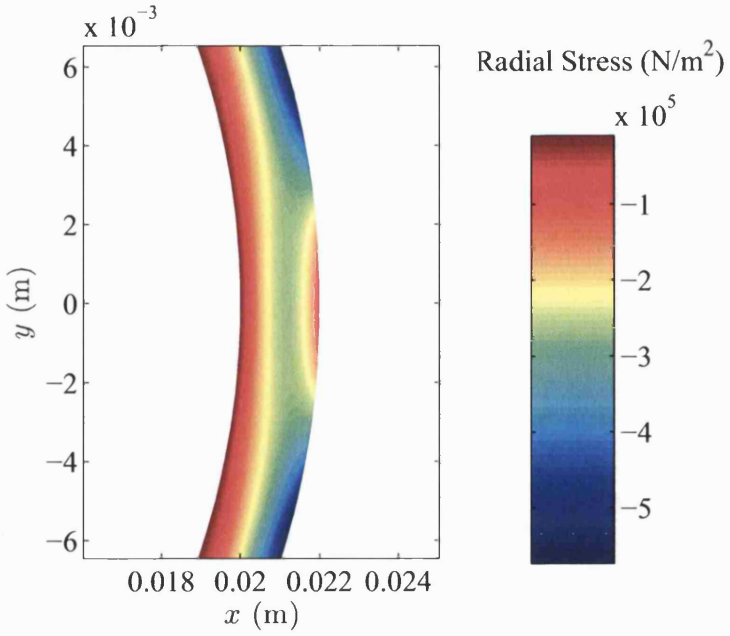

Figure 8.12: Radial stress field in a rigidly mounted steel bearing at 1s (Ω = 1000rad/s, f_{cmax} = 10kN, $\mu = 0.1$ and t_p = 1ms).

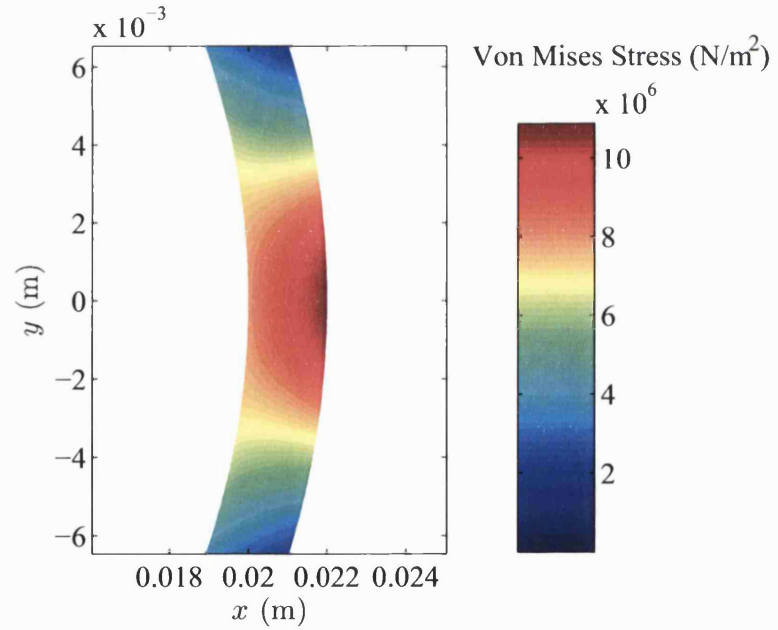

Figure 8.13: Von Mises stress field in a rigidly mounted steel bearing at 1s (Ω = 1000rad/s, f_{cmax} = 10kN, $\mu = 0.1$ and t_p = 1ms).

8.4.2 Resiliently Mounted Bearing

Figure 8.14 shows the radial stress in a resiliently mounted steel bearing 10ms after being subjected to inner surface heating. It is seen that the outer boundary is under tensile loading, but the stress level is lower than for the rigidly mounted problem. The shear stress distribution of the bearing subjected to similar operating conditions is shown in figure 8.15. Meanwhile, the Von Mises stress (figure 8.16), which is dominated by hoop stress (figure 8.17), is seen to be localised at the subsurface region close to the location where the heat source applied. For longer times, the bearing would eventually experience radial compressive loading since the bearing would expand radially outwards (figure 8.18). High Von Mises stress (figure 8.19) is seen to be located in two different regions for the resiliently mounted problem at longer time in contrast to the rigidly mounted problem. In general, the stresses of the resiliently mounted bearing were found to be lower than for the rigidly mounted bearing.

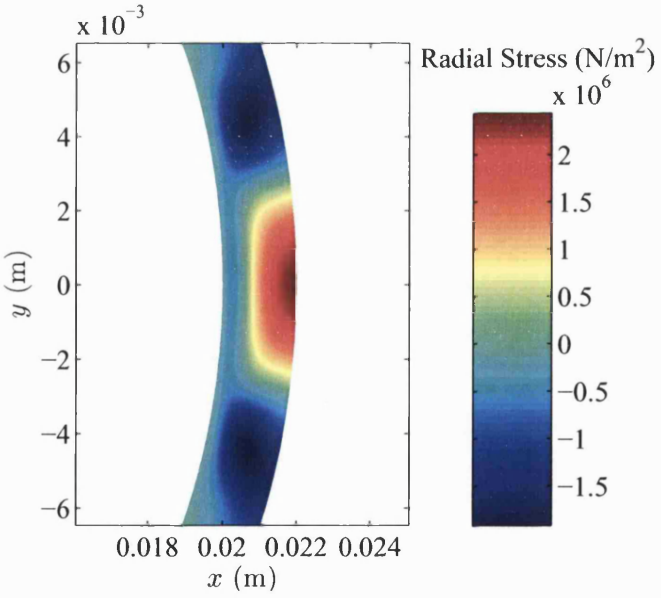

Figure 8.14: Radial stress field in a resiliently mounted steel bearing at 10ms ($\Omega = 1000$rad/s, $f_{cmax} = 10$kN, $\mu = 0.1$ and $t_p = 1$ms).

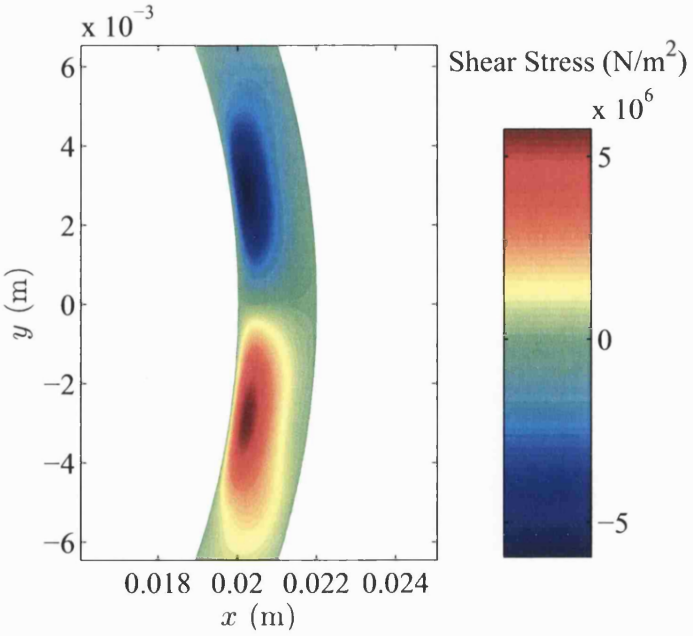

Figure 8.15: Shear stress field in a resiliently mounted steel bearing at 10ms ($\Omega = 1000$rad/s, $f_{cmax} = 10$kN, $\mu = 0.1$ and $t_p = 1$ms).

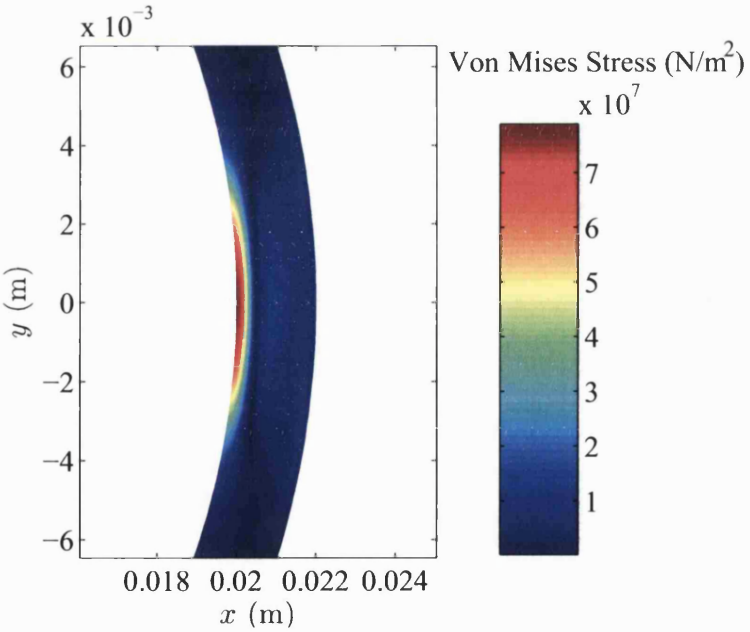

Figure 8.16: Von Mises stress field in a resiliently mounted steel bearing at 10ms ($\Omega = 1000$rad/s, $f_{cmax} = 10$kN, $\mu = 0.1$ and $t_p = 1$ms).

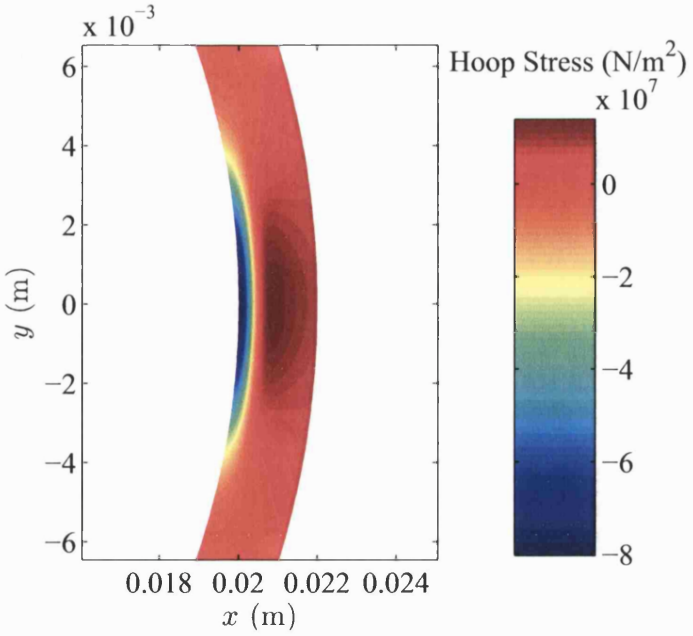

Figure 8.17: Hoop stress field in a resiliently mounted steel bearing at 10ms ($\Omega = 1000$rad/s, $f_{cmax} = 10$kN, $\mu = 0.1$ and $t_p = 1$ms).

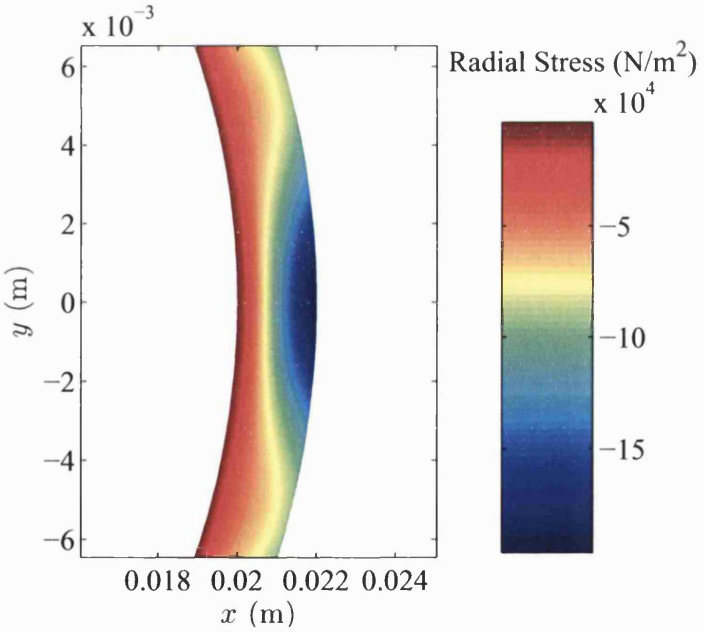

Figure 8.18: Radial stress field in a resiliently mounted steel bearing at 1s ($\Omega = 1000$rad/s, $f_{cmax} = 10$kN, $\mu = 0.1$ and $t_p = 1$ms).

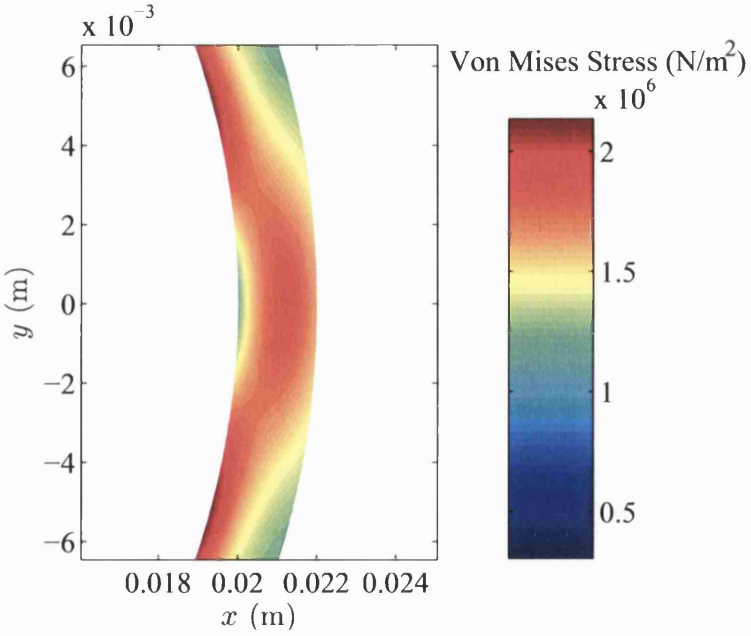

Figure 8.19: Von Mises stress field in a resiliently mounted steel bearing at 1s ($\Omega = 1000$rad/s, $f_{cmax} = 10$kN, $\mu = 0.1$ and $t_p = 1$ms).

8.5 Assessment of Surface Growth Due to Repeated Contact and Forward Rubbing

It has been shown in chapter 2 that the dynamic response of a rotor making contact with an auxiliary bearing may involve bounce and rub type motions. There is also experimental evidence that the same point on an auxiliary bearing may experience repeated and persistent contact [99]. The fact that points on the inner surface of the auxiliary bearing may experience repeated contact means that significant thermoelastic deformation may occur.

8.5.1 Repeated Contact at the Same Point

Consider a rigidly mounted auxiliary bearing experiencing repeated contact from a rotor at a frequency that in synchronous with the rotational speed Ω. Thus a contact event will occur with a time spacing of $t_s = 2\pi/\Omega$. For the example cases considered in chapter 2, the resulting radial displacement at $\theta = 0$ arising from a single event are shown in figure 8.1. Typically, the radial displacement rises to a maximum during the contact period, then decays after loss of contact. For the first contact the initial radial displacement at $t = 0$ is $u_{cr}(r_{bi}, 0, 0) = 0$. However, this becomes $u_{cr}(r_{bi,}, 0, (j-1)t_s)$ at the start of the nth contact event. Thus the thermoelastic growth at the contact point will depend on the number of contact events together with the contact force and period. Taking the distortion at the instance when the heat is removed, the deformation is $u_{cr}(r_{bi}, 0, t_p)$. The total deformation at $(r_{bi}, 0)$ after n contacts is

$$\hat{u}_{cr}^{n} = \sum_{j=1}^{n} u_{cr}(r_{bi}, 0, (j-1)t_s + t_p) \tag{8.22}$$

For the example considered, the nominal radial clearance of the auxiliary bearing is $c_r = 5 \times 10^{-4}$m. Table 8.1 shows the number of contacts that may be sustained until the thermoelastic distortion exceeds 50% of the available clearance for a range of operating parameters. These results are based on the period of contact $t_p = 1$ms. It is seen that fewer contacts are required for higher synchronous speed and contact force to achieve 50% of c_r. This condition would be reached in the worst case of Table 8.1 after $171t_s = 0.34$s.

Table 8.1: Number of contacts that may sustained until the thermoelastic distortion exceeds 50% of c_r.

f_{cmax} (kN)	Ω (rad/s)	Number of contacts, n
10	1000	2423 (approximation)
20	1000	1107 (approximation)
30	1000	805
40	1000	662
50	1000	571
10	2000	945
20	2000	483
30	2000	362
40	2000	302
50	2000	264
10	3000	510
20	3000	296
30	3000	229
40	3000	194
50	3000	172

8.5.2 Thermoelastic Growth Arising from Synchronous Forward Rub

When a synchronous forward rub develops, each point on the inner surface of the auxiliary bearing experiences a heat input. Consider a case in which a forward rub is initiated at $\theta = 0$. Every cycle of the synchronous rub through $\theta = 0$, the surface deformation will increase. To assess the scale of the problem, a simple rubbing model is developed. For a rub condition,

$$\phi(t) = 1 \tag{8.23}$$

In addition, the heat source is moving at a synchronous speed Ω with moving angular position of $\theta_m = \Omega t$. In this section, investigations of both thermoelastic

and thermal responses of the inner surface subjected to forward rubbing are undertaken.

8.5.2.1 Statement of Thermoelasticity

The radial contact displacement components for the rubbing problem are

$$u_{chr}(r,\theta,t) = l_b \int_{\tau=0}^{t} \int_{\beta=-\theta_0+\theta_m}^{\theta_0+\theta_m} q_b(\beta-\theta_m,\tau) u_{Ghr}(r,\theta-\beta,t-\tau) d\beta d\tau \quad (8.24)$$

$$u_{cRrn}(r,\theta,t) = l_b \int_{\tau=0}^{t} \int_{\beta=-\theta_0+\theta_m}^{\theta_0+\theta_m} q_b(\beta-\theta_m,\tau) u_{GRrn}(r,\theta-\beta,t-\tau) \times e^{in(\theta-\beta)} d\beta d\tau \quad (8.25)$$

The I_r from equation (8.11) becomes

$$I_r(r,\theta,t) = \theta_0^2 \int_{\tau=0}^{t} \int_{u=-1}^{1} \int_{y=0}^{1} \frac{e^{\frac{(y^2-1)r_{bi}^2}{4\kappa(t-\tau)}(1+\eta^2-2\eta\cos(\theta-\theta_0 u)-\theta_m)}}{\sqrt{t-\tau}} \times \cos(\theta-\theta_0 u)\sqrt{1-u^2} dy du d\tau \quad (8.26)$$

The remainder function harmonics of radial displacement are

$$u_{cRrn}(r,\theta,t) = \begin{cases} l_b \alpha q_0 \int_{\tau=0}^{t} \frac{1}{2}\pi\theta_0^2 u_{GRrn}(r,t-\tau) d\tau & (n=0) \\ l_b \alpha q_0 \int_{\tau=0}^{t} \frac{\pi\theta_0\phi(\tau)}{n} J_1(n\theta_0) u_{GRrn}(r,t-\tau) d\tau e^{in(\theta-\theta_m)} & (n\neq 0) \end{cases} \quad (8.27)$$

8.5.2.2 Statement of Temperature

The general expression of the contact temperature for the rubbing problem becomes (see equation (7.21))

$$T_{ch}(r,\theta,t) = l_b \int_{\tau=0}^{t} \int_{\beta=-\theta_0+\theta_m}^{\theta_0+\theta_m} q_b(\beta-\theta_m,\tau) \times T_{Gh}(r,\theta-\beta,t-\tau)\,d\beta\,d\tau \tag{8.28}$$

$$\hat{T}_{ch}(r,\theta,t) = l_b \int_{\tau=0}^{t} \int_{\beta=-\theta_0+\theta_m}^{\theta_0+\theta_m} q_b(\beta-\theta_m,\tau) \times \hat{T}_{Gh}(r,\theta-\beta,t-\tau)\,d\beta\,d\tau \tag{8.29}$$

$$T_{cRn_{annulus}}(r,\theta,t) = l_b \int_{\tau=0}^{t} \int_{\beta=-\theta_0+\theta_m}^{\theta_0+\theta_m} q_b(\beta-\theta_m,\tau) \times T_{GRn_{annulus}}(r,t-\tau)e^{in(\theta-\beta)}\,d\beta\,d\tau \tag{8.30}$$

The half-plane temperature is

$$T_{ch}(r,\theta,t) = \frac{\alpha l_b q_0 \theta_0^2}{2\pi k_b} \int_{\tau=0}^{t} \int_{u=-1}^{1} \frac{1}{(t-\tau)} e^{-\frac{r_{bi}^2\left(1+\eta^2-2\eta\cos(\theta-\theta_0 u-\theta_m)\right)}{4\kappa_b(t-\tau)}} \times \sqrt{1-u^2}\,du\,d\tau \tag{8.31}$$

The second term of half-plane temperature is

$$\hat{T}_{ch}(r,\theta,t) = -\frac{\alpha l_b q_0 \theta_0^2}{2\pi k_b} \int_{\tau=0}^{t} \int_{u=-1}^{1} \int_{v=0}^{t-\tau} \frac{g(v)}{(t-\tau-v)} e^{-\frac{r_{bi}^2\left(1+\eta^2-2\eta\cos(\theta-\theta_0 u-\theta_m)\right)}{4\kappa_b(t-\tau-v)}} \times \sqrt{1-u^2}\,dv\,du\,d\tau \tag{8.32}$$

and the remainder function harmonics are

$$T_{cRn}(r,\theta,t) = \begin{cases} l_b \alpha q_0 \int_{\tau=0}^{t} \frac{1}{2}\pi\theta_0^2 T_{GRn}(r, t-\tau)d\tau & (n=0) \\ l_b \alpha q_0 \int_{\tau=0}^{t} \frac{\pi\theta_0}{n} J_1(n\theta_0) T_{GRn}(r, t-\tau)d\tau e^{in(\theta-\theta_m)} & (n \neq 0) \end{cases} \quad (8.33)$$

8.5.2.3 Case Study for Forward Rubbing Problem

Consider a rotor to be undergoing a forward synchronous rub with steady contact force around 15kN and a speed $\Omega = 1000$rad/s (see figure 2.7). Assuming the heat input starts from $\theta = 0$ at $t = 0$ and moves in $+\theta$-direction. The contact arc induced by the contact force is $2\theta_0$ and the contact period over the point $\theta = 0$ is $2\theta_0/\Omega$. The synchronous period is $2\pi/\Omega$, and each repeated cycle of heat input may be considered by a superposition argument. Figure 8.20 shows the time variation of maximum surface temperature and radial displacement when the bearing is subjected to forward rub contact. It is noted that the surface displacement increases steadily. In addition, it is also to be deduced that the bearing would melt before the surface displacement reaches 50% of c_r. This implies that temperature would be the dominant factor for bearing failure. Based on the growth rate of the temperature ($\approx$ 354K/s), the bearing would begin to melt after 3s.

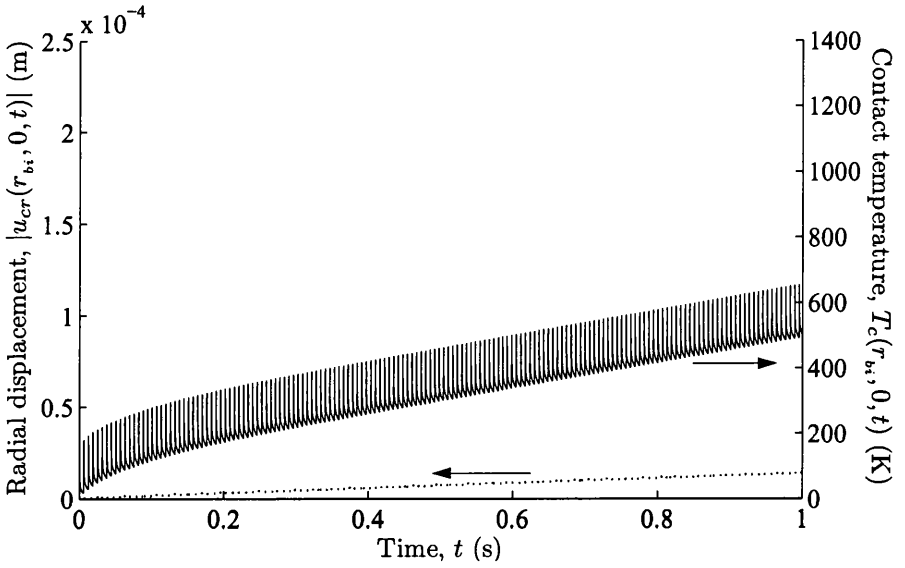

Figure 8.20: Time variation of surface temperature and maximum surface radial displacement when subjected to synchronous forward rub ($f_{cmax} = 15$kN, $\mu = 0.1$ and $\Omega = 1000$rad/s).

8.5.3 The Growth of a Small Surface Imperfection

Consider the case of an initial imperfection that is to be equivalent to that caused by a Hertzian stress distribution of

$$p(\theta) = p_0\sqrt{\theta_d^2 - \theta} \qquad -\theta_d \leq \theta \leq \theta_d \tag{8.34}$$

where θ_d is the half-width angle of the imperfection. Thus the equivalent surface distortion at $O' = (r_{bi}, 0)$ is [17]

$$u_{r0} \approx -\frac{r_{bi}^2\theta_d^2}{2R^*} \tag{8.35}$$

Figure 8.21 shows the expected time variation of the contact force $f_{cmax}\phi(t)^2$ at O'. The compressive loading is applied at the edge $\theta = -\theta_d$ initially. As the rotor sweeps along the surface, the bump is compressed flat and the heat

dissipation is similar to the rub contact with $\phi(t) = 1$. The rotor then passes completely over the imperfection and the contact force decays to zero until the next contact event. Assuming instantaneous strain recovery ensues upon removal of compressive loading, the surface distortion would be $u_{r0} + u_{cr}(r_{bi}, 0, t_s)$ at the instant prior the 2nd contact event. To assess the scale of the problem, a simple model is used to investigate the growth rate of the imperfection.

The term θ_0 in equations (8.4-8.13) is now replaced by θ_d for this particular problem. However, the contact period over the point O′ becomes $2(\theta_d + \theta_0)/\Omega$, where θ_0 is the half-width angle arc corresponding to the contact force $f_{cmax} =$ 15kN. Figure 8.22 shows the growth rate of the imperfection $\partial u_{cr}/\partial t|_{u_{r0}} = u_{cr}(r_{bi}, 0, t_s)/t_s$ corresponding different half-width angle of the bump θ_d/θ_0 with different synchronous speeds. It is seen that the larger the width θ_d gives rise to higher surface deformation due to longer heat input periods. Moreover, higher synchronous speed Ω leads to higher imperfection growth rate. Although not included in the results, the constant rub deformation of the type given in previous section may also be superimposed.

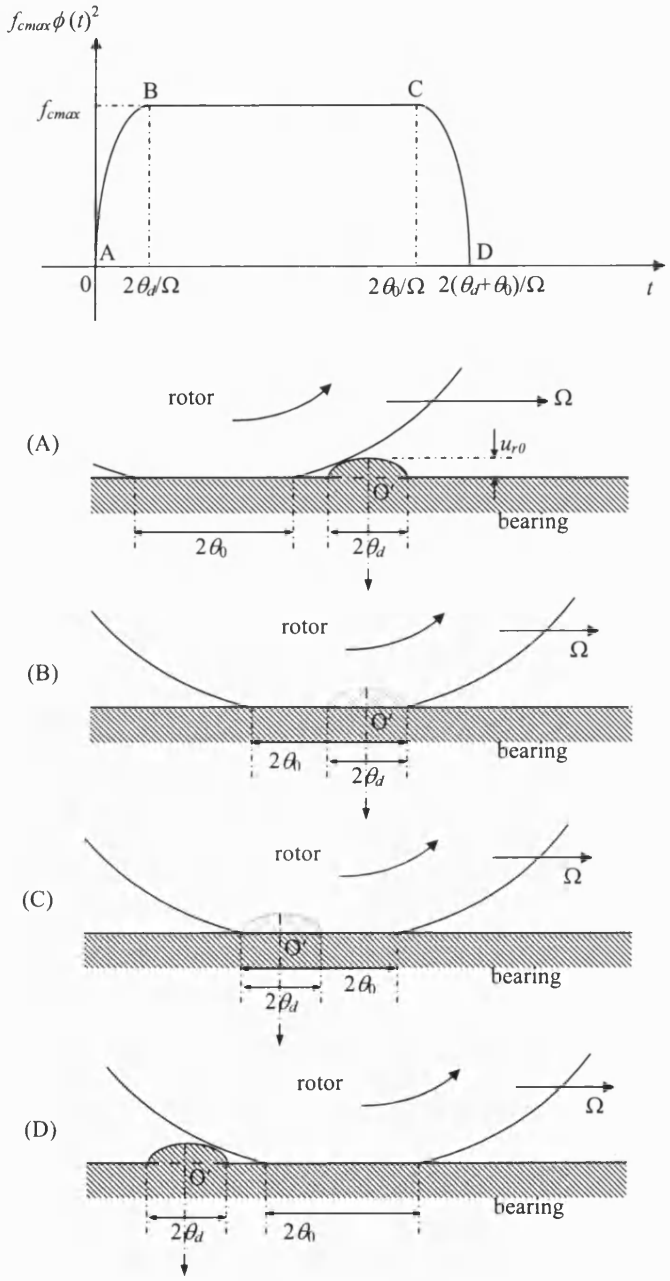

Figure 8.21: Time variation of contact force experienced at $O' = (r_{bi}, 0)$ when a small imperfection is swept over by a rubbing rotor. (A) Compressive load is applied from the edge $\theta = -\theta_d$ when $t = 0$. (B) Rotor fully compresses the imperfection at $2\theta_d/\Omega$, and undergoes rubbing with $\phi(t) = 1$. (C) Compressive load is removed from the edge $\theta = -\theta_d$ at $2\theta_0/\Omega$. (D) Loading is totally removed and instantaneous recovery is assumed.

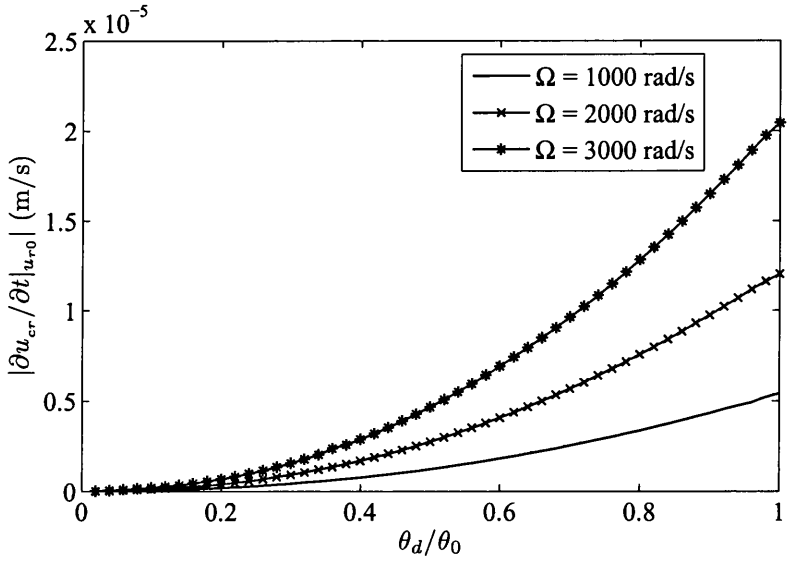

Figure 8.22: Surface growth rate of the imperfection at O′ corresponding to different sizes θ_d.

8.6 Closure

An investigation has been undertaken to study the thermoelastic response of a bearing subjected to inner surface heating due to rotor/bearing contact. Two types of boundary problem were considered, namely, for a rigidly mounted bearing and a resiliently mounted bearing. The approach to determine the stresses in the bearing used the dynamic contact temperature distribution evaluated in Chapter 7 together with the state-space displacement solution from Chapter 5. An assessment was also carried out to investigate the thermoelastic growth induced by repeated rotor contact and synchronous rubbing. It was noted that the surface deformation grows and the rate is dependent on the synchronous speed and the contact force. In addition, a comparison was made between the surface temperature rise and the surface deformation. It was found that the rise of the surface temperature may be more significant than the surface deformation. A simple model was the used to investigate the growth rate of a small imperfection

when subjected to rubbing contact.

Chapter 9

Conclusions and Future Research

Research has been undertaken into the development and application of Green's functions for thermal and thermoelastic contact problems between a rotor and auxiliary bearing in an AMB system. The rotor dynamic interaction of the auxiliary bearing during contact induces localised heating. The transient thermal Green's functions for hole and annular problems were developed. The Green's functions, which were expressed in direct Fourier series form, are poorly convergent as $t \rightarrow 0$. This meant that they are not suitable for accurate representation of short timescale localised contact problems. A remainder function concept was therefore introduced to improve the the convergence of the thermal Green's functions by utilising the half-plane solution in Fourier series form. The remainder function yields the correct boundary conditions that are not satisfied by the half-plane solution.

The thermoelastic responses associated with temperature rise in an elastic annulus were investigated. A general solution for the thermoelastic annular problem was developed using a state-space technique. Solutions were developed corresponding to rigidly mounted and resiliently mounted outer boundary problems. A state-space solution method was used with the Green's function temper-

ature distribution and found to be poorly convergent as $t \rightarrow 0$ because it inherits the singular nature of the thermal Green's function. A thermoelastic remainder function was used to improve the convergence.

The Green's function solutions were applied to several contact problems. The heat source was developed based on Hertzian and non-Hertzian contact together with Coulomb friction. Three types of heat source were considered, namely, for a spinning steel rotor interacting with

(a) a fixed steel bush

(b) a free to rotate steel inner race

(c) a fixed bronze bush

It was found that the inner bearing surface temperatures could rise rapidly over a short time period. The operating parameters evaluated from a rotor dynamic analysis were utilised. The results showed that the contact involving a high speed rotor is likely to initiate localised melting if the contact force is high enough. However, lower surface temperature rise was noted in the bronze bush contact problem due to its high diffusivity and lower heat partition coefficient. Hence, the bronze bush bearing is more suitable as an auxiliary bearing comparing to stainless steel bush bearing.

For the quasi-static thermoelastic contact problem, two boundary problems was investigated when subjected to Hertzian contact pressure, namely, for rigidly and a resiliently mounted bearing. An alternative approach was introduced to evaluate stresses in the bearing using the results from the thermal contact analysis. This approach was found to be convenient in analysing problems corresponding to different stress boundary conditions. Investigations were also conducted to assess the bearing surface deformation when subjected to repeated and cyclic

rubbing contacts. It was found that higher synchronous speed and contact force leads to higher surface imperfection growth rate. The mechanistic model showed that the surface temperature rise is an important issue for assessing failure in a rubbing contact problem.

In conclusion, the following suggestions are made:

1. For a given rotor speed the maximum contact force should be limited to avoid high contact temperature and thermoelastic growth.
2. The contact forces may be reduced by using softer resiliently mounted material with a high damping coefficient (to decrease the contact period).
3. Rubbing contact over long time period should be avoided, say by appropriate magnetic bearing control.

The following issues are suggested for future research:

- Conduction between bearing rolling elements and bearing/housing - It was assumed that the bearing outer surface was adiabatic in the thesis. However, conduction will take place between the bearing and rolling elements or the bearing and housing.
- Thermal instability - The thermal and thermoelastic problems are coupled to give the temperature rise associated with the change of the contact area during the contact.
- Impact force of rotor - When a rotor drops onto the bearing, the impact force will initiate compressive loading of bearing internal components.

- The rotor dynamic simulations indicate that multiple contacts are possible around the bearing. It would be an interesting area to investigate the thermal and thermoelastic responses of the bearing subjected to multiple and distributed contact events.
- Consider a three-dimensional analysis to cover the profiled bearings and skewed contact.
- Assess the thermoelastic distortion of the rotor.

Bibliography

[1] Schweitzer, G., Bleuler, H., and Traxler, A., 1994. *Active Magnetic Bearings.* Hochschulverlag AG abder ETH Zurich. ISBN 3 7281 2132 0.

[2] Schweitzer, G., Fumagalli, M., and Fenny, B., 1992. "Dynamics of Rigid Rotors in Retainer Bearings". *3rd Int. Symp. on Magnetic Bearings, Washington*, July, pp. 157–166.

[3] Schweitzer, G., and Fumagalli, M., 1996. "Motion of a Rotor in Retainer Bearings". *5th Int. Symp. Magnetic Bearings*, August, pp. 509–514.

[4] Schweitzer, G., and Fumagalli, M., 1996. "Measurements on a Rotor Contacting its Housing". *6th Int. Conf. on Vibrations in Rotating Machinery*, September.

[5] Ishii, T., and Kirk, R. G., 1996. "Transient Response Technique Applied to Active Magnetic Bearing Machinery During Rotor Drop". *J. Vibration and Acoustics,* **118**, April, pp. 154–163.

[6] Kirk, R. G., Swanson, E. E., Kavarana, F. H., Wang, X. Q., and Keesee, J., 1994. "Rotor Drop Test Stand for AMB Rotating Machinery. Part I: Description of Test Stand and Initial Results". *4th Int. Symp. on Magnetic Bearings*, August. ETH Zurich.

[7] Ramesh, K., and Kirk, R. G., 1994. "Rotor Drop Test Stand for AMB Rotating Machinery. Part II: Steady State Analysis and Comparison to Experimental Results". *4th Int. Symp. on Magnetic Bearings*, August.

[8] Kirk, R. G., Raju, K. V. S., and Ramesh, K., 1997. "Modeling of AMB Turbomachinery for Transient Analysis". *Proc. MAG*, pp. 139–153.

[9] Kirk, R. G., 1999. "Evaluation of AMB Turbomachinery Auxiliary Bearings". *ASME J. Vibration and Acoustics,* **121**, April, pp. 156–161.

[10] Lawen, J. L., and Flowers, G. T., 1997. "Synchronous Dynamics of Coupled Shaft/Bearing/Housing System with Auxiliary Support from a Clearance Bearing: Analysis and Experiment". *ASME J. Eng. for Gas Turbines and Power,* **119**, April, pp. 430–435.

[11] Wang, X., and Noah, S., 1998. "Nonlinear Dynamics of Magnetically Supported Rotor on Safety Auxiliary Bearings". *ASME J. Vibration and Acoustics,* **120**, April, pp. 596–606.

[12] Lawen, J. L., and Flowers, G. T., 1999. "Interaction Dynamics of a Magnetically Support Rotor on Safety Auxiliary Bearing". *ASME J. Vibration and Acoustics,* **121**, pp. 183–189.

[13] Keogh, P. S., Cole, M. O. T., Sakinkaya, M. N., and Burrows, C. R., 2002. "On the Control of Synchronous Vibration in Rotor/Magnetic Bearing Systems Involving Auxiliary Bearing Contact". *Paper GT-2002-30292, ASME Turbo Expo.* Amsterdam.

[14] Keogh, P. S., and Cole, M. O. T., 2003. "Rotor Vibration with Auxiliary Bearing Contact in Magnetic Bearing Systems, Part I: Synchronous Dynamics". *Proc. Instn Mech. Engrs, Part C: J. Mechanical Engineering Science,* **217**, pp. 377–392.

[15] Cole, M. O. T., and Keogh, P. S., 2003. "Rotor Vibration with Auxiliary Bearing Contact in Magnetic Bearing Systems, Part II: Robust Synchronous Control for Rotor Posision Recovery". *Proc. Instn Mech. Engrs, Part C: J. Mechanical Engineering Science,* **217**, pp. 393–409.

[16] Keogh, P. S., Burrows, C. R., and Cole, M. O. T., 2002. "The Rotor Behavior of a Rolling Element Auxiliary Bearing Following Rotor Impact". *ASME J. Tribol.,* **124**, pp. 406–413.

[17] Johnson, K. L., 1999. *Contact Mechanics.* Cambridge University Press.

[18] Harris, T. A., 1966. *Rolling Bearing Analysis.* John Wiley and Sons, Inc.

[19] Adam, G. G., and Nosonovsky, M., 2000. "Contacting Modeling - Forces". *Tribology International,* **33**, pp. 431–442.

[20] Tripp, J. H., 1985. "Hertzian Contact in Two and Three Dimensions". *NASA Technical Paper 2473.*

[21] Tanaka, N., 2001. "A New Calculation Method of Hertz Elliptical Contact Pressure". *ASME J. Tribol.,* **123**, p. 887=889.

[22] Houpert, L., 2001. "An Engineering Approach to Hertzian Contact Elasticity - Part I". *ASME J. Tribol.,* **123**, pp. 582–588.

[23] Houpert, L., 2001. "An Engineering Approach to Non-Hertzian Contact Elasticity - Part II". *ASME J. Tribol.,* **123**, July, pp. 589–594.

[24] Comninou, M., and Dundurs, J., 1982. "An Educational Elastic Problem with Friction - Part II: Unloading for Strong Frictional and Reloading". *ASME J. Appl. Mech.,* **49**, pp. 47–51.

[25] Ciavarella, M., 1998. "The Generalized Cattaneo Partial Slip Plane Contact Problem. I-Theory". *Int. J. Solids Structures,* **35**, pp. 2349–2362.

[26] Jäger, J., 1997. "Half-Planes without Coupling Under Contact Loading". *Archieve of Applied Mechanics,* **67**, pp. 247–259.

[27] Ciavarella, M., 1998. "The Generalized Cattaneo Partial Slip Plane Contact Problem. II - Examples". *Int. J. Solids Structures,* **35**, pp. 2363–2378.

[28] Jäger, J., 1998. "A New Principle in Contact Mechanics". *ASME J. Tribol.,* **120**, pp. 667–684.

[29] Ibrahim, R. A., 1994. "Friction-induced Vibration, Chatter, Squeal, and Chaos, Part II: Dynamics and Modelling". *ASME J. Appl. Mech. Reviews,* **47**, pp. 227–253.

[30] Adam, G. G., 1995. "Self-Excited Oscillations of Two Elastic Half-Spaces Sliding with a Constant Coefficient of Friction". *ASME J. Appl. Mech.,* **62**, pp. 867–871.

[31] Adam, G. G., 1998. "Steady Sliding of Two Elastic Half-Spaces with Friction Reduction due to Interface Stick-Slip". *ASME J. Appl. Mech.,* **65**, pp. 470–475.

[32] McMillan, A. J., 1997. "A Non-linear Friction Model for Self-excited Vibrations". *J. Sound and Vibration,* **205**, pp. 323–335.

[33] Michaux, M. A., Ferri, A. A., and Cunefare, K. A., 2005. "Effect of Tangential Dither Signal on Friction Induced Oscillations in The SDOF Model". *ASME Int. Design Engineering Technical Conferences and Computers and Information in Engineering Conference*, September 24-28.

[34] Cho, H., and Barber, J. R., 1999. "Stability of the Three-dimensional Coulomb Friction Law". *Proc. Roy. Soc. Lond. Series A,* **455**, pp. 839–861.

[35] Becker, E. B., and Oden, J. T., 1994. "Numerical Modeling of Friction-induced Vibrations and Dynamic Instabilities". *ASME J. Appl. Mech. Reviews,* **47**(7), pp. 255–273.

[36] Baillet, L., Linck, V., D'Errico, S., Laulagnet, B., and Berthier, Y., 2005. "Finite Element Simulation of Dynamic Instabilities in Frictional Sliding Contact". *ASME J. Tribol.,* **127**, pp. 652–657.

[37] Greenwood, J. A., and Williamson, J. B. P., 1966. "The Contact of Nominally Flat Surfaces". *Proc. Roy. Soc. Lond. Series A,* **295**, pp. 300–319.

[38] Bush, A. W., Gibson, R. D., and Thomas, T. R., 1975. "The Elastic Contact of a Rough Surface". *Wear,* **35**, pp. 87–111.

[39] Chang, W. R., Etrsion, I., and Bogy, D. B., 1987. "An Elastic-Plastic Model for Contact of Rough Surfaces". *ASME J. Tribol.,* **101**, pp. 257–263.

[40] Zhao, Y. W., and Chang, L., 2001. "A Model of Asperity Interactions in Elastic-Plastic Contact of Rough Surfaces". *ASME J. Tribol.,* **123**, pp. 857–864.

[41] Kogut, L., and Etslon, I., 2004. "A Static Friction Model for Elastic-Plastic Contacting Rough Surfaces". *ASME J. Tribol.,* **126**, pp. 34–40.

[42] Liu, G., and Wang, Q., 2000. "Thermoelatic Astperity Contacts, Frictional Shear, and Parameter Correlations". *ASME J. Tribol.,* **122**, pp. 300–307.

[43] Lin, Y., and Ovaert, T. C., 2004. "A Two-Dimensional Thermoelastic Rough Surface Contact Model". *ASME J. Tribol.,* **126**, pp. 430–435.

[44] Ciavarella, M., Decuzzi, P., and Monno, G., 2000. "Frictionally-excited Thermoelastic Contact of Rough Surfaces". *Int. J. Mech. Sci.,* **42**, pp. 1307–1325.

[45] Liu, S., and Wang, Q., 2001. "A Three-Dimensional Thermomechanical Model Contact Between Non-Conforming Rough Surfaces". *ASME J. Tribol.,* **123**, pp. 17–26.

[46] Solberg, J. M., and Papadopoulos, P., 1998. "A Finite Element Method for Contact/Impact". *Finite Elements in Analysis and Design,* **30**, pp. 297–311.

[47] Baillet, L., and Sassi, T., 2002. "Finite Element Method with Lagrange Multipliers for Contact Problems with Friction". *C. R. Acad. Sci. Paris,* **334**(Ser. I), pp. 917–922.

[48] Hild, P., 2002. "On Finite Element Uniquesness Studies for Coulomb's Frictional Contact Model". *Int. J. Appl. Math. Comput. Sci.,* **12**(1), pp. 41–50.

[49] Hassani, R., Patrick Hild, I. R. I., and Sakki, N.-D., 2003. "A Mixed Finite Element Method and Solution Multiplicity for Coulomb Frictional Contact". *Comput. Methods Appl. Mech. Engrg,* **192**, pp. 4517–4531.

[50] Bittencourt, E., and Creus, G. J., 1998. "Finite Element Analysis of Three-Dimensional Contact and Impact in Large Deformation Problems". *Computers and Structures,* **69**, pp. 219–234.

[51] Zavarise, G., Wriggers, P., and Schrefler, B. A., 1998. "A Method for Solving Contact Problems". *Int. J. Numer. Math. Engng,* **42**, pp. 473–498.

[52] Leahy, J. G., and Becker, A. A., 1999. "The Numerical Treatment of Local Variables in Three-Dimensional Frictional Contact Problems using Boundary Element Method". *Computers and Structures,* **71**, pp. 383–395.

[53] Ghaderi-Panah, A., and Fenner, R. T., 1998. "A General Boundary Element Method Approach to the Solution of Three-Dimensional Frictionless Contact Problems". *Engineering Analysis with Boundary Elements,* **21**, pp. 205–316.

[54] Paris, F., Blazquez, A., and Canas, J., 1995. "Contact Problems with Non-Conforming Discretization using Boundary Element Method". *Computers and Structures,* **57**, pp. 829–839.

[55] Guyot, N., Kosior, F., and Maurice, G., 2000. "Coupling of Finite Elements and Boundary Elements Method for Study of the Frictional Contact Problem". *Comput. Methods Appl. Mech. Engrg,* **181**, pp. 147–159.

[56] Ju, Y., and Farris, T. N., 1996. "Spectral Analysis of Two Dimensional Contact Problems". *ASME J. Tribol.,* **118**, pp. 320–328.

[57] Ju, Y., and Farris, T. N., 1997. "FFT Thermoelastic Solutions for Moving Heat Sources". *ASME J. Tribol.,* **119**, pp. 156–161.

[58] Timoshenko, S. P., and Goodier, J. N., 1970. *Theory of Elasticity.* McGraw-Hill. ISBN 0070858055.

[59] Love, A. E. H., 1944. *The Mathematical Theory of Elasticity*, 4th ed. New York Dover Publication.

[60] Mindlin, R. D., 1936. "Force at a Point in the Interior of a Semi Infinite Solid". *Physics,* **7**, pp. 195–202.

[61] Muskhelishvili, N. I., 1963. *Some Basic Problems of The Mathematical Theory of Elasticity: Fundamental Equations Plane Theory of Elasticity, Torsion and Bending.* P. Noordhoff Ltd.

[62] Sokolnikoff, I. S., 1956. *Mathematical Theory of Elasticity.* McGraw-Hill Book Company.

[63] Stevenson, A. C., 1945. "Complex Potential in Two Dimensional Elasticity". *Proc. Roy. Soc. Lond. Series A,* **184**, pp. 129–179.

[64] Thompson, M., 1968. *Plane Elastic Systems.* Springer-Verlag Heidelberg.

[65] Dundur, J., 1963. "Concentrated Force in an Elastically Embedded Disk". *ASME J. Appl. Mech.,* **30**, pp. 568–570.

[66] Hanson, M. T., and Wang, Y., 1997. "Concentrated Ring Loading in a Full Space or Half Space: Solution for Transverse Isotropy and Isotropy". *Int. J. Solids Structures,* **34**, pp. 1379–1418.

[67] Worden, R. E., and Keer, L. M., 1991. "Green's Functions for a Point Load and Dislocation in an Annular Region". *ASME J. Appl. Mech.,* **58**, pp. 954–959.

[68] Chao, C. K., and Tan, C. J., 2000. "On The General Solutions for Annular Problems with a Point Heat Source". *ASME J. Appl. Mech.,* **67**, pp. 511–518.

[69] Chao, C. K., and Shen, M. H., 1997. "On Bonded Circular Inclusions in Plane Thermoelasticity". *ASME J. Appl. Mech.,* **64**, pp. 1000–1004.

[70] Sternberg, E., and McDowell, E. L., 1957. "On the Steady-State Thermoelastic Problem for Half-Space". *J. Appl. Math,* **14**, pp. 381–398.

[71] Barber, J. R., and Martin-Moran, C. J., 1982. "Green's Function for Transient Thermoelastic Contact Problems for the Half-Plane". *Wear,* **79**, pp. 11–19.

[72] Barber, J. R., 1984. "Thermoelastic Displacements and Stresses due to a Heat Source Moving over the Surface Moving over the Surface of a Half Plane". *ASME J. Appl. Mech.,* **51**, pp. 636–639.

[73] Barber, J. R., 1987. "Thermoelatic Distortion of the Half-Space". *J. Therm. Stresses,* **10**, pp. 221–228.

[74] Azarkhin, A., and Barber, J. R., 1988. "Green's Functions for Subsurface Thermal Stresses Due to Surface Heating". *J. Therm. Stresses,* **11**, pp. 1–16.

[75] Yevtushenko, A. A., and Kovalenko, Y. V., 1995. "The Interaction of Frictional Heating and Wear at a Transient Sliding Contact". *J. Appl. Maths. Mechs,* **59**(3), pp. 459–466.

[76] Yevtushenko, A. A., and Kulchytsky-Zhyhailo, R. D., 1995. "Axi-Symmetrical Transient Contact Problem for Sliding Bodies with Heat Generation". *Int. J. Solids Structures,* **32**(16), pp. 2369–2376.

[77] Pauk, V. J., and Yevtushenko, A. A., 1997. "Frictional Heating in Sliding Contact of Two Thermoelastic Bodies". *Int. J. Solids Structures,* **34**(12), pp. 1505–1516.

[78] Pauk, V., and Zastrau, B., 2002. "2D Rolling Contact Problem Involving Frictional Heating". *Int. J. Mech. Sci,* **44**, pp. 2573–2584.

[79] Liu, S., and Wang, Q., 2003. "Transient Thermoelastic Stress Fields in a Half-Space". *ASME J. Tribol.,* **125**, pp. 33–43.

[80] Carslaw, H. S., and Jaeger, J. C., 1959. *Conduction of Heat in Solids*, 2nd ed. Clarendon Press.

[81] Blok, H., 1958. "The Flash Temperature Concept". *Wear,* **2**, pp. 438–455.

[82] Tian, X., and Kennedy, F. E., 1993. "Temperature Rise at the Sliding Contact Interface for a Coated Semi-Infinite Body". *ASME J. Tribol.,* **115**, pp. 1–9.

[83] Tian, X., and Kennedy, F. E., 1994. "Maximum and Average Flash Temperatures in Sliding Contacts". *ASME J. Tribol.,* **116**, pp. 167–174.

[84] Gao, J. Q., Lee, S. C., and Ai, X. L., 2000. "An FFT-Based Transient Flash Temperature Model for General Three-Dimensional Rough Surface Contacts". *ASME J. Tribol.,* **122**, pp. 519–523.

[85] Burton, R. A., Nerlikar, V., and Kiliparti, S. R., 1972. "Thermoelastic Instability in Seal-like Configuration". *Wear,* **24**, pp. 177–188.

[86] Barber, J. R., 1969. "Thermoelastic Instabilities in the Sliding of Conforming Solids". *Proc. Roy. Soc. Lond. Series A,* **312**, pp. 381–394.

[87] Zagrodzki, P., Lam, K. B., Bahkali, E. A., and Barber, J. R., 2001. "Nonlinear Transient Behaviour of a Sliding System with Frictionally Exicited Thermoelastic Instability". *ASME J. Tribol.,* **123**, pp. 699–708.

[88] Pelesko, J. A., 2001. "Nonlinear Stability, Thermoelastic Contact, and the Barber Condition". *ASME J. Appl. Mech.,* **68**, pp. 28–33.

[89] Quinn, D. D., and Pelesko, J. A., 2002. "Generic Unfolding of The Thermoelastic Contact Instability". *Int. J. Solids and Structures,* **39**, pp. 145–157.

[90] Jang, J. Y., and Khonsari, M. M., 2002. "A Generalized Thermoelastic Instability Analysis". *Proc. Roy. Soc. Lond. Series A,* **459**(02PA042), pp. 309–329.

[91] Lee, K., and Barber, J. R., 1993. "Frictionally-excited Thermoelastic Instability in Automotive Disk Brakes". *ASME J. Tribol.,* **115**, pp. 607–614.

[92] Lee, K. J., 2000. "Frictionally Excited Thermoelastic Instability in Automotive Drum Brakes". *ASME J. Tribol.,* **122**, pp. 849–855.

[93] Hartsock, D. L., and Fash, J. W., 2000. "Effect of Pad/Caliper Stiffness, Pad Thickness, and Pad Length on Thermoelastic Instability in Disk Brakes". *ASME J. Tribol.,* **122**, pp. 511–518.

[94] Young, W. C., 2002. *Roark's formulas for stress and strain,* 7th ed. McGraw-Hill.

[95] Bateman, H., 1954. *Tables of Integral Transforms,* Vol. 1. McGraw-Hilll.

[96] Abramowitz, M., and Stegun, I. A., 1965. *Handbook of Mathematical Functions with Formulas, Graphs and Mathematical Tables.* Dover. ISBN 0-486-61272-4.

[97] Gradshteyn, I. S., and Ryzhik, I. M., 1994. *Table of Integrals, Series and Products.* Academic Press. ISBN 012294755X.

[98] *Schaum's Outline of Theory and Problems Feedback And Control Systems: Continuous (Analog) and Discrete (Digital),* 2nd ed. McGraw-Hill.

[99] Cole, M. O. T., and Keogh, P. S., 2003. "Asynchronous Periodic Contact Modes for Rotor Vibration Within an Annular Clearance". *Proc. Instn Mech. Engrs, Part C: J. Mechanical Engineering Science,* **217**, pp. 1101–1115.

Appendix A

Inverse Laplace Transform for Circular Hole Problem.

Based on equation (3.13) deduced in Chapter 3, the complex inversion formula is

$$T_{Gn_{hole}}(r,t) = -\frac{1}{2\pi k} \times \frac{2\kappa}{\pi i} \int_0^\infty \left[-\frac{K_n(\lambda r)}{2\pi k \lambda r_i K_n'(\lambda r_i)} \right] e^{-\kappa v^2 t} v dv \qquad \text{(A.1)}$$

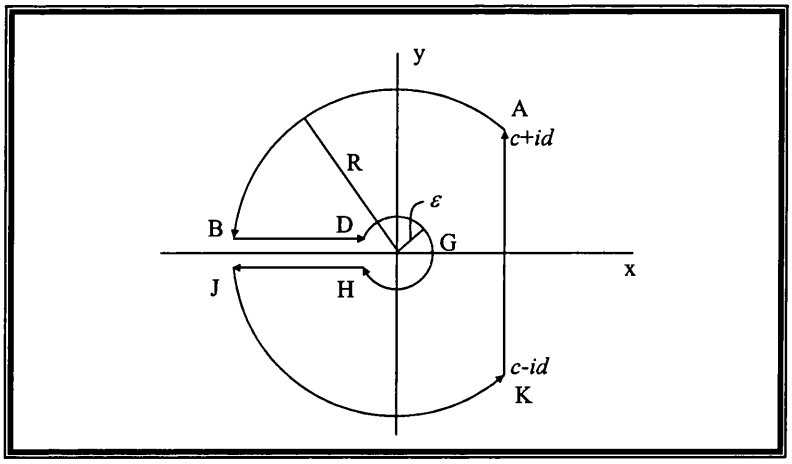

Figure A.1: Bromwich contour for inverse Laplace transform with branch cut along the negative x-axis.

Now, $d \to \infty$,

$$\begin{aligned}
&\lim_{\substack{R\to\infty \\ \varepsilon\to 0}} \int_{c-i\infty}^{c+i\infty} \left(-\frac{K_n(\lambda r)}{\lambda r_i K_n'(\lambda r_i)}\right) e^{st} ds \\
&= \lim_{\substack{R\to\infty \\ \varepsilon\to 0}} \left\{ \begin{array}{l} \int_{BD} \left(-\frac{K_n(\lambda r)}{\lambda r_i K_n'(\lambda r_i)}\right) e^{st} ds \\ + \int_{DGH} \left(-\frac{K_n(\lambda r)}{\lambda r_i K_n'(\lambda r_i)}\right) e^{st} ds \\ + \int_{HJ} \left(-\frac{K_n(\lambda r)}{\lambda r_i K_n'(\lambda r_i)}\right) e^{st} ds \end{array} \right\}
\end{aligned} \tag{A.2}$$

Let,

$$f_n(\lambda r) = -\frac{K_n(\lambda r)}{2\pi k \lambda r_i K_n'(\lambda r_i)} \tag{A.3}$$

Along BD, let $s = \kappa v^2 e^{\pi i}$and $\sqrt{s/\kappa} = \lambda = v e^{\pi i/2}$. The integration along BD takes place between $\{\varepsilon \le s \le R\}$. It follows that,

$$\begin{aligned}
&\lim_{\substack{R\to\infty \\ \varepsilon\to 0}} \left\{ -\frac{1}{2\pi i} \int_{BD} \left(-\frac{K_n'(\lambda r)}{\lambda r_i K_n'(\lambda r_i)}\right) e^{st} ds \right\} \\
&= -\frac{1}{2\pi i} \int_{-\infty}^{0} f_n(\lambda r)\, e^{st} ds \\
&= -\frac{\kappa}{\pi i} \int_0^{\infty} f_n\left(v e^{-\pi i/2} r\right) e^{-\kappa v^2 t} v dv
\end{aligned} \tag{A.4}$$

Similarly, along the line HJ, the integration is carried out with negative phase, where $s = \kappa v^2 e^{-\pi i}$. Hence,

$$\lim_{\substack{R\to\infty \\ \varepsilon\to 0}} \left\{ -\frac{1}{2\pi i} \int_{HJ} \left(-\frac{K_n(\lambda r)}{\lambda r_i K_n'(\lambda r_i)}\right) e^{st} ds \right\} = \frac{\kappa}{\pi i} \int_0^{\infty} f_n\left(v e^{\pi i/2} r\right) e^{-\kappa v^2 t} v dv \tag{A.5}$$

Along the curve DGH, set $s = \varepsilon e^{i\theta}$, $z = e^{i\theta/2}\sqrt{\varepsilon/\kappa}$ so that

$$\begin{aligned}
&\frac{1}{2\pi i} \int_{-\pi}^{\pi} \frac{K_n\left(\sqrt{\frac{\varepsilon}{\kappa}} e^{i\theta/2} r\right)}{r_i \sqrt{\frac{\varepsilon}{\kappa}} e^{\frac{i\theta}{2}} K_n'\left(r_i \sqrt{\frac{\varepsilon}{\kappa}} e^{\frac{i\theta}{2}}\right)} e^{\varepsilon e^{i\theta} t} i\varepsilon e^{i\theta} d\theta \\
&= \frac{1}{2\pi i} \int_{-i\sqrt{\varepsilon/\kappa}}^{i\sqrt{\varepsilon/\kappa}} \frac{K_n(zr)}{r_i z K_n'(z r_i)} e^{z^2 \kappa t} i z^2 \kappa d\theta
\end{aligned} \tag{A.6}$$

Since $\varepsilon \to 0$, $z \to 0$, from [96, pg 375],

$$\lim_{z\to 0} K_n(z) = \frac{1}{2}\Gamma(n)\left(\frac{1}{2}z\right)^{-n} \tag{A.7}$$

$$K_n'(z) = -K_{n+1}(z) + \frac{n}{z}K_n(z) \tag{A.8}$$

Equation (A.6) can be reduced to,

$$\begin{aligned}
&\lim_{\substack{\varepsilon\to 0\\ z\to 0}} \frac{i}{r_i}\int_{-i\sqrt{\varepsilon/\kappa}}^{i\sqrt{\varepsilon/\kappa}} \frac{\frac{1}{2}\Gamma(n)\left(\frac{1}{2}zr\right)^{-n}}{-\frac{1}{2}\Gamma(n+1)\left(\frac{1}{2}zr_i\right)^{-(n+1)} + \frac{n}{2zr_i}\Gamma(n)\left(\frac{1}{2}zr_i\right)^{-n}} e^{z^2\kappa t} z\kappa dz \\
&= \frac{i}{r_i}\int_{-i\sqrt{\varepsilon/\kappa}}^{i\sqrt{\varepsilon/\kappa}} \frac{\Gamma(n)r^{-n}}{-2\Gamma(n+1)r_i^{-(n+1)} + \frac{n}{r_i}\Gamma(n)r_i^{-n}}(1)(0)\kappa dz = 0
\end{aligned} \tag{A.9}$$

Therefore, it yields,

$$\begin{aligned}
&\frac{\kappa}{2\pi i}\int_{c-i\infty}^{c+i\infty} f_n(\lambda r)\, e^{st} ds \\
&= \underbrace{-\frac{\kappa}{\pi i}\int_0^\infty f_n\left(rve^{\frac{\pi i}{2}}\right) e^{-\kappa v^2 t} dv}_{\text{Integration along the positive phase of the branch cut}} \\
&+ \underbrace{\frac{\kappa}{\pi i}\int_0^\infty f_n\left(rve^{-\frac{\pi i}{2}}\right) e^{-\kappa v^2 t} dv}_{\text{Integration along the negative phase of the branch cut}} \\
&= -\frac{2\kappa}{\pi i}\int_0^\infty \text{Imag}\left[f_n\left(rve^{\frac{\pi i}{2}}\right)\right] e^{-\kappa v^2 t} dv
\end{aligned} \tag{A.10}$$

Appendix B

Inverse Laplace Transform for Annulus Solution

Introduction of an angular ratio γ during the inversion process eliminates the possibility of the contour integration being carried out through the singular points along the branch cut axis.

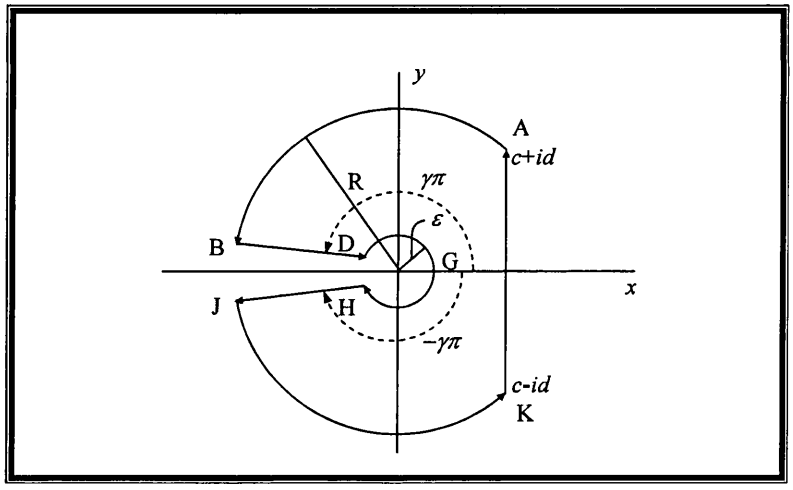

Figure B.1: Bromwich contour for inverse Laplace transformation of annulus solution. The angular ratio γ, must be chosen less than unity to bypass the singularities along the negative x-axis.

The inversion process is similar to that of Appendix A and the integration involves

$(d \to \infty)$,

$$\begin{aligned}
&\frac{1}{2\pi k} \times \frac{1}{2\pi i} \int_{c-i\infty}^{c+i\infty} f_n(\lambda r) e^{st} ds \\
&= \frac{1}{2\pi k} \times \frac{1}{2\pi i} \int_{c-i\infty}^{c+i\infty} \left(\frac{-K_n(\lambda r) I_n'(\lambda r_o) + I_n(\lambda r) K_n'(\lambda r_o)}{\lambda r_i \Delta_n} \right) e^{st} ds
\end{aligned} \tag{B.1}$$

The complex integration along KA gives,

$$\begin{aligned}
&\frac{1}{2\pi i} \int_{c-i\infty}^{c+i\infty} f_n(\lambda r) e^{st} ds \\
&= - \lim_{\substack{\varepsilon \to 0 \\ R \to \infty}} \frac{1}{2\pi i} \left\{ \int_{BD} f_n(\lambda r) e^{st} ds + \int_{DGH} f_n(\lambda r) e^{st} ds + \int_{HJ} f_n(\lambda r) e^{st} ds \right\}
\end{aligned} \tag{B.2}$$

Along BD, $s = \kappa v^2 e^{i\gamma\pi}$ and $\lambda = \sqrt{s/\kappa} = v e^{i\pi\gamma/2}$, so that

$$\begin{aligned}
\lim_{\substack{\varepsilon \to 0 \\ R \to \infty}} \int_{BD} f_n(\lambda r) e^{st} ds &= \lim_{\substack{\varepsilon \to 0 \\ R \to \infty}} \int_{Re^{i\gamma\pi}}^{\varepsilon e^{i\gamma\pi}} f_n(\lambda r) e^{st} ds \\
&= \int_{\infty}^{0} f_n\left(r v e^{i\pi\gamma/2}\right) e^{\kappa v^2 e^{i\pi\gamma} t} \left(2\kappa v e^{i\pi\gamma}\right) dv \\
&= -2\kappa \int_{\infty}^{0} f_n\left(r v e^{i\pi\gamma/2}\right) e^{\kappa v^2 e^{i\pi\gamma} t + i\pi\gamma} dv
\end{aligned} \tag{B.3}$$

Along JH, $s = \kappa v^2 e^{-i\gamma\pi}$ and $\lambda = \sqrt{s/\kappa} = v e^{-i\pi\gamma/2}$, so that

$$\begin{aligned}
\lim_{\substack{\varepsilon \to 0 \\ R \to \infty}} \int_{HJ} f_n(\lambda r) e^{st} ds &= \lim_{\substack{\varepsilon \to 0 \\ R \to \infty}} \int_{\varepsilon e^{i\gamma\pi}}^{R e^{i\gamma\pi}} f_n(\lambda r) e^{st} ds \\
&= \int_{0}^{\infty} f_n\left(r v e^{-i\pi\gamma/2}\right) e^{\kappa v^2 e^{-i\pi\gamma} t} \left(2\kappa v e^{-i\pi\gamma}\right) dv \\
&= 2\kappa \int_{0}^{\infty} f_n\left(r v e^{-i\pi\gamma/2}\right) e^{\kappa v^2 e^{-i\pi\gamma} t - i\pi\gamma} dv
\end{aligned} \tag{B.4}$$

The summation of these two terms gives,

$$
\begin{aligned}
&- \lim_{\substack{\varepsilon\to 0\\ R\to\infty}} \frac{1}{2\pi i}\left\{\int_{BD} f_n(\lambda r)e^{st}ds + \int_{HJ} f_n(\lambda r)e^{st}ds\right\} \\
&= \frac{\kappa}{\pi i}\left\{\int_0^\infty f_n\left(rve^{i\pi\gamma/2}\right)e^{\kappa v^2 e^{i\pi\gamma}t+i\pi\gamma}dv - \int_0^\infty f_n\left(rve^{-i\pi\gamma/2}\right)e^{\kappa v^2 e^{-i\pi\gamma}t-i\pi\gamma}dv\right\} \\
&= \frac{2\kappa}{\pi}\int_0^\infty \text{Imag}\left\{f_n\left(rve^{i\pi\gamma/2}\right)e^{\kappa v^2 e^{i\pi\gamma}t+i\pi\gamma}\right\}vdv
\end{aligned}
\tag{B.5}
$$

Putting $v = x/r_i$, equation (B.5) reduces to,

$$
\begin{aligned}
&\frac{2\kappa}{\pi}\int_0^\infty \text{Imag}\left\{f_n\left(rve^{i\pi\gamma/2}\right)e^{\kappa v^2 e^{i\pi\gamma}t+i\pi\gamma}\right\}vdv \\
&= \frac{2\kappa}{\pi r_i^2}\int_0^\infty \text{Imag}\left\{f_n\left(\frac{x}{r_i}e^{i\pi\gamma/2}\right)e^{\kappa x^2 e^{i\pi\gamma}t/r_i^2+i\pi\gamma}\right\}xdx
\end{aligned}
\tag{B.6}
$$

For the contour along DGH, $s = \varepsilon e^{i\theta}$ and $z(\theta) = \sqrt{\varepsilon/\kappa}e^{i\theta/2}$, so that

$$
\begin{aligned}
&- \frac{1}{2\pi i}\lim_{\varepsilon\to 0}\int_{\pi\gamma}^{-\pi\gamma} \frac{\left\{\begin{array}{l} I_n\left(\sqrt{\frac{\varepsilon}{\kappa}}e^{\frac{i\theta}{2}}r\right)K_n'\left(\sqrt{\frac{\varepsilon}{\kappa}}e^{\frac{i\theta}{2}}r_o\right) \\ -K_n\left(\sqrt{\frac{\varepsilon}{\kappa}}e^{\frac{i\theta}{2}}r\right)I_n'\left(\sqrt{\frac{\varepsilon}{\kappa}}e^{\frac{i\theta}{2}}r_o\right)\end{array}\right\}}{\sqrt{\frac{\varepsilon}{\kappa}}e^{\frac{i\theta}{2}}r_i\left\{\begin{array}{l} K_n'\left(\sqrt{\frac{\varepsilon}{\kappa}}e^{\frac{i\theta}{2}}r_i\right)I_n'\left(\sqrt{\frac{\varepsilon}{\kappa}}e^{\frac{i\theta}{2}}r_o\right) \\ -I_n'\left(\sqrt{\frac{\varepsilon}{\kappa}}e^{\frac{i\theta}{2}}r_i\right)K_n'\left(\sqrt{\frac{\varepsilon}{\kappa}}e^{\frac{i\theta}{2}}r_o\right)\end{array}\right\}} e^{\varepsilon e^{i\theta}t}i\varepsilon e^{i\theta}d\theta \\
&= \frac{1}{\pi i}\lim_{\varepsilon\to 0}\int_{\sqrt{\varepsilon/\kappa}e^{-i\pi\gamma/2}}^{\sqrt{\varepsilon/\kappa}e^{i\pi\gamma/2}} \frac{I_n(zr)K_n'(zr_o) - K_n(zr)I_n'(zr_o)}{zr_i\left\{K_n'(zr_i)I_n'(zr_o) - I_n'(zr_i)K_n'(zr_o)\right\}}e^{\kappa z^2 t}z\kappa dz
\end{aligned}
\tag{B.7}
$$

As $\varepsilon \to 0$, $z \to 0$, taking the limiting form for small argument of each Bessel

function,

$$I_n(zr) = \frac{1}{\Gamma(n+1)}\left(\frac{1}{2}zr\right)^n \tag{B.8}$$

$$K_n(zr) = \frac{\Gamma(n)}{2}\left(\frac{1}{2}zr\right)^{-n} \tag{B.9}$$

$$I'_n(zr) = \frac{1}{\Gamma(n+2)}\left(\frac{1}{2}zr\right)^{n+1} + \frac{n}{zr\Gamma(n+1)}\left(\frac{1}{2}zr\right)^n \tag{B.10}$$

$$K'_n(zr) = -\frac{\Gamma(n+1)}{2}\left(\frac{1}{2}zr\right)^{-(n+1)} + \frac{n\Gamma(n)}{2zr}\left(\frac{1}{2}zr\right)^{-n} \tag{B.11}$$

For $n = 0$ and taking $\varepsilon = 0$, the integration reduces to,

$$\begin{aligned}\int_{\sqrt{\varepsilon/\kappa}e^{-i\pi\gamma/2}}^{\sqrt{\varepsilon/\kappa}e^{i\pi\gamma/2}} \frac{-\frac{1}{zr_o}}{\pi i r_i\left\{-\frac{r_o}{2r_i}+\frac{r_i}{2r_o}\right\}}\kappa dz &= \int_{-\pi\gamma}^{\pi\gamma}\frac{-\frac{1}{r_o}}{\pi r_i\left\{-\frac{r_o}{2r_i}+\frac{r_i}{2r_o}\right\}}\times\frac{\kappa}{2}d\theta \\ &= \int_{-\pi\gamma}^{\pi\gamma}\frac{\kappa}{\pi\left(r_o^2-r_i^2\right)}d\theta \\ &= \frac{2\kappa\gamma}{\left(r_o^2-r_i^2\right)}\end{aligned} \tag{B.12}$$

For $n \neq 0$, the integration reduces to zero. Therefore, the Fourier coefficient can be written as,

$$\begin{aligned}&T_{Gn_{annulus}}(r,t) \\ &= \frac{1}{2\pi k}\times\frac{2\kappa}{\pi r_i^2}\times\begin{cases}\int_0^\infty \text{Imag}\left\{f_0\left(\frac{r}{r_i}xe^{\frac{i\pi\gamma}{2}}\right)e^{\frac{\kappa x^2 te^{i\pi\gamma}}{r_i^2}+i\pi\gamma}\right\}xdx \\ +\left(\frac{\pi\gamma}{\eta_o^2-1}\right)\end{cases}, \quad n=0 \\ &\qquad\int_0^\infty \text{Imag}\left\{f_n\left(\frac{r}{r_i}xe^{\frac{i\pi\gamma}{2}}\right)e^{\frac{\kappa x^2 te^{i\pi\gamma}}{r_i^2}+i\pi\gamma}\right\}xdx\Bigg\}, \quad n\neq 0\end{aligned} \tag{B.13}$$

Appendix C

Reduction of Half-Plane Vertical Displacement Integration

The following calculation is the work by Professor Barber, who personally delivered the transcript electronically. It simplifies the integration of the half-plane vertical displacement, u_y in [71] with infinite integrating limit. Define,

$$F(R') = \int_{-\infty}^{\infty} \left\{ \frac{\left(1 - e^{-S^2}\right)}{S^2} - 2e^{-S^2} \right\} \ln|R' - S| \, dS \tag{C.1}$$

Noting that,

$$\frac{d}{dS}\left[\frac{\left(1 - e^{-S^2}\right)}{S}\right] = -\left[\frac{\left(1 - e^{-S^2}\right)}{S^2} - 2e^{-S^2}\right] \tag{C.2}$$

we can integrate equation (C.1) by parts, giving,

$$F(R') = \left[-\frac{\left(1 - e^{-S^2}\right)}{S} \ln|R' - S|\right]_{-\infty}^{\infty} + \int_{-\infty}^{\infty} \frac{\left(1 - e^{-S^2}\right)}{S(S - R')} dS \tag{C.3}$$

The first term is zero, therefore,

$$F(R') = \int_{-\infty}^{\infty} \frac{\left(1 - e^{-S^2}\right)}{S(S - R')} dS \tag{C.4}$$

Then, factorise the integrand by means of partial fraction into following form,

$$\frac{1}{S(S - R')} = \frac{1}{R'(S - R')} - \frac{1}{R'S} \tag{C.5}$$

Hence, equation (C.4) expands to,

$$F(R') = \frac{1}{R'} \int_{-\infty}^{\infty} \frac{\left(1 - e^{-S^2}\right)}{(S - R')} dS - \frac{1}{R'} \int_{-\infty}^{\infty} \frac{\left(1 - e^{-S^2}\right)}{S} dS \tag{C.6}$$

The second term is zero by symmetry, leaving,

$$F(R') = \frac{1}{R'} \int_{-\infty}^{\infty} \frac{\left(1 - e^{-S^2}\right)}{(S - R')} dS \tag{C.7}$$

Now define,

$$f(R') = R'F(R') = \int_{-\infty}^{\infty} \frac{\left(1 - e^{-S^2}\right)}{(S - R')} dS \tag{C.8}$$

If $R' = 0$, then,

$$f(0) = \int_{-\infty}^{\infty} \frac{\left(1 - e^{-S^2}\right)}{S} dS = 0 \tag{C.9}$$

Also, differentiate equation (C.9) with respect to R', to give,

$$f'(R') = \int_{-\infty}^{\infty} \frac{\left(1 - e^{-S^2}\right)}{(S - R')^2} dS \tag{C.10}$$

Integrating the right hand side by parts, we obtain,

$$f(R') = \left[-\frac{\left(1 - e^{-S^2}\right)}{(S - R')} \right]_{-\infty}^{\infty} + \int_{-\infty}^{\infty} \frac{2Se^{-S^2}}{(S - R')} dS \tag{C.11}$$

Once again, the first term is zero and equation (C.11) reduces to,

$$\begin{aligned} f(R') &= \int_{-\infty}^{\infty} \frac{2Se^{-S^2}}{(S-R')} dS \\ &= 2\int_{-\infty}^{\infty} \frac{(S-R'+R')e^{-S^2}}{(S-R')} dS \\ &= 2\int_{-\infty}^{\infty} e^{-S^2} dS + 2R' \int_{-\infty}^{\infty} \frac{e^{-S^2}}{(S-R')} dS \\ &= 2\sqrt{\pi} - 2R' f(R') + 2R' \int_{-\infty}^{\infty} \frac{1}{(S-R')} dS \end{aligned} \tag{C.12}$$

The last term of equation (C.12) is negligible as,

$$[\ln|S-R'|]_{-\infty}^{\infty} \to 0 \tag{C.13}$$

Hence,

$$\begin{aligned} f(R') &= 2\sqrt{\pi} - 2R' f(R) \\ \Leftrightarrow f(R') &+ 2R' f(R') = 2\sqrt{\pi} \end{aligned} \tag{C.14}$$

Taking the homogeneous part of the equation,

$$f'(R') + 2R' f(R') = 0 \tag{C.15}$$

Solve the differential equation to give

$$f(R') = Ae^{-R'^2} \tag{C.16}$$

Solve the inhomogeneous equation, by writing

$$f(R') = g(R')e^{-R^2} \tag{C.17}$$

which is a multiple of the homogeneous solution. Differentiate equation (C.17), giving,

$$f'(R') = g'(R')e^{-R'^2} - 2R'g(R')e^{-R'^2} \tag{C.18}$$

Substituting equation (C.17) and equation (C.18) into equation (C.14),

$$g'(R)e^{-R^2} = 2\sqrt{\pi} \tag{C.19}$$

Integrating with respect to R', gives,

$$g(R') = 2\sqrt{\pi}\int_0^{R'} e^{S^2}dS + B \tag{C.20}$$

Based on equation (C.9) and equation (C.17) we can deduce that $B = 0$. Thus,

$$f(R') = 2\sqrt{\pi}e^{-R'^2}\int_0^{R'} e^{S^2}dS + Ae^{-R'^2} \tag{C.21}$$

Since $f(0) = 0$, $A = 0$. Finally from equation (C.8), we have,

$$F(R') = \frac{f(R')}{R'} = \frac{2\sqrt{\pi}e^{-R'^2}}{R'}\int_0^{R'} e^{S^2}dS \tag{C.22}$$

and,

$$F_1(R') = \frac{F(R')}{\pi} = \frac{2e^{-R'^2}}{\sqrt{\pi}R'}\int_0^{R'} e^{S^2}dS$$

Appendix D

Effective Inertia of Combined Race and Rollers

Consider a deep groove auxiliary bearing with a full complement of balls. The contact with normal loading of f_c take place at the angular position of $\theta = 0$ and corresponding frictional force is μf_c. Figure D.1(b) shows the (normal,tangential) tractions acting on the j^{th} ball as (G_j^I, F_j^I) are action forces from inner race while (G_j^O, F_j^O) are tractions from outer race. Sliding always take place at ball-ball contacts and the contribution from the $(j-1)^{\text{th}}$ ball is $(H_j, \mu_{rol} H_j)$ while from the $(j+1)^{\text{th}}$ ball it is $(H_{j+1}, \mu_{rol} H_{j+1})$. The outer race is assumed to be fixed and the inner race is free to rotate. For a rotating race, the rollers and inner race inertia can be calculated based on the following approach: (a) Formulate bulk motion of ball train, from individual ball considerations; (b) Assume that ball rolling conditions apply.

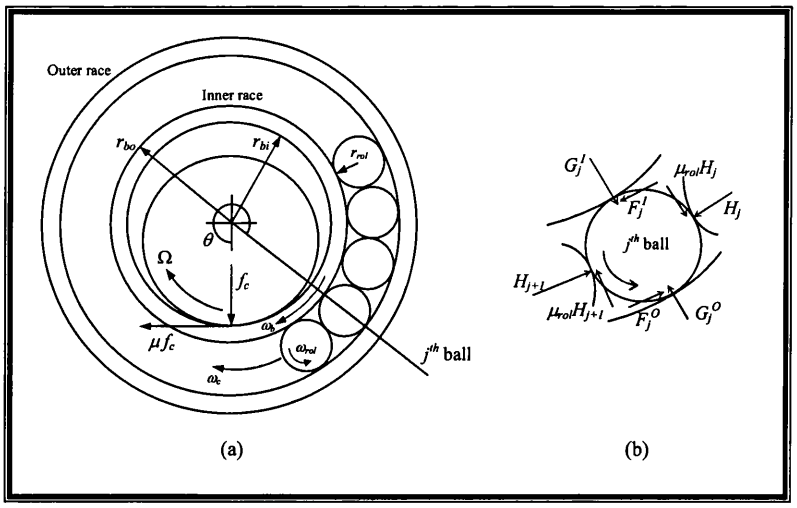

Figure D.1: (a) Cross section of bearing and rotor and (b) Forces acting on j^{th} ball

D.1 Inner Race Motion

The inner race angular acceleration is governed by,

$$I_b\dot{\omega}_b = r_{bi}\mu f_c - r_{bo}\sum_{j=1}^{n} F_j^I \tag{D.1}$$

where n is the number of ball elements, I_b is the inertia of inner race and F_j^I is the friction force between the outer boundary of the inner race and j^{th} ball element.

D.2 Ball Motion (Rolling/Circulatory Without Cage)

Individual ball rotational motion is governed by,

$$I_{rol}\dot{\omega}_{rolj} = r_{rol}\left[F_j^I + F_j^O - \mu_{rol}(H_j + H_{j+1})\right] \tag{D.2}$$

where F, H are the frictional and interaction forces on j^{th} ball. Radially, the balls are constrained to follow a circular path so that

$$m_{rol}(r_{bo}+r_{rol})\omega_{cj}^2 = G_j^O - G_j^I - \mu_{rol}(H_j - H_{j+1}) \tag{D.3}$$

where G_j^O and G_j^I are the normal forces as shown in figure D.1. The circulatory angular acceleration for a single ball is governed by

$$I_{cj}\dot{\omega}_{cj} = r_{bo}F_j^I - (r_{bo}+2r_{rol})\,F_j^O + (r_{bo}+r_{rol})\,(H_j - H_{j+1}) \tag{D.4}$$

where

$$I_{Cj} = m_{rol}(r_{bo}+r_{rol})^2 \tag{D.5}$$

D.3 Bulk Motion Equations

The equation involving ball motions may now be summed over all balls. This applied to equations (D.2) to (D.5) results in the system,

$$I_b\dot{\omega}_b = r_{bi}\mu f_c - r_{bo}\hat{F}^I \tag{D.6}$$

$$nI_{rol}\dot{\bar{\omega}}_{rol} = r_{rol}(\hat{F}^I + \hat{F}^O - 2\mu_{rol}\hat{H}) \tag{D.7}$$

$$nm_{rol}(r_{bo}+r_{rol})\bar{\omega}_c^2 = \hat{G}^O - \hat{G}^I \tag{D.8}$$

$$I_c\dot{\bar{\omega}}_c = r_{bo}\hat{F}^I - (r_{bo}+2r_{rol})\,\hat{F}^O \tag{D.9}$$

where

$$
\begin{aligned}
I_c &= n m_{rol}(r_{bo} + r_{rol})^2 \\
\hat{F}^I &= \sum_{j=1}^{n} F_j^I \quad ; \quad \hat{F}^O = \sum_{j=1}^{n} F_j^O \\
\hat{G}^I &= \sum_{j=1}^{n} G_j^I \quad ; \quad \hat{G}^O = \sum_{j=1}^{n} G_j^O \quad ; \quad \hat{H} = \sum_{j=1}^{n} H_j \\
\bar{\omega}_{rol} &= \frac{1}{n}\sum_{j=1}^{n} \omega_{rolj} \quad ; \quad \bar{\omega}_c = \frac{1}{n}\sum_{j=1}^{n} \omega_{cj} \quad ; \quad \bar{\omega}_c^2 = \frac{1}{n}\sum_{j=1}^{n} \omega_{cj}^2
\end{aligned}
\tag{D.10}
$$

Note that the interaction forces between ball element cancel out while summing up the forces and moments in equations (D.8) and (D.9).

D.4 Rolling Condition Kinematics

Assuming that all balls have the same rotational velocity $\bar{\omega}_{rol}$, the kinematic relations that apply are

$$\bar{\omega}_{rol} = \frac{\omega_b r_{bo}}{2 r_{rol}} \tag{D.11}$$

$$\bar{\omega}_c = \frac{\bar{\omega}_{rol} r_{rol}}{r_{bo} + r_{rol}} \tag{D.12}$$

D.5 Modified Inner Race Equation of Motion

Using equations (D.11) and (D.12), the equations (D.7) and (D.9) become,

$$\frac{n I_{rol} r_{bo}}{2 r_{rol}} \dot{\omega}_b = r_{rol}(\hat{F}^I + \hat{F}^O - 2\mu_{rol}\hat{H}) \tag{D.13}$$

$$\frac{I_c r_{bo}}{2(r_{bo}+r_{rol})} = r_{bo}\hat{F}^I - (r_{bo}+2r_{rol})\,\hat{F}^O \tag{D.14}$$

Removing $\hat{F}^O$, yields,

$$\left(\frac{(1+2s)nI_{rol}}{(1+s)4s^2} + \frac{I_c}{4(1+s)^2}\right)\dot{\omega}_b = r_{bo}\left(\hat{F}^I - \frac{(1+2s)}{(1+s)}\mu_{rol}\hat{H}\right) \tag{D.15}$$

where $s = r_{rol}/r_{bo}$. Eliminating $\hat{F}^I$ term using equation (D.1) gives,

$$\left(I_b + \frac{(1+2s)nI_{rol}}{(1+s)4s^2} + \frac{I_c}{4(1+s)^2}\right)\dot{\omega}_b = r_{bi}\mu f_c - r_{bo}\frac{(1+2s)}{(1+s)}\mu_{rol}\hat{H} \tag{D.16}$$

The effective inertia of combined rollers and inner race is therefore,

$$I = \left(I_b + \frac{(1+2s)nI_{rol}}{(1+s)4s^2} + \frac{I_c}{4(1+s)^2}\right) \tag{D.17}$$

where $I_b = m_b r_{bo}^2$, $I_{rol} = \frac{2}{5}m_{rol}r_{rol}^2$ and $I_c = m_{rol}(r_{bo}+r_{rol})^2$.